Aalborg University

DENMARK

Voltage control in the future power transmission systems

Qin, Nan

VOLTAGE CONTROL IN THE FUTURE POWER TRANSMISSION SYSTEMS

BY
NAN QIN

DISSERTATION SUBMITTED 2016

AALBORG UNIVERSITY
DENMARK

VOLTAGE CONTROL IN THE FUTURE POWER TRANSMISSION SYSTEMS

by

Nan Qin

AALBORG UNIVERSITY
DENMARK

Dissertation submitted to Faculty of Engineering, Science and Medicine
at Aalborg University
in Partial Fulfillment of the requirements for the Degree of
Doctor of Philosophy in Electrical Engineering

Department of Energy Technology
Aalborg University, Denmark
June 2016

See how easy it is, once you know how?

To my wife, Si Chen

and my sons, Bohan Qin and Rubin Qin

ABSTRACT

Wind energy in Denmark covers 42% of the total power consumption in 2015, and will share up to 50% by 2020. Consequently, the conventional power plants are decommissioning. Under the progress of the green transition, the national decision leads to underground many overhead lines in the future transmission system. These issues initiate the infrastructure constructions of the transmission system, i.e. transmission lines over 100 kV in the specific areas will be undergrounded. Many switchable and variable shunts will be placed in the grid for fully compensating the capacitive cables. In order to ensure a highly reliable transmission, e.g. balancing the generation and the consumption in large geographic regions, the exchange capacities will be enlarged by upgrading the interconnections. The Danish power system, the electricity transportation hub between the Nordic and continental European systems, driving by the market, is highly flexible. As more and more renewable energy integrating to the system, the voltage control in the future power system is becoming a challenging objective.

*This project considering the future challenges is to design a **robust** Automatic Voltage Control (AVC) system that **maintains the voltage** inside the acceptable band, optimally **reserves the reactive power** in the continuous reactive power components, and be operated in an **economic** way.*

The review of the existing AVC systems is presented in the thesis. A centralized voltage control system with decentralized fallback controllers is proposed, to address the challenges in the Danish transmission system. A national control center is expected to periodically dispatch the setpoints to the reactive power components in a closed loop. The optimal setpoints of the reactive power components are obtained from a decision making process, which formulates an optimization problem. The objective of the Danish AVC system is to minimize the operational cost including the grid loss and the regulation cost of discrete components while reserving the reactive power in the continuous reactive power components as much as possible. The cost of the grid loss and regulations are converted to the expense, coupling to the price signal from the spot market, which provides more precise and meaningful decisions than the existing AVC systems. Moreover, as a market-driven system, the transits in the main corridors vary according to the market price, which leads to frequent adjustments on the voltage profile. In order to taking into account the system variability, the proposed AVC system is coupled to the forecasting system, making decisions based on several snapshots in a time horizon. Such multi-stage optimization is verified superior than the existing AVC systems in term of the cost minimization. In the multi-stage optimization based AVC system, the forecasted snapshots representing the load flow in the upcoming stages are involved. Due to the high share of the wind energy being in the system, the forecasting errors exist in the predicted stages. The voltage uncertainty caused by the wind power forecasting errors is estimated, which is applied as a voltage security margin to further constrain the voltage magnitude in the optimization problem. The problem under the uncertainty is therefore converted to a deterministic problem, which is strongly tractable for improving the robustness.

In case the centralized AVC system is malfunctioning, e.g. telecommunications fails, the distributed fallback controllers will take the control responsibility to maintain the voltage in the acceptable band. The fallback scheme installed at substations monitoring local voltage, switch in/out shunts following inverse time characteristics, maintaining the voltage without telecommunications. The entire AVC system robustness is therefore improved.

In addition to the AVC system study, there is a chapter introducing the implementation of the advanced load flow calculation method, i.e. Holomorphic embedding load flow method (HELM). It can solve the load flow problem analytically without an initial guess, and thereby avoid the numerical non-convergence problem. In this way, the HELM algorithm can be an alternative method for the Newton-Raphson method for the load flow calculation to provide more insight on the system conditions.

This thesis focuses on the problem formulation and implementation. The AVC decision making and HELM algorithms are implemented in Matlab®, and the fallback scheme is modelled in DIgSILENT® Powerfactory. The functionalities of the proposed AVC system are simulated based on the measurement data from the Energy Management System in the Danish electricity control center, where the network model represents the western Danish transmission system. The studies provide the understandings of the proposed Danish AVC solution that is superior to the existing AVC systems in term of the cost minimization and the robustness, which shed light to the industrial applications.

RESUMÉ

For mere end 20 år har det været en sammenhængende plan, som alle danske regeringer for at slå den danske elproduktion væk fra fossile brændsler til vedvarende energi. Resultatet er, at 42% af det samlede danske elforbrug dækket af vindkraft i 2015, og sigter mod 50% i 2020. Derfor er de konventionelle kraftværker nedlukning. Én anden konsekvens er den offentlige måde generelt tækning af grønt, hvilket har ført til en national beslutning om kabellægning fremtidens transmissionssystem. Disse spørgsmål indlede infrastruktur konstruktioner af transmissionen systemet, dvs. en stor mængde af luftledninger over 100 kV vil blive undergrundede kabler. Mange koblerbar og variable reaktive shunter vil blive placeret i nettet for fuld kompensering af kabler. For at sikre en meget pålidelig transmission, tilstrækkelig elproduktion at balancere forbruger vil udveksle kapacitet udvides ved at opgradere sammenkoblinger gennem markedsmekanismen. Det danske elsystem som er én hub af el transport mellem de nordiske og kontinentale europæiske systemer og kørsel af markedet, er meget fleksibel. Som mere og mere vedvarende energi integration til systemet, er den spænding kontrol i fremtid systemet skal blive et udfordret mål.

*Dette projekt overvejer de fremtidige udfordringer er at designe et **robust** Automatic Voltage Control (AVC) system, der **fastholder den spænding** inde i acceptabel band, optimalt **forbeholder reaktive effekt** i de kontinuerlige reaktive effekt komponenter, og drives på en **økonomisk** måde.*

Afhandlingen starter fra gennemgangen af de eksisterende AVC systemer. Forskellige kraftsystemer står over for forskellige udfordringer, hvilket er grunden til AVC er skræddersyet efter de elementer i kraftsystemer, der skal styres. Imødegå udfordringerne i det danske elsystem, ét centraliseret system kontrol med decentrale fallback kontroller foreslås. Ét nationalt kontrolcenter jævnligt afsender setpunkter til de reaktive effekt komponenter i et lukket kredsløb. De optimale setpunkter af den reaktive effekt komponenter opnås fra en beslutningsproces, der formulerer en optimering problem. Formålet med det danske AVC system er at minimere de operationelle omkostninger, herunder nettabet og regulering omkostninger af diskrete komponenter, mens forbeholde den reaktive effekt i kontinuerlige reaktive effekt komponenterne så meget som muligt. Udgifterne til nettabet og reguleringer konverteres til bekostning, kobling til pris signalet fra spotmarkedet, hvilket giver mere præcise og meningsfulde beslutninger end de eksisterende AVC systemer. I øvrigt som ét markedsdrevet system, transitter i de vigtigste korridorer varierede ofte som resulterer, at spændingsprofil ofte justeres i overensstemmelse hermed. For at tage hensyn til systemets variabilitet, er det foreslået AVC systemet koblet til prognoser system, tage beslutninger baseret på flere snapshots i en tidshorisont i stedet for øjeblikkelig snapshot. Det formulerer sådan multiple-stage optimering som verificeres overlegen end de eksisterede AVC systemer i løbetid omkostningsminimering. I den multiple-stage optimering baseret AVC system, er de forventede snapshots repræsenterer effekt flow i de kommende stager involverede. På grund af den høje andel af vindenergi er i systemet, eksisterer prognosers fejler i de forventede stager. Spændings variationer forårsaget af vindkraft fejl i overslagene skønnes, som anvendes som en spænding sikkerhed margin for yderligere at begrænse spændingen størrelsesorden i optimeringsproblem. Problemet med usikkerhed konverteres derfor til ét deterministisk problem, som er stærkt medgørlig til forbedring af robusthed.

I tilfælde af centraliseret AVC systemet ikke fungerer, for eksampel telekommunikation mislykkes, de distribuerede fallback kontroller vil tage kontrol ansvar for at opretholde spændingen i acceptabel band. Fallback ordning installeret på understationer overvågning lokale spænding, kobler ind/ud shunter mht. inverse tid karakteristika og fastholde den spænding uden telekommunikation. På denne måde, hele systemet robusthed forbedres.

Ud over den AVC systemet undersøgelsen, er der ét kapitel om gennemførelsen den avancerede effekt flow beregningsmetode, dvs. Holomorphic Embedding Load Flow metode (HELM). Det kan løse effekt flow problem analytisk uden et indledende gæt, og derved undgå den numeriske ingen-

konvergens problem. På denne måde kan den HELM algoritme være en alternativ metode til Newton-Raphson metode for at løse effekt flow problemer og give mere indsigt i systemet betingelser.

Denne afhandling fokuserer på problems formulering og implementering. AVC beslutningstagning og HELM algoritme er implementeret i Matlab®, og fallback ordningen er modelleret i DIgSILENT® PowerFactory. De funktionaliteter i det foreslåede AVC system simuleres baseret på måledata fra Energy Management System i danske el kontrolcenteret, hvor netværket model repræsenterer det vestlige danske transmissionssystem. Undersøgelserne giver forståelser af den foreslåede danske AVC løsning, der er overlegen i forhold til de eksisterende AVC systemer i løbetid omkostningsminimering og robusthed, der forventes at inspirere de industrielle anvendelser.

ACKNOWLEDGEMENT

<div align="right">
Nan Qin
Taulov, Denmark
June 30, 2016
</div>

CONTENTS

NOMENCLATURE

C_P^d	Series branches losses cost
C_τ^d	Tap ratio changes cost
C_b^d	Shunt susceptance changes cost
C_g^d	Generator reactive power output cost
M^d, Z^d, Y^d	The ancillary variables for the transformer tap ratio, shunt susceptance and the generator reactive power at stage d, respectively
p_τ	The price of the transformer tap changing
p_b	The price of the shunt switching
p_Q	The price of the generator reactive power
kr	Danish krone (1€ = 7.5 kr)
e^j	Exponential operator
v_f, v_t	Sending and the receiving ends voltages
R_s, X_s	Series resistance and the reactance
τ, ϑ	Transformer tap ratio and phase shift angle
b	Shunt susceptance
Q_g	Generator reactive power output
d, i, k	Indices
K	Participation factor
V	Voltage magnitude
I	Current magnitude
$\emptyset$	Angle between the voltage and the current
ΔV_W	Voltage variations due to wind power forecasting errors
Q_{br}	Reactive power in a branch
Q_{brmin}, Q_{brmax}	Min. and max. reactive power in branch
G, B	Conductance and the susceptance
V_{min}, V_{max}	Min. and max. voltage magnitude
N_P	Number of P nodes in a P/PVQ group
N	Total number of stages
N_{br}	Total number of branches
N_τ	Total number of tap-able transformers
N_b	Total number of shunts
N_g	Total number of generators
N_v	Total number of busbar
N_W	Total number of wind turbine connected bus
$\mathcal{D}$	Stage set
$\mathcal{L}$	Branch set
$\mathcal{T}$	Tap-able transformer set
$\mathcal{B}$	Switchable shunt set
$\mathcal{G}$	Generator set
$\mathcal{V}$	Busbar set
$\{ref\}$	Reference busbar set
δ	Voltage angle
P_i, Q_i	Active power and reactive power at node i
P_l, Q_l	Active power, reactive power loads
P_G, Q_G	Active power, reactive power generations
$\widehat{P_W}, \widehat{Q_W}$	Expected active power and reactive power generations at wind turbine connected bus
b_{min}, b_{max}	Min. and max. susceptance of a shunt
τ_{min}, τ_{max}	Min. and max. tap ratio of a transformer

Q_{gmin}, Q_{gmax}	Min., max. generator reactive power limits
b_{Nmin}^d, b_{Nmax}^d	Min. and max. total susceptance change at stage d
$\tau_{Nmin}^d, \tau_{Nmax}^d$	Min. and max. total ratio change at stage d
S_P, S_Q	Voltage sensitivity matrices w.r.t active power and reactive power
μ_V	Expected voltage variation
ρ	Correlation coefficients
$\mathcal{N}$	Multivariate normal distribution
$cos\emptyset$	Power factor
Σ	Wind power forecasting errors covariance matrix
α	Confidence level
T	Transpose operation
P_W, Q_W	Actual active power and reactive power of wind production
ΔP_W	Wind power forecasting error
$\mathcal{U}$	Uncertainty set
$\mathcal{W}$	Set of wind turbine connected bus
$\underline{\Delta P_W}, \overline{\Delta P_W}$	Lower and upper boundary of wind power forecasting error
$\begin{bmatrix} J_{P\delta} & J_{PV} \\ J_{Q\delta} & J_{QV} \end{bmatrix}$	Jacobian matrix of active power and reactive power w.r.t. to voltage angle and magnitude, respectively
Σ_V	Voltage covariance matrix
σ^2	Variance of the forecasting errors
W_1, W_2, W_3, W_4	Weights in the objective function
Δt	Time interval between two stages
J	Objective function of MORPF
x_z	Discrete variable
x_{zmax}, x_{zmin}	Max. and min. limits of discrete variables
x_z^*	Target integer of discrete variable
N_{cont}	Max. iteration number for discretization
N_z	Number of discrete variables
γ	Weight of penalty function
K_γ	Parameter for increasing γ at each iteration
ε	Acceptable tolerance
$\Delta P, \Delta Q$	Active power and reactive power mismatch
$\Delta \delta, \Delta V$	Voltage angle, voltage magnitude mismatch
z	Set of zones
s	The embedding complex variable in HELM
z	The complex variable in HELM
AVC	Automatic voltage control
DK1	The western Danish transmission system
DK2	The eastern Danish transmission system
DKK	Danish currency
FACT	Flexible AC transmission system
SVC	Static var compensator
StatCom	Static synchronous compensator
HELM	Holomorphic embedding load flow method
TR	Trust region
VSM	Voltage security margin
PQ	Node type with known active power and reactive power
PV	Node type with known active power and voltage magnitude
SL	Slack node with known voltage angle and magnitude
P/PVQ	Node types with known active and reactive power and voltage magnitude/with known active power only
NR	Newton-Raphson
PVR	Primary voltage regulation

SVR	Secondary voltage regulation
TVR	Tertiary voltage regulations
AVR	Automatic voltage regulator
CSVC	Coordinated secondary voltage control
REPORT	Reactive power regulators
ORPF	Optimal reactive power flow
MORPF	Multi-stage optimal reactive power flow
VSC	Voltage source converter
VSR	Variable shunt reactor
IGBT	Insulated gate bipolar transistor
PLL	Phase lock loop
LCC	Line-commutated
HVDC	High-voltage direct current
OLTC	On-load tap changer
RPC	Reactive power controller
UCTE	Union for the coordination of the transmission of electricity
SCADA	Supervisory control and data acquisition
SE	State estimator
EMS	Energy management system
PDIPM	Primal-dual interior point method
TSO	Transmission system operator
DSO	Distribution system operators
NWP	Numerical weather prediction
CHP	Combined heat and power plants
NORTA	Normal-to-anything
MINLP	Mixed integer nonlinear programming
PDF	Probability density function
SBA	Scenario based approach
BTS	Brainy's tree sorting
SK	Skagerrak
KS	KontiSkan
SB	Storebælt
KO	Kontek
PCC	Point of common coupling
POC	Point of connection
WPFE	Wind power forecasting error
ITC	Inverse time characteristic
PMU	Phasor Measurement Unit

CHAPTER 1. INTRODUCTION

The aim of this chapter is to introduce the current Danish power system and the foreseen voltage control challenges in the future. The motivation and the objective of the whole project are presented, following by the outline of this presentation.

1. BACKGROUND

Denmark as the pioneer has been starting to integrate the wind energy into the power system in early 1980s. The penetration of wind energy is continually increasing in the Danish power system. As shown in Figure 1, the installed wind power capacity will be more than 5000 MW by 2016. The share of wind energy on covering the demand was 42% in 2015 [1]. Moreover, in order to achieve the political goal by 2020 that the share of wind energy will reach 50% by 2020 [2], several near-shore wind farms, new offshore wind farms will be built. In addition, the old wind turbines expiring the designed life time will be replaced by the new wind turbines with upgraded scales. In the future, the wind power as the major clean energy in Denmark, will greatly contribute to the electricity production.
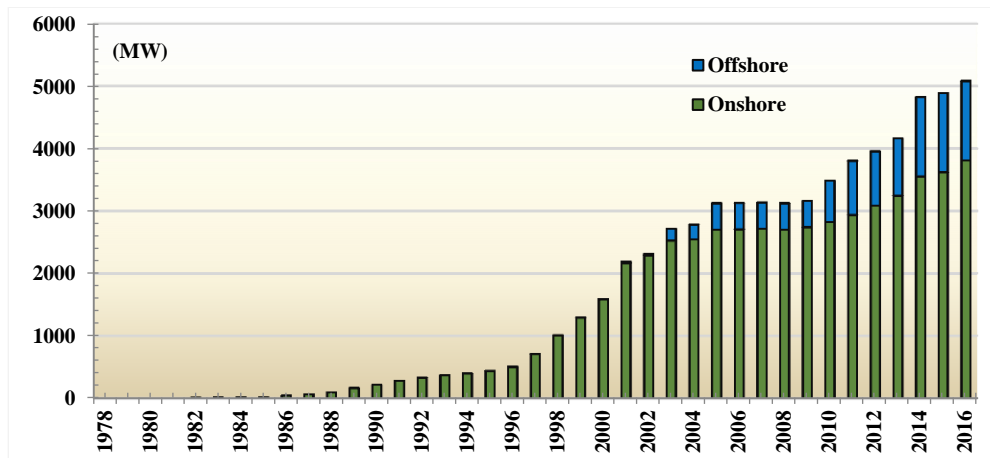
Figure 1. The installed wind power capacity since 1978.

The high share of wind energy in the power system significantly changes the electricity transmission pattern. The Danish power system in 1980s, as a conventional power system, the electricity is produced by the fossil fuel based large central power plants, and transmitted to the consumers through the bulk system. However, as more and more wind energy integrating to the system, the conventional power plants are gradually decommissioning. As a result, in the current Danish power system, in addition to the large offshore wind farms connected to the transmission grid, the distributed combined heat and power plants and the small scale wind turbines are connected to the distribution grids, spread in the system, as shown in Figure 2.

Denmark participated in the Nord Pool electricity market since 2000 [3]. One of the considerations is to use the market as a tool for maintaining the high security of supply in the transmission level. The power balance is thus kept in a large geographic area to overcome the potential power unbalances caused by the intermittence of the wind power production. For example, the hydro power in Norway can be storage for the wind power in Denmark, through trading mechanism of the electricity markets.
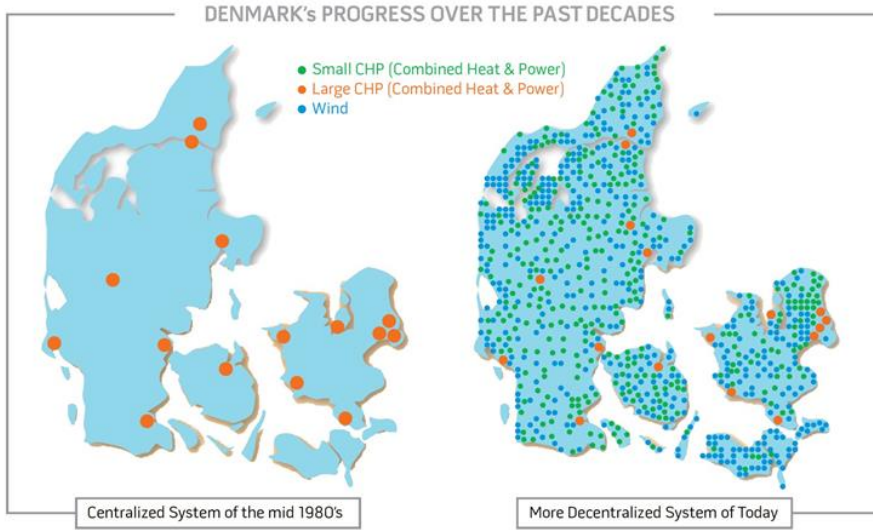
Figure 2. Danish power system transformation.

The Danish power system is an electricity transportation hub between the Nordic power systems and the continental European system. As shown in Figure 3, the western Danish power system (DK1) is synchronous with Germany and then the continental Europe, whereas the eastern Danish power system (DK2) is synchronous with Sweden and then the Nordic countries. A HVDC link is connected between DK1 and DK2. Referring to the installed generation capacity and the peak demand shown in Table 1, the interchange capacities between Denmark and the neighboring countries presented in Table 2 are relatively large. The total amount of transfer capacity over the borders is close to the peak demand. This is one of the essential factors to maintain the high security of supply, that the large transfer capacities ensure sufficient balancing power from neighboring systems via market trading.

Table 1. The key figures of the Danish power systems in 2015 [4]-[5].

Installed capacity	DK1	DK2	Total
Central power stations (MW)	2020	2180	4200
Local power plants (MW)	1845	645	2490
Offshore wind power (MW)	899	373	4897
Onshore wind power (MW)	3013	612	
Photovoltaic cells (MW)		608	608
Peak demand (MWh/h)	3622	2546	6168

Table 2. The interconnections between the Danish power systems to neighboring power systems [4].

Danish systems	Neighboring systems	Import (MW)	Export (MW)
Western Danish Power System (DK1)	Norway	1700	1700
	Sweden	680	740
	Germany	1500	1640
	DK2	600	600
Eastern Danish Power System (DK2)	Sweden	1300	1700
	Germany	600	600
	DK1	600	600
Bornholm	Sweden	60	60
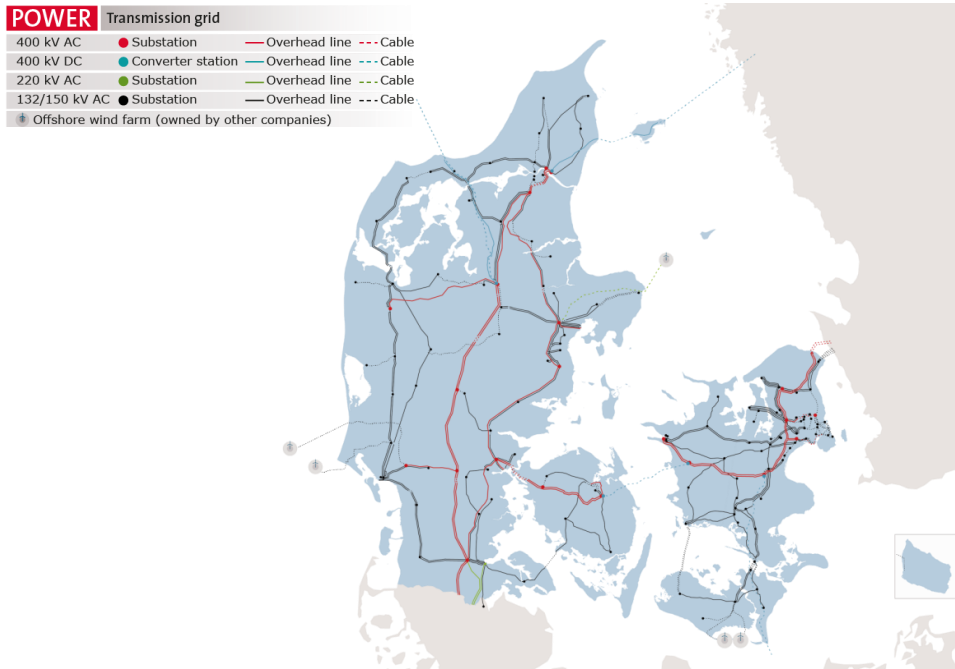
Figure 3. The Danish power transmission system in 2016.

In addition to largely integration of the wind power and expansion of the interchange capacities to the neighboring systems, the public decision starts the constructions of undergrounding the future transmission system [6]. The entire 150/132 kV grids will be undergrounded and the new 400 kV connections will be built with underground cables. It will not be only for beautification but also reduce the contingencies in the future system that less affected by weather conditions.

2. CHALLENGES OF THE VOLTAGE CONTROL IN THE DANISH SYSTEM

As the Transmission System Operator (TSO) in Denmark, Eneginet.dk is responsible to operate the transmission system in a most economical way while maintaining the system security of supply. Voltage control is one of the critical issues, which requires system operators pay much attention in the daily operations. As mentioned above, integration of the renewable energy changes the power transmission pattern from the centralized production to the dispersed generation while driving the system in a flexible manner via trading in the markets. Voltage control in such system is becoming a challenge objective.

2.1. REACTIVE POWER RESERVE

Among the present wind turbines in Denmark, nearly 60% of the installed capacity is of the "Danish concept" type, i.e. fixed speed wind turbines with asynchronous generators directly connect to the grid (Type I), which consumes reactive power for excitations. The conventional central power plants are typically equipped with excitation system to control the voltage. They are the backbone of the voltage control system. As central power plants are being forced out of service, the system may potentially lack of the reactive power resource to support the voltage in emergent situations. Therefore, it is necessary to maintain sufficient reactive power reserves in the continuous reactive power sources. In order to ensure the voltage stability in the future grid, many ancillary components e.g. synchronous condenser, SVC and StatCom will be placed in the grid. In addition, the new wind

farms should comply with the grid code, not only be capable of low-voltage-ride-through, but also be able to participate in the centralized voltage control system in the normal operational conditions [7]. Optimally operate these continuous reactive power components for the voltage control is one of the important tasks in the future system.

2.2. COORDINATED VOLTAGE CONTROL

The conventional power plants continuously control the voltage with the Automatic Voltage Regulator (AVR) devices. In contrast, shunts and transformer taps with a certain size represent a type of discrete regulation devices that introduce step-wise voltage changes. As central power plants are decommissioned, the short-circuit capacity of the system will be low. In this case, an adjustment of the reactive power flow on a control device may result in an unacceptable voltage change. This may lead to cascading adjustments on many control devices.

In the Danish grid, many discrete reactive power components that normally control the reactive power flow on the branches are partially autonomous via local Reactive Power Control (RPC) devices. For example, some RPCs are placed in the HVDC stations to compensate the reactive power consumption by coupling the filters. The control center can thus adjust the setpoints of RPCs through remote control interface. The voltage control should take into account the impacts from the shunt devices, especially in the cases where the short-circuit capacity is low that may lead to the unacceptable voltage changes after the shunt is cut in/out. Therefore, a coordinated control scheme should maintain the voltage and be capable of regulating the control devices with as few adjustments as possible. Moreover, it should reduce the system loss by minimizing the reactive power flow in the grid.

2.3. EFFECTIVE AND EFFICIENT ADJUSTMENTS

The overhead lines in the transmission levels are presently being replaced by underground cables. In the future, partial 400 kV lines and all 150/132 kV transmission lines will be constructed as underground cables. A 400 kV air insulated transmission line typically generate reactive power about 0.7 MVar/km. In contrast, a corresponding 400 kV cable generate reactive power about 12 MVar/km, which is almost 20 times large of the overhead line [8]. As shown in Figure 4, a large number of shunt reactors, i.e. shunts with fixed size and variable shunts, will thus be placed in the grid to fully compensate the cable network for maintaining the voltage levels. If without updating the current manual adjustment based voltage control system, it will be a challenge for operators to regulate the highly increased number of discrete reactive power control devices to obtain a satisfied voltage profile in time, especially when the system is flexible and only few or even no conventional power plants in operation.
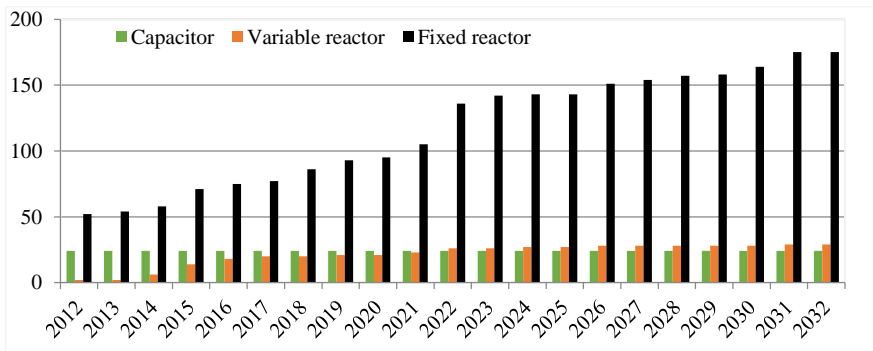
Figure 4. Number of shunt compensation devices in the future grids, including the capacitors, reactors with fixed sizes and variable reactors.

The flexible transit power on the transmission lines can introduce voltage variations, which requires adjusting the reactive power flow in the branches to maintain the voltage within the acceptable band. Most of the Danish interconnections are established as HVDC links during the past 40 years. Nowadays, the ramping speed for the HVDC links limits the changing of transit power to 30 MW/min per HVDC link [9]. One of the main reasons is to provide the operators enough time to manually adjust the reactive power components for the voltage control purposes. It is planned to construct more HVDC links as interconnections to the neighboring systems [4]. The ramping limit, 30 MW/min per HVDC link, is foreseen to be unacceptable for the trading mechanisms of the Nordic electricity market in the future. One of the main issues should be addressed for faster ramping is to effectively and efficiently adjust the reactive power components with few or even no central power plants.

3.   MOTIVATION, PROBLEM FORMULATION AND LIMITATIONS

The power system is energized by the large central power plants that connected at the transmission levels. All the consumptions are connected at the distribution levels. The large amount of power from the central power plants is therefore transferred from the transmission levels to the distribution levels. The produced power is regulated according to the variable consumptions that caused by the human activities. In addition, the voltage is mainly maintained by the large central power plants. This is the conventional power transmission pattern.

The operation of the power system can be classified as normal operational conditions and emergent operational conditions. The normal operational conditions are considered to be steady-state conditions without large disturbances. The load changes over time are relatively small and slow, which belongs to normal operational conditions. Emergent operational conditions occur when the systems are subjected to large disturbances, where the voltage drops significantly and very fast, in a matter of milliseconds. The voltage control system is responsible for maintaining the voltage magnitudes in the normal operational conditions.

The renewable energy penetration increases in the power system. Consequently, the power transmission pattern is significantly changed, i.e. the central power plants are forced out of market that results in less reactive power source in the system; the dispersed production units located in the distribution levels can result in the power flows from the distribution levels to the transmission levels hereafter to change the reactive power balance; the interconnections are enhanced for improving the transmission security that introduces the high flexibility on the power transits in the systems. The present voltage control system based on manual adjustments in normal situations and automatic preventive control in normative emergent situations may be insufficient to overcome the abovementioned challenges in the future grid. An Automatic Voltage Control (AVC) system is therefore expected.

Voltage control in the power system is strongly related to regulation of reactive power flow in the branches. Unlike the active power, the reactive power cannot be efficiently transmitted over a long distance, as the transmission of the reactive power leads to an additional demand in the grid branches, thereby causing voltage violations and extra loss. In addition to maintain the voltage in the acceptable band, the system is typically required to be operated in an economic way, for example, minimizing the grid power loss. In order to obtain an acceptable voltage level while minimizing the grid power loss, the reactive power flow in the grid branches should be as little as possible. Minimizing the reactive power flow is therefore known as optimal reactive power flow (ORPF) problem, which should be solved to obtain the optimal setpoints to the reactive power components, dispatched from the control centers.

In Denmark, Energinet.dk as the TSO maintains the voltage security in the transmission levels. The voltage is kept mainly based on the manual adjustments on the tap changers of transformers, the shunt compensation components and the setpoints of the continued reactive power regulation units i.e. the central power plants, the synchronous condensers and the SVC etc. This process is subjected to more

and more stress as the power system develops for integrating more wind power to the system. In order to overcome the challenges of the voltage control in the future Danish power system, Energinet.dk initializes the implementation of the AVC system in the beginning of 2014. An automatic voltage control scheme is expected to be embedded with the advanced functionalities to enhance the system reliability and efficiency as well as the voltage security. In addition, the optimal power flow based system is expected to reduce the system loss by reducing the reactive power flow in the grid.

Implementation of such voltage control system is another challenge. Typically, the real time system requires that the optimal solution should be obtained within 1 to 2 minutes, during which the voltage control system acquires the measurement data and calculates the optimal setpoints for all control components. An efficient solver is needed to be able to find the solution in time. Moreover, the future voltage control system is supposed to be robust, intelligent and effective, which is able to probably assist the system operators to make the decision for the voltage control purposes. In order to achieve the goals, the following issues are considered to be the most relevant, i.e. representation of the voltage control problem in mathematic expressions; demonstration of the control effects in the simulation tools. The proposed method is expected to be embedded on the control center, where a robust voltage control scheme should be proposed considering the fallback strategy e.g. the system should be operated in case a single station or a part of grid loses the telecommunications to the control center. In addition, the forecast data can be integrated to the voltage control system to enhance the decision making process for obtaining better solutions.

The voltage control system with the aforementioned capabilities can enhance the control capability. It assists the system operators in the control center to understand and efficiently control the system voltage. It allows faster changing rate of the power transits than it today over the countries boundaries. It potentially increases the system feasibility to integrate more renewable energy to achieve the goal of the Danish energy policy i.e. 50% electricity demand is covered by the wind power by 2020.

The proposed method of this project is not able to be demonstrated on the real time system, as only permitted and highly secured operations are allowed to be performed in the control center. Before implementation of the proposed AVC system, many tests should be proofed in advance, for example, system model validation, measurement calibrations and etc. However, the gained knowledge, experience and skills through this project can be transferred to the competence for successfully construct the AVC system for the real time system in Denmark.

4. PROJECT OBJECTIVES

This project is relevant to an ongoing project in Energinet.dk, i.e. implementation of the AVC system in the Danish transmission grid. According to the description of the AVC concept in Energiet.dk, the outcome from this Ph.d project is supposed to shed light to innovate the present voltage control system and inspires the AVC to be more robust and intelligent. For example, the transmission loss can be minimized by minimizing the reactive power flow; the voltage stability margin can be improved by maximizing the dynamic reactive power reserve of the reactive power sources; the switching actions can be minimized for saving the components' life time.

The concept of Danish AVC system is proposed in this Ph.d project together with colleagues from Energinet.dk. The AVC running in the normal operational conditions is supposed to be the centralized control system, which dispatches the setpoints for different control components in each cycle. The following studies are intended to track on the design and implementation of the specified functions. The main objective of this project is:

*How to establish a **robust** automatic voltage control system to **maintain the voltage** inside the acceptable band, optimally **reserve the reactive power** in the continuous reactive power components and be operated in an **economic** way?*

This objective can be broken down to the following 5 sub-objectives.

(i). *Is it beneficial to reduce the system active power losses by improved voltage control?*

The decision making algorithm should be well established. A promising method should be selected for solving the problem.

(ii). *How can switching costs be included in the optimizations?*

The regulating actions of control components should be minimized. The formulation should be updated for addressing the cost of the adjustments. The reactive power schedule based on the forecasting data should be studied and used to reduce the switching cost.

(iii). *How to consider the continuous dynamic reactive power reserve?*

The reactive power in the continuous reactive power components should be reserved as much as possible. The discrete reactive power components are used to assist the central power plants and the synchronous condensers to be operated close to the neutral.

(iv). *How to make the AVC system robust for real time applications?*

In case the centralized AVC is malfunctioning, the local control is expected to be activated that regulates the connected components itself without communication to the control center. The impact of the fallback strategy in the system level should be studied.

(v). *What is the scalability of Danish concept AVC to other systems and types of components?*

The effectiveness of different components on the control objective is investigated to answer, for example, how good a wind farm is for voltage control and what the constraint is.

5.   THESIS OUTLINE

This project focuses on the problem formulation, solution and demonstration the proposed approach to the Danish power system through simulations.

The thesis starts from the introduction of the most popular load flow calculation method in Chapter 2, following the introduction of the new method, Holomorphic Embedding load flow method (HELM). The numerical optimization techniques for the nonlinear programming, i.e. prime-dual interior point method (PDIPM) and trust-region (TR) method, are introduced in Chapter 3. The combined PDIPM and TR method is finally selected to solve the formulated optimization problem.

In Chapter 4, the state-of-the-art AVC systems are reviewed. Based on the knowledge of the existing AVC systems, a Danish concept AVC is proposed. The abovementioned challenges are well formulated to an optimization problem. The cost of the objective function is converted to the expense where the market price signal is coupled to the grid loss. The found cost of the objective is therefore the actual cost in value, which is more understandable for the operators to drive the system. The system variability is considered in the multi-stage optimal reactive power flow (MORPF) algorithm, where the wind power forecasting system is coupled to provide the predicted load flow conditions for

the upcoming stages. In order to get rid of the uncertainty from the forecasting systems in the decision making algorithm, the scenario based method and the Voltage Security Margin (VSM) are conducted. The VSM based method is selected for improve the decision robustness due to its strong tractability.

An offline simulation platform is built to assess the proposed approach applying the measurement data from Danish electricity control center. The implementation work is described in Chapter 5, where a simple example is presented to demonstrate the calculation procedure. All mathematic derivations for the modelling and problem formulations are collected in Appendix.

The systematic case studies based on the measurement data of the DK1 system are carried out in Chapter 6. The demonstration starts from the conventional algorithm, loss minimization, and finally ends up at the proposed MORPF framework. The superiority of the proposed approach in the term of the cost minimization and robustness is demonstrated.

The fallback scheme is introduced in Chapter 7, as a backup solution once the centralized AVC is malfunctioning or the telecommunication between the local stations to the control center is lost. The proposed fallback scheme is modelled in DIgSILENT power factory, where the case studies are carried out based on the DK1 system model to demonstrate the effectiveness.

Conclusion is given in Chapter 8. The defined questions of the 5 sub-objectives are well answered. The future work is proposed.

CHAPTER 2. LOAD FLOW CALCULATIONS

The load flow is one of the most fundamental concepts in the power system engineering. The basic function of the AVC system is to find out a feasible load flow in the grid, where the voltage profile of the whole system is within the acceptable operational band. This chapter will introduce the most popular and the newly proposed analytical method for the load flow calculations.

1. LOAD FLOW ANALYSIS

The objective of the load flow calculations is to obtain all node voltages and all branch currents. Generally, for a grid with n independent nodes, the following equations (2.1)-(2.2) are valid.

$$\begin{bmatrix} Y_{11} & Y_{12} & \cdots & Y_{13} \\ Y_{21} & Y_{22} & \cdots & Y_{23} \\ \vdots & \vdots & \ddots & \vdots \\ Y_{n1} & Y_{n2} & \cdots & Y_{nn} \end{bmatrix} \begin{bmatrix} v_1 \\ v_2 \\ \vdots \\ v_n \end{bmatrix} = \begin{bmatrix} i_1 \\ i_2 \\ \vdots \\ i_n \end{bmatrix} \tag{2.1}$$

$$[Y][v] = [i] \tag{2.2}$$

where $[v]$ is the node voltage vector and $[i]$ is the node current injection. Matrix $[Y]$ is the admittance matrix, where the diagonal element Y_{ii} is the self-admittance at node i that equals to the sum of all branch admittances connected to node i. The off-diagonal element of the admittance matrix Y_{ij} equals to the negative of branch admittance connected between nodes i and j. If there is no branches between nodes i and j, then Y_{ij} equals to zero. For a normal transmission network, the admittance matrix is a sparse matrix, but not necessarily symmetrical due to the phase-shifting transformers. Figure 5 shows an example of an admittance matrix that represents the Danish transmission grid. It is highly sparse that requires fewer matrix factorizations than dense impedance matrix based approaches, which is the reason for using admittance matrix instead of the impedance matrix in load flow calculations.
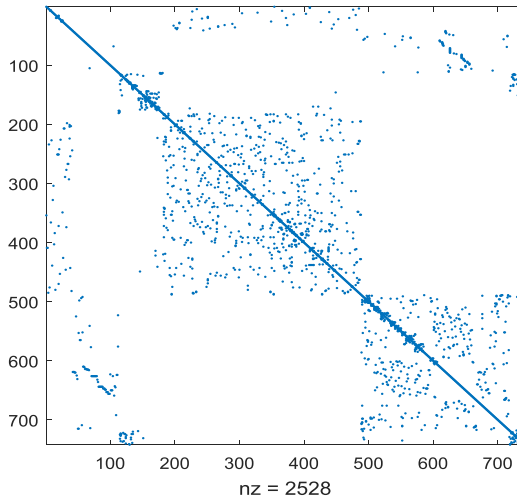
Figure 5. The Danish transmission system admittance matrix.

Loads connected at nodes are included in branches. If all branch impedances are constant including the constant impedance load, the load flow equations are linear, (2.3), where the constant impedance load is included in the system admittance matrix.

$$[Y][v] = 0$$	(2.3)

However, the load at each node is typically modelled as constant power in the transmission grid, which turns the load flow equations to be nonlinear. The complex power is expressed as the product of the voltage and current vectors, which is represented in the polar form, (2.4). The current flow at each node is therefore represented in (2.5), where the current flowing into each node equals to the current drawn by the complex power at the nodes.

$$vi^* = VIe^{j(\delta_V - \delta_I)} = VIe^{j\emptyset}$$	(2.4)
$$\sum_{k=1}^{n} Y_{ik} v_k = \frac{P_i - jQ_i}{v_i^*}, i \in \mathcal{V}$$	(2.5)

Where P_i and Q_i are the total power injection at node i, (2.6)-(2.7).

$$P_i = P_{li} - P_{Gi}$$	(2.6)
$$Q_i = Q_{li} - Q_{Gi}$$	(2.7)

Equation (2.5) can be divided into real and imaginary parts. It results two equations and four variables for each node, i.e. the node voltage magnitude V, the voltage angle δ, the node active power injection P and the node reactive power injection Q. Typically, to solve (2.5), two of them should be given at each node. According to the known variables, the nodes are classified.

(i). PV node. The active power and the voltage magnitude at this type of node are known. This type of node usually represents the busbar where the voltage source is connected, e.g. generators equipped with excitation systems. The voltage angle and the reactive power are unknown. There are typically limits to constrain the reactive power variables, e.g. the generation capability curve constrains the generator reactive power output according to the active power production.

(ii). PQ node. The active power and reactive power are known. This type of node usually represents the busbar where the load is connected, e.g. the power consumptions. However, the generator without voltage control abilities is also connected to PQ node, as a negative load to produce the current instead of consume it. The PQ nodes are passive nodes, where the voltage magnitude and the voltage angle are the results of the current flow in the grid.

(iii). Slack (SL) node. It is also called reference node, as the voltage magnitude and the voltage angle are given. The voltage angles in other nodes are referred to the voltage angle at SL node. Since the system power loss is unknown, the active power and the reactive power at SL node are used to balance the system power. For each synchronous system, only one SL node can provide the reference voltage angle. However, the system power mismatches due to the grid losses can be shared among different SL nodes under predefined proportions.

(iv). P and PVQ nodes. In practical applications, the voltage magnitudes at some nodes are remotely controlled by one or a group of generators [10]. As shown in Figure 6, the node under control is typically a PQ node, e.g. a pilot node in a voltage control system. In the case of a PQ node under remote control, this node becomes to a PVQ node, as the active power, the reactive power and the voltage magnitude are known. The controlling node that generators connected, changes from PV node to P node, as the generator reactive power is adjusted according to the needs at PVQ node. The voltage magnitudes at P nodes are therefore unknown due to the reactive power regulations for maintaining the voltage at the PVQ node. In the case of several generators remotely control the voltage at a PVQ node, a participation factor of each generator is needed to share the reactive power

outputs among them. The PVQ and P nodes are coupled, where the voltage magnitudes at PVQ nodes are maintained by the corresponding generators at P nodes.
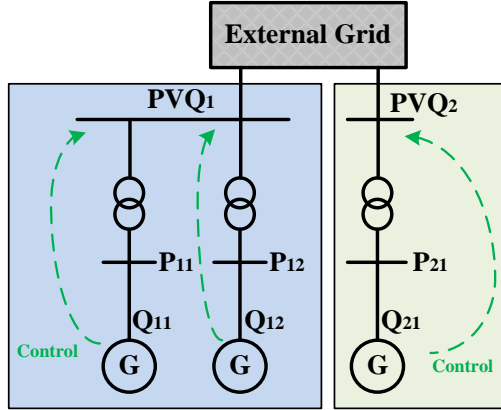
Figure 6. Some nodes are remotely controlled by one of a group of generators.

Table 3. Summarized node type in the load flow calculation.

Bus Type		Data inputs	Unknown variables
SL		V, δ	P, Q
PQ		P, Q	V, δ
PV		P, V	δ, Q
Coupled	P	P, K	V, δ, Q
	PVQ	P, V, Q	δ

Table 3 summarizes the node types in the load flow calculations, where K is the participation factor for the generators to share the reactive power contribution for controlling the voltage. For each P/PVQ group, the individual generator output complies with (2.8).

$$Q_i = K_i \sum_i^{N_{p,i}} Q_i \tag{2.8}$$

Since the voltage at SL node is already known, only $n - 1$ node voltages need to be calculated. The total number of load flow equations is $2(n - 1)$. The power injection at SL node is found when all voltages are obtained.

2. NEWTON-RAPHSON METHOD

The most popular approach to solve the load flow equations is Newton-Raphson (NR) method [11]. The principle is to linearize the load flow equations by expanding the load flow equations with the Taylor series and neglecting the second and higher order terms. The compact form of the load flow equation can be expressed in (2.9), where x is unknown variables. The objective of (2.9) is to find out x, that (2.9) can be valid, i.e. the system power is balanced.

Applying NR method to solve it, an initial guess for the unknown variables, x^0, is needed. The difference between the initial guess and the final solution is thus Δx^0. Equation (2.10) is obtained, by replacing the final solution x with the initial guess, x^0, and the differences, Δx^0. Therefore, if Δx^0 is

known, then x can be obtained and the problem is solved. In order to derive the differences, Δx^0. Equation (2.10) is expanded with Taylor series, shown in (2.11).

$$g(x) = 0$$	(2.9)
$$g(x^0 + \Delta x^0) = 0$$	(2.10)
$$g(x^0 + \Delta x^0) = g(x^0) + g_x(x^0)\Delta x^0 + \cdots + g_x^n(x^0)\frac{(\Delta x^0)^n}{n!} = 0$$	(2.11)

If neglecting the second and higher order terms in (2.11), a linear equation is obtained, shown in (2.12).

$$g(x^0) + g_x(x^0)\Delta x^0 = 0$$	(2.12)
$$\Delta x^0 = -\frac{g(x^0)}{g_x(x^0)}$$	(2.13)

where g_x is the first order derivative of the load flow function $g(x)$ w.r.t. x, which is also called Jacobian matrix in the case that more than one unknown variables presenting in the calculation. The differences, Δx^0, is then obtained via (2.13). The new values of the unknown variables can thus be obtained, as shown in (2.14).

$$x^1 = x^0 + \Delta x^0 = x^0 - \frac{g(x^0)}{g_x(x^0)}$$	(2.14)

Substituting x^1 to (2.9) for evaluating the result, if (2.9) is not valid, then x^1 is the new guess and a new iteration is needed to carried out. A general iteration step is presented in (2.15). The iteration will stop if (2.16) is fulfilled, i.e. the maximum power mismatch at the nodes in the load flow equation, $\left\| g(x^k) \right\|_n$, is less than the predefined convergence precision, ε, that is a small positive number.

$$x^{k+1} = x^k + \Delta x^{k+1} = x^k - \frac{g(x^k)}{g_x(x^k)}$$	(2.15)
$$\left\| g(x^k) \right\|_n < \varepsilon$$	(2.16)

2.1. LOAD FLOW WITH NEWTON-RAPHSON METHOD

To apply NR method to the load flow equations, the node voltages and branch admittances can be expressed in the polar form, (2.17)-(2.18).

$$V_i \sum_{k=1}^{N_v} V_k(G_{ik} \cos \delta_{ik} + B_{ik} \sin \delta_{ik}) = P_i, \qquad \forall i \in \mathcal{V} - \{ref\}$$	(2.17)
$$V_i \sum_{k=1}^{N_v} V_k(G_{ik} \sin \delta_{ik} - B_{ik} \cos \delta_{ik}) = Q_i, \qquad \forall i \in \mathcal{V} - \{ref\}$$	(2.18)

If define the left-hand-side of (2.17) and (2.18) are $P(x)$ and $Q(x)$, respectively, then the load flow equations are expressed in (2.19).

$$g(x^k) = \begin{bmatrix} P(x^k) - P_i \\ Q(x^k) - Q_i \end{bmatrix} = \begin{bmatrix} \Delta P^k \\ \Delta Q^k \end{bmatrix}, \qquad k = 0, 1, 2 \ldots$$	(2.19)

where the right-hand-side of (2.19) is the power mismatches at node i in the iteration k. In the polar form, only the voltage magnitudes, V, and the voltage angles, δ, are needed to be determined via NR method. The unknown reactive power injections at PV and P nodes, and the active power and the reactive power injections at SL nodes are calculated through (2.17)-(2.18) afterwards. Substituting (2.19) to (2.15), yields (2.20).

$$\begin{bmatrix} \Delta P^k \\ \Delta Q^k \end{bmatrix} = -J \begin{bmatrix} \Delta \delta^{k+1} \\ \Delta V^{k+1} \end{bmatrix}, \qquad k = 0,1,2 \dots$$	(2.20)
$$\Delta P = [\Delta P_{PV} \quad \Delta P_{PQ} \quad \Delta P_P \quad \Delta P_{PVQ}]^\mathsf{T}$$	(2.21)
$$\Delta Q = \left[\Delta Q_{PQ} \quad [\Delta Q_{PVQ} \quad \Delta Q_{P(n_P - n_{PVQ})}]^\mathsf{T}\right]^\mathsf{T}$$	(2.22)
$$\Delta x = [\Delta \delta_{PV} \quad \Delta \delta_{PQ} \quad \Delta \delta_{PVQ} \quad \Delta \delta_P \quad \Delta V_{PQ} \quad \Delta V_P]^\mathsf{T}$$	(2.23)

where J is the Jacobian matrix representing the first-order derivatives of the power mismatches w.r.t. the voltage angles and the voltage magnitudes, respectively. The same color marked in (2.21)-(2.23) indicates that the vectors have the same size. According to Table 3, in the polar form, the active power mismatches are found for PQ, PV, P and PVQ nodes, and the reactive power mismatches are found for PQ and PVQ nodes at each iteration. Moreover, the reactive power mismatch at PVQ nodes is mainly removed by regulating the voltage at the corresponding P nodes. Therefore, if defining the power mismatches as (2.21)-(2.22) according to Table 3 and unknown variables as (2.23), then the Jacobian matrix is expressed in (2.24).

Notice that if a PVQ node is remotely controlled by several P nodes, then only one of the P nodes will be used to accommodate the reactive power mismatch caused by controlling the voltage at PVQ node, i.e. ΔQ_{PVQ} is corresponding to only one ΔV_P though there may be several P nodes in this PVQ/P pair. It is used to maintain the full rank of the Jacobian matrix. The reactive power injections for the other P nodes are dispatched according to the contribution factors through (2.8).

$$J = \begin{bmatrix} J_1 & J_2 \\ J_3 & J_4 \end{bmatrix}$$	(2.24)

If defining the numbers of nodes are n_{PV}, n_{PQ}, n_P and n_{PVQ}, and total number of nodes is n, then:

J_1 is a $(n-1) \times (n-1)$ matrix, where the entry is $\frac{\partial P}{\partial \delta}$.

J_2 is a $(n-1) \times (n_{PQ} + n_P)$ matrix, where the entry is $\frac{\partial P}{\partial V}$.

J_3 is a $(n_{PQ} + n_P) \times (n-1)$ matrix, where the entry is $\frac{\partial Q}{\partial \delta}$.

J_4 is a $(n_{PQ} + n_P) \times (n_{PQ} + n_P)$ matrix, where the entry is $\frac{\partial Q}{\partial V}$.

The expressions of the entries in Jacobian matrix are presented in Appendix B – Derivative.

The algorithm for solving the load flow equations is shown in Table 4, where the inputs to the algorithm are the system admittance matrix, the initial guess of the unknown variables and the known data for different type of nodes according to Table 3. In case P/PVQ nodes are absent from the systems, then only ΔP for PV and PQ nodes and ΔQ for PQ nodes are used to find out the corresponding incremental variables $\Delta \delta$ and ΔV. The corresponding Jacobian matrices, J_2, J_3 and J_4, are then modified to exclude the P and PVQ nodes. Line 8 in Table 4 is removed, accordingly.

Notice that, though the reactive power injections and the voltage magnitudes at PVQ nodes are known, the attendance of reactive power mismatch at PVQ nodes in (2.22), is to provide the relation between the reactive power mismatches at PVQ nodes and the voltage magnitudes at corresponding P nodes. In other words, PVQ and P nodes comply with two relations that should be addressed in the algorithms: (i). Maintaining the voltage magnitude at PVQ nodes resulting in reactive power

mismatch at PVQ nodes, which should be removed by adjusting the voltage magnitudes at corresponding P nodes. (ii). The share of the reactive power injections at P nodes comply with (2.8).

Table 4. The load flow algorithm applying Newton-Raphson method.

1	*Calculate ΔP for PV, PQ, PVQ and P nodes, and ΔQ for PQ, PVQ and P nodes, (2.19);*
2	*if $\|\Delta P\|_n \geq \varepsilon$ or $\|\Delta Q\|_n \geq \varepsilon$*
3	*while $i_{tr} \leq N_{max}$*
4	*Calculate Jacobian matrix, (2.24);*
5	*Calculate $\Delta \delta$ for PV, PQ, PVQ and P nodes, and ΔV for PQ and P nodes;*
6	*Update δ and V, (2.15);*
7	*Calculate power flow in the branches through (2.17)-(2.18);*
8	*Accommodate the reactive power output for each P node with participation factor K, (2.8);*
9	*Calculate ΔP for PV, PQ, PVQ and P nodes, and ΔQ for PQ, PVQ and P nodes, (2.19);*
10	*if $\|\Delta P\|_n < \varepsilon$ and $\|\Delta Q\|_n < \varepsilon$*
11	*break;*
12	*end*
13	*end*
14	*end*

An example is demonstrated applying the algorithm in Table 4, where the IEEE-39 bus system is used with modifications. Two P/PVQ pairs are defined, as marked in Figure 7, i.e. Gen 31 and Gen 32 remotely control the voltage magnitude at Bus 11, and Gen 35 and Gen 36 remotely control the voltage magnitude at Bus 22, presented in Table 5. Generator Gen 30, Gen 33, Gen 34, Gen 37 and Gen 38 are connected to PV nodes, which control their terminal voltage magnitudes. Gen 39 is the slack machine. For the PV and PVQ nodes, the initial voltage magnitudes are set as target values.

Table 5. Defined PVQ/P pairs in the test grid shown in Figure 7.

P nodes	PVQ nodes	V at PVQ nodes (pu)	K for P nodes
31	11	1.03	0.468
32			0.532
35	22	1.02	0.537
36			0.463

The calculation is converged after 6 iterations, where the maximum power mismatch is smaller than $1e - 8$ pu. In contrast, if the reactive power mismatch at PVQ nodes in (2.22) is absence, the calculation will also be converged, after 18 iterations. Some of the node results from two study cases are summarized in Table 6. In both cases, the voltage magnitudes at PVQ nodes are maintained as target values. However, reactive power injections at corresponding P nodes are different. It can be seen from Table 6, the share of the reactive power contributions for P nodes at each P/PVQ pair are the same for both cases, but the total reactive power injections at each P/PVQ pair are different due to missing the sensitivities of reactive power change at PVQ node w.r.t. the corresponding voltage magnitudes at P nodes in each P/PVQ pair. In fact, without taking power mismatches at PVQ nodes in (2.22), the corresponding voltage magnitudes at P nodes will also be absence. These P nodes are therefore treated as PV nodes, i.e. the voltage magnitudes are known and then do not participate in iterations. The rest of P nodes are still presented in the iterations, treated as PQ nodes. There is only one more constraint, i.e. the share of reactive power injections among the P nodes in the same PVQ/P pair should be corresponding to the contribution factor. Therefore, the reactive power dispatch among P nodes is carried out in each iteration, where the terminal voltages of the presented P nodes are adjusted in order to comply with the contribution factors of the reactive power injections. In Table 6,

though the result in Case (ii) without ΔQ_{PVQ} terms in (2.22) seems also reasonable, it needs more iterations than Case (i) due to missing the derivation of $\frac{\Delta Q_{PVQ}}{\Delta V_P}$. These cases also demonstrate that multiple solutions exist for the load flow equations complying with generator remote voltage control constraints.
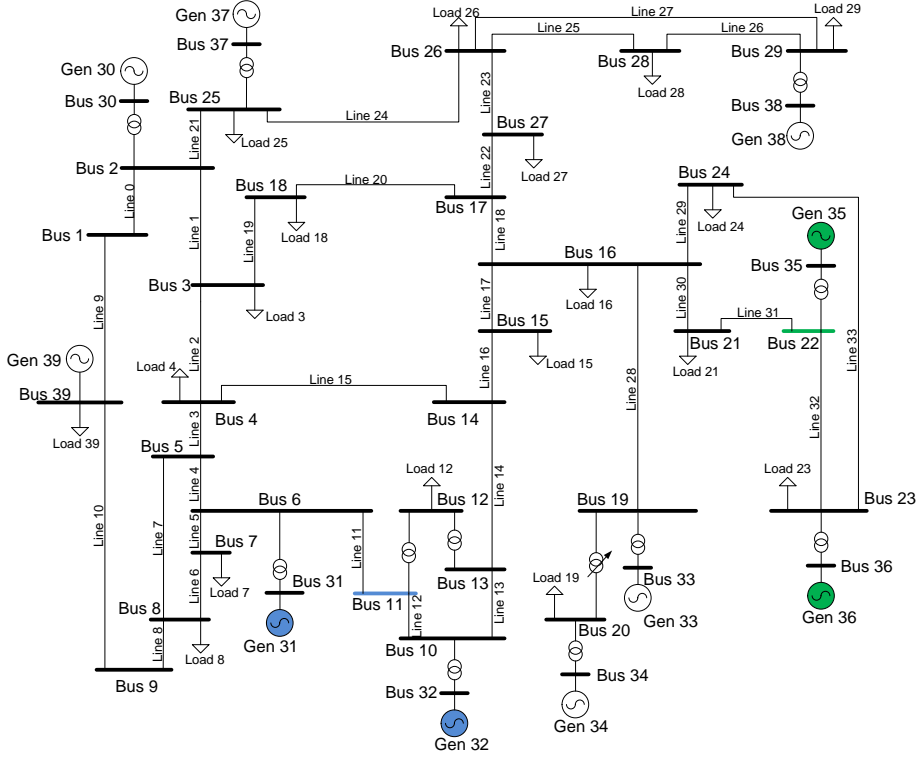
Figure 7. IEEE-39 bus system, where Gen 31 and Gen 32 remotely control Bus 11 voltage, and Gen 35 and Gen 36 remotely control Bus 22 voltage.

Table 6. Results comparison. (i) with ΔQ_{PVQ} in (2.22); (ii) without ΔQ_{PVQ} in (2.22);. Two P/PVQ pairs marked with blue and green respectively, according to Figure 7.

Case		(i). with ΔQ_{PVQ}				(ii). without ΔQ_{PVQ}			
Iterations		6				18			
Nodes		V (pu)	δ (deg)	P (MW)	Q (MVar)	V (pu)	δ (deg)	P (MW)	Q (MVar)
Type	**Index**								
PVQ	11	**1.030**	3.898	-	-	**1.030**	3.933	-	-
PVQ	22	**1.020**	10.933	-	-	**1.020**	10.953	-	-
P	31	1.087	9.801	572.93	**294.62**	1.030	10.375	572.93	**100.60**
P	32	1.024	12.219	650.00	**334.91**	0.974	12.756	650.00	**114.36**
P	35	1.017	16.201	650.00	**187.90**	1.020	16.207	650.00	**207.28**
P	36	1.053	18.830	560.00	**162.00**	1.058	18.796	560.00	**178.71**
PQ	1	1.041	1.559	-	-	1.040	1.564	-	-
PV	33	0.997	13.643	632.00	187.88	0.997	13.669	632.00	192.55
SL	39	1.030	0	108.18	158.20	1.030	0	108.84	137.99

In summary, NR method can be applied to solve the load flow equations. It is a tangent-based search method that iteratively calculates the adjustment quantities at unknown variables based on the known mismatch values at nodes. The slack nodes are used to absorb the power mismatches to keep the validity of the power balance equations. This method requires initial guesses for unknown variables that should be sufficiently close to the target points. Some control functions can be embedded into the load flow equations, such as generator local/remote voltage control. The transformer taps and the shunts can also be adjusted in the load flow calculations.

The main challenge of NR method is to provide a "good" initial guess that sufficiently close to the target, which in many cases, especially in the abnormal situations are very difficult. It means that some physically existing solutions are incapable to be found by NR method if the initial guesses are "far away" from the target values. In addition, the exact convergence boundary is not able to be identified.

A variety of robust improvements of the basic NR method have been proposed in the literature for solving ill-conditioned cases [12]-[14]. The wildly used method is optimal multiplier method, which adjusts the step-size of the updated unknown variables to improve the convergence properties of the iterative process. For the unsolvable cases where no solution exists, either the continuation power flow techniques can be applied to track on the maximum loadability [15], or Holomorphic embedding load flow method (HELM) can be applied for identifications [16].

3. HOLOMORPHIC EMBEDDING LOAD FLOW METHOD

HELM is proposed by Antonio Trias, which is a breakthrough approach to solve the load flow equations [16]. In contrast to NR method, HELM provides an analytical solution in a recursive manner, which is independent of initial guesses. It guarantees to provide the stable equilibrium point of the load flow problem if it physically exists [16]-[20]. The load flow calculation with pure PQ nodes and a slack node is presented in [16]. Furthermore, the model including PV nodes is more complex, which is presented in [17]-[20]. However, HELM is still not popular in the power system engineering society, as there are few papers to present the detailed implementations that can be used for inspiring other researches and applications.

3.1. THE CONCEPT

A holomorphic function is a complex-valued function of one or several complex variables. It is complex differentiable in the neighborhood of every point in the complex domain. The holomorphic function is also an analytical function that can be represented by a converged power series, where the coefficients are complex values [16], (2.25).

$$f(z) = \sum_{n=0}^{\infty} C_n (z - z_0)^n \tag{2.25}$$

The idea of HELM is to embed the load flow equations into a large solution space by casting the voltage variables to complex-valued power series, in which the analytical solution is trivial to find under a certain condition, e.g. no load condition [18]. This solution is so called a germ solution, (2.26), that is an analytical solution of the power series (2.25) under a specified condition, where z_0 is the constant complex value, and $C_1, C_2, \ldots$ are the complex power series coefficients for different orders.

$$g = (z_0, C_1, C_2, \ldots) \tag{2.26}$$

The solution of the original load flow equations representing by power series, are then obtained based on this germ solution through the analytical continuation techniques, i.e. Padé approximants [21].

The concept can be demonstrated in Figure 8. After embedding the load flow equations to the s-plane, the load flow equations are analytical and can be casted to power series. In Figure 8, a quadratic function is used to demonstrate the analytical function. For the embedded load flow equations, it is generally a Taylor series with several orders. The coefficients of the power series in the load flow equations are trivial to be found under a certain condition, e.g. $s = 0 + j0$. The coefficients under $s = 0 + 0j$, is thus a germ solution of the load flow equation w.r.t s. In order to obtain the solution to the original load flow equation, e.g. $s = 1$ should be substituted. However, the convergence radius of Taylor series may not sufficiently cover the solution space where $s = 1$. Therefore, analytical continuation technique is applied to extend the convergence radius to be the largest value [16]. In addition, if the embedded load flow can be converged with the analytical continuation, then there is a physical solution. Otherwise, there is not any solution [16].
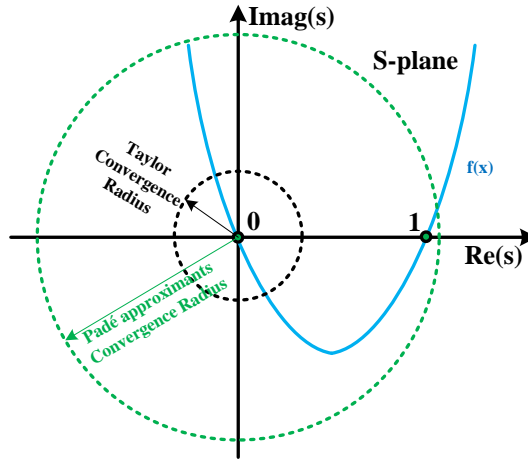
Figure 8. The sketch of HELM concept.

Comparing to continuation load flow that uses the numerical prediction-correction step to track the "nose" curve, HELM is not able to be converged at the maximum loadability point, as the numerical continuation method adds a new dimension to overcome the singularity of the Jacobian matrix at the breaking point whereas HELM applies the analytical continuation techniques that fails to be converged at the breaking point. In other words, HELM theoretically needs at least two germ solutions for drawing the upper and lower branches of "nose" curve separately.

3.2. PADÉ APPROXIMANTION

Padé approximants are rational approximants to the power series, whose convergence has been known to be much better than that of power series. The largest radius of convergence for these power series can be obtained through Padé approximants, as stated by Stahl's Padé convergence theory [22]-[23]. The Padé approximation method is briefly introduced.

A Taylor series with $M + N$ orders is able to be approximated by rearranging into a ratio of two such expansions with M orders in nominator and N orders in the denominator, (2.27), where a_n and b_n are coefficients. The denominator is normalized that $b_0 = 1$.

$$C_0 + C_1 x + C_2 x^2 + \cdots = \frac{a_0 + a_1 x + a_2 x^2 + \cdots}{1 + b_1 x + b_2 x^2 + \cdots} = \frac{\sum_{n=0}^{N} a_n x^n}{\sum_{n=0}^{M} b_n x^n} \qquad (2.27)$$

Moving the denominator to the left-hand-side and equating the coefficients of each order, yields (2.28).

$$
\begin{aligned}
a_0 &= C_0 \\
a_1 &= C_1 + C_0 b_1 \\
a_2 &= C_2 + C_1 b_1 + C_0 b_2 \\
\vdots \quad &\vdots \qquad\qquad \vdots \\
\underline{a_N} &= \underline{C_N + C_{N-1} b_1 + \cdots + C_0 b_N} \\
0 &= C_{N+1} + C_N b_1 + \cdots + C_{N-M+1} b_M \\
\vdots \quad &\vdots \qquad\qquad \vdots \\
0 &= C_{N+M} + C_{N+M-1} b_1 + \cdots + C_N b_M
\end{aligned}
\tag{2.28}
$$

As shown in (2.28), there is total $(M + N)$ orders for C-series, $\{C_n x^n\}$ but only N orders for $\{a_n x^n\}$. Therefore, the coefficients of $\{b_n x^n\}$ can be obtained by solving M equations in the bottom of (2.28), which is formulated in (2.29). The coefficients of $\{a_n x^n\}$ are thus obtained by solving the fist N equations afterwards, (2.30). This is also called Direct Method of Padé approximation [19].

$$
\begin{bmatrix}
C_{N-M+1} & C_{N-M+2} & C_{N-M+3} & \cdots & C_N \\
C_{N-M+2} & C_{N-M+3} & C_{N-M+4} & \cdots & C_{N+1} \\
C_{N-M+3} & C_{N-M+4} & C_{N-M+5} & \cdots & C_{N+2} \\
\vdots & \vdots & \vdots & \ddots & \vdots \\
C_N & C_{N+1} & C_{N+2} & \cdots & C_{N+M-1}
\end{bmatrix}
\begin{bmatrix}
b_M \\ b_{M-1} \\ b_{M-2} \\ \vdots \\ b_1
\end{bmatrix}
= -
\begin{bmatrix}
C_{N+1} \\ C_{N+2} \\ C_{N+3} \\ \vdots \\ C_{N+M}
\end{bmatrix}
\tag{2.29}
$$

$$
\sum_{k=0}^{n} C_k b_{n-k} = a_n, \qquad n = 1,2 \dots N
\tag{2.30}
$$

The results of Padé approximation create a $M \times N$ matrix with entry representing quotients of two power series, $\{a\}$ and $\{b\}$ at a certain value of x. The matrix is so called Padé table [26], shown in (2.31). If $M = 0$, then only the first row is remained, which is the original power series.

$$
\begin{matrix}
r_{0,0} & r_{0,1} & r_{0,2} & r_{0,3} & \cdots \\
r_{1,0} & r_{1,1} & r_{1,2} & r_{1,3} & \cdots \\
r_{2,0} & r_{2,1} & r_{2,2} & r_{2,3} & \cdots \\
r_{3,0} & r_{3,1} & r_{3,2} & r_{3,3} & \cdots \\
\vdots & \vdots & \vdots & \vdots & \ddots
\end{matrix}
\tag{2.31}
$$

3.3. CONTINUED FRACTION

As stated in Stahl's Padé convergence theory [22]-[23], the diagonal and paradiagonal Padé approximants provides the maximal analytic continuation. The diagonal and paradiagonal Padé approximants coincide with the continued fraction approximation to the power series. The continued fraction is connected to Padé approximants according to the theory [24].

"Let $f(x)$ be a given Finite Taylor Series. If every three consecutive elements in the descending staircase of Padé approximants sequence are distinct, then there exists a regular continued fraction corresponding to $f(x)$."

In the theory stated in [25], the partial numerators of the regular continued fraction correspond to the coefficients of the Taylor series, (2.32), where K_m^∞ stands for the continued fraction operation.

$$f(x) = C_0 + \cfrac{\bar{C}_{10}x}{1 + \cfrac{\bar{C}_{20}x}{1 + \cfrac{\bar{C}_{30}x}{1 + \cfrac{\bar{C}_{m0}x}{1 + \cdots}}}} = K_{m=1}^{\infty}\left(\frac{\bar{C}_{m0}}{1}\right), \quad \bar{C}_{m0} \neq 0 \tag{2.32}$$

In order to connect the Taylor power series, the Viskovatov method can be applied [26]. Considering a Taylor series $\{C_n x^n\}$, if define two series, $\bar{C}_{0j}$ and $\bar{C}_{1j}$ complying with (2.33)-(2.34), then (2.35) can be derived [26]. Once $\bar{C}_{m,0}, m = 1,2 \ldots$ is found, $f(x)$ can be evaluated through (2.32).

$$\bar{C}_{0j} = \begin{cases} 1, & j = 0 \\ 0, & j > 0 \end{cases} \tag{2.33}$$

$$\bar{C}_{1j} = C_{j+1}x^{j+1}, \quad j \geq 0 \tag{2.34}$$

$$\bar{C}_{m,j} = \frac{\bar{C}_{m-2,j+1}}{\bar{C}_{m-2,0}} - \frac{\bar{C}_{m-1,j+1}}{\bar{C}_{m-1,0}}, \quad m \geq 2, \quad j \geq 0 \tag{2.35}$$

In the load flow calculation, a matrix for each node voltage is created, as shown in (2.36), and filled by the two power series, $\{\bar{C}_{0j}\}$ and $\{\bar{C}_{1j}\}$ shown in (2.33)-(2.34), into the first two rows. The purpose is to find out $\bar{C}_{m,0}$ as many as possible according to the original Taylor series coefficients, i.e. expanding the matrix (2.36) as much as possible until convergence if there is a physical solution.

$$\begin{matrix} 1 & 0 & 0 & 0 & 0 & \cdots \\ C_1 & C_2 & C_3 & C_4 & C_5 & \cdots \\ \bar{C}_{2,0} & \bar{C}_{2,1} & \bar{C}_{2,2} & \bar{C}_{2,3} & \bar{C}_{2,4} & \cdots \\ \bar{C}_{3,0} & \bar{C}_{3,1} & \bar{C}_{3,2} & \bar{C}_{3,3} & \bar{C}_{3,4} & \cdots \\ \bar{C}_{4,0} & \bar{C}_{4,1} & \bar{C}_{4,2} & \bar{C}_{4,3} & \bar{C}_{4,4} & \cdots \\ \vdots & \vdots & \vdots & \vdots & \vdots & \ddots \end{matrix} \tag{2.36}$$

Pick up the **first column** to construct the continued fraction $K_{m=1}^{\infty}\left(\frac{\bar{C}_{m0}}{1}\right)$. The value of $f(x)$ can be obtained hereafter by adding the constant value C_0 through (2.32).

Alternatively, the value of the continued fraction can be found through a three-term recursion relationship, which is equivalent to either a diagonal or paradiagonal Padé approximant, red marked in (2.31). The recurrence relations of the continued fraction, (2.32), can be expressed in (2.37) [26].

$$\begin{bmatrix} A_m \\ B_m \end{bmatrix} := \begin{bmatrix} A_{m-1} \\ B_{m-1} \end{bmatrix} + \bar{C}_{m0}\begin{bmatrix} A_{m-2} \\ A_{m-2} \end{bmatrix}, \quad \bar{C}_{m0} \neq 0 \; for \; m \geq 1 \tag{2.37}$$

where $A_{-1} := 1$, $B_{-1} := 0$, $A_0 := C_0 \; and \; B_0 := 1$. Equation (2.37) is finally applied to evaluate the Padé approximation in the load flow calculations.

3.4. LOAD FLOW SOLUTION WITH HELM

As mentioned above, the idea to solve the load flow equations with HELM is to place the load flow equations into a large solution space through embedding. After embedding a complex variable, the load flow equations are infinitely differentiable w.r.t. this complex variable, which is analytical, also called holomorphic in the complex analysis.

The power flow equations, shown in (2.5), are embedded with a complex variable s, where the voltage is considered as a function of the embedded variable s, as shown in (2.38). It can be seen that,

if $s = 0$, (2.38) is converted to (2.3), which is trivial to be solved. If $s = 1$, then (2.38) represents the original load flow equations without the embedding.

$$\sum_{k=1}^{n} Y_{ik} v_k(s) = \frac{(P_i - jQ_i)s}{v_i^*(s^*)} \tag{2.38}$$

The holomorphicity guarantees that the voltage can be represented as an equivalent power series of the embedding complex variable s, (2.39) [18], where $v_i[n]$ represents a complex coefficient at order n of the power series w.r.t. s at the node i.

$$v_i(s) = \sum_{n=0}^{\infty} v_i[n]s^n \tag{2.39}$$

Notice, the conjugate voltage in (2.38), is embedded as $v_i^*(s^*)$ in order to maintain holomorphicity, as shown in (2.40) [20], where the conjugated voltage is also a function of the embedding s.

$$v_i^*(s^*) = v_i[0]^* + v_i[1]^*s + v_i[2]^*s^2 + \cdots + v_i[n]^*s^n \tag{2.40}$$

Equation (2.38) is generally valid for all nodes in the system. For the PV nodes where the voltage magnitude is constant and the reactive power injection is unknown. It means, there is one more unknown variable, Q_i, and one more voltage magnitude constraint than (2.38) at each PV node. The unknown reactive power can be embedded, as $Q_i(s)$, for the PV node i [25]. Similarly, for the PVQ nodes, not only the active power and the reactive power but also the voltage magnitude is known.

Equation (2.41)-(2.47) can be obtained, which is so called the canonical embedding [25]. Other embedding methods are also valid as shown in [27]-[28]. The equations (2.44)-(2.45) are the same with (2.41) and (2.43) for the PQ and PV nodes, respectively. The voltage magnitudes and the reactive power injections at the corresponding P nodes are unknown, where (2.46) is similar to (2.42) but the unknown reactive power injections complies with the contribution factors among the P nodes in the same P/PVQ pair. Notice that the embedded variable s in the unknown reactive power variable, $Q_i(s)$ in (2.42) and (2.46), is a real variable. This condition indicates that the analytical path from $s = 0$ to $s = 1$ is along the real axis, though s itself is a complex variable. However, the calculations will not trace the whole path, only two points are needed to be solved, i.e. $s = 0$ for the no load condition as a germ solution, and $s = 1$ for the original load flow equations.

Type	Load flow equations with embedding variable s	
PQ	$\sum_{k} Y_k^{tr} v_k(s) = s\dfrac{P_{PQ} - jQ_{PQ}}{v_{PQ}^*(s)} - sY^{sh}v_{PQ}(s)$	(2.41)
PV	$\sum_{k} Y_k^{tr} v_k(s) = \dfrac{sP_{PV} - jQ_{PV}(s)}{v_{PV}^*(s)} - sY^{sh}v_{PV}(s)$	(2.42)
	$v_{PV}(s)v_{PV}^*(s) = 1 + s\left(V_{PV}^{sp\,2} - 1\right)$	(2.43)
PVQ	$\sum_{k} Y_k^{tr} v_k(s) = s\dfrac{P_{PVQ} - jQ_{PVQ}}{v_{PVQ}^*(s^*)} - sY^{sh}v_{PVQ}(s)$	(2.44)
	$v_{PVQ}(s)v_{PVQ}^*(s^*) = 1 + s\left(V_{PVQ}^{sp\,2} - 1\right)$	(2.45)
P	$\sum_{k} Y_k^{tr} v_k(s) = \dfrac{sP_P - jK_i \sum Q_P(s)}{v_P^*(s^*)} - sY^{sh}v_P(s)$	(2.46)
SL	$v_{slack}(s) = 1 + s\left(V_{SL}^{sp\,2} - 1\right)$	(2.47)

If casting all embedded variables of (2.41)-(2.47) to the power series, by defining (2.39) and (2.48)-(2.50) for the unknown voltages and the reactive power injections, the equations (2.51)-(2.55) can be obtained. These equations are completely to determine the load flow solutions analytically, where V_i^{sp} are the known voltage magnitude at node i for P and PV nodes. Y_i^{sh} is the shunt admittance at node i. Y_{ik}^{tr} is the series admittance between node i and k.

$$Q_i(s) = \sum_{n=0}^{\infty} Q_i[n]s^n$$	(2.48)
$$\frac{1}{v_i(s)} = w_i(s) = \sum_{n=0}^{\infty} w_i[n]s^n$$	(2.49)
$$\frac{1}{v_i^*(s^*)} = w_i^*(s^*) = \sum_{n=0}^{\infty} w_i^*[n]s^n$$	(2.50)
$$\sum_k Y_{ik}^{tr} \sum_{n=0}^{\infty} v_k[n]s^n = (P_i - jQ_i) \sum_{n=0}^{\infty} w_i^*[n]s^{n+1} - Y_i^{sh} \sum_{n=0}^{\infty} v_i[n]s^{n+1}$$	(2.51)
$$\sum_k Y_{ik}^{tr} \sum_{n=0}^{\infty} v_k[n]s^n = \left(sP_i - j\sum_{n=0}^{\infty} Q_i[n]s^n\right) \sum_{n=0}^{\infty} w_i^*[n]s^n - Y_i^{sh} \sum_{n=0}^{\infty} v_i[n]s^{n+1}$$	(2.52)
$$\sum_{n=0}^{\infty} v_i[n]s^n \sum_{n=0}^{\infty} v_i^*[n]s^n = 1 + s\left(V_i^{sp2} - 1\right)$$	(2.53)
$$\sum_k Y_{ik}^{tr} \sum_{n=0}^{\infty} v_k[n]s^n = \left(sP_i - j\sum_{n=0}^{\infty} K_i Q_\Sigma[n]s^n\right) \sum_{n=0}^{\infty} w_i^*[n]s^n - Y_i^{sh} \sum_{n=0}^{\infty} v_i[n]s^{n+1}$$	(2.54)
$$\sum_{n=0}^{\infty} v_i[n]s^n \sum_{n=0}^{\infty} w_i[n]s^n = 1$$	(2.55)

As shown in Table 7, for PQ nodes, there are 2 unknown variables, i.e. $v_i(s)$ and $w^* = \frac{1}{v_i^*(s^*)}$, and 2 sets of corresponding equations, (2.51) and (2.55) for power flow and the reciprocal relation of the 2 unknown variables. For PV nodes, there are 1 more unknown variables, $Q_i(s)$, and total 3 sets of corresponding equations, (2.52)-(2.53) and (2.55), where (2.53) is used to constrain the voltage magnitude. For PVQ nodes, the unknown variables are the same with the PQ nodes, but 1 more set of corresponding equations than PQ nodes, (2.53), for the voltage magnitude constraints. For the P nodes, there are 3 unknown variables, but only 2 sets of corresponding equations are valid. However, P and PVQ nodes are always coupled. Therefore, the redundant set of equations for PVQ nodes is needed to compensate the missing set of equations of P nodes. The total numbers of unknown variables and the corresponding equations are equal. The problem can be solved.

Table 7. Unknown variables and corresponding equations

Type	Unknown variables	Corresponding equations		
		Power balance	*V* constrant	Reciprocal relation
PQ	v, w^*	(2.51)	--	(2.55)
PV	v, w^*, Q	(2.52)	(2.53)	(2.55)
PVQ	v, w^*	(2.51)	(2.53)	(2.55)
P	v, w^*, Q	(2.52)	--	(2.55)
SL	--	--	(2.53)	--

In each equation of (2.52)-(2.55), there is a multiplication of two power series. A common convolution formula can be derived in (2.56). The coefficient of each order in (2.56) should be determined. The calculation procedure is presented in the next section.

$$
\begin{aligned}
\sum_{n=0}^{\infty} c_i[n]s^n & \sum_{n=0}^{\infty} d_i[n]s^n \\
& = c_i[0]s^0 \cdot d_i[0]s^0 \\
& + s^1 \sum_{k=0}^{1} c_i[1-k] \cdot d_i[k] \\
& + s^2 \sum_{k=0}^{2} c_i[2-k] \cdot d_i[k] + \cdots + s^n \sum_{k=0}^{n} c_i[n-k] \cdot d_i[k] + \cdots
\end{aligned}
\tag{2.56}
$$

Tap-able transformers are always used to maintain a voltage magnitude at a target node by regulating the winding ratios, whereas phase-shifting transformers are used to control the active power flow in the parallel branches by regulating the voltage angles across the transformers. In the load flow calculations, the general branch model can be presented in Figure 9. The formulation is expressed in (2.57), where the branch model includes the transmission line and the transformers. y_s and b_c are the series admittance and the shunt susceptance, respectively. τ and θ_{shift} are the transformer tap-ratio and the phase-shifting angle, i.e. $\tau = 1$ and $\theta_{shift} = 0$ in the case of representing a transmission line and the matrix (2.57) is symmetrical. The phase-shifting angles can change the off-diagonal entries of the branch models, which results in an asymmetrical admittance matrix in the load flow calculations.
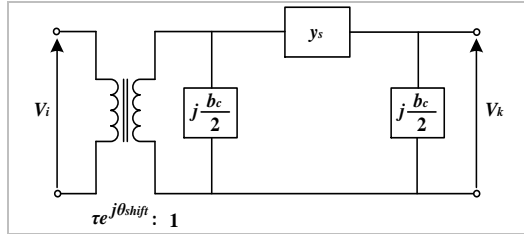
Figure 9. The general branch model in load flow calculations [89].

Notice that, the general branch model shown in Figure 9, is split into series and shunts parts, Y_{ik}^{tr} and Y_i^{sh} in the canonical embedding. Therefore, the general branch model (2.57) is the summation of (2.58) and (2.59).

$$
Y_{br} = \begin{bmatrix} \left(y_s + j\dfrac{b_c}{2}\right)\dfrac{1}{\tau^2} & -y_s\dfrac{1}{\tau e^{-j\theta_{shift}}} \\ -y_s\dfrac{1}{\tau e^{j\theta_{shift}}} & y_s + j\dfrac{b_c}{2} \end{bmatrix}
\tag{2.57}
$$

$$
Y^{tr} = \begin{bmatrix} y_s\dfrac{1}{\tau e^{-j\theta_{shift}}} & -y_s\dfrac{1}{\tau e^{-j\theta_{shift}}} \\ -y_s\dfrac{1}{\tau e^{j\theta_{shift}}} & y_s\dfrac{1}{\tau e^{j\theta_{shift}}} \end{bmatrix}
\tag{2.58}
$$

$$
Y^{sh} = \begin{bmatrix} \left(y_s + j\dfrac{b_c}{2}\right)\dfrac{1}{\tau^2} - \dfrac{y_s}{\tau e^{-j\theta_{shift}}} & 0 \\ 0 & \left(y_s + j\dfrac{b_c}{2}\right) - \dfrac{y_s}{\tau e^{j\theta_{shift}}} \end{bmatrix}
\tag{2.59}
$$

At the no-load condition, (2.60) can be obtained. In the no-load condition, i.e. $s = 0$, equation (2.60) is generally not valid if the phase-shifting angle is not 0 or the ratio is not 1, as the value of the diagonal element is not equal to the summation of the off-diagonal elements in (2.57). This is the reason to split the admittance matrix, where the values of the diagonal elements of the matrix Y_{ik}^{tr} equals to the summation of the off-diagonal elements at each row, as the shunt admittance Y^{sh} is separated from Y^{tr} and all current injections are zeros as $s = 0$ in the equations (2.51), (2.52) and (2.54). If assuming the slack voltage is $1\angle 0°$ at the no load condition, then the voltages at all nodes will be $1\angle 0°$. Based on this assumption, the germ solution can ensure the converged solution being on the upper branch of the "nose" curve.

$$\sum_k Y_{ik}^{tr} v_k[0] = 0, \qquad v_k[0] = 1 \tag{2.60}$$

After modifying the admittance matrix, the validity of the load flow equations (2.51)-(2.55) and the calculation procedure are unchanged, where only the admittance matrix is replaced by Y^{tr} and Y^{sh}. The original load flow equations are changed at the no load condition due to the changes on the admittance matrix and the slack voltage. However, the load flow equations recovery to the original load flow equations at $s = 1$.

3.5. HELM CALCULATION PROCEDURE

The complete formulation of the embedded load flow equations are presented in (2.39) and (2.51)-(2.55), where the admittance matrices are modified to include tap-able and phase-shifting transformers. The power series can be applied to expand the unknown variables to the power series w.r.t. s.

A simple pattern can be demonstrated for PQ nodes [16].

$Y(v[0] + v[1]s^1 + v[2]s^2 + \cdots v[n]s^n) = (P + jQ)(w^*[0] + w^*[1]s^1 + w^*[2]s^2 + \cdots w^*[n]s^n)s$	
To obtain $v[0]$	$s = 0$
	$Y(v[0]) = 0 \rightarrow v[0]$ then $w^*[0] = f(v[0])$
To obtain $v[1]$	Differentiating both sides w.r.t. s, and then substitute $s = 0$
	$Y(v[1]) = (P + jQ)(w^*[0]) \rightarrow v[1]$ then $w^*[1] = f(v[1])$
To obtain $v[2]$	Differentiating both sides w.r.t. s for 2 times, and then substitute $s = 0$
	$Y(v[2]) = (P + jQ)(w^*[1]) \rightarrow v[2]$ then $w^*[2] = f(v[2])$
	$\vdots$
To obtain $v[n]$	Differentiating both sides w.r.t. s for n times, and then substitute $s = 0$
	$Y(v[n]) = (P + jQ)(w^*[n-1]) \rightarrow v[n]$ then $w^*[n] = f(v[n])$
Solution	$v = v[0] + v[1] + v[2] + \cdots v[n]$

This pattern can be generalized for calculation of the power series coefficients at $s = 0$. It is carried out order by order, i.e. differentiating the power flow equations after power series expansions w.r.t s at both sides and evaluating at $s = 0$. The found coefficients of the power series order by order compose the germ solution, which are used for Padé approximation. The following content introduce the systematical way to implement HELM in the computer routine.

Step 1: $n = 0$
Calculate the coefficients at no load condition by setting $s = 0$, then the power vanishes in the power flow equations, representing the no load condition. Assuming the voltage at slack node is $V_{sl}^{sp} = 1\angle 0°$, and then the voltage at all nodes are equal to V_{sl}^{sp}. It can be considered as a "flat start", shown in (2.61). It is a physical solution of the original load flow. It represents a condition that no power flows between any two nodes in the system. All calculations start from (2.61), which is also one of the reasons that HELM is independent of initial guess.

	$v_i[0] = 1 \ and \ Q_i[0] = 0$	(2.61)

Step 2: $n = 1$

Differentiating the load flow equation w.r.t s at both sides, evaluating at $s = 0$, and substituting the calculated coefficients from Step 1, obtain (2.62)-(2.69).

SL	$v_i[1] = V_{sl}^{sp} - 1$	(2.62)
PV	$\sum_k Y_{ik}^{tr} v_k[1] = P_i - Y_i^{sh}$	(2.63)
	$v_{i,re}[1] = \dfrac{V_i^{sp2} - 1}{2}$	(2.64)
PQ	$\sum_k Y_{ik}^{tr} v_k[1] = (P_i - jQ_i) - Y_i^{sh}$	(2.65)
PVQ	$\sum_k Y_{ik}^{tr} v_k[1] = (P_i - jQ_i) - Y_i^{sh}$	(2.66)
	$v_{i,re}[1] = \dfrac{V_i^{sp2} - 1}{2}$	(2.67)
P	$\sum_k Y_{ik}^{tr} v_k[1] = P_i - Y_i^{sh}$	(2.68)
All nodes	$W_i[1] = -W_i[0]$	(2.69)

Step 3: $n > 1$

The real and the imaginary parts of the voltage variables can be calculated separately, as the reactive power variables at PV and P nodes are embedded with s along the real axis. Continuously calculate finite numbers of orders using (2.70)-(2.77) until the active power mismatches at all nodes except for the slack node, and the reactive power mismatches at PQ and PVQ nodes are respectively within an acceptable band.

SL	$V_{slack}[n] = 0$	(2.70)
PV	$\sum_k Y_{ik}^{tr} v_k[n] = P_i \cdot w_i^*[n-1] - j\left(\sum_{k=1}^{n-1} Q_i[k] w_i^*[n-k]\right) - Y_i^{sh} v_i[n-1]$ $- j\boldsymbol{Q_i[n]}$	(2.71)
	$v_{i,re}[n] = -\dfrac{1}{2}\left(\sum_{k=1}^{n-1} v_i[k] v_i^*[n-k]\right)$	(2.72)
PQ	$\sum_k Y_{ik}^{tr} v_k[n] = (P_i - jQ_i) w_i^*[n-1] - Y_i^{sh} v_i[n-1]$	(2.73)
PVQ	$\sum_k Y_{ik}^{tr} v_i[n] = (P_i - jQ_i) w_i^*[n-1] - Y_i^{sh} v_i[n-1]$	(2.74)
	$v_{i,re}[n] = -\dfrac{1}{2}\left(\sum_{k=1}^{n-1} v_i[k] v_i^*[n-k]\right)$	(2.75)
P	$\sum_k Y_{ik}^{tr} v_k[n] = P_i \cdot w_i^*[n-1] - j\left(\sum_{k=1}^{n-1} K_i Q_\Sigma[k] w_i^*[n-k]\right) - Y_i^{sh} v_i[n-1]$ $- j\boldsymbol{K_i Q_\Sigma[n]}$	(2.76)
All nodes except for SL	$w_i[n] = -\sum_{k=0}^{n-1} \dfrac{w_i[k] \cdot v_i[n-k]}{v_i[0]}$	(2.77)

The real part of the voltage variables at PV and PVQ nodes in (2.64) and (2.67) at $n = 1$, and (2.72) and (2.75) when $n > 1$, are derived in (2.78) by (i) applying (2.56) to (2.53) and equating the coefficients for each order of s; (ii) starting from (2.61).

$$
\begin{array}{|c|c|}
\hline
\begin{aligned}
v_i[0] \cdot v_i[0]^* = 1 &\rightarrow v_i[0]^* = 1 \\[4pt]
v_i[0] \cdot v_i[1]^* + v_i[1] \cdot v_i[0]^* = V_i^{sp2} - 1 &\rightarrow v_{i,re}[1] = \frac{V_i^{sp2} - 1}{2} \\[4pt]
v_i[0] \cdot v_i[2]^* + v_i[1] \cdot v_i[1]^* + v_i[2] \cdot v_i[0]^* = 0 &\rightarrow v_{i,re}[2] = -\frac{1}{2} v_i[1] \cdot v_i[1]^* \\[4pt]
v_i[0] \cdot v_i[3]^* + v_i[1] \cdot v_i[2]^* + v_i[2] \cdot v_i[1]^* + v_i[3] \cdot v_i[0]^* = 0 &\rightarrow v_{i,re}[3] \\
&= -\frac{1}{2} (v_i[1] \cdot v_i[2]^* + v_i[2] \cdot v_i[1]^*) \\[4pt]
\vdots \\[4pt]
V_{i,re}[n] = -\frac{1}{2} \left(\sum_{k=1}^{n-1} V_i[k] V_i^*[n-k] \right) &
\end{aligned}
& (2.78) \\
\hline
\end{array}
$$

If splitting the admittance matrix and the voltage into real and imaginary parts, as shown in (2.79), then (2.71)-(2.76) can be represented in (2.80), where the unknown reactive power injections at PV and PVQ nodes are moved to the left hand sides of equations, whereas the known voltage real parts at PV and PVQ nodes are moved to the right hand sides.

$$ \sum Y^{tr} v = \sum \left((G v_{re} - B v_{im}) + j(B v_{re} + G v_{im}) \right) \qquad (2.79) $$

In (2.81), $PQ[n-1]$ and $PVQ[n-1]$ are the right hand sides of (2.73) and (2.74), respectively. $PV[n-1]$ and $P[n-1]$ are the right hand sides of (2.71) and (2.76), respectively, after moving the unknown $Q_{pv}[n]$ and $Q_p[n]$ to the left hand side of (2.81). From Step 3, the voltage at the slack node is absent from calculations. Each entry in (2.81) represents a matrix or a vector, where $Q_\Sigma[n]$ represents the total required reactive power at corresponding PVQ node to maintain the voltage magnitude, which is placed in the corresponding PVQ rows in (2.81). $K_{p,pvq}$ is the participation factor matrix for all coupled P/PVQ pairs, which is presented in form of (2.82). $I_{pv,pv}$ is an identity matrix.

Equation (2.81) is a recursive step of (2.80) for $n > 1$, where the coefficients of s^n are found based on the coefficients of s^0 to s^{n-1} orders that are shown in (2.83)-(2.86).

$$ \begin{pmatrix} V[n] \\ Q[n] \end{pmatrix} = f\left(\sum_{k=0}^{n-1} V[k], \quad \sum_{k=0}^{n-1} Q[k] \right) \qquad (2.80) $$

In the recursive calculation, the individual reactive power injection at each P node, $Q_{p1..N}$, is obtained via (2.8) and found $Q_\Sigma[n] \in \mathcal{R}^{(N_{pvq} \times 1)}$ in each order.

$$
\begin{bmatrix}
I_{ref,ref} & 0 & 0 & 0 & 0 & 0 & 0 & 0 & 0 & 0 \\
0 & I_{ref,ref} & 0 & 0 & 0 & 0 & 0 & 0 & 0 & 0 \\
G_{pq,ref} & -B_{pq,ref} & G_{pq,pq} & -B_{pq,pq} & -B_{pq,pv} & G_{pq,pv} & -B_{pq,pvq} & G_{pq,pvq} & G_{pq,p} & -B_{pq,p} \\
B_{pq,ref} & G_{pq,ref} & B_{pq,pq} & G_{pq,pq} & G_{pq,pv} & B_{pq,pv} & G_{pq,pvq} & B_{pq,pvq} & B_{pq,p} & G_{pq,p} \\
B_{pv,ref} & G_{pv,ref} & B_{pv,pq} & G_{pv,pq} & I_{pv,pv} & G_{pv,pv} & B_{pv,pvq} & G_{pv,pvq} & B_{pv,p} & G_{pv,p} \\
G_{pv,ref} & -B_{pv,ref} & G_{pv,pq} & -B_{pv,pq} & 0 & -B_{pv,pv} & G_{pv,pvq} & -B_{pv,pvq} & G_{pv,p} & -B_{pv,p} \\
B_{pvq,ref} & G_{pvq,ref} & B_{pvq,pq} & G_{pvq,pq} & 0 & G_{pvq,pv} & B_{pvq,pvq} & G_{pvq,pvq} & B_{pvq,p} & G_{pvq,p} \\
G_{pvq,ref} & -B_{pvq,ref} & G_{pvq,pq} & -B_{pvq,pq} & 0 & -B_{pvq,pv} & G_{pvq,pvq} & -B_{pvq,pvq} & G_{pvq,p} & -B_{pvq,p} \\
G_{p,ref} & -B_{p,ref} & G_{p,pq} & -B_{p,pq} & 0 & -B_{p,pv} & G_{p,pvq} & \boldsymbol{K_{p,pvq}} & G_{p,p} & -B_{p,p} \\
-B_{p,ref} & G_{p,ref} & -B_{p,pq} & G_{p,pq} & G_{p,pv} & G_{p,pv} & B_{p,pvq} & B_{p,pvq} & -B_{p,p} & G_{p,p}
\end{bmatrix}
\cdot
\begin{bmatrix}
V_{sl,re}[n] \\
V_{sl,im}[n] \\
v_{pq,im}[n] \\
v_{pv,im}[n] \\
v_{pvq,im}[n] \\
\boldsymbol{Q_{pv}[n]} \\
\boldsymbol{Q_{sl}[n]} \\
v_{p,re}[n] \\
v_{p,im}[n]
\end{bmatrix}
=
\begin{bmatrix}
V_{sl}^{SP} - 1,\ if\ n = 1\ and\ 0,\ if\ n > 1 \\
0 \\
Real(PQ[n-1]) \\
Imag(PQ[n-1]) \\
Imag(PV[n-1]) \\
Real(PV[n-1]) \\
Imag(PVQ[n-1]) \\
Real(PVQ[n-1]) \\
Real(P[n-1]) \\
Imag(P[n-1])
\end{bmatrix}
-
\begin{bmatrix}
0 \\
0 \\
-B_{pq,pv} \\
G_{pq,pv} \\
G_{pv,pv} \\
B_{pv,pv} \\
G_{pvq,pv} \\
-B_{pvq,pv} \\
G_{p,pv} \\
B_{p,pv}
\end{bmatrix}
\cdot v_{pv,re}[n]
-
\begin{bmatrix}
0 \\
0 \\
-B_{pq,pvq} \\
G_{pq,pvq} \\
B_{pv,pvq} \\
G_{pv,pvq} \\
G_{pvq,pvq} \\
-B_{pvq,pvq} \\
B_{p,pvq} \\
B_{p,pvq}
\end{bmatrix}
\cdot v_{pvq,re}[n]
\tag{2.81}
$$

$$K_{p,pvq} = \begin{bmatrix} K_{p_1,pvq_1} \\ \vdots & 0 & \cdots & 0 \\ K_{p_n,pvq_1} \\ & K_{p_2,pvq_2} \\ 0 & \vdots & \cdots & 0 \\ & K_{p_n,pvq_2} \\ \vdots & \vdots & \ddots & K_{p_1,pvq_n} \\ 0 & 0 & \cdots & \vdots \\ & & & K_{p_n,pvq_n} \end{bmatrix}^{N_p \times N_{pvq}}$$ (2.82)

$$PQ[n-1] = \left(s_{pq} \cdot w_{pq}[n-1]\right)^* - Y_{pq}^{sh} v_{pq}[n-1]$$ (2.83)

$$PV[n-1] = Real(s_{pv}) \cdot w_{pv}^*[n-1] - j\left(\sum_{k=1}^{n-1} Q_{pv}[k] w_{pv}^*[n-k]\right) - Y_{pv}^{sh} v_{pv}[n-1]$$ (2.84)

$$PVQ[n-1] = \left(s_{pvq} \cdot w_{pvq}[n-1]\right)^* - Y_{pvq}^{sh} v_{pvq}[n-1]$$ (2.85)

$$P[n-1] = Real(s_p) \cdot w_p^*[n-1] - j\left(\sum_{k=1}^{n-1} K_{p,pvq} Q_{\Sigma}[k] w_p^*[n-k]\right) - Y_p^{sh} v_p[n-1]$$ (2.86)

Step 4: Obtain the values of the power series
As long as coefficients of a new order of the power series are obtained, the variables' values can be found by summation of their power series. However, as mentioned, this approach is limited by the radius of convergence of the series. Therefore, the analytical continuation is applied to obtain the maximum convergence radius of the power series. As long as a new order of power series is solved by (2.81), the analytical continuation should perform to update the voltage values. The recursive calculation stops if the active power mismatches at PQ, PV, PVQ and P nodes and the reactive power mismatches at PQ and PVQ nodes are within an acceptable band. Other types of control functions can also be embedded to HELM, for example, the voltage magnitude controlled by the transformer tap ratio that is shown in the Appendix A – Voltage control by tap ratio in HELM.

Table 8. The load flow algorithm applying HELM.

1	*Calculate ΔP for PV, PQ, PVQ and P nodes, and ΔQ for PQ and PVQ nodes;*
2	*if $\|\Delta P\|_n \geq \varepsilon$ or $\|\Delta Q\|_n \geq \varepsilon$*
3	*Construct the left-hand-side of (2.81)*
4	*Construct the right-hand-side of (2.81) for n = 1, (2.62)-(2.69)*
5	*Calculate unknown variable for n=1.*
6	*while $n \leq N_{max}$*
7	*Construct the right-hand-side of (2.81) for n > 1, (2.83)-(2.86)*
8	*Calculate coefficients of the power series for the unknown variables at n^{th} order*
9	*if $n \geq 3$*
10	*Construct the matrix (2.36) of Padé approximation for each node, v_i*
11	*Find the value of power series for each node via three-terms recursive formula (2.37)*
12	*Calculate ΔP for PV, PQ, PVQ and P nodes, and ΔQ for PQ and PVQ nodes;*
13	*if $\|\Delta P\|_n < \varepsilon$ and $\|\Delta Q\|_n < \varepsilon$*
14	*break;*
15	*end*
16	*end*
17	*end*
18	*end*

As shown in Table 8, the calculation is straightforward through (2.81), where the left-hand-side is constructed only once and the right hand side needs some loops for the convolution calculations for (2.84) and (2.86). The most time consuming task is Padé approximation, i.e. line 10 in Table 8. However, the Padé approximation is carried out independently for each node, which can be calculated in parallel. Moreover, the matrix (2.36) for each node can be stored and reused if there is sufficient RAM [16], i.e. the matrix will be extended only when there is a new order available.

3.6. CASE STUDY WITH HELM

The same example shown in Figure 7 is used to demonstrate HELM, where the active power consumption at Bus 25 is increased from 224 MW until the load flow calculation is failed to be converged. The voltage collapses when the load at Bus 25 increases beyond 2500 MW. A new case is created every instant, where the load at Bus 25 is stepwise increased by 100 MW. In different load levels at Bus 25, the voltage magnitudes at PVQ nodes, i.e. Bus 11 and Bus 22, are kept constant due to the generator remote voltage control.

The reactive power outputs from Gen 31, Gen 32, Gen 35 and Gen 36 at P nodes are shown in Figure 10. In order to keep the voltage at P nodes, i.e. Bus 11 and Bus 22 in Figure 7, the reactive power outputs at Gen 31, Gen 32, Gen 35 and Gen 36 are needed to be respectively increased, where their contributions are according to the predefined participation factors that are constants for different simulated cases, as shown in the dash lines in Figure 10. The calculations stops at non-convergence case, i.e. Case 25 where no result is presented in Figure 10.

In all cases, Padé approximation is carried out sequentially node by node and the matrix (2.36) is reconstructed once a new order is available. In these studies, the generator reactive power limits are not considered in the calculations, which can be implemented in the outer loop, changing the PV to PQ nodes once the reactive power limit is reached.
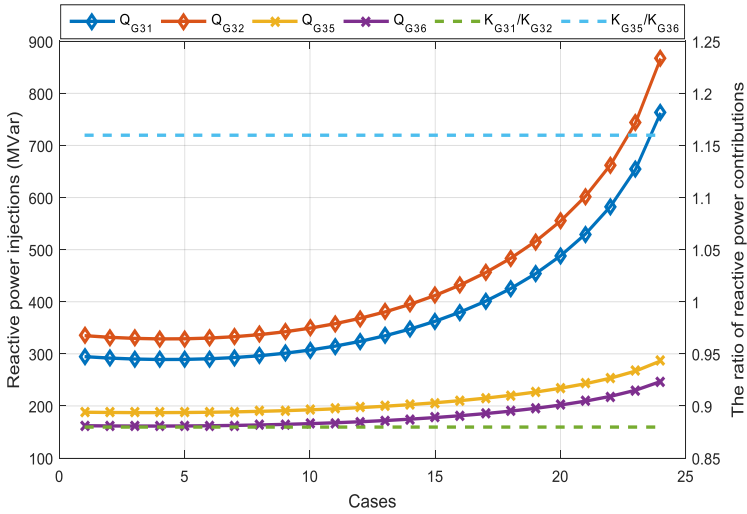
Figure 10. The reactive power at P nodes to control the voltage at corresponding PVQ nodes.
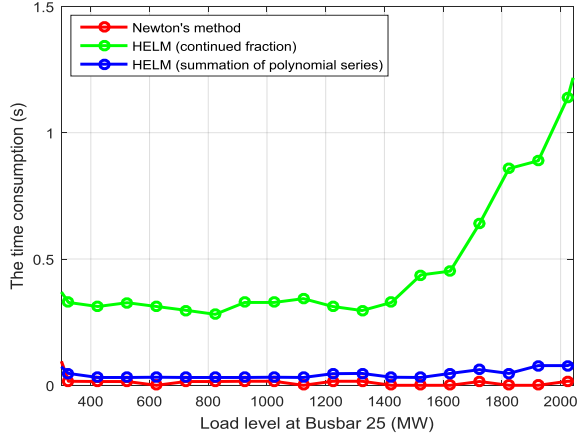
Figure 11. Comparisons of the time consumptions for (i). Summation of the power series; (ii). Continued fraction and (iii). Newton-Raphson method.

The studies are carried out at a PC with Intel® Core i7-4600M dual 2.90GHz CPU and 16 GM RAM. As shown in Figure 11, compared to the NR method, the time consumption of the simulated cases for HELM are generally longer. In these cases, HELM needs to reconstruct the matrices (2.36) for the power series in the continued faction calculations that significantly increases the time consumption. However, HELM with continued faction approach is independent of initial guesses, and guarantees the convergence if the solution is physically existing, which is superior to the approach based on NR method. For example, if the initial voltage magnitudes at Bus 24 and Bus 28 are changed, the approach based on NR method is failed to be converged in many cases, as shown in Figure 12, where each pixel in this map represents a load flow calculation with different initial guesses of the voltage magnitudes at Bus 24 and Bus 28. Moreover, many results are in fact the infeasible solutions, which locate at the lower branches of the "nose" curves. In contrast, HELM provide the solutions with the same time consumptions no matter what the initial values are, as HELM starts from the no-load condition without any initial guess.
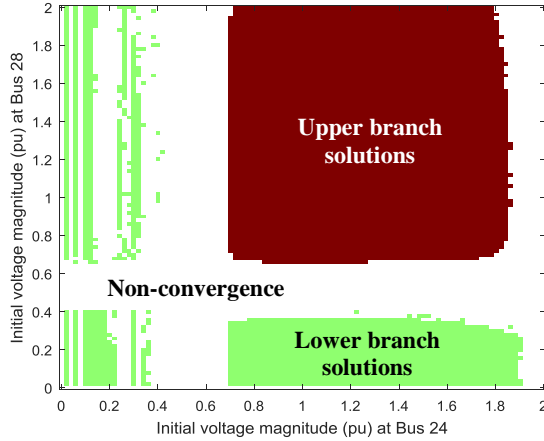
Figure 12. The convergence map of different initial points for total 101x101 load flow calculations based on the Newton-Raphson method in the test grid. The initial voltage magnitudes at Bus 24 and Bus 28 are varied from 0 to 2 pu with 0.02 pu. interval. Red: upper-branch solutions; Green: lower-branch solutions.

The system condition is changed, i.e. the active power and the reactive power consumptions at Bus 25 is changed to 100 MW and 500 MVar, respectively. Different voltage magnitude at PVQ nodes, Bus 11 and Bus 22, are set that vary from 0.6 pu to 1.6 pu, respectively. The voltage set points at Bus 11 and Bus 22 in some cases are unrealistic. However, this case is only used to compare the convergence ability of HELM with the continued fraction to NR method with the flat start.

The convergence maps of the NR method with the flat start and HELM with the continued fraction are respectively presented in Figure 13 and Figure 14, where both the maximum iteration number of the NR method and the maximum order of the power series in HELM are set to 50. More cases are converged based on HELM than NR method. Moreover, the solutions based on HELM are guaranteed to be feasible, whereas the solutions based on NR method may be unstable equilibrium points.
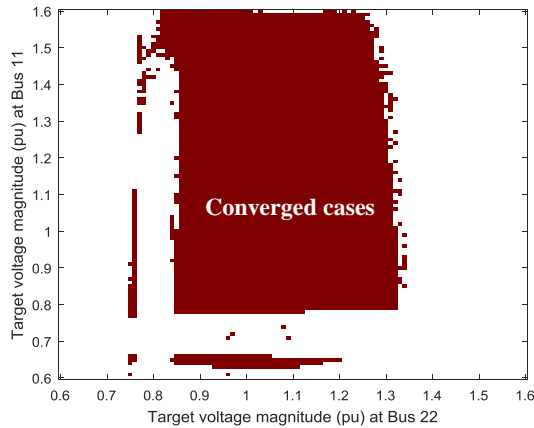
Figure 13. The convergence map of the NR method in the test grid with different voltage magnitudes at PVQ nodes, i.e. Bus 11 and Bus 22 respectively. The target voltage magnitudes at Bus 11 and Bus 22 are varied from 0.6 pu to 1.6 pu with 0.01 pu. interval. Red: the converged cases without identifying the upper or lower branch solutions.
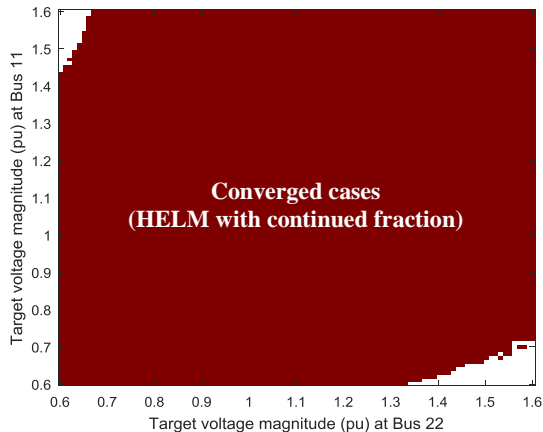
Figure 14. The convergence map of HELM in the test grid with different voltage magnitudes at PVQ nodes, i.e. Bus 11 and Bus 22 respectively. The target voltage magnitudes at Bus 11 and Bus 22 are varied from 0.6 pu to 1.6 pu with 0.01 pu. interval. Red: the converged cases.

4. SUMMARY

The load flow equations are nonlinear that can be solved by NR method. An alternative solution applying the complex analysis to solve load flow equations is HELM. In the real time system, the system load flow condition is obtained via the State Estimator (SE), where redundant inputs are available from the measurement devices. The purpose is to project the measurement data into a predefined network model, where the errors are minimized. The objective of SE is thus to formulate the load flow problem into an optimization framework and then minimizes the total error via least-square concept. In this framework, NR is better than HELM, as the optimization requires the Jacobian matrix to determine the searching direction for achieving the objective while complying with all constraints. In contrast, HELM is not able to provide the information for searching direction. However it is an alternative and useful tool for the load flow calculation, especially in the abnormal condition where NR is difficult to be converged. HELM can be applied as an identification tool to verify if a load flow condition is physically existing after the AVC find a solution. Moreover, the potential of utilization HELM in the AVC system is to develop a promising optimization algorithm that can compete to the existing Newton iteration based optimization framework for the decision making process.

CHAPTER 3. NUMERICAL OPTIMIZATION

AVC system is basis on a decision making process to find out the optimal setpoints of the reactive power components, to control the voltage profile. In another word, AVC is to find out the load flow solutions that comply with the operational requirements and expectations. The intuitive method is to find out all possible load flow conditions and then pick up the one that the voltage profile is mostly expected. More efficient method to achieve the goal is to formulate the problem into an optimization framework, where the solution is obtained by solving the formulated problem to comply with the optimality conditions. The optimization problem for the optimal reactive power flow is typically nonlinear and nonconvex. The formulated problem is always simplified, e.g. get rid of the discrete variables by using linear functions to represent the shunts and transformer tap changers. In this way, it can be solved by the nonlinear programming techniques. In this chapter, the prime-dual interior point method (PDIPM) and the trust-region (TR) method are briefly introduced.

1. NONLINEAR PROGRAMMING

The general optimization frame can be expressed as (3.1)-(3.3).

$$\min_{x} f(x), x \in \mathbb{R}^n$$	(3.1)
subjects to	
$$g_i(x) = 0, i = 1,2 \dots m$$	(3.2)
$$h_j(x) \leq 0, j = 1,2 \dots r$$	(3.3)

Where x is a real vector containing n decision variables. $f(\cdot)$ is the objective function. $g_i(\cdot)$ is i numbers of equality constraints and $h_j(\cdot)$ is j number of inequality constraints. Typically, there is more than one constraint. However, not all constraints have impact on the final solution. The constraints that are finally active, are binding constrains, where all these constrains turn to equality constraints. Changes on the binding constraints will change the objective value. The nonlinear programming is the process of solving the optimization problem, (3.1)-(3.3), where the objective and some of the constraints are nonlinear.

2. OPTIMALITY CONDITIONS

In nonlinear programming, the Karush-Kuhn-Tucker (KKT) conditions are the first order necessary conditions for a solution to be optimal [31]. The KKT condition can be summarized in Table 9. The KKT conditions of the problem (3.1)-(3.3) are typically solved via numerical optimization algorithms. If the inequality constraint is absent, i.e. $j = 0$, then the problem will converted to an objective under only the equality constraints, where the method of Lagrangian multiplier can be applied to search for the minima [31].

Table 9. The KKT condition.

Stationarity	$\nabla f_x^\top + \nabla g_x^\top \lambda_g + \nabla h_x^\top \lambda_h = 0$
Primal feasibility	$g_i(x) = 0$ and $h_j(x) \leq 0$ for all i and j
Dual feasibility	$\lambda_h \geq 0$ for all j
Complementary slackness	$\lambda_h \cdot h_j(x) = 0$ for all j
Linear independence constraint	∇g_x and ∇h_x have full row rank

3. PRIME-DUAL INTERIOR POINT METHOD

PDIPM is an approach to convert the general nonlinear programming problem with inequality constraints to the equality constrained problem. In this way, avoid identifying the binding constraints during the searching process, which can greatly improve the performance of solving the nonlinear programming problem via Lagrangian multiplier method [29], [31]. A compact form is shown in (3.4)-(3.6).

$$\min_{x,s} f_\mu(x) - \mu \sum_i log(s_i)$$	(3.4)
subjects to	
$g(x) = 0$	(3.5)
$h(x) + s = 0$	(3.6)

where μ is a positive small scalar. In the searching process, μ will be decreased close to zero, in order to restore the original objective. i is the inequality constraint index. s_i is the positive slack variables, with which the inequality constraints are converted to the equality constraints. The necessary optimality condition is the optimal point complying with KKT conditions. The Lagrangian equation is presented in (3.7), and the KKT conditions of PDIPM are expressed in (3.8)-(3.12) [31].

$$L(x, s, \lambda_h, \lambda_g) = f(x) - \mu \sum_i log(s_i) + \lambda_g^\top g(x) + \lambda_h^\top(h(x) + s)$$	(3.7)
$L_x = \nabla f_x^\top + \nabla g_x^\top \lambda_g + \nabla h_x^\top \lambda_h = 0$	(3.8)
$L_s = \lambda_h - \dfrac{\mu}{s} = 0 \equiv s\lambda_h - \mu$	(3.9)
$L_{\lambda_g} = g(x) = 0$	(3.10)
$L_{\lambda_h} = h(x) + s = 0$	(3.11)
$s > 0$ and $\lambda_h^\top > 0$	(3.12)

where λ_g and λ_h are the Lagrangian multipliers corresponding to the equality and inequality constraints, respectively. $\top$ is the matrix transpose operation. Equation (3.8)-(3.11) formulates a zero-finding problem that is normally solved by Newton's iteration method. The Newton step is expressed in (3.13).

$$\begin{bmatrix} L_{xx} & 0 & L_{x\lambda_g} & L_{x\lambda_h} \\ 0 & \lambda_h & 0 & s \\ L_{\lambda_g x} & 0 & 0 & 0 \\ L_{\lambda_h x} & I & 0 & 0 \end{bmatrix} \begin{bmatrix} \Delta x \\ \Delta s \\ \Delta \lambda_g \\ \Delta \lambda_h \end{bmatrix} = - \begin{bmatrix} L_x \\ L_s \\ L_{\lambda_g} \\ L_{\lambda_h} \end{bmatrix}$$	(3.13)

In order to apply the Newton's method to solve (3.13), the Hessian matrix is required that is the first derivative of the gradients w.r.t. the variables. If there are n variables, each gradient will produce a $n \times n$ Hessian matrix. All secondary partial derivative terms in the left hand side of (3.13) should be derived. The analytical Hessian matrices of the Lagrangian function are shown in (3.14)-(3.18), where $L_{x\lambda_g}, L_{x\lambda_h}, L_{\lambda_g x}$ and $L_{\lambda_h x}$ are straightforward to be derived from (3.8)-(3.11).

$L_{xx} = \nabla f_{xx} + \nabla g_{xx}\lambda_g + \nabla h_{xx}\lambda_h$	(3.14)
$L_{x\lambda_g} = \nabla g_x^\top$	(3.15)
$L_{x\lambda_h} = \nabla h_x^\top$	(3.16)
$L_{\lambda_g x} = \nabla g_x$	(3.17)

$$L_{\lambda_h x} = \nabla h_x \qquad (3.18)$$

Equation (3.13) can be further arranged by solving the second row of (3.13) for Δs yields (3.19).

$$\Delta s = -h(x) - s - \nabla h_x \Delta x \qquad (3.19)$$

Solving the fourth row of (3.13) for $\Delta \lambda_h$ yields (3.20).

$$\Delta \lambda_h = -\lambda_h - s^{-1}(\mu - \lambda_h \Delta s) \qquad (3.20)$$

Therefore equation (3.13) can be reduced by substituting (3.19) and (3.20), as shown in (3.21) [89].

$$\begin{bmatrix} M & \nabla g_x^T \\ \nabla g_x & 0 \end{bmatrix} \begin{bmatrix} \Delta x \\ \Delta \lambda_g \end{bmatrix} = \begin{bmatrix} -N \\ -g(x) \end{bmatrix} \qquad (3.21)$$

where

$$M = \left(\nabla f_{xx} + \nabla g_{xx} \lambda_g + \nabla h_{xx}\right) + \left(\nabla h_x^T s^{-1} \lambda_h \nabla h_x\right) \qquad (3.22)$$

$$N = \left(\nabla f_x^T + \nabla g_x^T \lambda_g + \nabla h_x^T \lambda_h\right) + \left(\nabla h_x^T s^{-1}(\mu + \lambda_h h(x))\right) \qquad (3.23)$$

Newton iteration step is therefore shown in Table 10.

Table 10. An example of the Newton step for PDIPM.

1	Calculate Δx and $\Delta \lambda_g$ via (3.21).	
2	Calculate Δs via (3.19).	
3	Calculate $\Delta \lambda_h$ via (3.20).	
4	Update the variables.	
	$x = x + \alpha_p \Delta x$	(3.24)
	$s = s + \alpha_p \Delta s$	(3.25)
	$\lambda_g = \lambda_g + \alpha_d \Delta \lambda_g$	(3.26)
	$\lambda_h = \lambda_h + \alpha_d \Delta \lambda_h$	(3.27)
	$\alpha_p = min\left(\gamma \min_{\Delta s_i < 0}\left(-\frac{s_i}{\Delta s}\right), 1\right)$	(3.28)
	$\alpha_d = min\left(\gamma \min_{\Delta \lambda_{h_i} < 0}\left(-\frac{\lambda_{h_i}}{\Delta \lambda_{h_i}}\right), 1\right)$	(3.29)

where α_p and α_d are adapted according to (3.28)-(3.29) in each iteration in order to keep s and λ_h to be positive. γ is constant scalar being less than 1. The barrier parameter, μ, needs to be converged to zero in order to restore to the original objective function. It is updated at each iteration by (3.30) [89].

$$\mu^{k+1} = \sigma \frac{s^T \mu^k}{n_i} \qquad (3.30)$$

where σ is a constant scalar between zero and one and n_i is the number of the inequality constraints.

PDIPM is demonstrated to be efficiently to solve the reactive power dispatch problem. It offers the key advantages over other approaches, including taking all constraints in the searching process

without identifying the active set of constraints and be able to start from infeasible initial point [30]. Many improvements are made specifically considering the nature of the power flow equations. For example, the merit function is proposed to enhance the convergence properties [31], where the search direction for minimizing the objective will be determined by minimizing the merit function taking into the feasibility violation into account. Another approach to improve the PDIPM is to use predictor-corrector steps in the search iterations. In iterations, the prediction step searches the moving direction neglecting the bounds on the decision variables, and the correction step dynamically estimates the barrier parameter μ and restores centrality to the solution.

4. TRUST REGION METHOD

The Trust Region (TR) algorithms are a class of optimization algorithms, which minimizes a quadratic approximation of an objective function in a specified region. This closed region is so called trust region, in which the quadratic model can be considered to be a good approximation to the original objective function. Minimizing the quadratic approximation in the closed region leads to the reduction of the original objective function. Otherwise, the size of the TR should be reduced for better approximation. TR method is initially developed to solve unconstrained minimization problems [31]. The method is to build up an approximate *model function* $m(x + d)$ around the current solution, i.e. the Taylor series expansion of $f(x)$ around x, and then find out the step size d to adjust solution vector x for minimizing the objective function $f(x)$.

The objective is expanded with respected to the decision variables, where the terms up to second order are kept. It is then a quadratic function w.r.t the decision variables, which is considered to be a good approximation of the original objective function, as expressed in (3.31).

$$m(x + d) = f(x) + \nabla f_x{}^T d + \frac{1}{2} d^T \nabla^2 f_x d$$	(3.31)

The closed region is usually defined by the Euclidean norm $\|d\|_2 \leq \Delta$, where scalar Δ is the *trust region radius*. It formulates the sub-problem to be solved around the point x for the unconstrained minimization problem, as presented in (3.32)-(3.33).

$$\min_x f(x) + \nabla f_x{}^T d + \frac{1}{2} d^T \nabla^2 f_x d$$	(3.32)
subjects to:	
$$\|d\|_2 \leq \Delta$$	(3.33)

A sketch of TR method is demonstrated in Figure 15. The parabola representing (3.32) open upwards only when $\nabla^2 f_x$ is positive, or positive definite in the matrix form. There will be an analytical minimum point, where the step length d could reach in the TR defined by (3.33). During the searching process, if the candidate solution $x_{k+1} = x_k + d_k$ is incapable of producing a sufficient decrease in $f(x)$ of a designed merit function, then the radius Δ_k should be reduced according to the predefined rules and (3.32)-(3.33) should be solved again.

For the constraint problem in the form (3.34)-(3.36),

$$\min f(x)$$	(3.34)
subjects to:	
$$g(x) = 0$$	(3.35)
$$\underline{x} \leq x \leq \overline{x}$$	(3.36)

The TR method is to solve the constrained problem as follows, (3.37)-(3.41) [31].

$$\min_x f(x) + \nabla f_x{}^T d + \frac{1}{2} d^T H_x d$$	(3.37)
subjects to:	
$$\|d\|_2 \leq \Delta$$	(3.38)
$$g(x) + \nabla g_x{}^T d = 0$$	(3.39)
$$\underline{x} \leq x + d \leq \overline{x}$$	(3.40)

where

$$H_x = \nabla^2 f_x + \sum_{i=1}^{m} \lambda_i \nabla^2 g_x$$	(3.41)
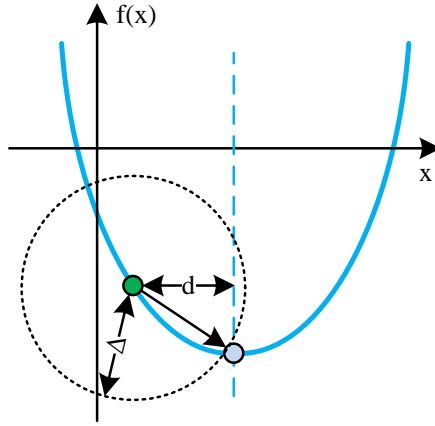
Figure 15. A sketch of the TR method.

Combination of PDIPM and TR is proposed in [32], where it tackled two problems: (i). Define the search direction when the quadratic model used by the algorithm is not convex; (ii) Handle the rank deficiency of the Hessian of the Lagrangian and constraint Jacobian. The robustness of combined PDIPM and TR is studied in [33]. Lots of commercial software applying the combined PDIPM and TR methods solves the nonlinear programming problems. In this project, *"fmincon"* in Matlab Optimization Toolbox [64] is used to solve the optimization problems for the proposed AVC system.

5.   ARTIFICIAL INTELLEGENT METHOD

The heuristic algorithms are proposed to solve the reactive power dispatch problems [34]-[36]. The basic idea is to embed the ORPF problem into the predefined search rules that are not based on the gradients and Newton's iteration method. For example, the Particle Swarm Optimization (PSO) method emulates the movement of particle swarm in the search hyperspace. Though they can in certain degree find the global optimal solution, they are generally time-consuming and computational expensive. However, they can be used for the situations that the formulated problem is non-differentiable. In the power system engineering, the load flow equations and the constraints can be well formulated. The algorithms to solve the equations are intended to be applied in the real time system where strong tractability, high performance and high reliability are expected. Therefore, the numerical optimization methods based on the Newton's iteration techniques are preferred for the AVC systems.

5. SUMMARY

The voltage control problem is formulated in an optimization framework, where the numerical optimization techniques are applied to solve the problem. The combined PDIPM and TR method is finally applied that can efficiently solve the large scale nonlinear programming problem. This approach combined the high performance of PDIPM and strong reliability of TR methods, which is considered the most promising method to solve the formulated problems of the AVC systems. The solution from this approach is not guaranteed to be the global optimal solution but a local optimal solution. However, the AVC system is expected to be operated in the real time system, where the solution should be found in very short term, e.g. 1 to 5 minutes. The artificial intelligent based methods are generally time-consuming that are difficult to solve the problem in time. Moreover, as the acceptable voltage band is generally narrow, e.g. between 0.9 to 1.1 pu., obtaining the feasible solution in short time is more expectable than searching out the time-consuming global optimal solution in the industrial applications. Especially for the small scale system, the difference between the global and the local optimal solutions are expected to be non-significant. Therefore, the combined PDIPM and TR method, as the *"fmincon"* provided by Matlab® Optimization toolbox [64], is applied to solve the optimization problems in this project, as a tool for the preliminary studies to assess the proposed AVC system.

CHAPTER 4. DANISH AVC SYSTEM

1. STATE-OF-THE-ART

In the transmission power systems, the voltage level is maintained within a certain range, normally a few kilovolts. This is always achieved by controlling the reactive power components via voltage control system. This section survey existing AVC systems to inspire the design of the Danish AVC system.

1.1. HIERARCHICAL CONTROL

The hierarchical control is proposed in 1972 by the French company Electricité de France [37]. The principle is shown in Figure 16. V_P and q_P are voltage magnitude at pilot bus and the required reactive power to maintain V_P, respectively. V_G and q_G are the power plant voltage magnitude and the required reactive power to maintain V_G, respectively. E_{fd} is the field voltage of the generator that is under control. The hierarchical structure is typically split to 3 levels according to the response time: (i). PVR with response time in several milliseconds (ii). SVR with response time in several minutes and (iii). TVR with response time up to an hour [38]-[40].
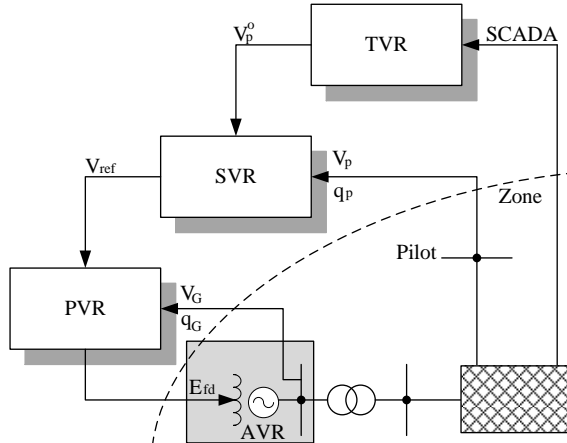
Figure 16. The general hierarchical AVC system for the large scale power systems.

PVR is fully automatic and response to the voltage disturbances to maintain the voltage at the target busbar. The generators including the conventional power plants and the synchronous condensers equipped with Automatic Voltage Regulator (AVR) devices to control the excitation voltage are typically employed by PVR. Moreover, the transformer tap changer and switchable shunts in the station levels are always employed by PVR as well. In the case of the system condition changes significantly e.g. from low load to peak load conditions, the setpoints of the PVR should be adjusted by corresponding SVR for achieving the satisfied voltage profile. PVR dispatches the setpoints afterwards to control the voltage at the target busbar while maintaining the reactive power reserve among employed generators.

The whole system is typically decomposed for several zones where a SVR is placed in each zone [38][40]. SVR is the core of the hierarchical control system. It secures the system voltage by dispatching the setpoints for components regulated by PVR. A pilot bus in each zone is defined, which is then monitored and controlled by the regulators to maintain the voltage profile. Normally the pilot bus is a load bus that represents the maximum resemblance to the area voltage profile i.e. the values of voltage deviations throughout all load buses due to small disturbances are minimized [41].

For each zone that contains a pilot bus, the regulatory components are capable of providing sufficient reactive power to maintain the pilot voltage within an acceptable band. The interactions between different zones are minimized after decomposition to avoid interactions like "hunting", i.e. the zones are "electrically far away" from each other [38]. Moreover, the pilot bus in each zone is sufficiently robust against the topological changes or variations of the operational conditions. Various techniques are therefore proposed for pilot bus selection and grid decomposition. The most common method is based on the "electrical distance" concept and clustering algorithms [41]-[42]. Sophistically defining the pilot buses will provide the possibility to efficiently control the voltage in a large scale power system with limited information, by focusing on maintain the voltage at pilot buses.

TVR on the top of the hierarchical control system coordinates SVRs in different zones, in the control of the voltage profile for the common objective, e.g. minimizing the overall grid loss. In the real time environment, TVR dispatches the setpoints to SVRs for the pilot buses on the basis of the actual state of the electrical system and of the optimal voltage profiles. TVR consider zones are electrically far away from each other, the interactions between zones are considered to improve the performance. For example, Coordinated Secondary Voltage Control is firstly proposed in the French system to take the interactions between adjacent zones into account [43]. The method performed in TVR in [44] preserves the decentralized nature of SVR by using the reactive power tie-line flow measurements in the control function, and shares the reactive power reserve when control limits are reached.

1.2. CENTRALIZED CONTROL

The centralized control is another scheme for a voltage control system, e.g. in Switzerland [45], there is no formal SVR and TVR in the AVC system. The centralized control center coordinates the AVR of the synchronous generators and the transformer tap positions to maintain voltages at all nodes within the acceptable band. In a centralized voltage control system, there is no pilot bus. The synchronous generators and other reactive power components receive the setpoints from the control center periodically in the same AVC loop. Unlike the hierarchical AVC system, the reactive power reserve among the power plants may not be shared with the equal percentage of their capacity. Without defining the pilot bus, the voltages at all buses are needed to be taken into account as constraints in the optimization model, which is suitable for small scale systems with a limited number of nodes and reactive power components, limiting the heavy calculation burden to ensure the strong tractability in the real time systems.

1.3. SUMMARY

In the hierarchical systems, the pilot bus in SVR is normally predefined offline [37][40][48]-[49]. However, it can also be determined in the real time system via the adaptive pilot bus selection method [42], considering the fast system expansions that lead to significant topological and operational changes. SVR in each region is responsible for maintain the voltage and correct the voltage violations on the pilot bus, and ensures the sufficient reactive power reserve in the generators in each region [39]-[40]. The reactive power production is typically shared among the power plants homogeneously proportional to their capacity [40][48]-[49]. TVR optimizes the overall system voltage profile and dispatch the setpoints of the pilot buses to SVRs [40]. In contrast, the centralized system considering all nodes in a common optimization platform is applied for the relatively small scale systems.

As shown in Table 11, the existing AVC systems in different power systems are briefly summarized. In the conventional bulk power system, the power is generated by the large synchronous generators, which is transferred to the consumers via the power grids. The large synchronous generators normally equipped with the AVR systems that are not only produce the power, but also provide the ancillary service, such as frequency response and voltage control. They are able to response the disturbances in milliseconds. The AVC systems in the conventional power systems employing the large generators maintain the voltage, and minimize the grid loss by optimizing the voltage profiles. The reactive power is always shared among the generators in a power plant. The status of the shunt components

and the transformer tap positions are adjusted to compensating the reactive power outputs of the generators, for reserving the reactive power as much as possible and reducing the loss inside the generators.

Table 11. The existing AVC systems and the expected Danish AVC system [46].

Country	Structure	Closed loop	Forecast	Functions/Goals	Controllers	Considerations
France [37]-[39]	H	x		• Correction of voltage violation at pilot bus • Correction of terminal voltage for generators • Correction of reactive power violation for generators	• Generator • Capacitor	• Voltage variation at generator terminals • Voltage at the sensitive buses • Voltage magnitude at the high-voltage side of generator • Reactive power of generator
Italy [40]	H	x	x	• Correction of voltage violation of pilot bus including the effect of forecast setpoints for grid loss minimization • Correction of reactive power violation of zones including the effect of forecast setpoints for loss minimization	• Generator • Shunt • Transformer • FACT	• Voltage limits • Components regulation limits
Belgium [48]	H			• Maximization of the reactive power margin on each group of synchronous generators • Minimize the switching of capacitor banks • Restricted inter reactive power flow to neighbor systems • Voltage correction	• Generator • Capacitor • Transformer	• Voltage limits • Components regulation limits
Spain [49]	H		x	• Solve congestions • Correction of voltage violation primary for low-voltage problem	• Generator • Reactor • Transformer	• Voltage limits • Components regulation limits • Auxiliary services limits
Switzerland [45]	C		x	• Cost minimization of loss plus reactive power payments	• Generator • Transformer	• Voltage limits for all nodes • Voltage differences among nodes • Reactive power flow on ties • Components regulation limits
China [42]	H	x		• Adaptive Pilot selection • Losses minimization • Correction of voltage violation	• Generator • Transformer • Shunt	• Voltage limits • Components regulation limits
British Columbia [50]	C			• Losses minimization • Correction of voltage violation	• Shunt • Condenser • SVC	• Voltage limits of selected nodes • Components regulation limits
Denmark [46]	*C*	*x*	*x*	• *Correction of voltage violation* • *Cost minimization*	• *Shunt* • *Generator* • *FACTs* • *Transformer*	• *Voltages limits for all nodes* • *Components regulation limits* • *Reactive power flow on ties*

In different countries, the AVC systems are designed based on the features of the power systems. In France, an approach called CSVC is implemented that is able to coordinately control generators to maintain the voltage at several pilot buses with 10-second samplings [39]. By doing such, the effectiveness is greatly enhanced. In Italy, the TVR minimizes the overall grid loss, based on the forecasting system [40]. The forecasted voltage profile and the reactive power limit are found in advance. The real operation focuses on minimizing the differences of the forecasted and the real voltage profiles [40]. This approach is valid, as the Italian power system is also conventional, where many power plants are in service and the energy flow is more or less fixed every day. The system reliability enhancement is also considered in the Italy AVC system. The REPORTs are installed at power plants, to automatically maintain the predefined voltage setpoints at the high voltage side of the transformer, in case the telecommunication is malfunctioning [40]. In Switzerland, thanks to the fixed power transfer pattern, the AVC system can also employ the forecasting system for the voltage control. It is called "Day-ahead Reactive Planning" [45], where the day-ahead voltage setpoints of the generators and the tap positions are therefore found in advance based on the day-ahead congestion forecast. The objective is to minimize the operational cost including the cost of the grid loss and the reactive power payments to the generators. In Spain, a long term plan, so called "voltage plan", for one year is made [49]. In the Belgium, the objective of the AVC system also considers the reactive power reserve in the generators, and the switching times of the capacitor banks, to minimize the total

operational cost [48]. In China, the AVC system applying the adaptive-zone division algorithm controls the voltage in the fast expanding system [42]. In Canada, the AVC minimizes the grid loss and corrects the voltage violations [50]. In case the remedial action schemes are activated, the so called "Automatic VAR schemes" will automatic switch in/out shunts at important 500 kV stations to meet the voltage targets.

1.4. EXISTING PRODUCT FOR THE DANISH AVC SYSTEM

An existing product embedded in the current Energy Management System (EMS) is shown in Figure 17, which is so called Voltage Var Dispatch (VVD). It can be applied for the decision making process of the AVC system. This is basis on a centralized voltage control system to maintain the system voltage for all buses. The setpoints are obtained periodically via State Estimator (SE) and a classical ORPF algorithm to minimize the system loss in the transmission lines or correct the voltage violation, as shown in Figure 17. Discrete reactive power components, i.e. the switchable shunts and tap-able transformers that are not controlled by local Reactive Power Controller (RPC), as well as the continuous reactive power components, e.g. thermal power plants and synchronous condensers, will be assigned to participate in this AVC system. A control loop including data acquisition, optimization and setpoint dispatch is capable of being carried out every minute.
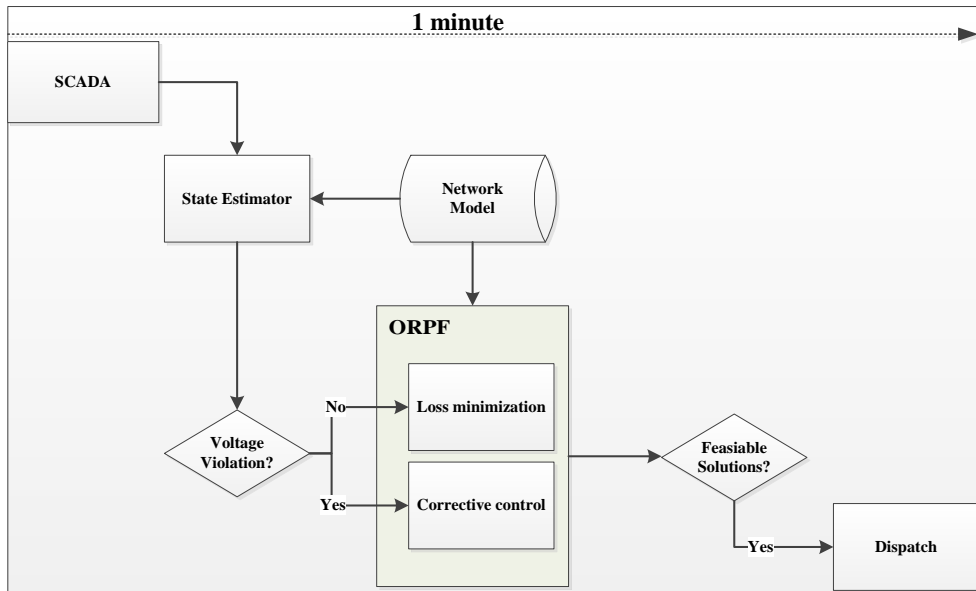
Figure 17. AVC process from data acquisition to dispatch in a single loop.

The ORPF in this AVC system did not take into account the regulation cost of the assigned components. It means that this approach assumes the potential loss saving in most of time is larger than the regulation cost. However, in the relatively small system with many shunts and transformers, like Danish transmission system, the regulation cost could be larger than the cost saving from the grid loss, which leads to the negative profit. In this case, a post-process can be applied to assess if the saved loss can cover the proposed regulations, and then update the setpoints of the reactive power components only when the system can beneficial from regulations, i.e. earn "profit" by reducing the loss with limited regulation cost. In addition, this approach does not consider the reactive power reserve in the continuous reactive power components. The system may require a large amount of reactive power injections after a contingency, which is considered important in the current Danish power system with fewer and fewer central power plants.

1.4.1. Estimated saving from loss minimization

In the transmission grid, the loss is largely due to the current flowing in the branches, $P_{loss} = I^2 R$, which can be reduced by optimizing the voltage profile to reduce the current quantity for reactive power consumption in the series branches. Two aspects should be taken into account:

- Voltage magnitudes, $\hat{I} = \frac{S^*}{\sqrt{3}\hat{U}^*}$. For transmitting a certain amount of power, s, higher the voltage level, U, smaller the current flowing in the branches, I, then less loss introduced. For example, the system voltage is controlled to close to the upper limit for loss reduction.

- Voltage difference between two ends of each branch, $I = \frac{\hat{U}_1 - \hat{U}_2}{R + jX}$. For transmitting a certain amount of power at a given voltage level, less voltage differences between two ends of branches, less current flowing in the branches, and then less loss introduced.

In other words, for transmitting a certain amount of power, the loss can be minimized if maximizing the voltage level and simultaneously minimizing the voltage differences between ends of branches i.e. minimizing the reactive power flow in the branches. As known, control the nodes voltage is mainly achieved by regulating the reactive power injections. If only increasing the voltage level without considering the voltage deviations, it may result in large voltage differences between two ends of the branches. In this case, raising the voltages improperly may result in more cost than saving on the loss due to the introduced voltage differences among the nodes.

The transmission losses were recorded by SE every minute from 10:58 am, February 10th, 2014. The statistic characteristic is obtained to find out the loss pattern, from the starting time to 14:40 pm, September 8th, 2014. In the existing system, if the calculation in SE is not converged, the grid loss will be extremely high. Therefore, a simple rule is used to filter out these non-converged samples, i.e. if the system loss in DK1 higher than 130 MW and DK2 higher than 80 MW, respectively, then the state estimator at this time point is considered to be not converged.

The data availability for assessing the loss in this period is 99.96% (302,431 out of 302,548 samples). The system losses in DK1 and the eastern Danish grid (DK2) are represented in Figure 18 and Figure 19, respectively. Considering the losses in the transmission level could be influenced by the time frame, e.g. seasons, the monthly losses are also found as shown in Table 12 and Figure 20, where the average loss in February, July and August are higher than in April and May.
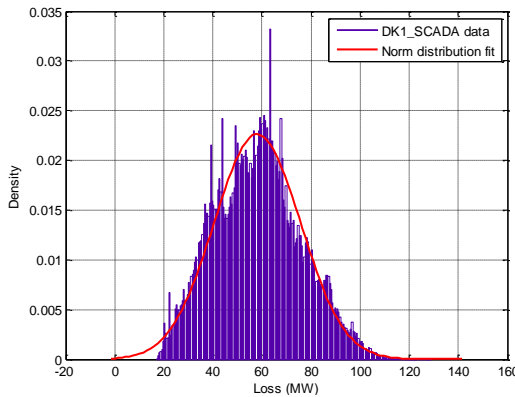
Figure 18. The histogram of losses in DK1 for the selected period and its norm distribution fit.
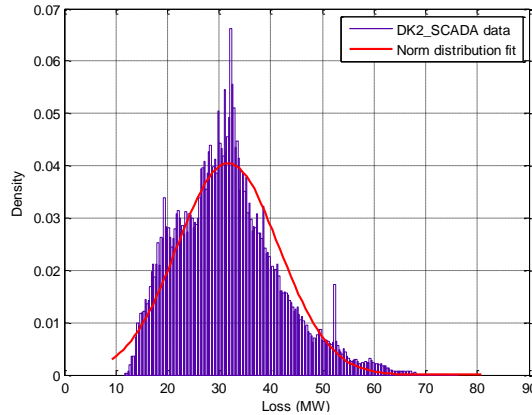
Figure 19. The histogram of losses in DK2 for the selected period and its norm distribution fit.
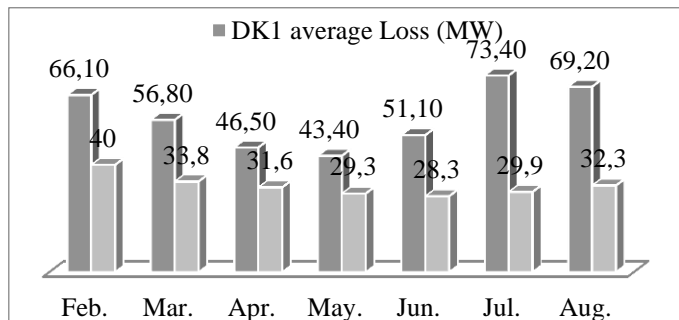
Figure 20. The monthly average losses for the selected period.

The existing VVD was running offline to briefly assess the potential loss saving, where the snapshot of the western Danish grid (DK1) was optimized for loss minimization. The obtained setpoints were not dispatched. The assessment result was applied for the business case in Energinet.dk. The VVD results were recorded from 13:29 pm, August 6th, 2014. The suggested setpoints by VVD were not dispatched in the real system. The potential loss saving is the differences between the values from the SE and VVD.

In the VVD function, if no results are available due to the non-convergence, the obtained loss will be close to zero. The data availability is therefore assessed by inspecting if the calculated loss with VVD lower than 10 MW due to the non-convergence and if the loss saving with VVD higher than 5 MW or negative due to the infeasible solutions of VVD.

The data availabilities of VVD solutions and the SE are respectively 60.4% (31353 out of 47585 samples) and 100% (47585 out of 47585 samples) in this period. It indicates that parameters tuning is needed in order to obtain a better performance and reliable results. During the trial period, almost all transformer tap positions and the breakers of the switchable shunts in the transmission grid of DK1 system are controlled by VVD. The variable shunts, the generators and VSC-HVDC are not included, though they are capable of participating in the AVC system. This is considered that the generators are owned by power companies. It should evaluate the internal cost for them before employing them for the voltage control. VSC-HVDC is not well presented in the EMS during the trial period, and is not included in the VVD function. In addition, if the continuous reactive power components, such as generators are employed in the VVD, the convergence is expected to be greatly improved.

The average saving was about 0.3 MW in the trial period, as shown in Table 12. The saved loss is rare to be higher than 1 MW as shown in Figure 21. However, it is considered to be a very conservative value, as no continuous reactive power components participated in the voltage control during trial period. The loss saving is expected to be larger if more controllers are available and better performance of VVD is approached after well tuning the parameters. In addition, more data in different time frame is expected to assess the loss saving comprehensively.

Table 12. The average losses founded by the State Estimator (SE) and the estimated potential saving after execution of VVD in DK1.

From	To	DK1_SE (MW)	DK1_VVD (MW)
Feb.10th	Feb.28th	66.1	None
Mar.1st	Mar.31st	56.8	None
Apr.1st	Apr.30th	46.5	None
May.1st	May.31st	43.4	None
Jun.1st	Jun.30th	51.1	None
Jul.1st	Jul 31st	73.4	None
Aug.1st	Sep. 8th	69.2	None
Aug.6th	Sep.8th	69.6	69.3
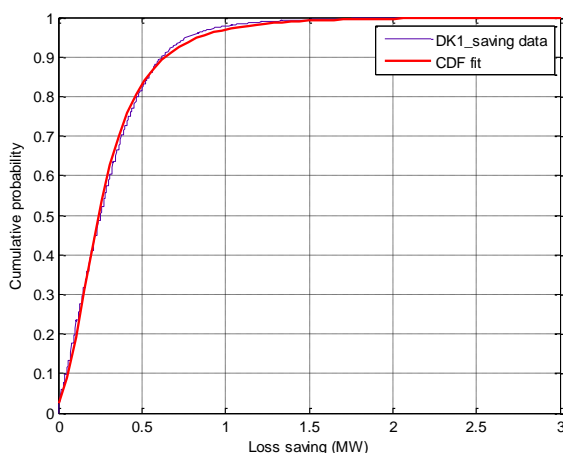
Figure 21. The cumulative probability fit of loss saving in the period between Aug.6th and Sep. 8th.

Similar offline studies carried out in DIgSILENT powerfactory to assess the potential loss saving with all available controllers including the central power plants in the present system based on the selected historical measurement data. Total 25 snapshots of DK1 system for 2013-01-11 2:30 am to 2013-01-11 6:30 am with 15-minute intervals are investigated, where the power flow in the main corridor was reversed in this period. It required many control actions to maintain the voltage. The results show that average around 0.8 MW losses can be saved in the selected snapshots if only controlling the shunts and tap-positions of the transformers. The saved average losses can reach 1 MW if also controlling the central power plants and meanwhile limiting the reactive power output of the central units close to the neutral by setting hard constraints with reduced generator regulation capabilities. Hard limits on the central power plants are used to ensure sufficient reactive power reserve from the generators. However, the main saving comes from switching off the shunts to save the shunt conducting loss in these studies. It indicates that the shunt conductance should be well included in the grid mode of the

real time system, which is exceptional importance for the Danish system as many shunts will be placed in the grid to compensate the cable network.
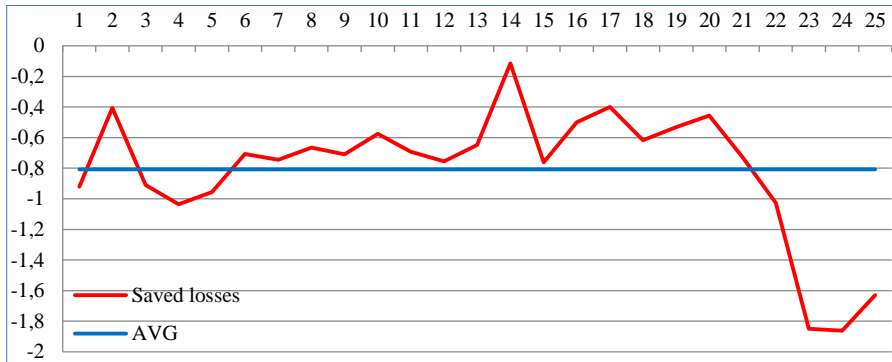
Figure 22. The loss saving in MW for the 25 snapshots in the offline studies.

In summary, the loss saving strongly depends on the power balances that are influenced by the time frame and the number/types of the regulators as well as the performance of ORPF algorithm. Potential loss saving assessment based on several single snapshots is not sufficient. Continuously recording losses from SE and VVD is required for comprehensive investigations, which can also be used to improve the VVD performance. More important, a simulation platform is needed, where different optimization formulations for the Danish power system can be applied.

1.5. THE EXPECTED DANISH AVC SYSTEM

The Danish transmission system is very flexible due to its transit-dominated characteristics, the high penetration of wind power and a large number of dispersed generation units in the distribution levels. To address the voltage control challenges mentioned in Chapter I, a Danish AVC is proposed [46].

1.5.1. Centralized AVC

The pilot bus approach utilized in existing AVC systems provides the promising results to effectively control the overall system voltage in large power systems. However, this approach is not considered for the Danish system, since the Danish power system is relatively small and flexible, i.e. only limited numbers of conventional power plants locate in a relative small area; the commissioning of conventional power plants determined by the market price. The small scale system is not easy to be split to zones, and the flexible transits may lead to different zone divisions along the time. Therefore the centralized control scheme in the Danish transmission grid is preferred.

1.5.2. AVC Objective

The goal of the Danish AVC system is to automatically maintain the voltage for all buses and minimize the loss at the transmission level due to reactive power flows in the branches. The difficulty is to achieve the goal while reserving the reactive power as much as possible with high share of wind power in the system. In addition, large number of discrete controllers, i.e. the taps of the power transformers, the switchable and the variable shunts are planned to be used for regulations, which should be well handled in the optimizations. The cost of regulating these components in the AVC system should be taken into account, since the benefit from loss saving may be less than the regulation cost on the reactive power components.

1.5.3. Priority

The regulation cost of discrete components can be estimated, e.g. summation the cost of the capital investment and the maintenance over the possible switching times to estimate the regulation cost per time. It provides AVC to prioritize the controllers according to the sensitivities. The priority of

control actions should refer to the cost of regulations. If the cost of generators for adjusting the reactive power output is lower than the switching cost of discrete components, then the generators will be preferred to be regulated prior to the discrete components. The reactive power reserve in the generators can be considered by either assigned high cost in the objective function or hard constraints for limiting the regulation capabilities in the optimization framework.

1.5.4. Forecast

The fluctuation of the renewable energy could dominate the voltage variations in the future. In order to efficiently maintain the voltage, the forecast systems may be required, as the AVC systems in Italy, Switzerland and Spain [40][45][49]. The real time system can thus optimize the control actions taking into account the forecasted solutions to enhance the voltage security. Another expectation from the forecast system is to reduce the regulation cost. The states of the system are expected to be found considering the short-term forecasting snapshots. The decision making is to optimize the system for a certain horizon instead of individual snapshots, in this way, to address the system variability [51].

1.5.5. Fallback scheme

As the function of REPORTs in Italian AVC system [40], a fallback scheme is expected to be implemented in the Danish AVC system, in case a certain substation loses the telecommunication to the control center or several stations are isolated from the main grid [52]. Local fallback controllers are expected to be operated autonomously without telecommunications. The logic can thus be made to trigger the control actions, to maintain the voltage close to the pre-fault value. Another application of fallback controllers is to help AVC to correct the voltage violations in the normal operations. For examples, in case the voltage violates the operational limits but not triggers the existing over/under voltage relays, the voltage violation will be corrected after AVC dispatches the setpoints in the next loop. In this case, the fallback controllers can be activated to correct the violations prior to AVC, to enhance the voltage security.

1.5.6. Scalability

There are currently 18 stations equipped with RPC embedded in Remote Terminal Unit (RTU), which controls the shunts and the transformer taps to regulate the reactive power locally. The loop of the typical RPC is much shorter than 1 second, normally from 100 to several hundred milliseconds. In order to avoid frequent switching of the discrete components by either RPC or AVC, a preliminary solution is to exclude RPC from AVC system, and later integrate RPCs as normative regulators in the AVC system. The AVC system dispatches setpoints to RPCs after ORPF is carried out.

The wind power plants, e.g. the offshore wind farms are capable of control the voltage at PCC. They are not required to participate in the voltage control system in Denmark in the time being. However, the potential benefit to include them in the proposed AVC system can be investigated.

The dispersed units in the distribution grids may participate in the voltage control in the transmission level e.g. the "cell controller pilot project" demonstrates that cell controllers at a 150 kV station can coordinate the dispersed units in the distribution level to supply reactive power regulations for the transmission grid as virtual power plants [53]. The effect from active distribution grids should be further investigated for different system topologies and operational conditions. This mixed centralized and decentralized AVC system is considered for a later stage of the Danish AVC solution.

1.5.7. Summary

The voltage control in the future Danish system is becoming a challenging problem. The existing AVC systems in different countries are mainly designed for the conventional power system, where the power transmission patter is more or less fixed for every day. In the future Danish system, the conventional power plants are likely phased out. Instead, the wind power plants, the spread combined heat and power plants will dominate the energy production. The power balance is more flexible in the future than today, as the interchange capacities to the neighboring systems will be continually

increasing and the transits in the grid are determined by the market. The AVC in such system is expected to be able to efficiently control all reactive power components including the wind power plants, taking into the system variability, to minimize the total operational cost including the both grid loss cost and the regulation cost, while maintaining the voltage in the acceptable band.

The Danish system is relatively small. Therefore all busbar voltage will be maintained in the AVC system. All reactive power components are controlled by the national control center via the SCADA system, which composes the centralized voltage control system, as shown in Figure 23. The reactive power components comprise of the breakers and taps of the shunts, the transformer tap positions, the generator AVRs and the status of FACTs. The objective of such system is to minimize the total operational cost including the grid loss cost and the regulation cost, taking into the system variability via the short-term forecasting system. The forecasting system is intended to be integrated, which provides predicted power balance for the decision making process, i.e. ORPF algorithm. The operator can either approve or reject the solutions suggested by the AVC system before dispatching the setpoints to the reactive power components. In the final stage, the AVC system is able to be operated in the closed loop. In addition, the reliability can be enhanced with, so called fallback scheme [52], to automatically control the assigned shunts to maintain the voltage in case the telecommunication between control center and the stations are malfunctioning.
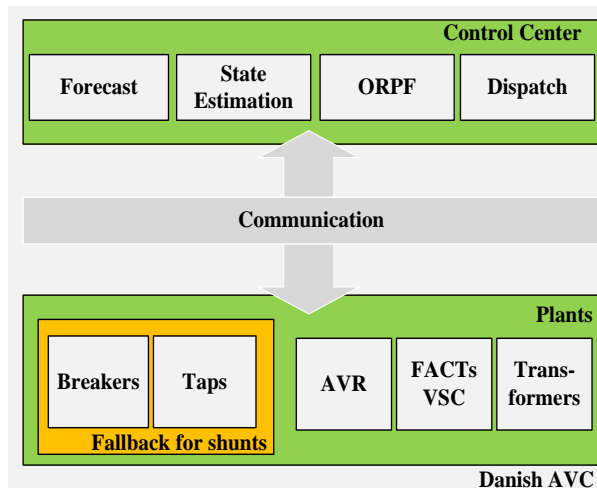
Figure 23. The proposed Danish AVC system [46].

2. REACTIVE POWER COMPONENTS

In the transmission system, the reactive power components are defined as the apparatus that used to manage the reactive power to support the voltage, for correcting the power factors and mitigating the voltage fluctuation at a given terminal of a branch.

2.1. SYNCHRONOUS GENERATOR

Synchronous generators are equipped with the AVR devices to control the excitation voltage. The excitation voltage is controlled by regulating the filed current. The generator therefore produces or absorbs the reactive power at the terminal node as required, e.g. to maintain the terminal voltage.

The synchronous generators are typically placed in the large power plants for the energy conversions. As shown in Figure 24, the reactive power regulation capability depends on the active power production levels, which is also known as the generator capability curve that limits the total generator

current output by typically considering the heat limits of components inside the machine, e.g. the armature and the field current limits [47].
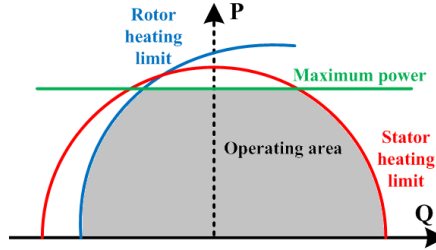
Figure 24. An example of a conventional power plant.

A synchronous condenser is simply a synchronous generator connected to the power system with excitation system. There is no governor system and relevant components for power conversion, as it does not produce any active power. The inertia is less for synchronous condenser than the conventional power plants, due to absence of the turbine. Comparing to other reactive power components, the loss and the cost are much higher than those associated with static compensators. Their advantages lies in their high short-circuit power contributions.

Typically, the voltage setpoint is received from the operators, and then the excitation voltage is regulated accordingly. Droop function is always applied to avoid the hunting problem, i.e. conflict regulation among reactive power components. In the Danish power system, the compounding factor instead of droop factor is applied. In contrast to the droop factor, the compounding factor is positive scalar based on the measurement at the low-voltage side of the step-up transformer. The resulted droop characteristic can be found as shown in Figure 25.
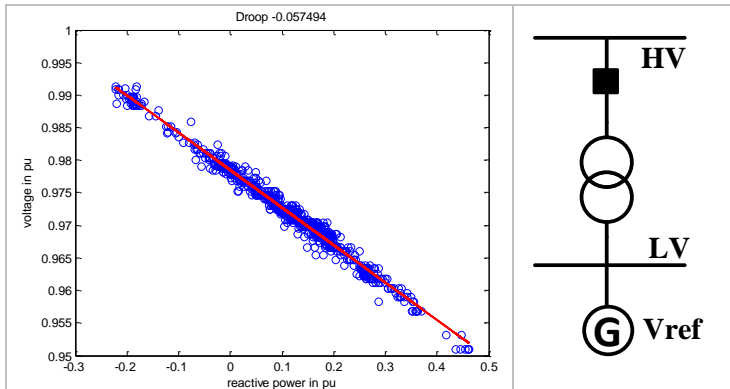
Figure 25. The resulting droop function of a generator controlling the voltage. The 1-minute intervals measurements at 150 kV busbar in TJE150 station are applied for linear regression.

In the voltage control system, the reactive power outputs are defined as controllers in the optimization process. As long as the optimization problem is solved, the terminal voltages of the power plants can be found. Hereafter, the voltage set-points of AVR in power plants, V_{refL}, can be obtained via:

$$V_{ref} + K_q Q_{LV} = V_{LV}$$ (4.1)

where V_{LV} is the found optimized voltage magnitude at the terminal of power plants. K_q is the voltage/reactive power compensation factor, which is a fixed *positive* value inside the AVR settings. Q_{LV} is the reactive power flow out of the power plant, which is the controller of the generators in the AVC systems. In the static situations, V_{ref} is adjusted as the setpoints to AVR that dispatched from the control center. In the transient situations, V_{ref} is typically fixed and Q_{LV} is fast adjusted to trace the voltage set points V_{LV}, normally by Proportion Integration (PI) controllers inside AVR system.

The equation (4.1) is also called compounding relation, where the terminal voltage V_{LV} and the reactive power output Q_{LV} at the terminal of power plant are measured. In the case of the voltage, V_{HV}, and the reactive power, Q_{HV}, at the remote bus, e.g. the high voltage side of the step-up transformer, are measured, it is so called droop relation, shown in (4.2).

$$V_{ref} - D_q Q_{HV} = V_{HV} \qquad (4.2)$$

where V_{ref} is the reference voltage for AVR system. D_q is a *negative* voltage/reactive power compensation factor. In the calculations, Q_{HV} is negative when the power plant injects reactive power to the grid, which is opposite to Q_{LV} that is positive when the power plant injects reactive power to the grid. The compounding/droop is not associated to the reactive power sign. They can be found as (4.3).

$$K_q - D_q = Z_{eq} \qquad (4.3)$$

where Z_{eq} is the equivalent impedance between the terminal bus and the remote bus. K_q is a positive virtual impedance and D_q is a negative virtual impedance.

2.2. SHUNT COMPENSATOR

The passive compensation device that is connected in parallel with the transmission line is called the shunt compensator. They regulate the reactive power flow in the system by changing the branch admittance. They are discrete reactive power components including shunts with or without taps.

2.2.1. Switchable shunt
Switchable shunt includes capacitor with capacitance and reactor with inductance, for which the admittance stays constant. The total loss of a high-voltage shunt reactor, e.g. size larger than 50 MVA and voltage higher than 100 kV, is typically 0.2% of its rated power [54], where the copper loss is about 0.15% of the rated power and the iron loss is about 0.05% of the rated power. In the Danish transmission grid, the reactors are used to compensate the network, whereas the capacitors are only used in the HVDC stations for providing the reactive power and filtering the harmonics.

In the voltage control system, the shunt compensators are switchable by breakers, and used to change the system admittance and then the node voltages and branch currents.

2.2.2. Variable shunt reactor
A Variable Shunt Reactor (VSR) is a reactor whose inductance can be varied in steps. The design of a fixed shunt reactor to compensate the power factor for a transmission branch can only be optimized to a constant load and generation condition. Since the Danish power system is more and more flexible due to integration of the wind power, the use of the VSR is much preferable than the fixed shunts. Losses can be reduced through the best possible matching of the shunt reactor to the reactive power demand in the lines, which results in cost savings for the operations. In the applications, the VSR will be regulated to consume the minimum reactive power before connecting to the grid, in order to minimize the voltage step changes and avoid the zero missing phenomena.

For example, the VSR produced by ABB, is to regulate the reactive power consumption by changing the electrical turns in the reactor. A tap changer, that is the same type of tap changers used in power transformer, is to connect the minimum number of electrical turns at maximum power rating and to connect maximum electrical turns at minimum power rating, The reactive power output can be expressed as a function of the turn number, (4.4)-(4.6) [55].

$$Q = V^2 B = \frac{l}{\omega \mu A} \cdot \left(\frac{V}{N}\right)^2 \tag{4.4}$$

$$B = \frac{1}{\omega L} \tag{4.5}$$

$$L = \frac{\mu N^2 A}{l} \tag{4.6}$$

where μ is the material magnetic permeability of the core. l is the length of the inductive coil. A is the cross sectional area of the coil. N is the number of turns. The loss on the windings depends on the number of turns connecting to the system.
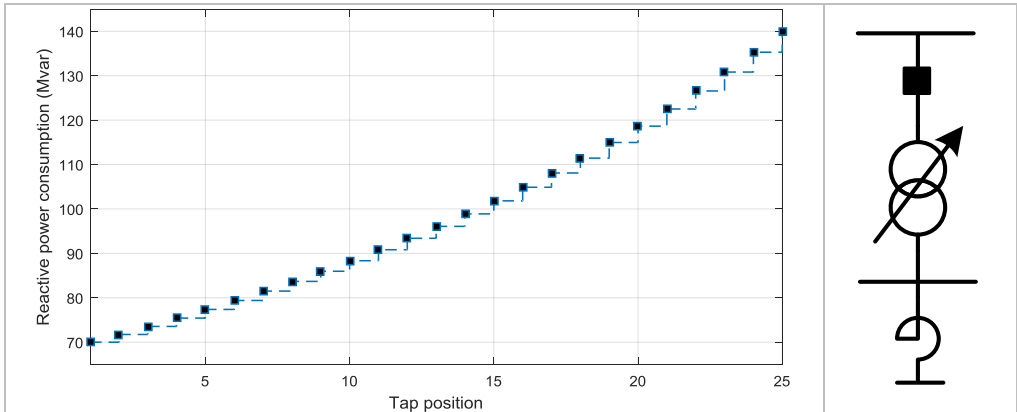
Figure 26. An example of VSR reactive power injection varying according to the tap position.

The VSR can be modelled as a tap-able transformer series connected to a fixed shunt reactor. The transformer regulates the tap ratio to change the shunt terminal voltage, consequently change the reactive power consumption. An example of reactive power consumption w.r.t. the tap position is shown in Figure 26, where the reactive power is varied from 70 to 140 MVar corresponding to 25 tap positions. VSR can also be entirely switched off by opening the breaker.

In the voltage control system, a variable shunt contains two controllers, i.e. the tap position varying the reactive power injection typically in the range of 50% to 100% nominal power and the circuit breaker connecting/disconnecting the whole component. In addition, the response time of a tap change is typically less than 10 seconds, as the conventional tap changer in the transformers.

2.3. POWER ELECTRONIC DEVICE CONTROLLED COMPENSATOR

The power electronic devices based compensators including Static Var Compensator (SVC) and Static synchronous Compensator (StatCom), are capable of controlling the voltage magnitude continuously. Voltage Source Converter based High Voltage Direct Current (VSC-HVDC) links, is able to be operated as StatCom to control the voltage.

2.3.1. SVC

The SVC typically composes banks of switchable capacitors or reactors, where at least one bank is regulated by semiconductors, like thyristor. For example, Figure 27 shows an SVC model representing the existing SVC in Rødsand, Denmark. In this configuration, the coarse voltage control is provided by the capacitor while the thyristor controlled reactor is to provide smooth control.
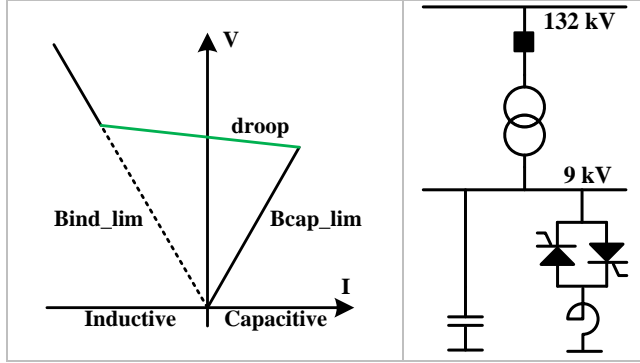
Figure 27. a SVC model.

In order to reduce the sizes of the components, a step-up transformer is typically applied. The high voltage side of the transformer is therefore controlled by SVC. The equivalent total admittance connected to the grid is therefore regulated to achieve the control target. As shown in Figure 27, the equivalent maximum capacitive susceptance can be obtained by controlling the reactive power of the thyristor-controlled reactor to zero. Similarly, the maximum inductive susceptance is achieved by allowing the maximum reactive power consumption at the reactor.

The voltage is always controlled within a certain range, where the droop is typically assigned, e.g. (4.7). X_d is the droop factor that is a negative scalar. V is the actual voltage at the measurement point that is typically the high voltage side of the step-up transformer. V_{ref} is the reference voltage at the high voltage side of the transformer in the SVC control system. The current injection of SVC in (4.7) can be regulated by controlling the equivalent susceptance, B_{SVC} in (4.8). The corresponding firing angle of the equivalent susceptance to control the thyristor can thus be found, e.g. via a lookup table.

$V_{ref} = V + X_d \cdot I$	(4.7)
$I = V \cdot B_{SVC}$	(4.8)
$Q_{SVC} = V^2 \cdot B_{SVC}, \qquad Q_{min} = V^2 \cdot B_{ind\_lim}, \qquad Q_{max} = V^2 \cdot B_{cap\_lim}$	(4.9)

In the AVC system, the transient for the control devices changing the states are not observable. Therefore the SVC components can be modelled as a power source regulating the reactive power to control the voltage, whose reactive power regulation capabilities are constrained within a band. For example, if defining the injecting power into the grid is positive, then the reactive power regulation capabilities can be found through (4.9). It is clear that the quantities of the reactive power output also depend on the voltage magnitudes, i.e. proportional to the square of the voltage. Therefore, if modelling SVC as a generator in the AVC system, whose reactive power output is under control, then the required susceptance can be obtained once the required reactive power injection and the voltage are found in a converged solution. The equivalent susceptance can thus be obtained via (4.9) accordingly to determine the firing angle for the thyristor inside the SVC.

2.3.2. StatCom

The StatCom typically comprises of the Insulated Gate Bipolar Transistor (IGBT) devices, regulate the current injection to control the grid voltage or the reactive power, where IGBT working as

electronic switches that can either turn on or turn off rapidly. The StatCom is considered as a voltage source in the power system, which comprises of DC side isolated by the IGBTs. The DC voltage is maintained to be constant. The StatCom can either inject or absorb the reactive power by shifting the current phase corresponding to the system voltage. It is carried out by regulating the IGBTs states that is fast electronic switching devices with frequency higher than kilohertz. Therefore, the response time of the StatCom to control the voltage is within several milliseconds.

In the StatCom, a Phase Lock Loop (PLL) is required to track the system voltage angle, with which the three-phase alternative voltage is converted to direct voltage in a so called dq-synchronous frame. The three-phase alternative current is therefore converted and projected on the voltage dq coordinators, where the current is regulated in this frame to maintain the voltages at DC side while controlling the voltage or the reactive power at AC side.

As shown in Figure 28, in contrast to SVC devices, the current injection of StatCom can be maintained though the system voltage is low, which indicates StatCom can provide more reactive power reserve than SVC. Normally, the entire StatCom will be blocked if the grid voltage is lower than a threshold to protect the power electronics devices.
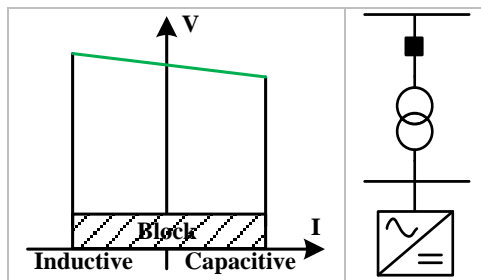
Figure 28. a StatCom model.

The reactive power control loop inside VSC-HVDC links is similar to StatCom. In fact, VSC-HVDC link controlling the voltage magnitude is always called "running in StatCom mode". The difference is that the active power output is also maintained while regulating the reactive power outputs. It is also carried out by controlling the current in the dq-synchronous rotating frame, where the current is decomposed to the active and the reactive currents that are regulated separately.

In the AVC system, similar to the SVC, the StatCom is modelled as power source injecting the reactive power under the constraints. However, it is different from the SVC, as the reactive power constraints are independent of the grid voltage. In the case of VSC-HVDC link running in the StatCom mode, the reactive power injection is corresponding to the active power injection, as the total current should be lower than the limit that is typically the maximum allowable current flowing through the power electronic devices.

2.4. TRANSFORMER TAP CHANGER

The on load tap changer of transformer is able to adjust the winding ratio in steps between the primary and the secondary sides, and then varies the equivalent impedance in the branch. The branch flow and the terminal voltages are therefore changed accordingly. The general model representing the transformer including the tap changer is presented in Chapter 2. The three-winding transformers are split to 3 two winding transformers in the calculations [88].

In the voltage control system, the tap ratio of the transformer tap changer is under determined that is converted to the tap position in the dispatching process. The tap changer typically takes about 5 to 10

seconds due to the mechanical constraints, which constrains the transformer tap changer regulation capabilities in the AVC loops.

2.5. SUMMARY

The reactive power components are categorized into continuous and discrete components. The generator, SVC and StatCom are able to continuously regulating the reactive power to control the voltage, whereas the shunts including the switchable and the variable shunts and the transformer tap changer change the equivalent impedance connecting to the grid in stepwise. The load as the main reactive power consumption connected to the distribution grid. The power factor at the interfaces between the transmission and the distribution grids are required to be maintained close to unity. Therefore, the voltage dependency characteristic of the load is out of consideration in the AVC decision making process. Moreover, switching off particular transmission lines is also proposed to alleviate congestion caused in particular situations [56], which may also affect the reactive power flow in the grid. The topological change as a measure for the voltage control purpose is not considered in this report. However, it is of great interesting for the future studies.

In the AVC system, the setpoints of the controllers are under determined periodically to obtain the optimal reactive power flow. The continuous reactive power components are modelled as power sources injecting the reactive power under constraints, where the control accesses to the load flow equations via power injections. The discrete components are modeled as controllable admittances in regulation ranges, where the control accesses to the load flow equations via the system admittance matrix. The detailed implementation is described in Chapter 5. The setpoints for different components are therefore derived from either reactive power injections or the admittances in the AVC decision making algorithms.

3. THE OPTIMIZATION FRAMEWORK OF THE DANISH AVC SYSTEM

The AVC system is used to control the voltage magnitudes to be within the acceptable band while optimizing the voltage profile to minimize the operational cost. The objective is formulated in an optimization framework, where the numerical optimization techniques are applied to solve the problem. The formulated optimization problem is also the core of the AVC system, to periodically determine the setpoints of the reactive power components, for operating the system in the expected conditions.

3.1. OBJECTIVE

In the large scale power system, the grid loss dominates the total operational cost, where the AVC system focuses on minimizing the grid loss without considering the regulation cost [40][42]. However, in the Danish transmission grid, the regulation cost can be significantly large comparing to the loss saving that should be taken into account.

The loss in the transmission grid is typically purchased by Transmission System Operator (TSO) who owns the transmission facilities and responses to operate the system in a secure manner. The loss purchased in the transmission grid includes the series loss in the transformers and the transmission lines, the conducting loss in the compensation devices and the no-load loss of the transformers, as shown in (4.10)-(4.12), respectively. The conducting loss of shunt depends on the energized susceptance. Therefore, the conductance of the shunts can be modelled as a function of the susceptance in (4.12). The variable shunts modelled as an ideal transformer connecting to a fixed shunt, either the conductance or the conducting loss can be modelled as a function of the connected susceptance. This function can either be an estimated linear function or a lookup table to represent the variable shunt reactive power consumption as shown in Figure 26.

Power plants are typically metered on the HV side of the step-up transformers. The loss in the plant itself consists of many components such as the losses on the transformer, generator winding, excitation system, bearings and cooling system etc. The losses inside the power plants are typically purchased by the plant owners. The price of the loss purchased by TSO in the transmission grid is referred to the market price, which are hourly price obtained day-ahead for 24 hours in the next day.

Theoretically, the price is found by the market clearing algorithm, where the production and the consumption is balanced without taking into account the loss. In the real operations, for example in Denmark, the TSO forecasts the transmission loss and purchases the amount day ahead. For example, the power produced from the net metering power plants will cover the loss in the power plants, which can lead to generation deficit. Purchase this amount of power in the day-ahead market is cheaper than from the regulating market or the balancing market. In addition, in the physical dispatches, the power flow normally differs from the purchased and sold volumes in the market clearing algorithm, which may due to some bilateral contracts between suppliers and consumers as well as the differences between the estimated and the measured grid losses in the grid. However, the total amount of the power traded in the regulating market and balancing market is much smaller than the day-ahead market, where the prices in the regulating market and the balancing market are not found from the market clearing algorithm considering the power balance [57]. Therefore, the prices in the regulating market and the balancing market are not able to represent the power balance but more about the severity of the system unbalance.

In order to taking into account the real price of the grid loss when dispatching the setpoints to minimize the operational cost, the price from the spot market, λ^d, is applied in (4.13), though it is found based on the predicted production and consumption day-ahead. The introduced unbalance due to the loss saving is not considered, as it is expected to have more or less the same chance for the loss saving to help or harm the power balance in the physical dispatch period.

$$P_{br} = \sum_{i=1}^{N_{br}} Real\left(\frac{\left| \frac{v_{f,i}}{\tau_i e^{j\vartheta_i}} - v_{t,i} \right|^2}{R_{s,i} + jX_{s,i}} \right), \forall i \in \mathcal{L} \tag{4.10}$$

$$P_{tr} = \sum_{i=1}^{N_{tr}} V_{trf,i}^2 \cdot G_{tr,i}, \forall i \in \mathcal{T} \tag{4.11}$$

$$P_{sh} = \sum_{i=1}^{N_{sh}} V_{sh,i}^2 \cdot G_{sh,i}(b_i), \forall i \in \mathcal{B} \tag{4.12}$$

$$C_p = \lambda^d (P_{br} + P_{tr} + P_{sh}), d = 1,2,3 \ldots .24 \tag{4.13}$$

$$C_\tau = p_{\tau,i} \sum_{i=1}^{N_\tau} \left| \tau_i - \tau_i^0 \right|, \forall i \in \mathcal{T} \tag{4.14}$$

$$C_b = p_{b,i} \sum_{i=1}^{N_b} \left| b_i - b_i^0 \right|, \forall i \in \mathcal{B} \tag{4.15}$$

$$C_g = p_{Q,i} \sum_{i=1}^{N_g} \left| Q_{g,i} \right|, \forall i \in \mathcal{G} \tag{4.16}$$

where τ_i and τ_i^0 are the optimal and the initial tap ratio in the transformer set $\mathcal{T}$, respectively. The tap changing price of each transformer tap is estimated as $p_{\tau,i}$. The total cost of tap changing C_τ is

expected to be reduced. b_i and b_i^0 are the optimal and the initial shunt susceptance in the shunt set $\mathfrak{B}$, respectively. The switching price of each shunt is estimated as $p_{b,i}$. The total cost of shunt switching C_b is expected to be reduced. $Q_{g,i}$ is the optimal generator reactive power output in the generator set $\mathcal{G}$ under the estimated price $p_{Q,i}$, which is expected to be minimized.

The tap changing cost and the shunt adjustment cost are considered in (4.14)-(4.15), respectively. The prices, $p_{\tau,i}$ and $p_{b,i}$, respectively, for the transformer tap change and shunt adjustment, can be estimated, e.g. convert to the cost/time considering the operational cost and the maximum allowable adjustment times over the life time [58].

As mentioned, the variable shunts comprises of an ideal transformer and a fixed shunt. The ideal transformer determines the voltage across the fixed shunt. As the transformer is without any impedance, once susceptance of the fixed shunt is controlled to zero, then the ideal transformer is a zero branch[1] that did not consume any power. Therefore, the variable shunts can be modelled as two controllers separately in the optimization framework. The switching cost is $p_{b,i}$ and the tap changing cost is $p_{\tau,i}$.

The reactive power regulation in power plants can result in additional loss inside the machines, though it is minor. The purchase can be required from the plant owners to provide the voltage control service to the grid, which can also introduce the regulation cost for these controllers. It means that the costs for generators in the AVC system comprises of two parts, i.e. the cost of the loss in the generator branch and the cost for providing the reactive power to the grid. The cost of the loss in the generator branch can be counted in (4.10) if neglecting the generator internal loss. The cost for providing the reactive power service to the grid is counted in (4.16).

The reactive power reserve is typically maintained as much as possible. It is not only for reducing the loss inside the components, but also for supporting the voltage by quickly injecting/absorbing the reactive power in the transient situations. It is even more important in the current Danish power system. This is due to the fact that the central power plants in the Danish power system is gradually decommissioning while many Type I wind turbines, i.e. induction generator directly connecting to the grid, are still being in the grid. After a fault clearance, these wind turbines can absorb reactive power from the grid to restore the rotational speed, which may cause the voltage slow recovery problem or even voltage collapse. Therefore, the sufficient dynamic reactive power support should be maintained, which provided by the continuous reactive power components.

In the current Danish power system, depending on the market price, there is no central power station being in service during some periods of the year. In these periods, the price of the reactive power outputs in (4.16) can be increased though the introduced extra physical cost by regulating the generator reactive power in (4.10), is negligible. It is not only to motivate the power plant owner to participant in the voltage control service, but also drive the optimization engine to search for least cost solution by reserving the reactive power in the generators as much as possible.

---

[1] In the implantation, the zero branch can be removed either by merging two nodes to one node or by inserting a small impedance, e.g. $1e - 7$ pu. to avoid the numerical problem. The impedance of the ideal transformer of the variable shunt will be non-zero after insertion. However, the power consumption on this ideal transformer is still negligible with the inserted impedance. The latter solution is preferred in the programming, as there is no topological change once the fixed shunt susceptance is controlled to zero, i.e. take off the ideal transformer from the admittance matrix. In this way, the discrete variables for disconnecting the ideal transformers in the optimization framework are avoided.

3.2. CONSTRAINTS

The objective of the AVC system should be achieved under a set of constraints that are typically the physical regulation limits of the components and the system operational limitations [78].

- Power balance

A feasible power balance should be obtained with the optimal setpoints of the reactive power components, i.e. the equations, (4.17)-(4.18), should be converged.

$$V_i \sum_{k=1}^{N_v} V_k (G_{ik} \cos \delta_{ik} + B_{ik} \sin \delta_{ik}) = P_{l,i} - P_{G,i}, \quad \forall i \in \mathcal{V} - \{ref\}, \quad \forall k \in \mathcal{V} \tag{4.17}$$

$$V_i \sum_{k=1}^{N_v} V_k (G_{ik} \sin \delta_{ik} - B_{ik} \cos \delta_{ik}) = Q_{l,i} - Q_{G,i}, \quad \forall i \in \mathcal{V} - \{ref\}, \quad \forall k \in \mathcal{V} \tag{4.18}$$

In fact, the power balance at the reference node can be taken into (4.17)-(4.18), if the reactive power injection at the reference node is considered as a controller within limits. However, it will bring the challenges to the convergence, e.g. slower converged with more iterations than cases without considering the power balance at reference nodes.

- Voltage magnitude limits

The voltage magnitudes at all nodes are maintained inside the predefined operational limits, (4.19). In the case of variable shunts being applied, the voltage magnitude at the junction node between the ideal transformer and the fixed shunt should be excluded from (4.19), as the voltage at the junction node can vary significantly. For example, if the variable shunt injects the half of the rated power, then the voltage at the junction node is about 70% of the rated voltage.

$$V_{min,i} \leq V_i \leq V_{max,i}, \quad \forall i \in \mathcal{V} \tag{4.19}$$

- Component regulation capability limits

The setpoints of the reactive power components, i.e. the shunt susceptance, the transformer tap ratio and the generator reactive power output, should be within their regulation capabilities, (4.20)-(4.22), respectively. Moreover, the regulation capability should consider the component response time within an AVC loop, e.g. transformer tap changer takes about 10 seconds to tap up/down one step.

$$b_{min,i} \leq b_i \leq b_{max,i}, \quad \forall i \in \mathcal{B} \tag{4.20}$$

$$\tau_{min,i} \leq \tau_i \leq \tau_{max,i}, \quad \forall i \in \mathcal{T} \tag{4.21}$$

$$Q_{gmin,i} \leq Q_{g,i} \leq Q_{gmax,i}, \forall i \in \mathcal{G} \tag{4.22}$$

- Maximum allowable regulation limits

In addition to the component physical limits, the total change of the setpoints of the shunt and transformer tap may be limited over a certain period as required by the system operators, which formulates the constraints, (4.23)-(4.24).

$$b_{Nmin} \leq \sum_{i=1}^{N_b} (b_i - b_i^0) \leq b_{Nmax}, \quad \forall i \in \mathcal{B} \tag{4.23}$$

$$\tau_{Nmin} \leq \sum_{i=1}^{N_\tau} (\tau_i - \tau_i^0) \leq \tau_{Nmax}, \quad \forall i \in \mathcal{T} \tag{4.24}$$

- • Reactive power flow limits

The reactive power on certain branches can be limited, e.g. the reactive power flow on the tie lines, $Q_{br,i}$, is normally constrained, as (4.25) [59].

$Q_{brmin,i} \leq Q_{br,i} \leq Q_{brmax,i}, \forall i \in \mathcal{L}$	(4.25)

Many other operational constraints can be included in the optimization framework. The price to pay is the heavy calculation burden leads to slow convergence. Moreover, the non-tractability problem may occur due to the improper constrains, where no feasible solution region exists.

3.3. DISCRETIZATION

The optimal reactive power flow is formulated in (4.10)-(4.25), where the shunts and the transformers are discrete controllers as they are operated in stepwise. There discrete variables are the non-smooth functions, which are not able to be handled by the nonlinear programming techniques. Mixed integer nonlinear programming (MINLP) provides the most accurate method to formulate the problem. However, MINLP is by far the most difficult type of optimization problem to be solved properly. The nondeterministic approaches are commonly used to search for the optimal solutions [60]-[61]. A tradeoff between the system representation accuracy and the tractability should be made.

In the AVC system that running in the real time, the strong problem tractability is preferred. The discrete variables are therefore treated as continuous variables in the proposed AVC optimization framework. The sophisticated nonlinear programming techniques can hereafter be applied to efficiently solve the approximated problem. A discretization method is needed to finally determine the values of the discrete variables.

The round-off method is to set the values of the discrete variables to the closest integers and lock them. The optimization problem is thus solved again with these fixed discrete variables to update the other continuous variables, e.g. the voltage angles and voltage magnitudes, to obtain a feasible solution. It can be seen that this method change the discrete values without considering the optimality conditions. Moreover, it cannot guarantees the solution feasibility after locking the discrete variables.

An alternative approach is to apply the penalty function for discretization [62]-[63]. The idea is to extend the objective function to include the cost of discrete variables being away from the integers. Therefore, a cost function of the discrete variables being away from the integers is required, which is expected to be smooth everywhere in the feasible region. As the value of discrete variables under discretization, can be either larger or smaller than the expected integers, a smooth and symmetrical function is expected, which penalizes the discrete variables being both larger and smaller than the target integers. The quadratic function, (4.26), is a candidate approach, where J represents the original objective function. In [62], the quadratic function based approach is solved by PDIPM, where the effectiveness is demonstrated. The penalty function is taken into account during the iterations of searching process. However, the timing to introduce the penalty function is a challenging task, where the well-tuning for the timing in the algorithm to include the penalty function is needed.

In [62], the author mentioned, if the penalty function introduces too early, then it can lead to non-optimal solutions. If the penalty function is introduced when essentially the continuous optimal solution is determined, the convergence may be difficult and even failed to be obtained. This is understandable, i.e. introducing the penalty function too early will lead to the optimization focuses on the discretization rather than minimize the operational cost, as the cost of the discretization penalty function may be much larger than the operational cost. It will thus force the discrete variables to be integers by minimizing the cost of discrete variables being away from the integers, in order to minimize the augmented objective function (4.26). Therefore, introducing the penalty function should

wait until the continuous optimization closes to be finished, i.e. the operational cost is nearly minimized. However, there is no clear sign for introducing the penalty function during the iterations.

On the other hand, if the continuous optimization is close to be finished, the expected integers of the discrete variables are found. The quadratic functions are therefore set up with the center at the expected integers, as shown in Figure 29. The discrete variables are forced to be moved towards to the expected integers. However, if there is no feasible solution found when discrete variable moves towards the expected integers, the problem will be failed to be converged. If the merit function is applied that normally combine the feasibility and the optimally into a common function [64], then the discrete variables may move opposite to the expected integers. The intractable problem may occur that the discrete variables are trapped in the intersections of two quadratic functions, as these points are non-smooth and non-differentiable. Therefore, the timing to introduce the penalty function is important in this approach, which is not straightforward to be determined.

$$\min_{x_{z,i}} J + \gamma \sum_{i=1}^{N_z} \left(x_{z,i} - x_{z,i}^* \right)^2$$	(4.26)
$$\min_{x_{z,i}} J + \gamma \sum_{i=1}^{N_z} \left[sin\left(\frac{x_{z,i}}{x_{zmax,i} - x_{zmin,i}} \pi \right) \right]^2$$	(4.27)

An alternative penalty function is basis on the sinusoidal function, (4.27) [63]. Comparing to (4.26), the discretization problem is embedded with the sinusoidal function, which is smooth and differentiable in the entire searching region, as shown in Figure 30. This approach greatly improves the tractability comparing to the quadratic function based approach. Moreover, the discrete variables can freely move in the entire regulation range of the discrete controllers, depending on the optimality and feasibility of the problem. However, similar to the quadratic function based approach, the cost of the penalty function should be less than the operational cost in the early iterations. Therefore, the weight of the penalty function γ is expected to be small in the beginning and slightly increased.

Table 13 shows the discretization algorithm. The continuous optimization without penalty function is solved firstly, and then the discretization employing the sinusoidal penalty function is carried out to solve the optimization problem again with the augmented objective function (4.27). As shown in Table 13, the weight of the penalty function should start from a small value, e.g. $\gamma_0 = 1e - 4$, and slowly increases e.g. multiplying $K_\gamma = 2$, and solve the problem with the updated weight of the penalty functions until the discrete variables sufficiently close to the integers.
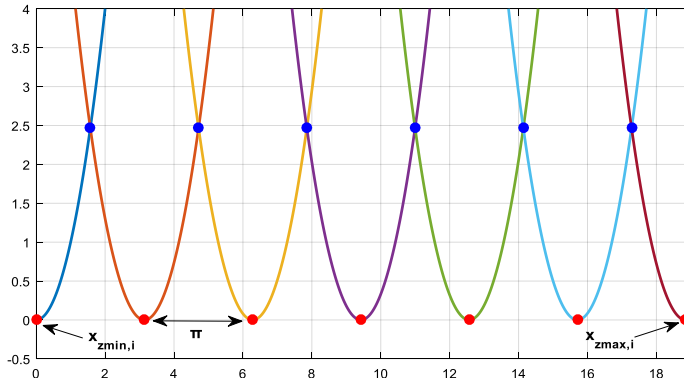
Figure 29. The quadratic penalty function, where the integers of the possible component setpoints are marked with red color. The intersections of two quadratic functions are marked with blue color.
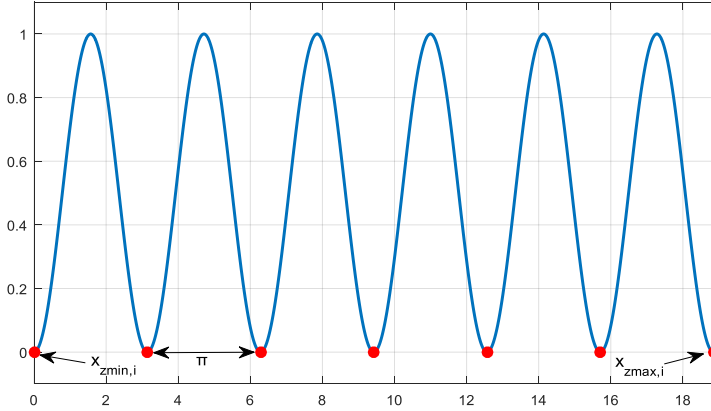
Figure 30. The sinusoidal penalty function, where the integers of the possible component setpoints are marked with red colors.

Table 13. An example of the discretization algorithm.

Solving the continuous optimization
$\gamma = \gamma_0$ and $counter = 1$
while $counter \leq N_{cont}$ *and* $\|x_z - x_z^*\|_\infty \geq \varepsilon$
    solving (4.27) s.b. constraints (4.17)-(4.25).
   if $\|x_z - x_z^*\|_\infty \geq \varepsilon$
     $\gamma = \gamma \times K_\gamma$
     $counter = counter + 1$
   else
     break
   end
end

Due to the problem non-convexity, all these mentioned approaches cannot guarantee to find the global optimal solution. However, the sinusoidal penalty function based approach is preferred, which can efficiently solve the problem applying the sophisticated nonlinear programming techniques to ensure a strong tractability that is essential in the real time system.

In order to solve the discretization problem with (4.27), the gradient and the hessian of the penalty function are derived, which are presented in detailed in Chapter 5 and Appendix B − Derivative.

4. EXTENSION OF THE DANISH AVC SYSTEM

The Danish transmission system is very flexible: (i). The generation fluctuation is affected by the wind speed due to the high share of the wind energy; (ii). The power flow is driven by the market; (iii). The significant variations of the transits in the main corridors can happen within short period due to the relatively large interchange capacities between Denmark and neighbor countries. Control the voltage profile in such flexible system may need to frequently adjust the reactive power components as long as the system state changes, which can be costly for the regulations.

Instead of focusing on optimizing the system voltage profile on each single snapshot, the AVC can optimize the voltage profiles for a period of time, i.e. addressing the impact of the regulations at the current stage on the upcoming stages to compromise the objective in the current stage against the regulations needed in the upcoming stages. It complies with the dynamic programming concept [65].

4.1. MULTI-STAGE OPTIMIZATION

The proposed algorithm by far is to include the regulation cost, in order to minimize the total operational cost in a comprehensive manner. This approach periodically finds the optimal decision variables at each system snapshot that obtained from the State Estimator (SE). The system variability, i.e. the system state changes over a time span, is not captured. However, is there any potential benefit to consider the system variability in the AVC system?

4.1.1. Motivation

The question will be answered by a simple example. Assuming there are two sequential system snapshots, Stage A and B, as shown in Figure 31. Assume that the grid loss is 50 kr in Stage A, and AVC suggests one shunt should be switched on that costs 12 kr. to reduce the grid loss to 30 kr. The shunt has initial status, i.e. disconnection, recorded as "0", and changes to "1" after switch on.

After a time interval, e.g. 1 minute, the system stands at Stage B. The grid loss at Stage B becomes to 40 kr. due to the variability. At Stage B, AVC is executed again and it suggests the worn shunt at Stage A should be switched off at Stage B to reduce the grid loss. The state of this shunt changes from "1" to "0", representing this shunt disconnects from the grid. It costs another 12 kr. on this shunt. Then the grid loss at Stage B becomes to 25 kr. During the whole period, i.e. from Stage A to B, the status of the shunt is "010". The total operational cost is 30 + 12 + 25 + 12 = 79 kr. In this case, it saves 8 kr. (50 - 30 -12 = 8) at Stage A, and 3 kr. (40 - 25 - 12 = 3) at Stage B, respectively. The results are summarized as Case 1 in Table 14.
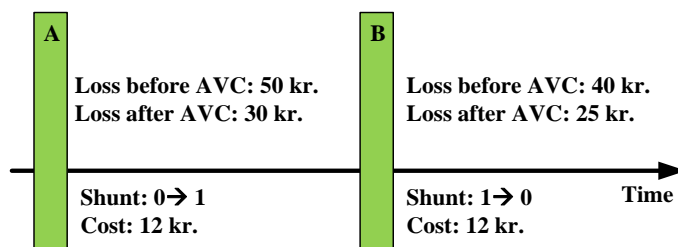
Figure 31. The example of impacts from system variability.

However, if the shunt is not switched on at Stage A and switched off at Stage B, then the total cost will be 50 + 25 = 75 kr., as recorded in Case 2 in Table 14. In addition, if the shunt is switched on at Stage A, but not switched off at Stage B, it will cost 30 + 12 + 40 = 82 kr., Case 3 in Table 14.

From this simple example, it can be seen that the total operational cost is less in Case 2 than Case 1, though the saving in Case 1 is more than in Case 2. The existing AVC systems, minimizes the system operational cost for each snapshot individually, will lead to the results in Case 1. If the AVC can take into account Stage A and Stage B together in the decision making process, then the optimal solution for the shunt status could be "000" as shown in Case 2, which is superior to the results in Case 1 in term of the minimizing the operational cost. Be notice that, if the shunt cost is negligible in this case, then Case 1 is more optimal than Case 2.

This example demonstrates the importance of including the look-ahead scheme in the AVC system, especially when the regulation cost is relatively large. Therefore, it concludes that in the case of regulation cost being significantly large comparing to the cost saving from the grid loss, taking into account the upcoming snapshots can potentially reduce more total operational cost over a period, than that focusing on optimization of the individual snapshot in the same period.

Table 14. Summarized results of the example.

Case	Shunt status			Loss (kr.)		Switching cost (kr.)	Saving in DKK		Operational cost A+B (kr.)
	Initial	A	B	A	B		A	B	
1		1	0	30	25	24	8	3	79
2	0	0	0	50	25	0	0	0	75
3		1	1	30	40	12	8	0	82

In the existing AVC system, the cost curve may be applied to the controllers, where the cost curve can be seen as the price of each controller to participate in the optimization in a certain snapshot. Tuning the cost curve may suppress the controller changes when the regulation cost is large. However, it cannot be used to avoid the redundant control actions, as shown in this simple example. These redundant control actions in fact are not a problem, since it is necessary to be carried out for minimizing the objective function at a certain stage.

However, the results can be better when the system knows what will happen in the upcoming stages. The solution to enhance the AVC decision making process is to introduce the forecasted snapshots, and minimize the total operational cost for a certain period, which formulates a "multi-stage optimal reactive power flow (MORPF) problem" [78].

4.1.2. Multi-stage optimization problem formulation

If considering each single snapshot is a stage, then MORPF stands for optimizing the reactive power flow involving several snapshots over a period, as shown in Figure 32. In MORPF framework, the system states and the control variables are assumed to be unchanged during two sequential stages. The proposed objective of AVC system is to minimize the total operational cost including the grid loss, the shunt switching cost and the transformer tap changing cost, while minimizing the generator reactive power output. The shunt can be either switched on or off, the tap position can be either tapped up or down and the generator can either inject or absorb reactive power. As long as the control variables are deviated from their initial values, the regulation costs are introduced, no matter how they are adjusted. Therefore, the cost functions of them should consider the sign conversion.
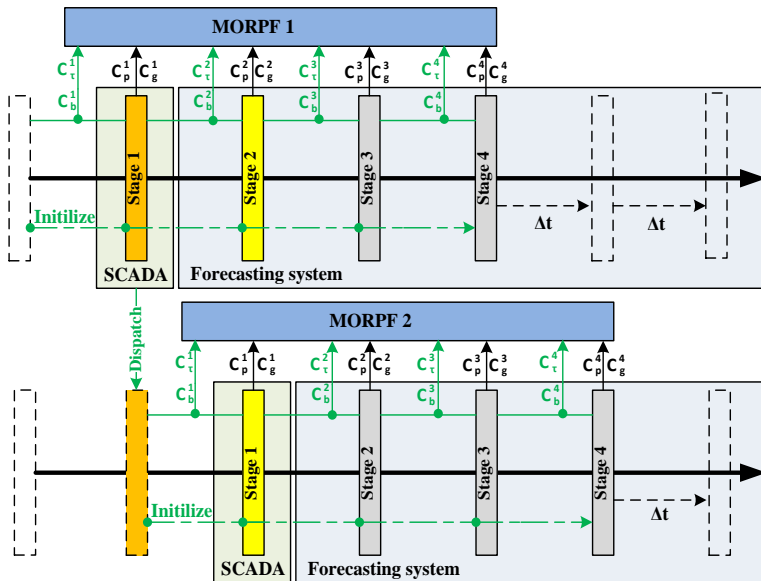
Figure 32.The multi-stage optimization [78].

As shown in Figure 33, though the changes of control variables can be either positive or negative, the cost should be always positive. Moreover, the control variables of shunt and transformer tap positions are the susceptance and the winding ratio, respectively, which are discrete variables. The generator reactive power regulation will increase the current that can introduce the extra loss inside the plants. In addition, the plant owner may ask for the payment to provide the ancillary service, which can also be counted as the operational cost in the AVC system.

In order to avoid the discrete variables in the optimization framework, the cost functions of shunts and transformers are approximated by the continuous functions. The changes of the transformer tap ratio and shunt susceptance at stages d and $d-1$ can be considered in the objective function, e.g. (4.29)-(4.30), where d denotes the stage index.

In the quadratic functions (4.29)-(4.30), the sign of the control variable changes can either be positive or negative while the introduced regulation cost is non-negative. The MORPF objective function to minimize the total regulation cost can be summarized in (4.28)-(4.31) [78].
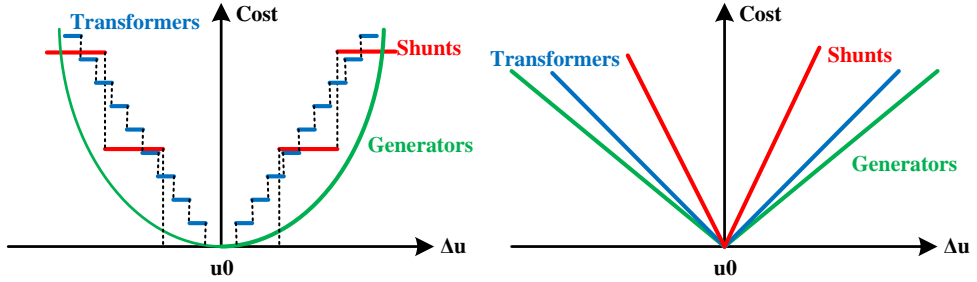
Figure 33. Linear approximations of the cost functions.

$$C_P^d = W_1 \sum_{i=1}^{N_{br}} Real \left(\frac{\left| \frac{v_{f,i}}{\tau_i e^{j\vartheta_i}} - v_{t,i} \right|^2}{R_{s,i} + jX_{s,i}} \right), \forall i \in \mathcal{L}, \forall d \in \mathcal{D} \tag{4.28}$$

$$C_\tau^d = W_2 \sum_{i=1}^{N_\tau} \left(\tau_i^d - \tau_i^{d-1} \right)^2, \forall i \in \mathcal{T}, \forall d \in \mathcal{D} \tag{4.29}$$

$$C_b^d = W_3 \sum_{i=1}^{N_b} \left(b_i^d - b_i^{d-1} \right)^2, \forall i \in \mathcal{B}, \forall d \in \mathcal{D} \tag{4.30}$$

$$C_g^d = W_4 \sum_{i=1}^{N_g} \left(Q_{g,i}^d \right)^2, \forall i \in \mathcal{G}, \forall d \in \mathcal{D} \tag{4.31}$$

where the decision variables are:

$$\begin{bmatrix} \delta^d & V^d & \tau^d & b^d & Q_g^d \end{bmatrix} \tag{4.32}$$

It can be seen that the physical cost of each term is not able to be accurately assigned in (4.29)-(4.31) due to the quadratic functions representing the cost of changes on the reactive power components. An alternative approach is to estimate the cost by linear functions, as shown in Figure 33, which introduces the absolute terms for the transformer tap ratio and the shunt susceptance in the objectives,

(4.33)-(4.34). Moreover, the cost function of the generator reactive power can also be modelled as absolute function, (4.35), by which to assign the cost in $kr/MVar$.

$$C_\tau^d = p_{\tau,i} \sum_{i=1}^{N_\tau} \left| \tau_i^d - \tau_i^{d-1} \right|, \forall i \in \mathcal{T}, \forall d \in \mathcal{D} \tag{4.33}$$

$$C_b^d = p_{b,i} \sum_{i=1}^{N_b} \left| b_i^d - b_i^{d-1} \right|, \forall i \in \mathcal{B}, \forall d \in \mathcal{D} \tag{4.34}$$

$$C_g^d = p_{Q,i} \sum_{i=1}^{N_g} \left| Q_{g,i}^d \right|, \forall i \in \mathcal{G}, \forall d \in \mathcal{D} \tag{4.35}$$

The absolute terms in the objective are neither continuous nor differentiable, which are replaced by auxiliary variables M, Z and Y in (4.36)-(4.38). In addition, constraints (4.39)-(4.44) are added in order to obtain the equivalent problem of (4.33)-(4.35).

$$C_\tau^d = \sum_{i=1}^{N_\tau} p_{\tau,i} M_i^d, \forall i \in \mathcal{T}, \forall d \in \mathcal{D} \tag{4.36}$$

$$C_b^d = \sum_{i=1}^{N_b} p_{b,i} Z_i^d, \forall i \in \mathcal{B}, \forall d \in \mathcal{D} \tag{4.37}$$

$$C_g^d = \sum_{i=1}^{N_g} p_{Q,i} Y_i^d, \forall i \in \mathcal{G}, \forall d \in \mathcal{D} \tag{4.38}$$

$$\tau_i^d - \tau_i^{d-1} \leq M_i^d, \qquad \forall i \in \mathcal{T}, \forall d \in \mathcal{D} \tag{4.39}$$

$$-\left(\tau_i^d - \tau_i^{d-1} \right) \leq M_i^d, \qquad \forall i \in \mathcal{T}, \forall d \in \mathcal{D} \tag{4.40}$$

$$b_i^d - b_i^{d-1} \leq Z_i^d, \qquad \forall i \in \mathcal{B}, \forall d \in \mathcal{D} \tag{4.41}$$

$$-\left(b_i^d - b_i^{d-1} \right) \leq Z_i^d, \qquad \forall i \in \mathcal{B}, \forall d \in \mathcal{D} \tag{4.42}$$

$$Q_{g,i}^d \leq Y_i^d, \qquad \forall i \in \mathcal{G}, \forall d \in \mathcal{D} \tag{4.43}$$

$$-Q_{g,i}^d \leq Y_i^d, \qquad \forall i \in \mathcal{G}, \forall d \in \mathcal{D} \tag{4.44}$$

Constraints (4.39)-(4.44) indicates that the ancillary variables, M_i, Z_i and Y_i are equal or higher than zero but not lower than zero. For example, by assuming $d = 1$, in constraints (4.39)-(4.40), if $\tau_i = \tau_i^0$, then $M_i = 0$. If $\tau_i > \tau_i^0$, then $\tau_i - \tau_i^0 > 0$ and $-\left(\tau_i - \tau_i^0 \right) < 0$. Constraints (4.39)-(4.40) are valid when and only when $M_i > 0$. It can be demonstrated in Figure 34, assuming $\tau_i^0 = 0$ without loss of the generality. The variable τ can be either larger or smaller than τ_i^0. However, $M \geq 0$ is always valid. In the optimization, the values of the ancillary variables are determined that are expected to be small, i.e. larger than zero but as close to zero as possible, in order to minimize the regulation cost.
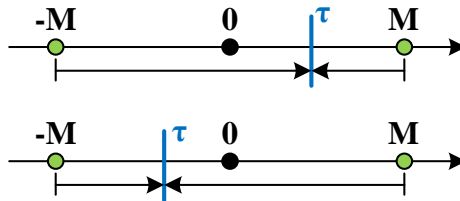
Figure 34. Demonstration of the validity of (4.39)-(4.40).

In this framework, the cost of regulation on the components can be well estimated representing by the linear function.

As mentioned, in the case of generator employing by the AVC system, the reactive power regulation can introduce the internal loss in the plants that is typically minor and negligible. If it is required to take the introduced loss into account, a function of power loss inside the plants w.r.t. the reactive power output is needed. The introduced costs include the extra loss on the windings due to the increased current and the loss inside the excitation system, which is the physical cost. If it is paid by the market price, then it can be counted in the grid loss as branch loss in the objective, (4.28). The price for the loss inside plants is kr/MW, where a function or a lookup table for $MW/MVar$ is required to convert kr/MW to $kr/MVar$. However, if the plant owners require the payment to participate in AVC system or they require higher price to cover their extra cost e.g. the maintenance cost, then (4.38) and (4.43)-(4.44) are needed. The price is $kr/MVar$, where all extra costs are included implicitly.

The cost of switchable shunt mainly includes the introduced conducting loss and the cost of the breaker's life time. As mentioned, the susceptance is the control variable of the shunt in the optimization. Similar to the introduced loss in the power plants, a function of the loss w.r.t. the susceptance connected to the grid is needed. The Q-factor is normally provided by the manufactory to represent the loss for the switchable reactors, which is a scalar function to obtain the consumed active power due to the loss corresponding to the rated reactive power. The shunt conducting losses are included in the grid loss of the objective, assigned with the price, kr/MW. As mentioned, the cost of the breaker's life time due to switching is estimated by using the summation of the capital cost and the estimated maintenance cost during the lifetime over the possible switching times, $kr/switching$. The price in the objective function, p_b, is $kr/siemens$, where the linear function is used for the unit conversion between the switching and the Siemens respected to the regulation cost, $switching/siemens$. All the terms are finally converted to per unit values.

The transformer tap adjustments change the branch admittance, and indirectly change the system voltage. The tap controllers are discrete variables, which are approximated by linear functions. The nominal winding ratio is 1, representing the tap is on the neutral position and the voltage is at the rated value. As the tap position changes, the voltage under control will be varied. The price of the transformer tap change in the objective is $kr/ratio$, derived from kr/tap.

Considering the response time of tap adjustments, the change of the tap ratio is then limited by (4.45) w.r.t. the periodical time of the AVC loops. In case, several shunts with the same types are connected to the same substation, then they are aggregated to a single shunt with steps. The step change numbers of aggregated shunts can be limited by (4.46). In addition, the total changes of the discrete controllers at a certain snapshot can be further limited by (4.47)-(4.48).

$M_i^d \leq M_{max,i}, \quad \forall i \in \mathcal{T}, \forall d \in \mathcal{D}$	(4.45)
$Z_i^d \leq Z_{max,i}, \quad \forall i \in \mathcal{B}, \forall d \in \mathcal{D}$	(4.46)
$\displaystyle\sum_{i=1}^{N_\tau} M_i^d \leq M_{tot\_max}, \quad \forall i \in \mathcal{T}, \forall d \in \mathcal{D}$	(4.47)
$\displaystyle\sum_{i=1}^{N_b} Z_i^d \leq Z_{tot\_max}, \quad \forall i \in \mathcal{B}, \forall d \in \mathcal{D}$	(4.48)

where the decision variables are expressed in (4.49).

$\begin{bmatrix} \delta^d & V^d & \tau^d & b^d & Q_g^d & M^d & Z^d & Y^d \end{bmatrix}, \quad \forall d \in \mathcal{D}$	(4.49)

It can be seen that either quadratic or absolute functions can be applied to model the cost of the regulations in the objective function. In contrast to the quadratic functions, the absolute functions can be converted to the linear functions with constraints. The prices of the regulations can be easily assigned in the objective function. In this way, the regulation cost between sequential stages over a period can be represented in the MORPF framework. However, if the absolute functions are used in the objective function, then the susceptance change, the tap ratio change in the two sequential stages and the generator reactive power at each stage should be determined, M^d, Z^d and Y^d in (4.49), which increases the calculation burden comparing to the quadratic functions based approach.

4.1.3. Recursive formulation
In [78], the relation of the MORPF approach to the dynamic programming concept is presented. The concept of the derivation is briefly introduced following.

The formulated nonlinear programming problem for the AVC decision making process is solved by the PDIPM. In PDIPM, all inequality constraints are converted to the equality constraints with help of the positive slack variables putting in the inequality constraints [29]. The augmented objective containing the barrier function is to be solved subjected to only the equality constraints. In this approach, the state variable, x, and the control variable, u, are not treated differently.

After solving for the MORPF problem through Lagrangian multiplier method, the first-order optimality condition at each stage should be obtained (see Chapter 3) [31], as expressed in (4.50).

$$\begin{pmatrix} x_1^* \\ u_1^* \end{pmatrix} = f(x_1, u_1) \tag{4.50}$$

where x_1 can be seen as the shunt susceptance and the transformer tap ratio. The changes of them between sequential stages are expected to be minimized, i.e. (4.33)-(4.34). u_1 are the rest of the decision variables of either (4.32) if the quadratic functions are applied or (4.49) if the absolute functions are used. These values are adjusted at each stage to satisfy the first-order optimality condition, $f(\cdot)$. After convergence, x_1^* and u_1^* are found to be their optimal values for the first stage.

The shunt susceptance and the transformer tap ratio in the secondary stage, x_2, can be derived accordingly, by substituting x_1^* to the load flow equation $g(\cdot)$ at the second stage (4.51). If $x_1^* = x_2$ after convergence, then it means that the shunt susceptance and the transformer tap ratio are unchanged since the Stage 1 while the system is under optimal conditions. if $x_1^* \neq x_2$ after convergence, then it means the shunt susceptance and the transformer tap ratio have to be changed from Stage 1, in order to comply with the first-order optimality. In return, it will introduce the adjustments backwards to Stage 1 when adjusting the variables in Stage 2. Therefore, the update is required in Stage 1 to regain the first-order optimality during the adjustments in Stage 2. The iterations to update the decision variables in Stage 1 and Stage 2 will continually until both stage 1 and stages 2 comply with the first-order conditions, i.e. (4.50) and (4.52) are satisfied.

$$x_2 = g(x_1^*, u_2) \tag{4.51}$$

$$\begin{pmatrix} x_2^* \\ u_2^* \end{pmatrix} = f(x_2, u_2) \tag{4.52}$$

Substituting (4.50) and (4.51) into (4.52), which yields (4.53).

$$\begin{pmatrix} x_2^* \\ u_2^* \end{pmatrix} = f(g(f(x_1, u_1), u_2), u_2) \tag{4.53}$$

The "value function" [65], $V_1(x_1, u_1)$, at the first stage is obtained by substituting the optimal decision variables at the first stage to the objective function, $C(\cdot)$. In the MORPF framework, the problem is solved forwards. It means that the value function at the first stage, (4.54), is also the "boundary condition" [65] of the whole problem.

$$V_1(x_1, u_1) = C(x_1^*, u_1^*) = C\big(f(x_1, u_1)\big) \qquad (4.54)$$

After applying the same procedure to several stages, a recursive form is obtained in (4.55).

$$V(x_{d+1}, u_{d+1}) = \min\Big(V(x_d, u_d) + C\big(f(g(f(x_d, u_d), u_{d+1}), u_{d+1}))\big)\Big), \qquad \forall d = 1, 2, \dots, N \qquad (4.55)$$

The MORPF problem is suggested to be solved simultaneously, as the algorithm itself will not specify the sequence of the stages. It will find the optimal values to satisfy the first-order optimality conditions for all involved stages simultaneously. The additive objective of all involved stages is therefore expressed in (4.56) that is equivalent to (4.55).

$$J = \min \sum_d \big(C_P^d + C_\tau^d + C_b^d + C_g^d\big) \qquad (4.56)$$

4.1.4. Rolling process

The MORPF formulation requires the forecasting snapshots in order to determine the setpoints for the current snapshot. As shown in Figure 32, the number of involved stages can be kept constant as the time passed. Only the setpoints of the first stage are dispatched in each AVC loop.

In the MORPF framework, the time window can be defined based on the forecasting accuracy, i.e. the forecasting errors should be less than a certain limit. If the forecasting errors are large, the predicted power flow may be meaningless. The decision made by MORPF based on the uncertain snapshots may lead to larger cost than the ORPF solution after realizations, to correct the voltage violation or regain the optimality in the upcoming stages. Therefore, the forecasting accuracy is essential to the MORPF solution quality, which is also an indicator to choose the time span for the rolling window.
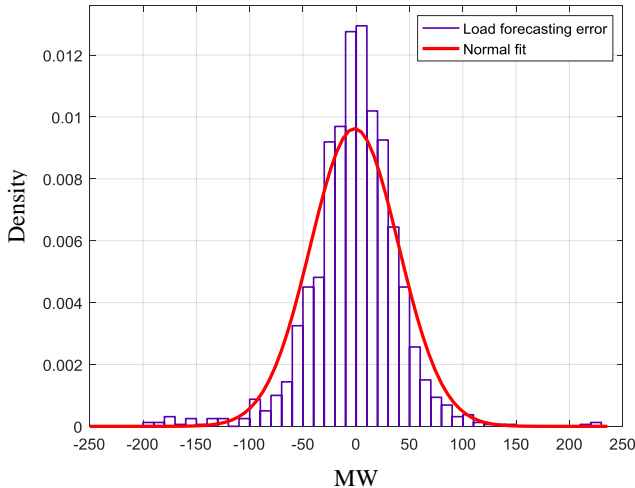
Figure 35. The histogram and the normal distribution fit of the load forecasting error with one-hour lead time in DK1 system for 2015. The load forecasting error is the difference between the forecasting and the settlement value at each time point.
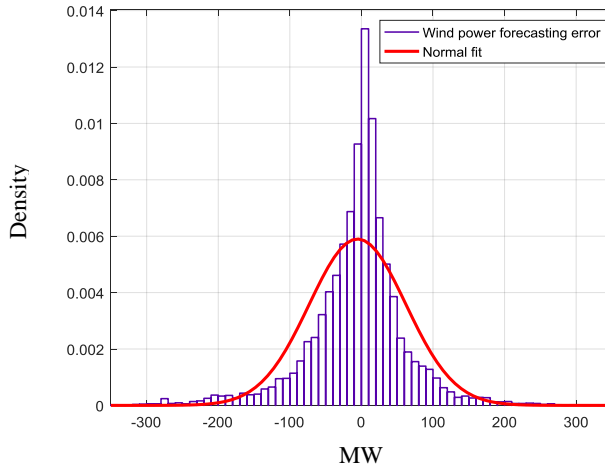
Figure 36. The histogram and the normal distribution fit of the wind power forecasting error with one-hour lead time in DK1 system for 2015. The wind power forecasting error is the difference between the forecasting and the measurement value at each time point.
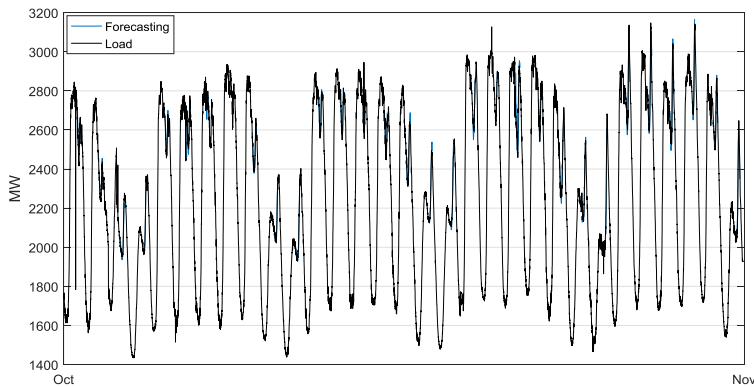
Figure 37. The DK1 load forecasting error in October month in 2015 with one-hour lead time.
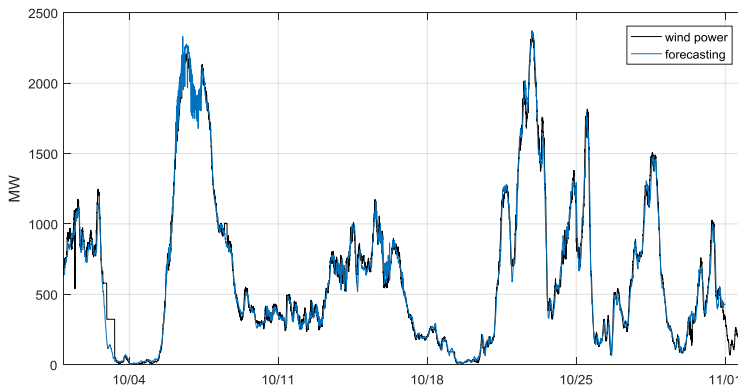
Figure 38. The DK1 wind power forecasting error in October month in 2015 with one-hour lead time.

In the current Danish power system, the load and the wind power are the main uncertain sources to the load flow forecasting. As shown in Figure 35 and Figure 36, respectively, the load and the wind power forecasting with one-hour lead time, most of the load forecasting errors in DK1 system are within ± 200 MW, and most of the wind power forecasting errors in DK1 system are within ± 300 MW. In addition, the load profile follows a pattern that reflects the human activities, as shown in Figure 37. In contrast, the wind power in Figure 38 is very flexible that leads to larger forecasting errors for the wind power than the load.

The forecasting errors will be reduces as the lead time is close to the real load flow condition. As shown in Figure 39, the wind power forecasting errors concentrate more to zero as the lead time is closer to the realization instant. It provides an indicator to the MORPF of the AVC system to choose the size of the rolling window, i.e. the forecasting error should be lower than a threshold while capturing the system variability. Moreover, other operational limits are also considered to determine the size of the rolling windows.

In the MORPF based Danish AVC system, the system is optimized for 45 minutes with 15 minute time intervals [78]. It considers that:

- The power generation and the load will not largely change within 15 minutes [66];
- The one-hour ahead load and the wind power forecasting errors are small [51];
- Power flow changes are continuously updated by the intra-day market until one hour before physical dispatch and only small unbalances are needed to be compensated through the balancing market;
- The tractability is stronger if only fewer stages are involved.

It can conclude that the forecasting system is a key element of MORPF scheme, which strongly affects the results quality of the decision making process.
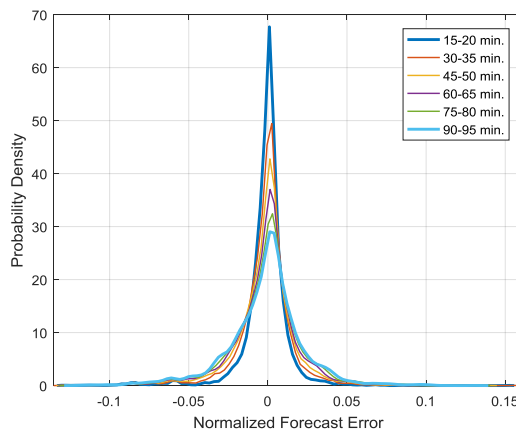
Figure 39. The historical forecasting errors of the wind power in DK1 system with different lead times. The values are normalized by the installed capacity.

5. THE DANISH WIND POWER FORECASTING SYSTEM

In the modern wind power forecasting system, the Numerical Weather Prediction (NWP) system is widely used to predict the wind speed based on the weather conditions. The predicted wind power is therefore obtained by converting the wind speed via a deterministic power curve, e.g. as shown in Figure 40. The power curve is a statistic model to present the relation of the wind speed and the wind power for the specific regions.
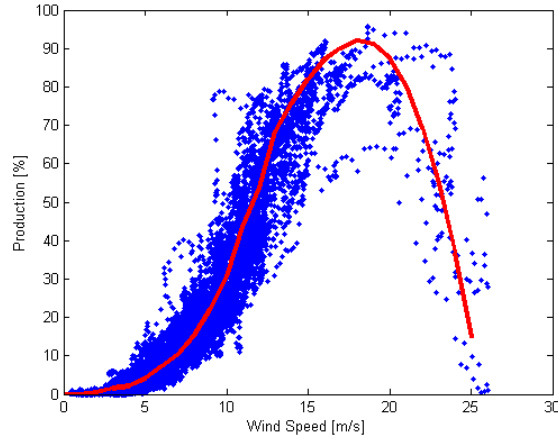
Figure 40. An example of power curve of converting the predicted wind speed to the wind power.

There are two major approaches to predict the wind speed [67], i.e. (i). point forecasting system and (ii) probabilistic forecasting system. The point forecasting system provides a single value for a certain instant as the predicted future wind speed, whereas the probabilistic forecasting system provides a probability density function for the future wind speed. The wind speed is predicted through a time series model. For example, if the historical observations are $h_1, h_2, \ldots h_t$, up to the instant t, and h_{t+k} is the predicted wind speed made at the instant t with the lead time k. A point forecasting system is to estimate h_{t+k} through a function based on the historical observations, whereas a probabilistic forecasting system estimates the probability density function of $f(h_{t+k}|\sigma)$, where σ describes the statistic characteristic of the density function.

In the probabilistic forecasting systems, either parametric or non-parametric approaches can be applied. The parametric approach requires a known distribution, of which the parameters are trained and improved through the historical observations [68]. In contrast, the non-parametric approach does not rely on any assumption of a known distribution. Instead, it applies the quantiles regression techniques to construct the distribution function [69]. In [69], both approaches of constructing predictive densities are described and analyzed. The results demonstrate that both performed similar for lead times up to 5 hours ahead, and with an advantage for non-parametric predictive densities for further lead times.

As shown in Figure 41, in the Danish national control center, there are primarily two tools for the short term and medium term wind power forecasting, i.e. providing, respectively, up to 10 hours ahead forecast with 5-minute resolution and up to 144 hours ahead forecast triggered by NWP [70]. These tools are based on the results from NWP systems that are provided by three suppliers. As the forecasted wind speeds by different NWP systems are rarely the same, the forecasted results are thus aggregated to improve the performance [71]. NWP is generally a forecasting system for the meteorological conditions. The various NWPs have different update rates, i.e. currently from 2 to 8 hours per day, and from 48 to 144 hours ahead. All the operational NWPs are currently in an hourly resolution. As shown in Figure 41, as the forecasted wind speed available, the wind power forecasting tools will convert the forecasted wind speed to the wind power through the deterministic wind power curve, subjected to the operational conditions. For example, if the market price changes to negative, some wind turbines in the system may shut down. In this case, though the wind speed is high, the actual wind power will be zero for these wind turbines.

The wind power forecasting errors are continuously recorded. The wind power forecasting is found as the difference between the forecasted wind power production and the measurement, which is recorded every 5 minutes. As shown in Figure 41, these wind power forecasting errors compose a time series

that can be used to predict the future wind power forecasting errors and correct the wind power predictions to improve the forecasting's accuracy [72].
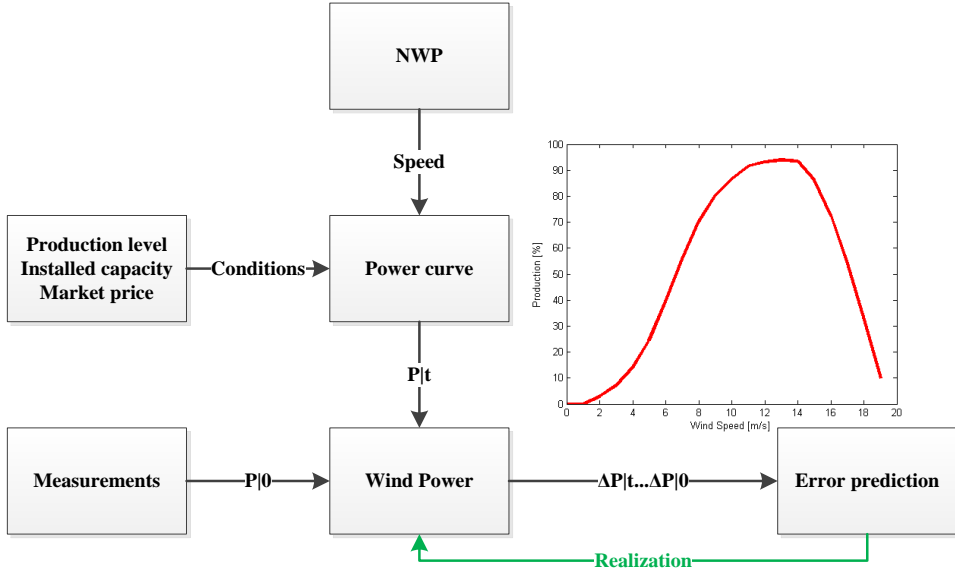
Figure 41. The wind power forecasting system in the Danish systems.

Wind is correlated both in time and space. It is driven by the air pressure differences due to the uneven heating of the earth's surface by the sun, where balancing the air pressure between two locations take time. In addition, the wind is affected by the terrains, where the wind speed and the direction are affected. In fact, there is spatio-temporal correlation in the wind power productions and the wind power forecasting errors [73]-[77]. The wind power forecasting systems considering the spatio-temporal correlations can greatly reduce the forecasting errors, especially for the short-term forecasts that have great influence on the system operations [72]-[74].

In the Danish electricity control center, the wind power forecasting errors (WPFE) are obtained that are the differences between the predicted and the measurement values. The WPFE are used to correct the future forecasting errors based on the auto regression technique and regime-switching models [74]. For example, the WPFE in Zone 12 in Figure 42, $E_{12}(h_t)$, can be estimated from (4.57)-(4.58), where the regime switches depending on the wind direction. Either (4.57) or (4.58) is applied to predict the WPFE if wind comes from east or west, respectively. The time dependent parameters $a(h)$ to $e(h)$ are trained to capture the spatio-temporal correlations [74].

$E_{12}(h_t) = a(h)E_{12}(h_0) + b(h)E_{11}(h_0) + c(h)E_{15}(h_0)$	(4.57)
$E_{12}(h_t) = d(h)E_{12}(h_0) + e(h)E_{13}(h_0)$	(4.58)

Figure 42. Zonal wind power prediction in the western Danish power system.

The historical WPFE are presented in Figure 43, which more or less symmetrically distributed around to zero. In [74]-[75], it comments that the correlation is weak if the prediction accuracy is high. Moreover, the WPFE distribution will more concentrate to zero if more wind turbines are erected in a large region, as they may face difference weather conditions at the same time, which will have less correlation due to the geographic diversity.
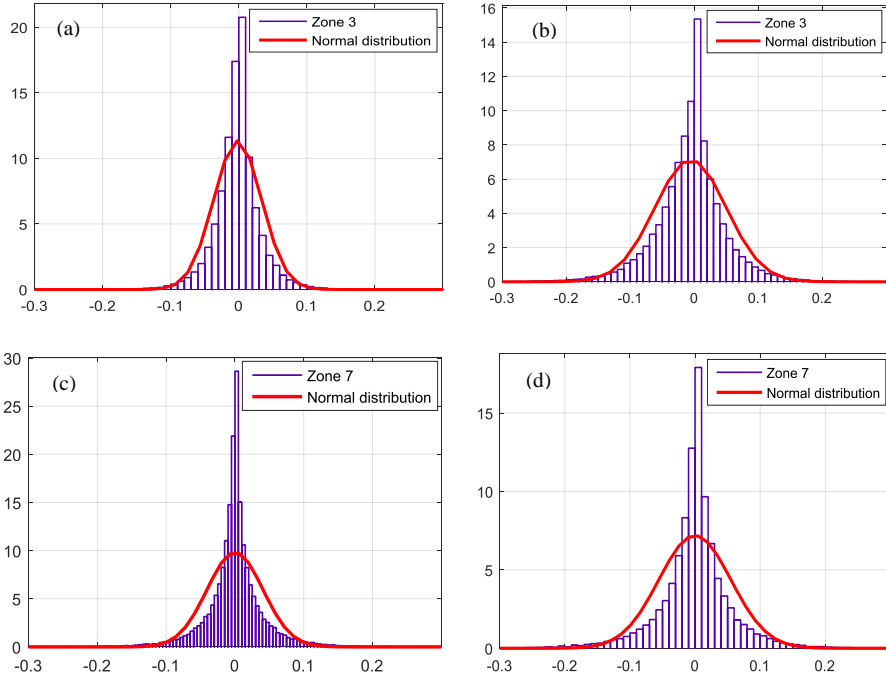
Figure 43. The distribution profile of the normalized WPFE, from 2012 March 31st 22:00 to 2014 March 31st 21:55, with 5-minute resolutions. (a) and (c):Errors for 15 minutes lead time for Zone 3 and 7, respectively. (b) and (d): Errors for 60 minutes lead time for Zone 3 and 7, respectively. [78].

The spatio-temporal correlations of WPFE in the western Denmark is shown in Figure 44 [78]. It can be seen that there is strong temporal correlation in the wind power forecasting errors. The strength of the correlation gradually reduces as the lead time increases. It means if there is a WPFE observed at the current stage in a particular zone, then this error is much likely to be observed in the upcoming stages. However, the spatio correlation is much weaker than the temporal correlations, as shown in Figure 44. This is also observed in [70], where the author states that the wind power forecasting errors correlation drops off rapidly with distance between wind power generators.

In [75], the authors suggest to convert a series of prediction errors to multivariate normal random variables. The spatial-temporal correlation of WPFE can then be expressed by the covariance matrix. It provides an analytical manner to address the WPFE into the decision making process of the AVC system, as introduced in the Section 6.3.
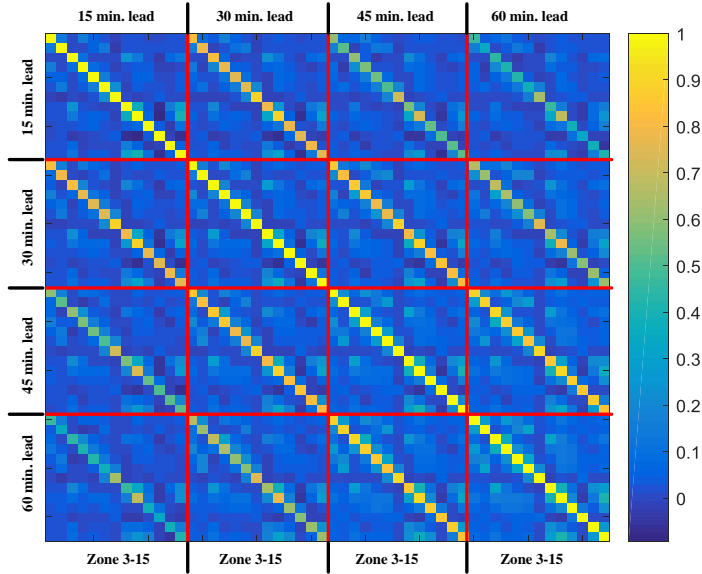
Figure 44. The WPFE spatio-temporal correlation for Zone 3-15 of the western Denmark with 15-minute, 30-minute, 45-minute and 60-minute lead times [78].

6.   INTEGRATION TO THE MULTI-STAGE OPTIMIZATION FRAMEWORK

The MORPF in the proposed Danish AVC system will require forecasting snapshots of the upcoming stages. In order to ensure the feasibility of MORPF solutions, the uncertainty in the upcoming stages should be considered in the MOPRF calculations. For example, a shunt reactor is switched off at the current stage by MORPF decision taking into account the forecasting stages, for saving the loss in the upcoming stage. However, the shunt terminal voltage violates the limits in the upcoming stage due to the wind power production is less than the predicted value, then this shunt should be switched on again that will result in regulation cost to correct the voltage at the upcoming stage. Therefore, the uncertainty due to the wind power fluctuation in the upcoming stages should be directly addressed in the MORPF to improve the solution robustness.

In the load flow calculation (4.17)-(4.18), the uncertainty includes the unplanned system topology change, i.e. changes on G_{ik} and B_{ik}, e.g. due to contingencies, the variations of the power injections including the load change, $\Delta P_{l,i}$ and $\Delta Q_{l,i}$, and the production fluctuation, $\Delta P_{G,i}$ and $\Delta Q_{G,i}$.

The topological uncertainty is addressed in the contingency analyses that are well carried out in the present power system engineering. It is known as $N-1$ assessment, i.e. one of the essential branches is taken off under a certain condition. The load flow calculation is then carried out to investigate if there is unacceptable problem, e.g. overloading in some branches. The contingency analyses are always carried out considering different operational conditions, e.g. different number of central power plants in operation, different consumption levels and etc. Though the contingency may introduce large disturbances in the system, it rarely occurs and be well handled in the real operations.

Comparing to the topology change occurs occasionally caused by contingencies, the load and the production change continuously. In the real operations, the active power injections are continuously being predicted in order to ensure the power balance at every instant, even after the topological changes due to the contingencies. The reactive power at component terminals is typically regulated close to the neutral in order to reduce the loss, which is also required by the grid codes. The reactive power flowing between the transmission and the distribution grids is always limited to save the grid

loss as well, i.e. limiting the power factor within ± 0.9. Therefore, in the model of the transmission grid in the AVC system, the distribution grids are aggregated as power injection nodes connecting to the power transformers between the transmission and the distribution grids, as shown in Figure 45, where the voltage at the low voltage side of the transformer are maintained by TSO through regulating the transformer taps, and the reactive power injection at the low voltage side of transformers are controlled by Distribution System Operators (DSO) to close to the neutral or vary according to the active power injections to maintain the power factor close to unity.
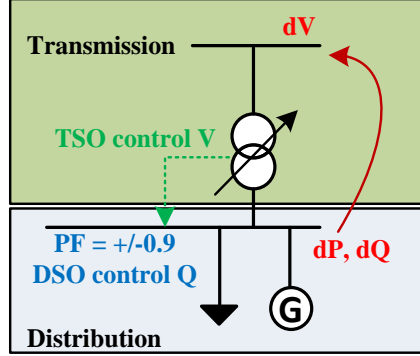
Figure 45. The control responsibilities of TSO and DSO in the power system.

The load changes day and night. However, the load is well predicted due to the regular human activities, as shown in Figure 37. Moreover, the load change is relatively slow comparing to the wind power variation. There are more than 5000 wind turbines in the Danish power system. The different types are mixed and spread in the system. In order to predict the production, the system is geographically split into zones, as shown in Figure 42. In each zone, the wind profile is assumed to be identical. In this way, the accuracy of the prediction is high, as shown in Figure 39. However, the forecasting errors still exist. In the MORPF framework, the uncertainty of the node power injection may lead to the voltage variations in the transmission grid, which is to be addressed in the proposed AVC system.

6.1. LINEAR ESTIMATION

In order to improve the solution robustness, the possible voltage variations corresponding to the changes on the node power injections should be estimated, e.g. sensitivity calculation, $\frac{\partial V}{\partial P}$ and $\frac{\partial V}{\partial Q}$. The sensitivity calculation is a linear approximation of the observation variable, the voltage magnitudes V, respected to the random variables, the node power injections P and Q. However, the load flow equations are generally nonlinear. Therefore, the estimation based on the sensitivity is only valid around the operating point, i.e. the voltage varies along the tangent of $\frac{\partial V}{\partial P}$ and $\frac{\partial V}{\partial Q}$ at the operating points, (4.59)-(4.62).

$$\begin{bmatrix} \Delta P \\ \Delta Q \end{bmatrix} = \begin{bmatrix} J_{P\delta} & J_{PV} \\ J_{Q\delta} & J_{QV} \end{bmatrix} \begin{bmatrix} \Delta\delta \\ \Delta V \end{bmatrix}$$	(4.59)
$$\Delta V_W = \sum_{i=1}^{N_W} \left(S_P \cdot \Delta P_{W,i} + S_Q \cdot \Delta Q_{W,i} \right)$$	(4.60)
$$S_P = (-J_{P\delta} J_{Q\delta}^{-1} J_{QV} + J_{PV})^{-1}$$	(4.61)
$$S_Q = (-J_{Q\delta} J_{P\delta}^{-1} J_{PV} + J_{QV})^{-1}$$	(4.62)

where ΔV_W is the voltage change e.g. due to variations in wind production. S_P and S_Q are sensitivity matrices of voltage changes w.r.t wind power changes, obtained via linearization of the load flow equation (4.59) by setting $\Delta P = 0$ or $\Delta Q = 0$, respectively.

Notice that, the voltage sensitivities respected to the power change are calculated for PQ nodes. In contrast, the voltage at PV nodes is normally kept constant regardless of the power flow changes. As mentioned, the spread wind turbines and the load are aggregated to a busbar connected the closest substation in the transmission grid model, where the busbar is modelled as PQ node. Therefore, equation (4.59)-(4.62) used to assess the voltage sensitivities w.r.t. the variations of the power injections at PQ nodes, which can be applied to estimate the voltage variations caused by the wind power fluctuations and loads. Be notice that the load flow (4.59) is generally a set of nonlinear equations, where the sensitivity based estimation is only valid close to the operating point, i.e. S_P and S_Q may vary significantly for different operating points.

The voltage variation due to the fluctuation of the node power injection can be estimated through (4.59)-(4.62), where the outputs of the forecasting system for the load and the wind power production can be applied. As demonstrated in Figure 35 and Figure 36, the forecasting errors of the power injections, dP can be approximately represented by the normal distribution. The question turns to how to take the statistic characteristic of the power injections into the decision making process of the AVC system. The following sections will describe the proposed approaches, where only the wind power uncertainties are addressed. However, the proposed approaches can be also applied to address the load uncertainties.

6.2. SCENARIO-BASED METHOD

A scenario based approach, e.g. stochastic programming, is proposed to solve unit commitment problems [79]. The stochastic characteristic of the uncertainty sources can be either known or unknown. The principle is to find a solution considering all possibilities caused by the uncertainties. It is normally carried out by performing the calculations on predefined scenarios that generated from the uncertainty probabilities. Therefore, the Probability Density Functions (PDFs) of all uncertainties are discretized into samplings, with each being the realization of a specific uncertainty, shown in Figure 46. Combinations of samplings from different uncertainties compose the scenarios that represent possible realizations associated with different uncertainties. If there is an existing solution that is feasible in all generated scenarios, then this solution is robust that is protected against the uncertainties.
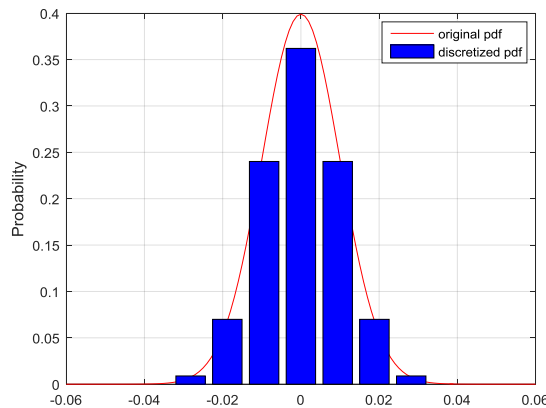
Figure 46. An example of discretization of PDF into bins [82].

As shown in Figure 47, considering the different power injections varying inside the uncertainty range, at the nodes connected with wind turbines, different realizations represented by the scenarios

formulated a new set of nonlinear equations for different load flow conditions. The solution in such AVC system is a set of setpoints of the reactive power components, with which the optimality condition is satisfied and all load flow equations are valid. It can be considered as the intersection points of different nonlinear functions, like shown Figure 47.

Be notice that, the uncertainty is different from the variability. The uncertainty is considered as the deviation from the expected values, which is observed only after the realizations. For example, the wind variability can be generally captured some hours ahead by the wind power forecasting system. However, there are always forecasting errors that are differences between the observations and the forecasted values. These errors are considered as the uncertainty. In contrast, the values provided by the forecasting system are expected values to capture the variability that are not uncertainty.
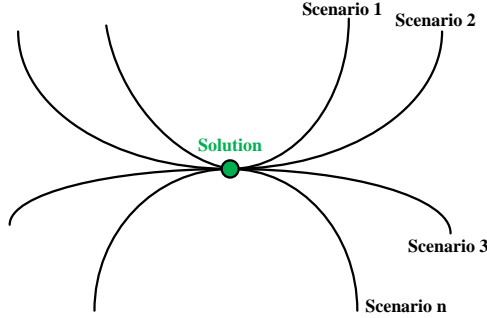
Figure 47. A sketch of scenario-based method.

If find a solution considering the wind power variability, then the solution shown in Figure 47 will not be necessarily identical for different realizations. The solution can be determined according to the most likely realization, e.g. if high wind case is observed, then Solution A is preferred; if low wind case is observed, then Solution B is preferred etc. However, if addressing the uncertainty caused by the wind power in the AVC system, the solution should be identical for different realizations, because the uncertainty is found only after a realization where the setpoints for the reactive power components are already fixed. It is identical to the decision making problem that making decision right now (only one solution) and wait for the consequences (can be any realization) later on.

In the implementation, the PDF is discretized to several bins, Figure 46. The center of each bin can be used to represent the aggregated random variable in each interval, while the area under the original PDF curve of each bin represents the aggregated probability. These aggregated PDFs should be normalized in order to obtain the unity value, as the summation of all probabilities for each aggregated PDF. If it is assumed that the uncertainties are independent of each other, then the probability of the generated scenarios is the product of the probabilities of bins from different aggregated PDFs. The number of scenarios normally needs to be reduced via scenario reduction techniques in order to solve the problem [80]. A scenario based approach (SBA) can be generalized expressed in (4.63)-(4.65).

$$\sum_{s=1}^{N_s} P_s \times \min_{\{x_s, u_s\}} f(x_s, u_s)$$	(4.63)
subject to	
$g_s(x_s, u_s) = 0$	(4.64)
$h_s(x_s, u_s) \leq 0$	(4.65)

where x_s and u_s are respectively the state and control variables in the scenario s. $f(\cdot)$ is an objective function, e.g. loss minimization. P_s is the probability of each scenario. N_s is the number of scenarios. The problem stated in (4.63)-(4.65) comprises N_s scenarios that can be solved independently. The

aggregated objective functions for all scenarios are considered as a fitness function and the control variables are aggregated as shown in (4.66).

$$u_{ag} = \sum_{s=1}^{N_s} P_s \times u_s \qquad (4.66)$$

where the aggregated control variables u_{ag} are the expected dispatching setpoints to the reactive power components. The problem of such an approach is that the aggregated decision variables may provide sub-optimal or even infeasible solutions, e.g. voltage violation occurs. Another approach suggests (4.67)-(4.69) to overcome this problem [81].

$$\min_{\{x_s, u_{ag}\}} \sum_{s=1}^{N_s} P_s \times f(x_s, u_{ag}) \qquad (4.67)$$

subject to

$$g_s(x_s, u_{ag}) = 0 \qquad (4.68)$$

$$h_s(x_s, u_{ag}) \leq 0 \qquad (4.69)$$

where the same control variables, u_{ag}, are obtained for different scenarios after the problem is solved. The difficulty of applying such an approach is the tractability, as the common control variables, u_{ag}, should be valid for all addressed scenarios, i.e. find x_s for each scenario associated with the common control variables, u_{ag}, to obtain the power balance for each scenario.

The binding constraints in (4.71)-(4.72), are released by introducing (4.73). It allows the control variables for different scenarios can be slightly different. The maximum differences are within in the acceptable band $[-\epsilon, +\epsilon]$ [82].

Solving problem (4.70)-(4.73) means to determine the similar control variables that comply with the first-order optimality conditions for different scenarios, which can greatly improve the tractability.

$$\min_{\{x_s, u_{si}\}} \sum_{si=1}^{N_s} P_s \times f(x_s, u_{si}) \qquad (4.70)$$

subject to

$$g_s(x_s, u_{si}) = 0 \qquad (4.71)$$

$$h_s(x_s, u_{si}) \leq 0 \qquad (4.72)$$

$$-\epsilon \leq u_{si} - u_{s1} \leq \epsilon \qquad (4.73)$$

where each scenario can be solved individually and u_{si} is obtained for Scenario i, or the whole problem (4.70)-(4.73) can be solved simultaneously. Equation (4.73) releases the common control variables with small differences to generate u_{si} that can be used to solve the corresponding scenario i, where the convergence is improved.

As only one set of control variables are expected for dispatching, the found optimal values for different scenarios should be aggregated. If the differences of the control variables in different scenarios are minor, (4.66) can thus be applied to aggregate the control variables.

Problem (4.70)-(4.73) can be solved simultaneously using the prime dual interior point method (PDIPM). Due to the nonlinearity and non-convexity of the voltage control problem, SBA generally needs a large number of scenarios, which introduces difficulties to solve the problem. As more

scenarios are solved, convergence becomes more challenging. So, the number of scenarios needs to be reduced for improved tractability. However, if too many scenarios are eliminated, critical conditions may be excluded, resulting in infeasibilities for some cases after realizations. An approach is proposed to improve the performance. As shown in Figure 48, the possible voltage variation in each scenario is estimated and then further constraints the voltage magnitudes feasibility region, (4.74). The voltage margin to protect the solution against uncertainty in each scenario can thus be estimated from (4.59)-(4.62). The voltage magnitude constraints considering the voltage protection margin is obtained in (4.74).

$$V_{min} \leq V_0 + \Delta V_W \leq V_{max} \tag{4.74}$$

where V_0 is the operating point. ΔV_W is the voltage margin estimated from (4.59)-(4.62). This approach relies on a sensitivity matrix that is only valid close to the operating point. This approach is so called sensitivity-based approach. With updated constraint (4.74), the solution for each scenario becomes more conservative, as the acceptable voltage band reduces in each scenario based on the linear estimation.
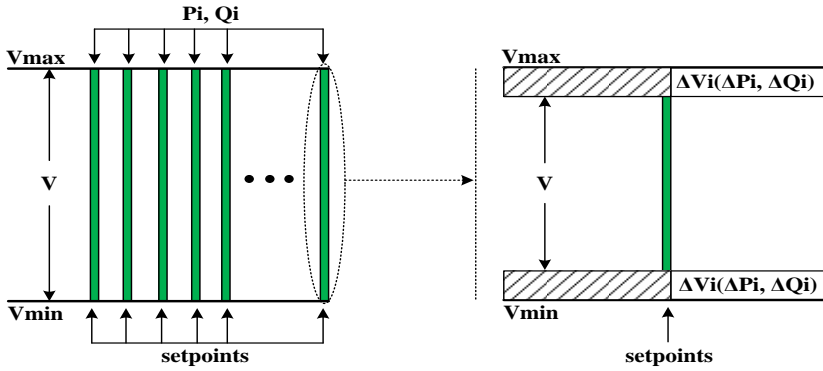
Figure 48. Sensitivity-based approach applied to improve the performance of the scenario-based approach.

In the AVC system, the voltage variation caused by the control actions should also be included. If the problem is formulated into the nonlinear programming framework, then the impacts of the control action will be addressed by the gradients and hessian matrices. The voltage margin to covert the control action is therefore excluded from (4.74). However, if the linear programming technique is applied, then the voltage variation caused by setpoint updates should be included.

The calculation procedure of the scenario-based approach with robustness improvement approach is described step by step in [82], and the algorithm flowchart is shown in Figure 49.

Step 0. Initialization
The proposed optimization is performed to obtain a converged solution as the operating point.

Step 1. Scenario generation/reduction
The uncertainties are represented as discrete PDFs, as shown in Figure 46. If assuming the uncertainties are independent, then the scenarios are the product of the probabilities corresponding to the bins of discrete PDFs.
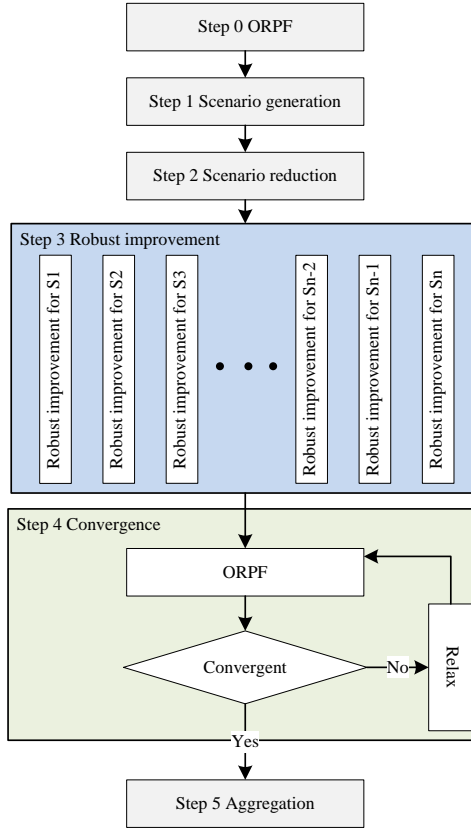
Figure 49. Flow chart SBA approach [82].

The cluttering method can be applied to reduce the number of scenarios. It is not only for reduce the computational burden but also improve the tractability. In case, the probabilities of some scenarios are extremely low, e.g. the scenarios normally represent the extreme situations that are close to the PDF boundaries, these scenarios can be removed, as the impacts of these rare happened scenarios are negligible.

The scenario matrix and probability array can be constructed, as shown in Table 15. In the scenario matrix, each row represents a realization of each uncertainty source, where its probability is listed in the probability array. If the PDFs of uncertainties are known, the scenarios in Table 15 can be prepared in advance, which will greatly reduce the calculation time.

Table 15. An example of a scenario matrix and probability array for 3 wind turbines.

Scenario	WG1	WG2	WG3	Probability
1	x_{11}	x_{12}	x_{13}	P_1
2	x_{21}	x_{22}	x_{23}	P_2
⋮	⋮	⋮	⋮	⋮
N	x_{N1}	x_{N2}	x_{N3}	P_N

Step 3. Update voltage constraints for robustness improvement
Voltage variations caused by the uncertainties are estimated via sensitivity calculations, (4.59)-(4.62). The voltage constraints are therefore updated to include the margin for each scenario.

Step 4. Solution

All scenarios are solved. Equation (4.73) can be tuned for tractability. The found optimal control variables should be aggregated via (4.66). If some of the scenarios are not able to be solved, then they should be marked and may be excluded from the final aggregation. It may indicate the extreme conditions that no feasible solution existing.

The sensitivity-based approach significantly improves the performance of the scenario-based method to protect the solution against the uncertainties of the node power injections [82]. The possible voltage variation at each scenario is estimated based on the sensitivity calculation, i.e. the linear relationship of the voltage variations caused by changes on the node power injections. The difficulty of this approach mainly lies to two aspects, i.e. (i). the number of scenarios increased exponentially as the number of uncertain power injections increases and the involved stages increases; (ii). a solution that valid for all load flow conditions may be difficult to be found or does not exist.

It concludes in [82] that if reserve the estimated voltage margin in each scenario, the solution can be in a certain degree protected against the uncertainty. The question therefore turns to how to properly estimate the voltage margin, and apply the voltage margin to the decision making process with strong tractability.

6.3. VOLTAGE SECURITY MARGIN

In an AVC system, the reactive power components receive setpoints periodically from the optimization engine in the control center. However, voltage violations may occur after dispatching these setpoints, e.g. due to fluctuations in wind power production, especially in the proposed MORPF framework, the predicted load flow condition of the upcoming stages are involved, in which the wind power forecasting errors may lead to infeasible solution after realizations. If the voltage variation corresponding to wind power production can be estimated, then the optimization process can incorporate voltage variation as a margin to protect decisions against uncertainty.

In the AVC system, the forecasting system can be integrated, not only to predict the power balance in the upcoming stages, but also used to estimate the voltage variations caused by WPFE. The decision making process can therefore be based on the chance-constraint OPF concept [83], reserve a margin to cover the voltage uncertainty. This margin is so called "voltage security margin" (VSM) [78].

Applying the linear estimation, the VSM can be found and reserved in the operations, as shown in Figure 48, which is used to improve the solution robustness. Comparing to the scenario based method that taken into account different realizations of the node power injections, the VSM based approach is to fix the uncertain node power injections but reduce the feasible voltage range to address the possible variations caused by changes on the node power injections. It is much easier to be solved with stronger tractability than the scenario-based approach.

In Figure 43, the WPFE have non-parametric distribution, which may be represented by random vectors generation techniques to generate samples covering possible realizations [84]. These samples are then used in the Monte Carlo simulations for the decision making process. However, the Monte Carlo simulation is generally time consuming that is not able to be applied in the AVC system. An approximation is expected, which can be analytically applied in the calculations. Though it may lead to suboptimal solutions, it can guarantee the strong tractability for the approximated problem.

The multivariate normal distribution can be a candidate to represent WPFE [72]-[73], where the WPFE spatial-temporal correlation can be captured in the covariance matrix, i.e. (4.75)-(4.76). The voltage variation caused by WPFE can hereafter be obtained through *affine transformation*, (4.77)-(4.78). It is the VSM in the decision making process, (4.79) [78].

$$\mathcal{U} := \{\Delta P_W | \Delta P_W \sim \mathcal{N}(0, \Sigma)\}$$	(4.75)

$$\Sigma = \begin{bmatrix} \sigma_1^2 & \rho_{12}\sigma_1\sigma_2 & \cdots & \rho_{1n}\sigma_1\sigma_n \\ \rho_{21}\sigma_2\sigma_1 & \sigma_2^2 & \cdots & \rho_{2n}\sigma_2\sigma_n \\ \vdots & \vdots & \ddots & \vdots \\ \rho_{n1}\sigma_n\sigma_1 & \rho_{n2}\sigma_n\sigma_2 & \cdots & \sigma_n^2 \end{bmatrix}, 1, \dots, n \in \mathcal{Z} \qquad (4.76)$$

$$\mu_V = [S_P^1, \dots, S_P^N] \times \begin{bmatrix} \widehat{\Delta P_{W,\iota}^1} \\ \vdots \\ \widehat{\Delta P_{W,\iota}^N} \end{bmatrix}, i \in \mathcal{W} \text{ and } 1, \dots, N \in \mathcal{D} \qquad (4.77)$$

$$\Sigma_V = [S_P^1, \dots, S_P^N] \times \Sigma \times [S_P^1, \dots, S_P^N]^T, 1, \dots, N \in \mathcal{D} \qquad (4.78)$$

$$VSM := \{\Delta V | \Delta V \sim \mathcal{N}(\mu_V, \Sigma_V)\} \qquad (4.79)$$

If the reactive power forecasting errors are known, then VSM can be extended to include the impacts from the reactive power forecasting errors. However, due to the grid code that the power factor should be maintained close to unity at the point of power connection (POC) of wind turbines, the voltage variations due to the reactive power uncertainties are considered to be negligible. Moreover, the wind turbines in the distribution grid are aggregated in the closest substation in the transmission level, as shown in Figure 45, the reactive power flows in the transformers between the transmission level and the distribution levels are normally limited to reduce the loss, which indicates that voltage variation caused by the reactive power uncertainties may not be observed in the transmission level due to the reactive power regulations in the distribution grids.

The obtained profile of the VSM is also the multivariate normal distribution. The confidence level can be specified to determine the size of the VSM at each node. As shown in Figure 43, the WPFE is a non-parametric distribution. Applying the multivariate normal distribution with the confidence level will lead to a conservative solution [78]. As shown in Figure 50, for the most of the cases, the found voltage variation from the fitted normal distribution is larger than the one from the observations, respected to the same probability. The extreme cases are always filtered out by setting the confidence level, as these rare happed cases can lead to large cost and intractability, which has less interest in the normal situations. The over-estimated VSM is acceptable, as the differences are generally minor, and the voltage security is more significant than the cost saving in the AVC systems [78].
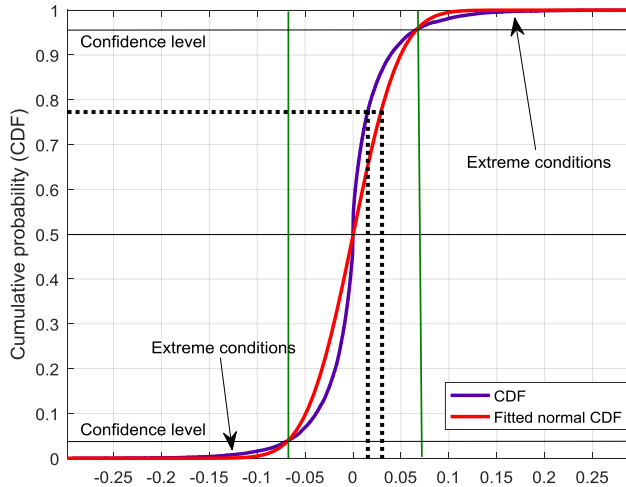
Figure 50. Comparisons between CDF of the observed WPFE and the fitted normal distribution [78].
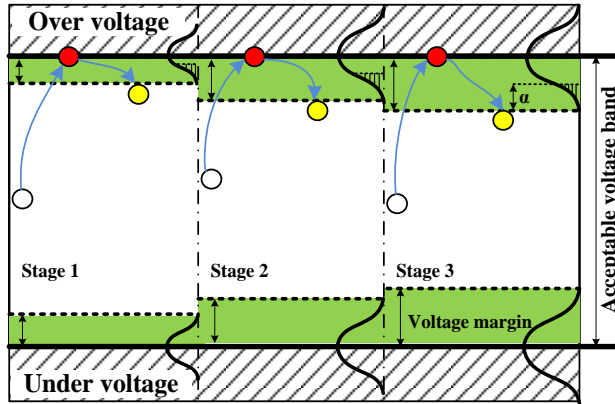
Figure 51. The VSM in 3 different stages [78]. The initial voltage are white balls, which are raised to the upper limit after optimization without VSM for loss saving, i.e. the red balls. It is updated to cover the uncertainty from the WPFE, represented by yellow balls.

The WPFE becomes larger and larger as the forecasting lead time increases, shown in Figure 43. It indicates that the VSM should be increasing along the time horizon in the involved stages, as shown in Figure 51. The voltage is expected to be raised to close to the upper limit in order to reduce the grid loss. After applying the VSM, the acceptable voltage band will be narrowed in order to avoid the violations due to the uncertainty from WPFE. In the case that the solution is too conservative, the confidence level can be adjusted to reduce the size of VSM.

7.   MONTE CARLO SIMULATIONS – NORMAL TO ANYTHING

Normal-to-anything (NORTA) can be applied to generate the samplings for Monte Carlo simulations, in order to verify the effectiveness of the proposed approach [84]. As shown in Figure 52, the random variables are generated for the wind power forecasting errors. NORTA does not require the parametric distributions. The samplings can be used for the Monte Carlo simulations.
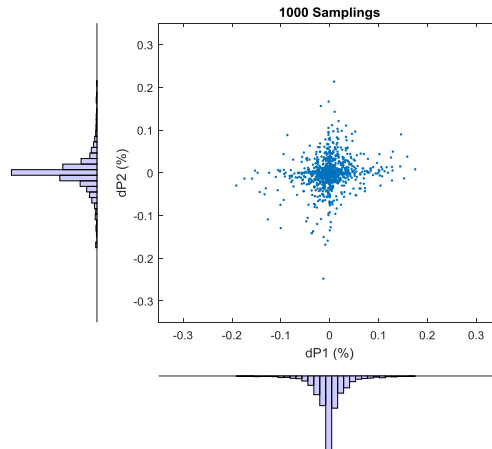
Figure 52. The random variables generated based on NORTA techniques.

NORTA is used to transform a generated multivariate normal random vector to obtain the desired marginal and correlation matrix for Monte Carlo simulations. The general NORTA expression can be expressed as (4.80) [84].

$$X_i = F_i^{-1}\big(\Phi(Z_i)\big), \qquad i = 1,2,\dots dim \qquad\qquad (4.80)$$

where X_i is the desired sampling. Φ is the standard normal cumulative distribution function. Z_i is the standard multivariate normal vector. i is the index of dimension. dim is the total dimensions. F_i^{-1} is the inverse of the desired distribution function, i.e. the empirical distribution profile for the WPFE. There is an analytical mapping between Spearman's rank correlation [85], ρ_s, and the linear correlation coefficient, ρ, in the case of F_i being continuous function, i.e. $F_i(X_i) = \Phi(Z_i)$ has the uniform distribution over $[0, 1]$, (4.81) [84].

$$\rho = 2sin\left(\frac{\pi\rho_s}{6}\right) \qquad\qquad (4.81)$$

Where ρ_s is desired rank correlation found from the real observations. ρ is applied as the correlation matrix to the multivariate normal distribution model. In the case of multivariate normal distribution, Spearman's rank correlation is almost identical to the linear correlation.

8. SUMMARY

This chapter starts from reviewing the existing AVC system, and then proposes the expected Danish AVC system according to the characteristics of the Danish transmission system. Beside the loss minimization, the relatively high regulation cost should be addressed and the reactive power reserve should be considered. The whole problem is formulated in terms of expense. The grid loss and the regulation cost are converted to the expense in the objective. The system variability is captured in the decision making process and the uncertainty from the WPFE is addressed. The proposed MORPF involves the forecasted load flow in the upcoming stages to determine the setpoints of the reactive power components in the current stage. The accuracy of the forecasting system is essential to this approach, as the poor forecasts may lead to suboptimal of even infeasible solutions after realizations. The robustness is improved by including the VSM to cover the voltage variations caused by the forecasting errors.

The wind power fluctuating will finally reflect on the voltage variations, results in the voltage uncertainty. In the voltage control system, as proposed, the objective is to minimize the operational cost including the grid loss. It is always achieved by increasing the voltage profile close to the upper limit. Therefore, once the power injections at nodes vary, which has high risk to introduce the voltage violations. The severity of the voltage variation depends on the deviation of the power injection from the expected value. The voltage violation can trigger the alarm in the control center, where the manual adjustments may be carried out to remove the alarm. Otherwise, it should wait for the next execution of the AVC system to correct the voltage. However, the regulation cost is expected to be minimized. The dispatch by AVC system is expected to be as rare as possible to reduce the regulation cost. If the voltage violation occurs frequently, then many actions will be carried out that leads to high regulation cost. Therefore, a robust AVC system is expected, which not only take into account the system variability but also can protect the solution against the uncertainty in a certain degree.

It is suggested, that the AVC system uses WPFE from an existing point forecasting system to improve the robustness of the voltage control system. In the Danish power system, the wind power forecasting errors concentrate on zero and symmetrically distributed around zero mean. The statistic characteristic of which is therefore approximated by multivariate normal distributions, where the covariance matrix captures the spatio-temporal dependency. The SBA and the VSM based approaches applying the approximated distribution models are described. The SBA is to generate scenarios to address possible node power injections to cover the uncertainty range, which composes a set of new load flow equations with different node power injections. In the optimization, the setpoints of the reactive power components are determined, with which all these load flow equations should be valid. This brings the challenges to the problem tractability. The VSM based method for improving the

overall voltage control security, is to maintain a safety margin that is obtained by estimating the possible voltage variations at the transmission grid, caused by the WPFE in the distribution grid. In contrast to the SBA, the VSM based approach employing the current load flow condition, search for the solution in the reduced feasibility region that reserves the possible voltage variations caused by the changes of the uncertain node power injections. This approach does not involve new nonlinear load flow constraints in the optimization, which has strong tractability. Therefore, the VSM based approach is preferred to be implemented for the proposed AVC system.

CHAPTER 5. IMPLEMENTATION

In Chapter 4, the MORPF based AVC system is proposed to optimize the system for a period capturing the system variability, where the voltage uncertainty caused by the WPFE are addressed by reserving a VSM in the optimization framework. The formulated optimization problem is the core of the AVC system, which should be solved in the real time system within limited time span. Figure 53 shows the overall structure of the proposed decision making process in the Danish AVC system.

The proposed method is implemented in an offline simulation platform, where the measurement data can be applied for simulations and assessments. This Chapter describes the implementation in detail. Small examples are presented for demonstrations.
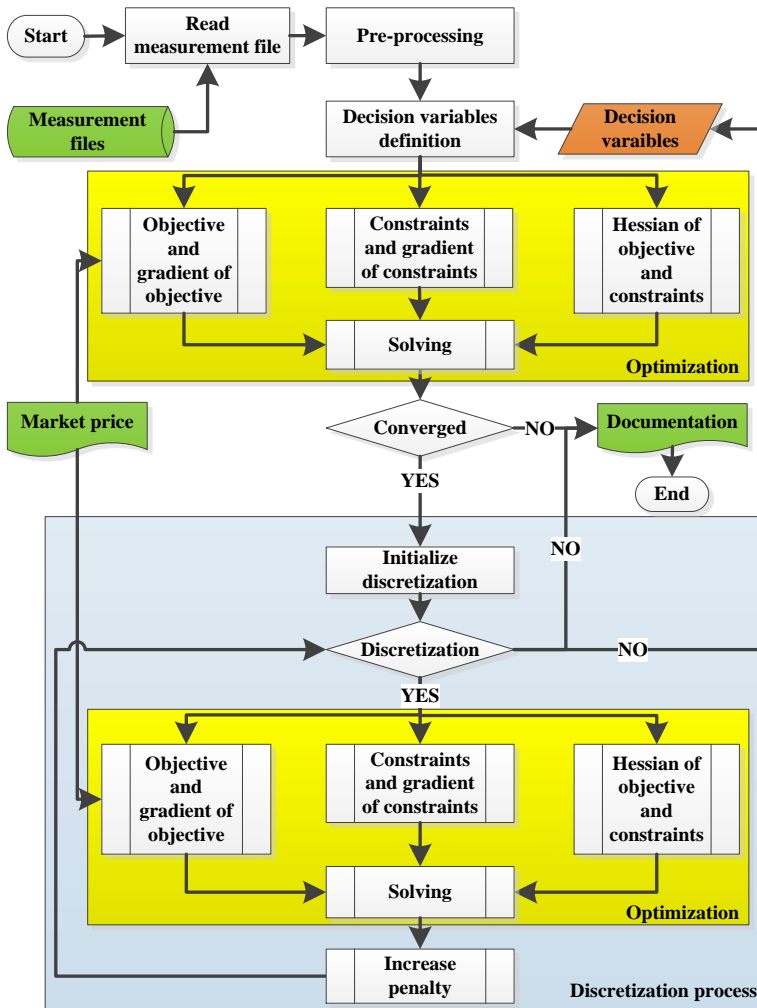
Figure 53. The proposed decision making process in AVC without the VSM.

1. DATA SOURCE

The AVC is intended to be implemented in the Danish national control center to assist the system operators to control the voltage. The proposed MORPF as the decision making process of the AVC system is about to embedded into the EMS that is wildly used in the electricity control center for monitoring and operating the power system. In EMS, the system condition is obtained from the local measurements in substations and the SE that is applied to estimate the system load flow condition based on the gathered measurements [86]. For example, a screen snapshot of the EMS system presenting the load flow condition of the DK1 system is shown in Figure 54, where the voltage magnitudes at busbar and the power flow inside the transmission line, transformers, shunts, generators etc., are obtained periodically. In the Danish EMS system, the system information is updated every 1 minute. The breaker conditions and the transformer tap positions are monitored and taken into the SE for estimations. The load flow condition obtained in the EMS system can be exported, which includes the necessary data to represent the network components. The load flow condition is therefore projected on this network, i.e. match the power injection at nodes for the components and find the voltage at nodes and the power flow in the branches. The AVC is intended to be operated based on system information from SE.
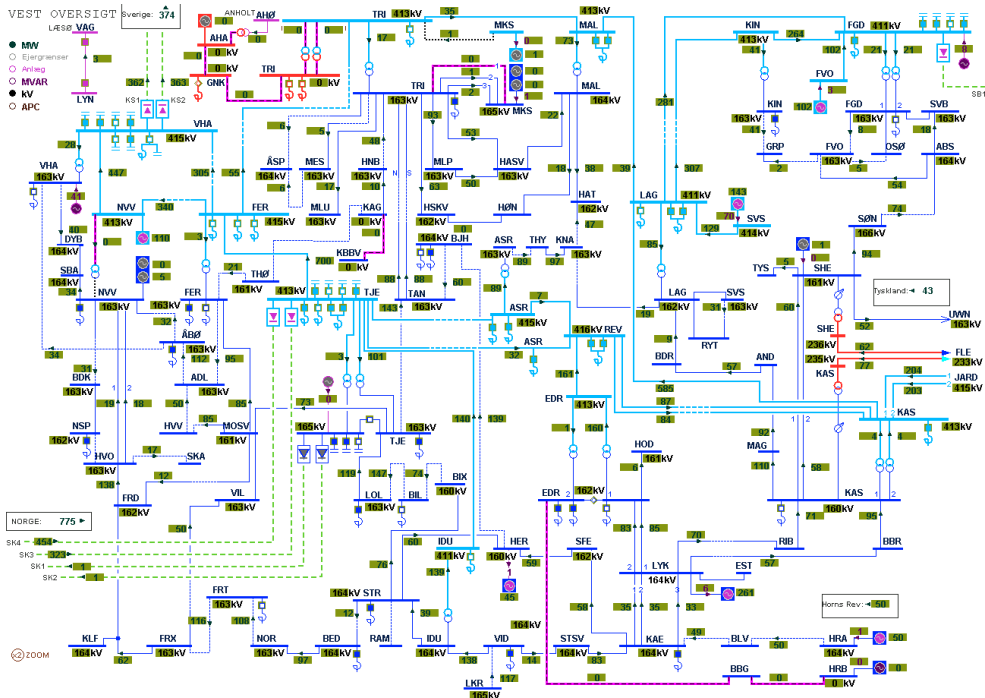
Figure 54. A snapshot of the western Danish power system in EMS in Danish national control center.

An offline platform is built in Matlab® to assess the proposed MORPF method for the decision making in the Danish AVC system. The data exported from SE to the raw "ArevaHDB" format containing full detailed grid representation that is further processed in PowerWorld® [87], in order to (i) perform topological network reduction from detailed busbar representation to single node; (ii) perform reduction of complex segmented branches to the equivalent node-to-node connections; (iii) delete the de-energized components; (iv) assign the fixed ID (with 5 digits) in numbers to the nodes; (v) assign the fixed ID to the specified areas (e.g. DK1 for the western Danish system, DK2 for the eastern Danish system, DE for the German system and SE4 for the Swedish system connected to DK2 etc.). Processed snapshots are then exported from PowerWorld® to PTI RAW® ver. 32 format [88].

In the processing, the de-energized components are not included, as they can be in the revision period. It means that if a switchable shunt is temporally disconnected in a snapshot, it will not be included in the RAW file. However, the disconnected components are still available for regulations in the real grid, but due to performed deletion of de-energized component, they are missing in the RAW files and thus cannon be taken as input for the optimization. If considering all available controllers to optimize the system, these missing shunts should be added after import the RAW file to the platform, e.g. by inserting the full list of the reactive power components after import the data into the platform.

2.   DATA STRUCTURE

MatPower implemented in the Matlab environment, is widely used in the power engineering educations [89]. It can be used to perform the load flow calculation and the economic operational dispatch calculations. In addition, it provides the interface to RAW format that can be read into the MatPower data format for performing the calculations. However, MatPower does not provide the functions for the ORPF calculations, where the necessary data for the ORPF are missing when read data from RAW files into MatPower. In order to perform MORPF for the AVC system, the data structure of MatPower is expanded to include the necessary data for the controllers, as shown in Appendix C – Dataset. Moreover, the relevant functions for MORPF calculations are developed.

3.   PRE-PROCESSING

The data read from EMS are organized in the predefined format, RAW format, which, in fact, contains data to represent a converged load flow snapshot of the system. In general, any RAW file can be imported to this platform, which may not represent a converged load flow condition but general known values of power injection and voltage at nodes. The platform is therefore needed to firstly find the converged load flow solution based on these known values.

Recall the general load flow equation described in Chapter 2, expressed in (5.1), if some isolated nodes exist, i.e. the nodes do not connect to any of other nodes, which can result in some zero rows in (5.1) i.e. the admittance of a node connecting to other nodes does not exit. In addition, if the branch impedance between two nodes is zero, then two nodes are in fact identical that can be merged to one node. It can results in two identical rows in the admittance matrix (5.1). Both cases cause the row rank deficiency in the admittance matrix. The Jacobin matrix constructed based on this admittance matrix is singular in the NR iterations. The load flow equations in these situations are not able to be solved.

$$\begin{bmatrix} Y_{11} & Y_{12} & \cdots & Y_{13} \\ Y_{21} & Y_{22} & \cdots & Y_{23} \\ \vdots & \vdots & \ddots & \vdots \\ Y_{n1} & Y_{n2} & \cdots & Y_{nn} \end{bmatrix} \begin{bmatrix} v_1 \\ v_2 \\ \vdots \\ v_n \end{bmatrix} = \begin{bmatrix} i_1 \\ i_2 \\ \vdots \\ i_n \end{bmatrix} \qquad (5.1)$$

In order to overcome the problems, preprocessing is required. It firstly filters out the isolated nodes from the study system, and then filters out the zero-impedance branches by inserting small impedance. Moreover, considering the Danish power system comprises of two synchronous systems, the study system can typically be defined to be one of them to reduce the number of nodes in (5.1).

3.1. BRAINY'S TREE SORTING METHOD

Brainy's Tree Sorting (BTS) is an efficient way to identify the separated systems, and group the elements into these separated systems. Therefore, it can also be used to filter out the isolated nodes.

For a given system, a connection matrix is constructed in Figure 55, where each node takes one column and each branch takes one row, respectively. The nodes are sorted in a consequence order along the column of the connection matrix. Each series branch is placed in this connection matrix

with two "1" entries in the corresponding columns representing the two ending nodes of this branch. Notice that each row in the connection matrix has only two "1" representing the series branch connection. Each transmission line or two-winding transformer takes one row in the matrix. The three-winding transformers are split into 3 two-winding transformers that take 3 rows for each in the connection matrix. The capacitor/reactor, load and generators are shunt branches that are not involved in the connection matrix, as they are connected to single nodes at their terminals.

		Node				
Indices	**1**	**2**	**3**	**...**		N_b
1	1		1			
2		1				1
3	1			1		
⋮					⋱	
N_{br}		1				1

Figure 55. The connection matrix.

After projecting all series branches into the connection matrix, the algorithm presented in Table 16 can be applied. The algorithm scans each column of the connection matrix to find if there is more than one "1" in this column. If so, it should be that more than one branch connect to this node. Then merging these rows by moving all "1" from the lower rows to the top row, and remove all the corresponding lower rows.

Table 16. Brainy's tree sorting algorithm.

1	*Sort the node in the consequence order, update the indices of the branch nodes accordingly*
2	*Construct the connection matrix*
3	*For each column C*
4	*n = count number of "1" at this column*
5	*If n ≥ 2*
6	*for each row from the second to the last in the connection matrix*
7	*R = find the row indices that have "1" at C. R is index vector.*
8	*Crow = Record two column indices of "1" in each row.*
9	*%Merging all rows whose index is listed in R*
10	*Setting "1" in the first row corresponding Crow*
11	*End*
12	*Removing rows from the second to the end, whose index is listed in Row*
13	*End*
14	*End*

After scanning all columns, there should be at least one row remains. If only one row left, it indicates all nodes are in the same network. If more than one row left, then the number of the remained rows indicates the number of the separated systems. In each remained row, "1" in each column indicates which node is located in this network.

3.2. ZERO IMPEDANCE

Two nodes with zero-impedance series branch in between, which can result in identical row entries representing these two nodes in the corresponding admittance matrix. The load flow Jacobian matrix based on this admittance matrix is singular, which is not able to be inverted in the NR iterations. This problem is solved by inserted a small impedance in these zero-impedance branches. Though the branch admittance is different from the original data, the load flow result with these changes is negligible, i.e. the differences are within the acceptable convergence tolerance.

By definition, the branch reactance and the resistance are set to the minimum values, $1e - 6$ and $1e - 7$, respectively, if their corresponding absolute values are lower than these minimum values. The convergence tolerance is normally set to $1e - 8$. Notice that, there could be negative values in the branches, e.g. splitting the three-winding transformers to 3 two winding transformers that can result in negative reactance. The method to split three-winding transformers to the 3 two-winding transformers are described in [88].

3.3. NETWORK REDUCTION

The load flow snapshots including both the western and the eastern Danish power systems, i.e. DK1 and DK2. As the HVDC link connecting between DK1 and DK2, the AVC can, in fact, optimizes the systems separately. Therefore, the network reduction is applied to split the system into two subsystems and keep the same power flow condition in each subsystem.

Table 17. The interconnections of the Danish power system to the other systems

Western Danish power system (DK1)			Eastern Danish power system (DK2)		
Name	Technology	Connect to	Name	Technology	Connect to
Skagerrak (SK) 1,2 and 3	LCC-HVDC	Norway	Storebælt (SB)	LCC-HVDC	DK1
Skagerrak (SK) 4	VSC-HVDC	Norway	Sweden (SE)	AC	Sweden
KontiSkan (KS) 1 and 2	LCC-HVDC	Sweden	Kontek (KO)	LCC-HVDC	Germany
Storebælt (SB)	LCC-HVDC	DK2			
Germany (GE)	AC	Germany			

In order to further simplify the model to reduce the node numbers in the calculations, the transmission grids of the neighboring systems are removed. Instead the neighboring systems are represented by simple equivalent generators and nodes to specify the power injections to the Danish systems. Considering different technologies of the interconnections, i.e. LCC-HVDC, VSC-HVDC and AC connections, as shown in Table 17, either load or generator models are used to replace the interconnections, shown in Figure 56.
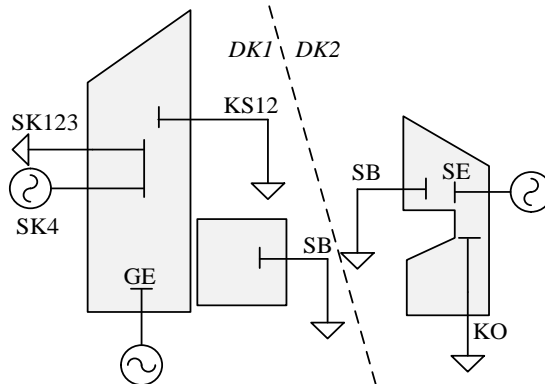
Figure 56. The equivalent models for optimizations.

As shown in Figure 56, the DK1 system is synchronized to the German system (GE) and the DK2 system is synchronized to the Swedish system (SE), respectively. The slack machines for DK1 and DK2 are, respectively, placed in Germany and Sweden. In the AVC system, the reactive power flow between Danish power system and the neighboring systems may be limited on the interconnections. If the VSC-HVDC link is applied, the reactive power is fully controlled at terminals (SK4). If the LCC-HVDC link is applied, the reactive power consumption at the terminal is related to the loading on the

HVDC links. The capacitive filters are therefore used to compensate the reactive power consumption at the terminal of LCC-HVDC link (SK123, KS12, SB and KO).

LCC-HVDC link is equivalent to the current source, as the current direction is unchanged. It relies on the voltage at the AC side for commutations, and it is not able to regulate the reactive power to support the voltage at the AC side. Therefore, the LCC-HVDC links are modelled as constant load. All capacitive filters are kept that can compensate the reactive power consumption according to the loading on the LCC-HVDC links. These shunt filters are currently controlled by the local RPC, which are not assigned by AVC system in the early implementation stage. In contrast to LCC-HVDC, VSC-HVDC can maintain the voltage by either injecting or absorbing the reactive power, which is represented by the voltage source model, or say, the generator model. The internal control functions of the HVDC links are not considered. Only either PQ or PV nodes are presented in the AVC system. If considering the regulations inside the HVDC links, e.g. the gamma angle control to prevent the communication failure, and then the reactive power output will be a function of the HVDC internal control variable. These functions can be integrated to this platform, where the calculation should be extended, e.g. firstly find the PQ/PV values at the HVDC terminals as initial values and then update these values by considering the HVDC internal functions.

If the AC inter-ties are modelled in the AVC system, and the slack machine is placed at one of the external node, then the reactive power flow on the inter-ties can be limited by formulating the flow limit as the nonlinear inequality constraints in the optimization framework. The flow limit is quadratic function that will be presented in the Hessian matrix. An alternative approach is to place the slack machines at the Danish sides of the AC inter-ties, and then constrain the reactive power regulation capabilities of the slack machines. In this approach, the AC inter-ties are not used in the formulations, and then the node in the external system is not observed. Moreover, the generator reactive power limits are linear constraints, which are not presented in the Hessian matrix. In the current platform, the slack machine is placed in the Danish side of the inter-tie lines to further simplify the calculations. The procedure of network reduction is presented as following.

Step 1.
Execute a load flow calculation and record the loading on SK, KS, SB, KO and tie lines to Germany and Sweden, respectively. In addition, record the voltage magnitude at the end of the AC-ties in the DK systems, e.g. Kassø 400 kV station, KAS400, in DK1.

- By rules, the bus ID with 5 digits are busbar, and with 4 digits are the internal junctions, e.g. the terminals of the large decentralized generators connecting to the transmission level via the step-up transformers or the internal junctions of the variable shunts.
- The branches include the step-up transformers of the large decentralized generators. It means that the loss on the step-up transformers of the large power plants is explicitly presented in the calculations, which will be included in the AVC objective function for minimization.

Step 2.
Remove the external grids and replace the HVDC links by equivalent models with the recorded data from *Step 1*. The loadings on the tie lines are aggregated as power injections to the Danish busbars. The external grids and the original tie lines are therefore removed. It may result in the isolated busbar, which needs the platform to be able to identify and remove the isolated busbar. Therefore, BTS method is applied again after removing the external grids.

Step 3.
Add a slack generator at the terminal of DK system, to keep the voltage magnitude constant after the network reduction, e.g. the slack machine is added at "80004" (KAS400) at DK1 system.

Step 4.
Execute the load flow calculation and validate the results respected to load flow results before *Step 1*. Report the comparison results, e.g. system loss before and after the reduction.

The AVC is typically carried out after the SE provides a converged load flow snapshot. In this case, the load flow with only PQ and SL node types can be applied after network reduction to check if the load flows are identical, e.g. the branch losses before and after the network reduction are equal. In this way, only the basic load flow function is required. Some control functions, like the generator remote voltage control is not needed. However, in the case of a general load flow calculation is performed, a feasible load flow condition considering operational conditions may be conducted.

4. DECISION VARIABLE DEFINITION

The reactive power components including the generators reactive power injection, the shunt susceptance and the transformer tap ratio, are defined as controllers in the AVC system. In the network definition, generators, shunts and transformers are also defined as branches. At each of these branches, one controller exits. In the AVC system, it is not possible controlling one node voltage by two separated controllers, e.g. a shunt and a generator connect at the same node and control the same node voltage. It may lead to conflict between two controllers and non-convergence. In addition, two identical branch controllers are not able to be presented for controlling the same node voltage. For example, if two parallel transformer taps control the same node voltage, then the gradients of them are equal. It can result in the same row entries in the gradient matrix, and finally leads to row rank deficiency. Therefore, the parallel branches are aggregated, via (5.2)-(5.4), where the controllers are also aggregated.

$$R_{agg} = \frac{1}{\sum \frac{1}{R_i}}, i \in \mathfrak{B}$$	(5.2)
$$X_{agg} = \frac{1}{\sum \frac{1}{X_i}}, i \in \mathfrak{B}$$	(5.3)
$$B_{agg} = \sum B_i, i \in \mathfrak{B}$$	(5.4)

The generators connecting to the same node is aggregated to one with enlarged regulation capability. The individual reactive power outputs can thus be determined as the required total reactive power injection is found by AVC system.

If more than one tap-able transformer exists between two nodes, then they will be aggregated to one controller in the programming. If the parallel transformers have different tap-ratio ranges, then the intersection range of theses transformers are defined as the feasible range of the aggregated transformer tap changer. In the programming, the costs of the tap changes are also estimated values for these aggregated controllers.

In Chapter 4, the MORPF framework is proposed that typically needs more than one stage. In this framework, each control variable is presented in each involved stage. All involved stages should be converged after the optimization problem is solved. Different numbers of components may be included in different stages, because of switching in/out some components. The unmatched numbers of components are needed to be carefully treated in the MORPF framework, i.e. link the control variables representing the same controller in different stages for optimizations. The control variables are defined in the following.

- PV generators

RAW files include the generator information. The PQ generators that are not assigned by AVC system can be identified by inspecting the reactive power capability limits, i.e. if the maximum and the minimum reactive power limits have the same values, then theses generators are identified as PQ generators. In the case of PV generators, the maximum/minimum reactive power outputs, the initial active and reactive power outputs as well as the initial terminal voltage are needed.

In the MORPF framework, the PQ generators representing the uncontrollable decentralized production units are power injections in the load flow calculations in each involved stage. The loads, fixed shunts and PQ generators are not interlinked in different stages. The switchable shunts and the tap-able transformers, assigned as controllers in the AVC systems, are interlinked between different stages, to minimize the control actions between sequential stages.

- Tab-able transformers

In the reactive power flow optimizations, the transformer off-nominal tap ratios are used as controllers. However, in the real system, the tap position is physically controlled by AVC system. The tap ratio, r, is therefore needed to be converted to the tap position, T. The maximum/minimum tap position, T_{max}/T_{min}, initial tap positon T_{ini} and the voltage change per tap Δu are read from RAW file into the platform. The total tap positions T_{nr}, can thus be found via (5.5). The resistance and the reactance of the transformer are updated with the initial tap ratio accordingly.

$T_{nr} = \left(\dfrac{r_{max} - r_{min}}{\Delta u}\right) + 1$	(5.5)
$T_{min} = Round\left(\dfrac{r_{min} - r_{ini}}{\Delta u}\right)$	(5.6)
$T_{max} = Round\left(\dfrac{r_{max} - r_{ini}}{\Delta u}\right)$	(5.7)
$T_{ini} = 0$	(5.8)

As described in Chapter 2, the tap changer in the platform is modelled at the primary side. It can be seen from (5.8) that the initial tap positon will always be zero when firstly read from the RAW file, and the minimum and the maximum tap positions are adjusted accordingly to ensure the regulation capability are unchanged after change the initial tap to zero, (5.6)-(5.8). It means that for the same transformer tap changer, the maximum and minimum tap positions in different stages can vary. However, the total tap numbers and the corresponding tap ratio regulation ranges in different stages are identical.

- Switchable shunts

Switchable shunts may be capacitive or inductive. In addition, shunts may contain several steps as a bank. In the platform, the negative sign is defined for the reactive power consumption by the inductive shunt reactor. In the RAW files, the rated reactive power injection per step and the total initial reactive power at bus are available. The rated reactive power injection is found by susceptance multiplying the square of the rated voltage. In the platform, the minimum step of each shunt is zero. The maximum step, the reactive power injection per step and the corresponding reactive power injection at the maximum step are gathered.

In the case of several shunts controlling the voltage at the same busbar, these shunts with the same reactive power injection per step are aggregated at each node, as shown in Table 19. The status of each shunt should be found by AVC system. A rule is defined in the platform, this is carried out by listing all the combinations of shunt status connected at the same bus, providing the required total reactive power injection at this node, and then select the combination with the least total steps.

Therefore, there are two datasets for shunt variables, (i). specifying the individual shunt total steps, reactive power injection per step and the step value; (ii). the dataset of the aggregated shunt controller at each node, specifying the minimum/maximum reactive power injection at each node. Converting the required reactive power injection at each node to the status of each individual shunt is defined by the abovementioned rule.

The different numbers of shunts in different stages may be due to some shunts are temporally disconnected, which are not recorded by RAW files. However they are still available for AVC controls. In order to ensure the correct interlinks of the same control variable across different stages, an assumption is made: In a MORPF problem that involves more than one stage, if a switchable shunt is found in any of the involved stage in an execution, then this shunt is considered to be available in all involved stages in this execution, i.e. the absence of such shunts are due to the temporal disconnection. The platform therefore updates the dataset for adding the missing shunts in the corresponding stages to have equal numbers of shunts before executing the optimizations.

Moreover, in the case that several shunts being connected to the same bus, the values of the total rated reactive power injection and the total step numbers in such stations should be updated as well. The initial rated reactive power injection of the missing shunts is set to zero in the specified stages. The regulation capabilities in such station are updated to include the capability of the missing shunts.

The different numbers of series branches in different stages are considered due to the revisions. The series branches in each stage are included in the admittance matrix for the load flow equations. Therefore, the numbers of series branches are not necessary to be equal for involved stages.

The different numbers of nodes in involved stages are either due to the revisions that some of the stations are de-energized, or due to the switchable shunts that are switched on/off. In the case of due to the switching on/off variable shunts, the internal junction nodes, whose "ID" are with 4 digits, are added in all involved stages, in order to ensure the temporal de-energized shunts are able to be switched in again by AVC.

In summary, in the MORPF, the decision variables are defined as (5.9) if the quadratic functions are applied to represent the regulation changes, or defined as (5.10) if the absolute functions are applied to represent the regulation changes (see Chapter 4), where the number of the voltage angle δ, the number of the voltage magnitude V, the number of the generator reactive power injection Q_g can be different in each stage. However, the numbers of the transformer tap ratio τ and the shunt susceptance b should be equal for different stages, respectively. Therefore, the indices of such variables in different stages are needed to be adjusted. The interface will "maximize" the control capabilities of the switchable shunts, as shown in the abovementioned statements. The numbers of shunts (b and the relevant ancillary variable Z) and tap-able transformers (τ and the relevant ancillary variable M) in the involved stages are, respectively, adapted to be equal. The numbers of nodes and PV generators are not necessarily equal.

$$x^d = \begin{bmatrix} \delta^d & V^d & \boldsymbol{\tau}^d & \boldsymbol{b}^d & Q_g^d \end{bmatrix}^\top$$	(5.9)
$$x^d = \begin{bmatrix} \delta^d & V^d & \boldsymbol{\tau}^d & \boldsymbol{b}^d & Q_g^d & \boldsymbol{M}^d & \boldsymbol{Z}^d & Y^d \end{bmatrix}^\top$$	(5.10)

5. SEQUENTIAL UPDATE

In the AVC system, the optimal setpoints will be dispatched to the reactive power components. In the next execution of the MOPRF calculation, the updated setpoints and the corresponding changes in the system states will be observed by the SE and then fed into the MORPF framework. However, in the simulations, the dispatching process is not included.

Therefore, in order to "observe" the optimal setpoints from the previous dispatch, once the MORPF is solved, a new execution of MORPF will be started sequentially after updating the setpoints of the controllers, i.e. the transformer tap-ratio, the shunt susceptance and the generator reactive power output, from the previous MORPF. The setpoints of the reactive power components in the first stage of each MORPF execution will be used to directly update the control variable in the data source files of the upcoming stages, as shown in Figure 57.

For example, a MORPF execution involves 5 stages for each execution. After an execution, the setpoints of the reactive power components in the Stage 1 will be extracted. In the next execution of MORPF, Stage 2 to 6 are involved by keeping the same size of the rolling window. The setpoints of Stage 1 are then used to update the initial values of the reactive power components at Stage 2 to 6 before the second execution. After setpoint update, the load flow in Stage 2 to 6 may not be converged. However, the MORPF execution will find the load flow solutions to regain the convergence. After the MOPRF is solved, the setpoints of Stage 2 is used to update the control variables in the upcoming 5 stages for the next execution. This process will be continually until the termination.
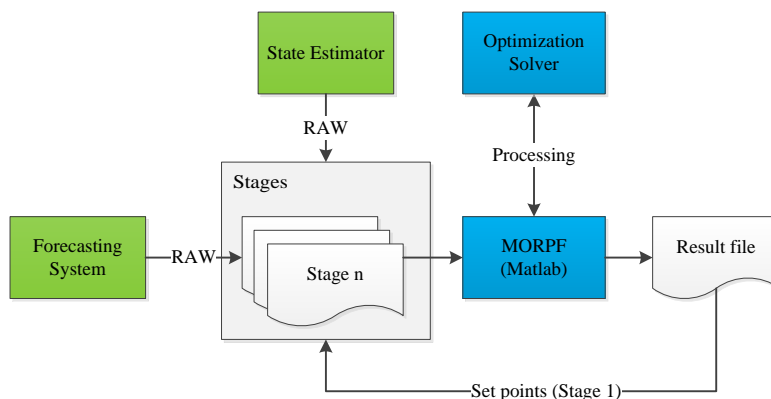
Figure 57. Emulation of the dispatching setpoints to the system for the sequential simulations.

In order to assess the potential saving, the grid loss should be obtained before and after the optimization. The load flow condition without any optimization is considered as the reference case. However, in the real time system, the setpoints found by AVC are dispatched periodically. If assuming the system condition is not able to be changed dramatically in this short period, then the load flow after updating the optimal setpoints previously dispatched by AVC will be already more optimal than the load flow condition without update, i.e. the grid loss right now after updating optimal setpoints in the last dispatch is less than the case without implementing the optimal setpoints. Then the potential saving by the optimization in the current snapshot could be lower than the case without any optimization in the past.

In this project, the potential loss saving by the AVC system is defined as the grid loss differences of the two cases, which are (i). all the involved stages are optimized and (ii). none of the involved stage is optimized. It is not the loss saving between sequential stages.

6. PROGRAMMING

The optimization applying the first optimally condition requires the Gradients and the Hessian matrices, as introduced in Chapter 3. In the programming, not only the formulation should be correctly represented, but also the indices of each variable should be carefully treated, to ensure the correctness of both the values and the positions in the relevant matrices for the calculations.

6.1. THE CONTINUOUS OPTIMIZATION

In the programming, the derived equations should be organized in a proper manner. For example, sort the nodes in a consequent order and then link the branches including the series and shunt branches to the node order. The decision variables are also sorted in an order, e.g. (5.9) or (5.10). The goal of programming is to bridge the objective and the constraints to the decision variables by allocating the objective and constraints derivatives w.r.t. the decision variables in the correct positions of the matrices. The numerical optimization algorithm is therefore able to be applied.

Recall the objective function (5.11) that is described in Chapter 4 Section 3.1.

$$J^d = C_p^d + C_\tau^d + C_b^d + C_g^d$$	(5.11)

where (5.11) can be expressed by (5.12)-(5.18). The **state variables** and the **control variables** are marked with blue and green colors, respectively.

$$C_p^d = p^d (P_{br} + P_{tr} + P_{sh}), d = 1,2,3 ....$$	(5.12)
$$P_{br} = \sum_{i=1}^{N_{br}} Real\left(\frac{\left\| \frac{v_{f,i}}{\tau_i e^{j\vartheta_i}} - v_{t,i} \right\|^2}{R_{s,i} + jX_{s,i}} \right), \forall i \in \mathcal{L}$$	(5.13)
$$P_{tr} = \sum_{i=1}^{N_{tr}} V_{trf,i}^2 \cdot G_{tr,i}, \forall i \in \mathcal{T}$$	(5.14)
$$P_{sh} = \sum_{i=1}^{N_{sh}} V_{sh,i}^2 \cdot G_{sh,i}(b_i), \forall i \in \mathcal{B}$$	(5.15)
$$C_\tau^d = \sum_{i=1}^{N_\tau} p_{\tau,i} M_i^d, \forall i \in \mathcal{T}, \forall d \in \mathcal{D}$$	(5.16)
$$C_b^d = \sum_{i=1}^{N_b} p_{b,i} Z_i^d, \forall i \in \mathcal{B}, \forall d \in \mathcal{D}$$	(5.17)
$$C_g^d = \sum_{i=1}^{N_g} p_{Q,i} Y_i^d, \forall i \in \mathcal{G}, \forall d \in \mathcal{D}$$	(5.18)

The objective is subjected to constraints, (5.19)-(5.24) for constraining the ancillary variables as described in Chapter 4 Section 4.1.2, and the other operational constraints (5.25)-(5.32).

$\tau_i^d - \tau_i^{d-1} \le M_i^d, \quad \forall i \in \mathcal{T}, \forall d \in \mathcal{D}$	(5.19)
$-\left(\tau_i^d - \tau_i^{d-1}\right) \le M_i^d, \quad \forall i \in \mathcal{T}, \forall d \in \mathcal{D}$	(5.20)
$b_i^d - b_i^{d-1} \le Z_i^d, \quad \forall i \in \mathcal{B}, \forall d \in \mathcal{D}$	(5.21)
$-\left(b_i^d - b_i^{d-1}\right) \le Z_i^d, \quad \forall i \in \mathcal{B}, \forall d \in \mathcal{D}$	(5.22)
$Q_{g,i}^d \le Y_i^d, \quad \forall i \in \mathcal{G}, \forall d \in \mathcal{D}$	(5.23)
$-Q_{g,i}^d \le Y_i^d, \quad \forall i \in \mathcal{G}, \forall d \in \mathcal{D}$	(5.24)
$V_i \sum_{k=1}^{N_v} V_k (G_{ik} \cos \delta_{ik} + B_{ik} \sin \delta_{ik}) = P_{l,i} - P_{g,i}, \quad \forall i \in \mathcal{V} - \{ref\}, \quad \forall k \in \mathcal{V}$	(5.25)

$V_i \sum_{k=1}^{N_v} V_k (G_{ik} \sin \delta_{ik} - B_{ik} \cos \delta_{ik}) = Q_{l,i} - Q_{g,i}, \qquad \forall i \in \mathcal{V} - \{ref\}, \qquad \forall k \in \mathcal{V}$	(5.26)
$V_{min,i} \leq V_i \leq V_{max,i}, \qquad \forall i \in \mathcal{V}$	(5.27)
$b_{min,i} \leq b_i \leq b_{max,i}, \qquad \forall i \in \mathfrak{B}$	(5.28)
$\tau_{min,i} \leq \tau_i \leq \tau_{max,i}, \qquad \forall i \in \mathcal{T}$	(5.29)
$Q_{gmin,i} \leq Q_{g,i} \leq Q_{gmax,i}, \forall i \in \mathcal{G}$	(5.30)
$M_i^d \leq M_{max,i}, \qquad \forall i \in \mathcal{T}, \forall d \in \mathcal{D}$	(5.31)
$Z_i^d \leq Z_{max,i}, \qquad \forall i \in \mathfrak{B}, \forall d \in \mathcal{D}$	(5.32)

The objective gradient at a certain stage ∇J^d, is derived by differencing the objective function respected to the **control variables** and the **state variables** in (5.13)-(5.18), respectively. However, the control variables and the state variables are not treated differently. The resulted objective gradient in (5.33) is a vector, representing the derivatives of (5.13)-(5.18) w.r.t. the decision variable x. In MORPF framework, all the involved stages are solved simultaneously. The required objective involving several stages is also a vector and in the form of (5.34).

$\nabla J^1 = \begin{bmatrix} \nabla J_\delta^1 & \nabla J_V^1 & \nabla J_\tau^1 & \nabla J_b^1 & \nabla J_{Q_g}^1 & \nabla J_M^1 & \nabla J_Z^1 & \nabla J_Y^1 \end{bmatrix}^\top$	(5.33)
$\nabla J^d = \begin{bmatrix} \nabla J^1 & \nabla J^2 & \cdots & \nabla J^{N_d} \end{bmatrix}^\top, \forall d = 1,2 \dots N_d$	(5.34)

The equality constraint gradients at a certain stage ∇G^d, is derived by differencing the constraints respected to the **control variables** and the **state variables** in (5.25)-(5.26), respectively. It can be seen as an expanded Jacobian matrix of the load flow calculation to include the derivatives of the load flow equation w.r.t. to the **control variables**. The equality constraints are sorted in the consequent order of the nodes. In the MORPF framework, the gradient matrix of each stage (5.35) is on the diagonal of the entire Jacobian matrix (5.36).

If without the flow limit constraints, all inequality constraints are linear constraints, which can be sorted in a certain order to construct the inequality constraint matrix. In some programming software, e.g. Matlab, the gradients of the box constraints (5.27)-(5.32) are not necessarily formulated by the users, but input as two vectors representing the lower and the upper limits, respectively [64]. In fact, the gradients of them are either 1 or -1 w.r.t. the corresponding variables for theses constraints. In the MORPF framework, the inequality constraints (5.37) of each stage is on the diagonal of the entire Jacobian matrix (5.38), where the constraints involving the interlinks (5.19)-(5.22) are placed in the off-diagonal areas, $\nabla H^{N_d-1,N_d}$ in (5.38).

$\nabla G^1 = \begin{bmatrix} Real(\nabla G_\delta^1 & \nabla G_V^1 & \nabla G_\tau^1 & \nabla G_b^1 & \nabla G_{Q_g}^1 & \nabla G_M^1 & \nabla G_Z^1 & \nabla G_Y^1) \\ Imag(\nabla G_\delta^1 & \nabla G_V^1 & \nabla G_\tau^1 & \nabla G_b^1 & \nabla G_{Q_g}^1 & \nabla G_M^1 & \nabla G_Z^1 & \nabla G_Y^1) \end{bmatrix}$	(5.35)
$\nabla G^d = \begin{bmatrix} \nabla G^1 & & & \\ & \nabla G^2 & & \\ & & \ddots & \\ & & & \nabla G^{N_d} \end{bmatrix}$	(5.36)
$\nabla H^1 = \begin{bmatrix} \nabla H_\delta^1 & \nabla H_V^1 & \nabla H_\tau^1 & \nabla H_b^1 & \nabla H_{Q_g}^1 & \nabla H_M^1 & \nabla H_Z^1 & \nabla H_Y^1 \end{bmatrix}$	(5.37)
$\nabla H^d = \begin{bmatrix} \nabla H^1 & \nabla H^{1,2} & & & \\ & \nabla H^2 & & & \\ & & \ddots & \ddots & \\ & & & \nabla H^{N_d-1} & \nabla H^{N_d-1,N_d} \\ & & & & \nabla H^{N_d} \end{bmatrix}$	(5.38)

The number of the decision variables, i.e. the length of j in Table 18, is expressed by (5.39). Therefore, for the single objective function, the number of ∇J^d, i.e. the length of i_J in Table 18, can also be determined by (5.39).

The number of ∇G^d, i.e. the length of i_G in Table 18, can be determined by (5.40), where the slack nodes are not taken into the power balance constraints and the power balance are split into the active power and the reactive power balances.

The number of ∇H^d except the box constraints, i.e. the length of i_H in Table 18, can be determined by (5.41). For each reactive power component at a stage, there are at least 4 inequality constraints are relevant. For example, for each tap ratio, (5.19)-(5.20) w.r.t. τ and (5.19)-(5.20) w.r.t. M are relevant.

$\left(N_{node} + N_{node} + N_{tr} + N_{sh} + N_{Q_g} + N_{tr} + N_{sh} + N_{Q_g} \right) \times N_d$	(5.39)
$(N_{node} - N_{SL}) \times 2 \times N_d$	(5.40)
$(N_{tr} \times 2 + N_{sh} \times 2 + N_{Q_g} \times 2) \times 2 \times N_d$	(5.41)

The required derivatives w.r.t. the decision variables are summarized in Table 18. The detailed expressions are presented in the Appendix B – Derivative.

Table 18. The functions, whose derivatives w.r.t. the decision variables are required.

Row index i_J	Row index i_G	Row index i_H	Column index j
Single objective function J	Equality constraints G	Inequality constraints H	Related variables x
(5.13)	(5.25) and (5.26)	--	δ
(5.13), (5.14) and (5.15)	(5.25) and (5.26)	(5.27)	V
(5.13)	--	(5.19), (5.20) and (5.29)	τ
(5.15)	--	(5.21), (5.22) and (5.28)	b
--	--	(5.23), (5.24) and (5.30)	Q_g
(5.16)	--	(5.19), (5.20) and (5.31)	M
(5.17)	--	(5.21), (5.22) and (5.32)	Z
(5.18)	--	(5.23) and (5.24)	Y

As shown in Chapter 3, the nonlinear programming techniques require the Hessian matrix that contains the secondary derivatives of the objective and the constraints respected to the decision variables. The Hessian matrix is a symmetrical matrix. For example, a Hessian matrix representing the equality constraints at a certain stage is shown in (5.42). As known, the equality constraints are the active power and the reactive power balances in the system. In the case of PDIPM is applied to solve the optimization problem, then for each node taking into account the load flow equations, there will be two constraints for the active power and reactive power balance, respectively. Correspondingly, there will be two Lagrangian multipliers, which are dual variables in PDIPM as described in Chapter 3. In (5.42), for each constraint, there will be a Hessian matrix multiplying the corresponding Lagrangian multiplier. The row and the column numbers are the same with the length of the decision variables. Typically, for each constraint, there are only few variables involved, which will result in a very sparse matrix. The general Hessian form for MORPF is shown in (5.43), where the Hessian matrices for the inequality constraints are zero if only the linear inequality constraints are considered in the formulations.

$$\lambda_G \cdot \nabla G_{xx} = \sum_i \lambda_{Gi} \cdot \begin{bmatrix} \nabla G_{\delta\delta} & \nabla G_{\delta V} & \nabla G_{\delta\tau} & \nabla G_{\delta b} & \nabla G_{\delta Q_g} & \nabla G_{\delta M} & \nabla G_{\delta Z} & \nabla G_{\delta Y} \\ \nabla G_{V\delta} & \nabla G_{VV} & \nabla G_{V\tau} & \nabla G_{Vb} & \nabla G_{bQ_g} & \nabla G_{VM} & \nabla G_{VZ} & \nabla G_{VY} \\ \nabla G_{\tau\delta} & \nabla G_{\tau V} & \ddots & & & & & \vdots \\ \nabla G_{b\delta} & \nabla G_{bV} & & \ddots & & & & \vdots \\ \nabla G_{Q_g\delta} & \nabla G_{Q_g V} & & & \ddots & & & \vdots \\ \nabla G_{M\delta} & \nabla G_{MV} & & & & \ddots & & \vdots \\ \nabla G_{Z\delta} & \nabla G_{ZV} & & & & & \nabla G_{ZZ} & \nabla G_{ZY} \\ \nabla G_{Y\delta} & \nabla G_{YV} & \cdots & \cdots & \cdots & \cdots & \nabla G_{YZ} & \nabla G_{YY} \end{bmatrix}_i$$ (5.42)

$$\nabla L_{xx}^d = \begin{bmatrix} \nabla J_{xx}^1 & & & \\ & \nabla J_{xx}^2 & & \\ & & \ddots & \\ & & & \nabla J_{xx}^{N_d} \end{bmatrix} + \begin{bmatrix} \lambda_{G^1} \cdot \nabla G_{xx}^1 & & & \\ & \lambda_{G^2} \cdot \nabla G_{xx}^2 & & \\ & & \ddots & \\ & & & \lambda_{G^{N_d}} \cdot \nabla G_{xx}^{N_d} \end{bmatrix}$$

$$+ \begin{bmatrix} \lambda_{H^1} \cdot \nabla H_x^1 & & & \\ & \lambda_{H^1} \cdot \nabla H_{xx}^2 & & \\ & & \ddots & \\ & & & \lambda_{H^1} \cdot \nabla H_{xx}^{N_d} \end{bmatrix}$$ (5.43)

The numerical optimization algorithms can therefore be applied employing the analytical gradients and Hessian matrices to solve the problem, as described in Chapter 3.

6.2. DISCRETIZATION

All discrete variables are treated as the continuous variables in the continuous optimization. The discrete variables are defined as the susceptance of the switchable shunts and the tap ratio of the tap-able transformers. The discretization is carried out after the continuous optimization is solved. As described in Chapter 4, the sinusoidal penalty function is applied to gradually force the discrete variables to the integers as the penalty factor increases, which formulates an extended objective function to include the penalty function. The gradients and the hessians of the objective should be therefore updated accordingly to include the gradients and the hessian matrices of the penalty function. The expressions of the gradient and the hessian of the penalty function are presented in Appendix B – Derivative.

As mentioned, in the case of several shunts connecting in the same busbar, then they are aggregated to a single controller at this busbar. It should be clarified that the data is read from RAW files that are extracted from the EMS of the electricity control center, where the shunts with the same rated reactive power are already aggregated, and a variable representing the "step" is used to specify the status of each shunt. In the programming, these shunts are further aggregated at each node, which results in only one control variable at each node. The actual status of the shunts connected to the same busbar will be obtained by firstly found the total required susceptance at the node, and finally determined based on the defined rule i.e. achieving the required total susceptance at each node by switching the shunts from the largest to the smallest size.

For example, Table 19 shows an example of station shunts read from a RAW file into the simulation platform. Three aggregated switchable shunts are read from the RAW file representing total 10 shunts with different rated MVar. As mentioned, these shunts are then further aggregated to a single controller in the station level with the aggregated minimum/maximum regulation capabilities, i.e. Min. Q and Max. Q in Table 19.

Table 19. Reactive power injection of switchable shunts in a station. Susceptance is control variable.

No.	MVar/Step	Total Steps	Min. Q	Max. Q	Q. Opt.	Actual step after optimization
1	50	2				2
2	20	5	-30	200	125	1
3	-10	3				0

In the case that the optimization found that 125 MVar is needed in this station, the logic is to start to switch the shunt from the largest size that results in the least switching times. The results are shown in Table 19, where 2 × 50 MVar and 1 × 20 MVar are switched in. The alternative solution could be 2 × 50 MVar, 2 × 20 MVar and 1 × -10 MVar are switched in. However, the latter solution leads to 5 switching times whereas the former solution based on the defined logic leads to 3 switching times. In the real operations, the formal solution is expected.

In this case, there is 5 MVar residual that will be removed in the discretization process. In the discretization process, only the shunt with the smallest size in each station is used in the calculations to remove the residuals. In this way, to avoid many shunts are touched and then reduce the redundant switching times. In the optimization framework, the cost of each controller that can represent several shunts in at a node should be estimated.

The variable shunt reactor is described in Chapter 4 Section 2.2.2, which is modelled as an ideal transformer connecting to a shunt in series. The tap can be adjusted to regulate the reactive power consumption and the breaker can be controlled to switch on/off the whole variable shunt. Therefore, for each variable shunt, there are two controllers in the optimization, i.e. the tap ratio and the shunt susceptance. In the continuous optimization, the shunt and the tap ratio are treated separately.

In the discretization process introduced in Chapter 4 Section 3.3, the tap ratio is related to the susceptance value in a variable shunt. The logic is defined to determine the tap positon w.r.t. the shunt susceptance, i.e. if the shunt susceptance is lower than a threshold, e.g. 0.3 of its rated value, then the tap ratio is set to minimum by equating the upper and the lower limits to the minimum value; if the shunt susceptance is higher than a threshold e.g. 0.7 of its rated value, then the tap ratio is treated as normal tap controller.

This definition is made to consider the operational requirements, i.e. the whole variable shunt can be switched off if the system requires no matter where the tap positon is, but the whole variable shunt can only be switched on when the tap is at the bottom to avoid the unexpected voltage jump and zero-missing problem.

The algorithm is presented in Table 20. In the optimizations during the discretization process, the algorithm is not able to count the regulation cost of the tap changes inside the variable shunts once the variables shunt susceptance is changed close to zero, as the tap ratio is manually set to the minimum as the susceptance is close to zero. Therefore, a post script is performed to assess the cost by counting the difference of the tap position between the initial value and the results after the discretization and multiplying the price of each tap change. It considers that the whole variable shunt is switched off as the susceptance changes below 0.3 of its rated value though the tap positon of the ideal transformer can be any value, the tap positon should be regulated down to the minimum offline to be ready for the reconnection, which also leads to the regulation cost.

Table 20. The algorithm for discretizing the variable shunts.

1	*Initialize the discretization*
2	*Check the errors of discrete variables*
3	*While errors > ε*
4	*Optimization with the penalty function in the objective function*
5	*If b of the variable shunt > 0.7 of its rated value*
6	*Lower/higher limit of τ of the variable shunt are set to its operational limits, respectively*
7	*End*
8	*If b of the variable shunt < 0.3 of its rated value*
9	*τ of the variable shunt are set to its minimum limits*
10	*Lower/higher limit of τ of the variable shunt are identically set to its minimum limits*
11	*End*
12	*Increase the penalty factor*
13	*Check the errors of discrete variables*
14	*end*

In the optimization, it can be seen that switching off a variable shunt is modelled as zero susceptance shunt connecting to an ideal transformer with minimum tap ratio. In this way to avoid the topological changes after switching off the variable shunt. It simplifies the problem in the MORPF framework, where the variable shunt could be switching on and off in different stages in a MORPF execution. Be notice that, the impedance of the ideal transformer in the pre-processing is set to the defined minimum values. However, the impact of these changes is negligible.

6.3. FINITE DIFFERENCE

Many optimization solvers can estimate the gradients and the hessian, e.g. *fmincon* in Matlab, through the finite difference methods [64]. For large scale system, where many constraints are involved, these approaches are slow, as they estimate the gradient and hessian for each function respected to each decision variable to fill in the large matrices. Therefore, these methods are not recommended to solve the large scale system optimization. However, they can be used to validate the analytical gradients and hessians in the programming implementation process.

The concept of the finite difference is to estimate the gradient function, $\nabla f(x)$, when the variable, x, is subjected to a small change, Δ, as shown in (5.44) the central difference approach [64].

$$\nabla f(x) = \lim_{\Delta \to 0} \frac{f\left(x + \frac{1}{2}\Delta\right) - f\left(x - \frac{1}{2}\Delta\right)}{\Delta} \tag{5.44}$$

In the programming, the validations of the analytical gradients and the hessians are carried out step by step, e.g. firstly validate the gradients through (5.44), and then substituting the analytical gradients to (5.44) again for validating the hessian matrices. The change, Δ, should be small, e.g. $1e-5$, by which the nonlinear functions are close to the linear functions. The differences between the numerical estimations and the analytical calculations should be lower than an acceptable threshold, i.e. $1e-5$. However, it also depends on the system nonlinearity and the system complexity, which can sometimes result in a relatively larger mismatch, e.g. higher than $1e-5$ but lower than $1e-4$. The accuracy of the gradients has significantly impacts on the calculation performance. In contrast, the hessian matrices are allowed to have larger mismatch. In fact, the hessian matrix is always adapted in the searching process of the numerical optimization algorithms, to approximate the original system to the convex system for solving the approximated problem [64].

6.4. INTEGRATION TO THE FORECASTING SYSTEM

In the MORPF framework, the forecasting system is intended to be integrated to provide the predicted short term load flow conditions. In Chapter 4 Section 6, the multivariate normal distribution model is proposed to approximate the statistic characteristic of the WPFE in the distribution network, where the covariance matrix is used to capture the WPFE spatio-temporal dependency.

The multivariate normal distribution model of the WPFE is therefore applied to estimate the VSM to cover the possible voltage variation due to the WPFE in the AVC system. It needs to project the WPFE in each predefined zone to the voltage variations at each node in the transmission level. This is carried out by *affine transformation* that is also a linear transformation, i.e. scaling the WPFE through the load flow sensitivity matrices to obtain the voltage variations, assuming wind power nodes at the same predefined zone are fully correlated. The sensitivity matrices of the voltage respected to the power injection can be found through the load flow equations, as described in Chapter 4 Section 6.1. The wind power covariance matrix is needed from the forecasting system, e.g. found from the historical observations.

In the simulation platform, the historical WPFE data is gathered to find the spatio-temporal covariance matrix for the wind power forecasting zones. The covariance matrix is therefore converted to voltage covariance matrix for the system nodes to which the wind turbines are connected. The covariance matrix can be updated hourly or daily depending on the performance of the wind power forecasting system.

7. EXAMPLE

A simple example is used to demonstrate the calculation process. The single line diagram of a modified 9-bus system is shown in Figure 58. The relevant data is presented in Table 21 to Table 26.
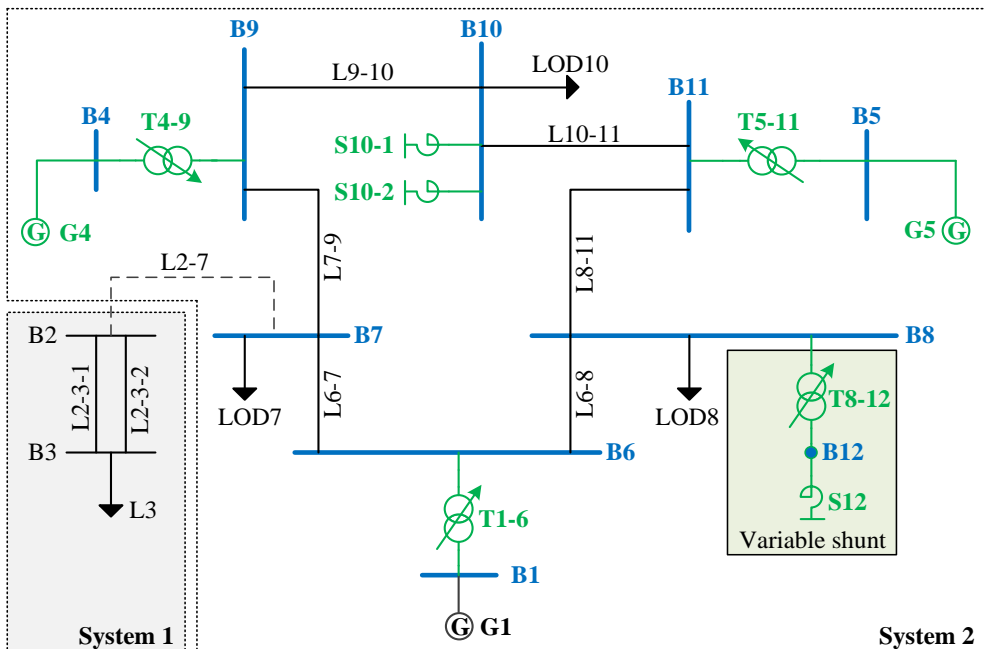

Figure 58. The test system. The line L2-7 is out of service.

Table 21. The node dataset.

Node	Type	V_{min}	V_{max}
1	Slack	1.02	
2	PQ	1.05	0.95
3	PQ	1.05	0.95
4	PV	1.05	0.95
5	PV	1.05	0.95
6	PQ	1.05	0.95
7	PQ	1.05	0.95
8	PQ	1.05	0.95
9	PQ	1.05	0.95
10	PQ	1.05	0.95
11	PQ	1.05	0.95
12	PQ	None	None

The voltage magnitude should be within the acceptable operational band. In this study, as shown in Table 21, it is between 0.95 p.u. to 1.05 p.u. for the PQ and PV nodes. The voltage magnitude is constant at Slack node, which is able to be varied if the reactive power output of the slack machine is also assigned as controller. The variable shunt comprises of an ideal tap-able transformer, T8-12, and a shunt, S12, in Figure 58. The internal junction point B12 in Figure 58 is without any voltage magnitude limit, as the voltage at B12 can vary from about 1 pu. to 0.7 pu. to vary the reactive power consumption, as described in Chapter 4, Section 2.2.2.

The reactive power output of G4 and G5 are control variables, the limits of which are typically referred to the regulation capability curve, i.e. for a certain active power production, the reactive power output limits are also determined correspondingly. As shown in Table 22, the generator G4 and G5 reactive power outputs are defined as **control variables**. The initial values before the optimization are presented. The estimated cost of the generator reactive power is assumed to be 0.1 DKK/MVar.

Table 22. The generator dataset except the slack machine.

Name	Node	P (MW)	Q_g (MVar)	Q_{min} (MVar)	Q_{max} (MVar)	Cost (DKK/MVar)
G4	4	163	105.4	-192	192	0.1
G5	5	85	85.3	-128	128	0.1

The required shunt data is presented in Table 23. There are two shunt banks connected to B10 and a shunt connected to B12. In the optimization, the shunts are further aggregated at each node. The susceptance is converted to the reactive power by multiplying the square of the nominal voltage. In the per unit system, the nominal voltage is typically set to unity. Then the value of the susceptance is identical to the reactive power injection. The cost of switching shunt is approximated by using the linear function, i.e. covert to the expense for the reactive power consumption, as shown in Table 23. The actual step of each individual shunt is found through the pre-defined rule as introduced in Chapter 5, Section 6.2.

Table 23. Switchable shunt dataset.

Node	Total steps	b/step (MVar)	Actual step	b (MVar)	b_{min} (MVar)	b_{max} (MVar)	Cost (DKK/MVar)
10	5	-20	5	-190	-190	0	0.2
10	3	-30	3				
12	1	-100	1	-100	-100	0	0.1

The transmission line and the transformer are collected in the branch dataset, converted to the per unit values, shown in Table 24. As described in [89], the general branch model is applied to the transmission line and the transformer, where the ideal transformer tap changer is placed at the branch sending end. The tap ratio is under control where the actual tap potion is not typically determined,

whereas the numbers of tap position changes are needed. Therefore, the initial tap positon is set to zero, and the maximum and the minimum tap positions are converted through (5.6)-(5.7) accordingly. The optimization will find out the optimal tap ratio that is finally converted to the changes of the tap position for dispatching. The tap changing cost is also approximated by the linear function, as described in Chapter 4 Section 4.1.2. The corresponding shunt switching cost and the tap regulation costs are also presented in Table 24.

Table 24. Branch dataset. Base power is 100 MVA.

Node f	Node t	R (pu.)	X (pu.)	B (pu.)	τ	τ_{min}	τ_{max}	$\Delta\tau/T$	T	T_{min}	T_{max}	Cost (DKK/τ)
6	1	1E-07	0.0576	0	1	0.8	1.2	0.02	0	-10	10	50
9	4	1E-07	0.0625	0	1	0.8	1.2	0.02	0	-10	10	50
11	5	1E-07	0.0586	0	1	0.8	1.2	0.02	0	-10	10	50
12	8	1E-07	1E-05	0	1.48	1	1.48	0.02	0	-24	0	50
6	7	0.010	0.085	0.176								
6	8	0.017	0.092	0.158								
7	9	0.032	0.161	0.306								
8	11	0.039	0.170	0.358								
9	10	0.009	0.072	0.149								
10	11	0.012	0.101	0.209								

Table 25. The summarized regulation costs and the grid loss price.

Element	Cost
Generators	0.1 DKK/MVar
Transformer taps	1 DKK/time
Shunt breakers	4-6 DKK/step
Grid loss	100 DKK/MW

The power balance is continuously changing. In this study, the loads and generations vary in the specified 3 stages, as shown in Table 26. This is an assumption without considering the power factor limits at the component terminals. Assuming the two generators, G4 and G5, are wind turbines, and the wind power forecasting errors in the 3 stages comply with the multivariate normal distribution, as shown in Figure 59, where the spatio-temporal correlation is shown. The temporal correlation is stronger than the spatio correlation in Figure 59, which comply with the general observations as presented in Figure 43 and Figure 44 for the historical data.

Table 26. The power injection change along the time.

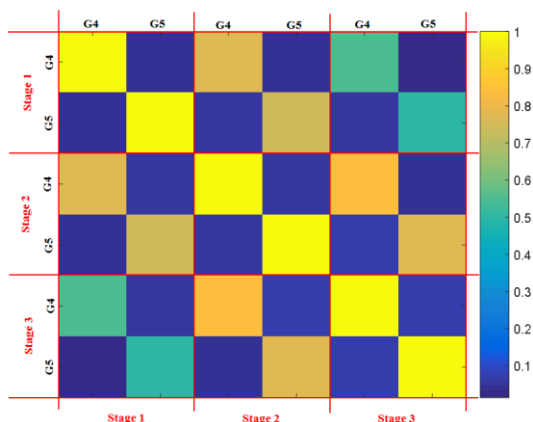| Stage	1		2		3	
Element	P (MW)	Q (MVar)	P (MW)	Q (MVar)	P (MW)	Q (MVar)
G4	163		100		250	
G5	85		100		150	
L7	125	50	50	5	300	100
L8	90	-100	50	-10	200	-100
L10	100	35	50	10	250	-150

Figure 59. The correlation matric of G4 and G5 in the test case.

7.1. SIMULATION RESULTS

As shown in Figure 58, the transmission line L2-7 is out of service, which splits the system to two subsystems, i.e. System 1 and System 2. The study system is System 2. There are nodes that are not connected with any generator in System 1. In this case, it is easy to exclude the irrelevant nodes in System 1 by manually check. However, in large scale systems, the irrelevant nodes are not able to directly targeted, which requires some techniques to filter them out, e.g. Brainy's tree sorting method.

These irrelevant nodes are filtered out through the pre-processing, described in Chapter 5 Section 3. The connection matrices before and after the pre-processing are shown in Table 27 and Table 28, respectively. It is to clearly identify two sub systems, where the irrelevant system is easily to be filtered out.

Table 27. The connection matrix before the pre-processing.

		Node											
		1	2	3	4	5	6	7	8	9	10	11	12
Branch	L2-3-1		1	1									
	L2-3-2		1	1									
	L6-7						1	1					
	L6-8						1		1				
	L7-9							1		1			
	L8-11								1			1	
	L9-10									1	1		
	L10-11										1	1	
	T1-6	1					1						
	T4-9				1					1			
	T5-11					1						1	
	T8-10								1				1

Table 28. The connection matrix after the pre-processing.

	Node											
	1	2	3	4	5	6	7	8	9	10	11	12
System 1		1	1									
System 2	1			1	1	1	1	1	1	1	1	1

The iterative calculation will stop if it is converged, i.e. both the feasibility and the optimality are lower than the defined small scalar, e.g. $1e - 5$ in this study. As shown in Figure 60, the value of the cost function reduces along the iterations until the calculation convergence.

- Results comparison

As shown in Figure 53, the continuous optimization is carried out and then the discretization process forces the discrete variables sufficiently close to the corresponding integers. As shown in Table 26, the load and generation change in the 3 sequential stages. Without any optimization, the total grid loss in this case is 34.25 MW. The possible regulations are carried out over the 3 stages, which results in the cost on the transformer taps and the reactive power output at generators. Considering the predefined prices for each element, the total operational cost is 3484.9 kr in Table 29. This is considered as the reference case.

In this study, MORPF involves 3 stages to minimize the system operational cost over the period covering the 3 stages. In contrast, the ORPF minimizes the operational cost for each stage individually. In both cases, the total operational cost is reduced comparing to the reference case. The saving comes from the reduction of the grid loss. In return, the regulation costs in both cases are higher than the reference case. However, the grid loss has higher price than the controllers, which results in the less total operational cost than the cases without optimizations.

In Table 29, MORPF provides a better solution than ORPF, in terms of the grid loss reduction and limitation of the regulation cost. The saving of the regulation cost in MORPF is mainly from the reduced numbers of tap changes, as marked in Table 29.
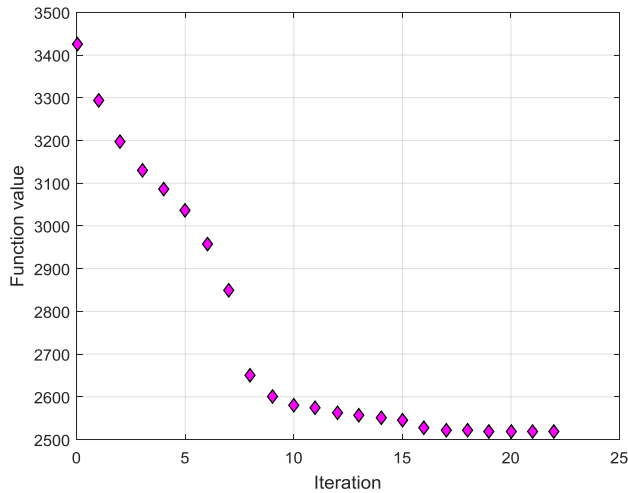
Figure 60. The value of the MORPF cost function respected to the iterations without discretization.

The variable shunt, i.e. T8-12 connected to S12, is entirely switched off at Stage 2 and not reconnected at Stage 3 in the MORPF case whereas it is disconnected at Stage 1 and reconnected at Stage 3 in the ORPF case. The operation requires that the variable shunt should always be switched in from the smallest reactive power consumption to avoid the unexpected voltage jump, but it can be switched off no matter what the tap position is. This variable shunt is cut off in MORPF case that results 19 tap changes to set the tap position to the bottom for reconnection. If disregarding this operational requirement, then more saving from the variable shunt adjustment in MORPF case than ORPF case can be expected.

Table 29. Simulation results.

	Stage	1		2		3		Total		Price	Cost (kr.)	Total cost (kr.)	
	Loss without Optimization	8.55		8.01		17.69		34.25		100	3425	**3425**	3484.9
	Total regulation cost										59.9	**59.5**	
MORPF (3 stages)	Loss (MW)	5.42		4.08		16.04		25.54		100	2554	**2554**	2625.4
	G4 (MVar)	28.70		-23.41		46.94		99.05		0.1	9.9		
	G5 (MVar)	5.05		-52.92		-20.99		78.96		0.1	7.9		
	T1-6 (ΔT)	1		-1		5		7		1	**7**		
	T4-9 (ΔT)	1		0		0		1		1	**1**		
	T5-11 (ΔT)	1		0		0		1		1	**1**	**71.4**	
	T8-12 (ΔT)	-5		-19		0		24		1	24		
	S10-1 ($\Delta step\|\Delta b$)	-3	190	0	0	2	120	5	310	0.2	0.62		
	S10-2 ($\Delta step\|\Delta b$)	-5		0		3		8					
	S12 ($\Delta step\|\Delta b$)	0	0	-1	100	1	100	2	200	0.1	20		
ORPF (Single stage)	Loss (MW)	5.72		3.98		16.08		25.78		100	2578	**2578**	2674.5
	G4 (MVar)	77.00		-26.70		47.50		151.20		0.1	15.1		
	G5 (MVar)	-60.90		-37.50		-19.70		118.10		0.1	11.8		
	T1-6 (ΔT)	-3		2		6		11		1	**11**		
	T4-9 (ΔT)	1		0		0		1		1	**1**		
	T5-11 (ΔT)	-6		5		1		12		1	**12**	**96.5**	
	T8-12 (ΔT)	-24		0		1		25		1	25		
	S10-1 ($\Delta step\|\Delta b$)	-3	190	0	100	2	120	5	310	0.2	0.62		
	S10-2 ($\Delta step\|\Delta b$)	-5		0		3		8					
	S12 ($\Delta step\|\Delta b$)	0	0	-1	100	1	100	2	200	0.1	20		

In Table 29, the tap position can freely vary in the capability range. If considering the response time of the tap changer per tap, then the tap ratio controller should be further constrained in the optimization. It can result in more operational cost, as the grid loss is increased due to the limited regulation capability of the tap changer. If increasing the price of the generator reactive power output, it can also lead to increased total operational cost. The systematic assessments are carried out in Chapter 6 based on the western Danish power system.

- MORPF with VSM

The VSM is obtained through the proposed method, i.e. converted from the given covariance of the forecasting errors to the voltage variations at each node connected with the wind turbines. In this study, the distribution of the forecasting errors of each generator at each stage is presented in Figure 64, where the correlation is captured in the covariance matrix, Figure 59. The results are therefore updated to reserve the VSM at each stage. As shown in Figure 62, the minimum and the maximum voltage magnitudes in the system with different power injections at G4 and G5 due to the forecasting errors are summarized. No voltage violation occurs with VSM after validation by Monte Carlo simulations employing 1000 samples generated from NORTA, e.g. shown in Figure 61. The acceptable voltage magnitudes bands for all the PQ and PV nodes are narrowed to reserve the VSM. However, the grid loss increases as shown in Figure 63. The increased grid loss cost is acceptable in this case.

- Conclusion

The study case demonstrates the calculation procedure of the offline simulation platform. It can systematically perform the optimization to simulate the decision making process of the AVC system. Different constraints can be considered. In this study, MORPF is verified superior to the ORPF in terms of the cost minimization, by considering the forecasting load flow conditions in the upcoming stages. The forecasting errors are approximately represented by the multivariate normal distribution, where the covariance matrix is used to capture the spatio-temporal dependency. The overall solution robustness is therefore improved, though the extra operational cost is introduced.

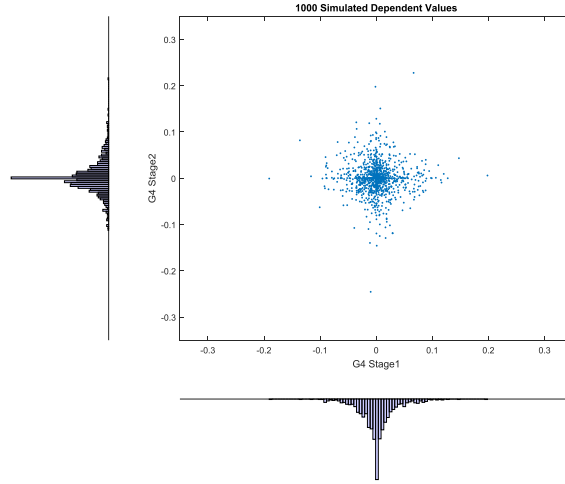*Figure 61.1000 Samples of forecasting errors of G4 at Stage 1 and Stage 2 for Monte Carlo simulations, generated from NORTA.*
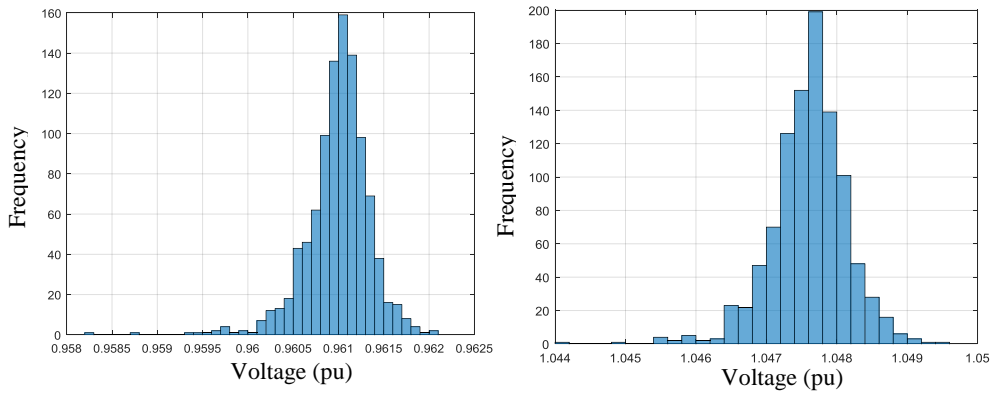

Figure 62. The histogram of the resulted minimum and maximum voltage at Stage 1 for 1000 samples with VSM in the MORPF.
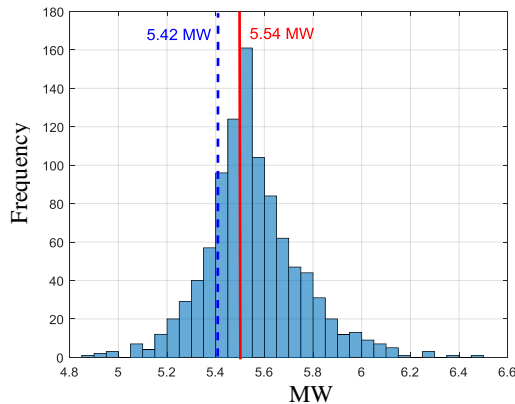

Figure 63. The histogram of the grid loss of the 1000 samples at Stage 1, with and without VSM.
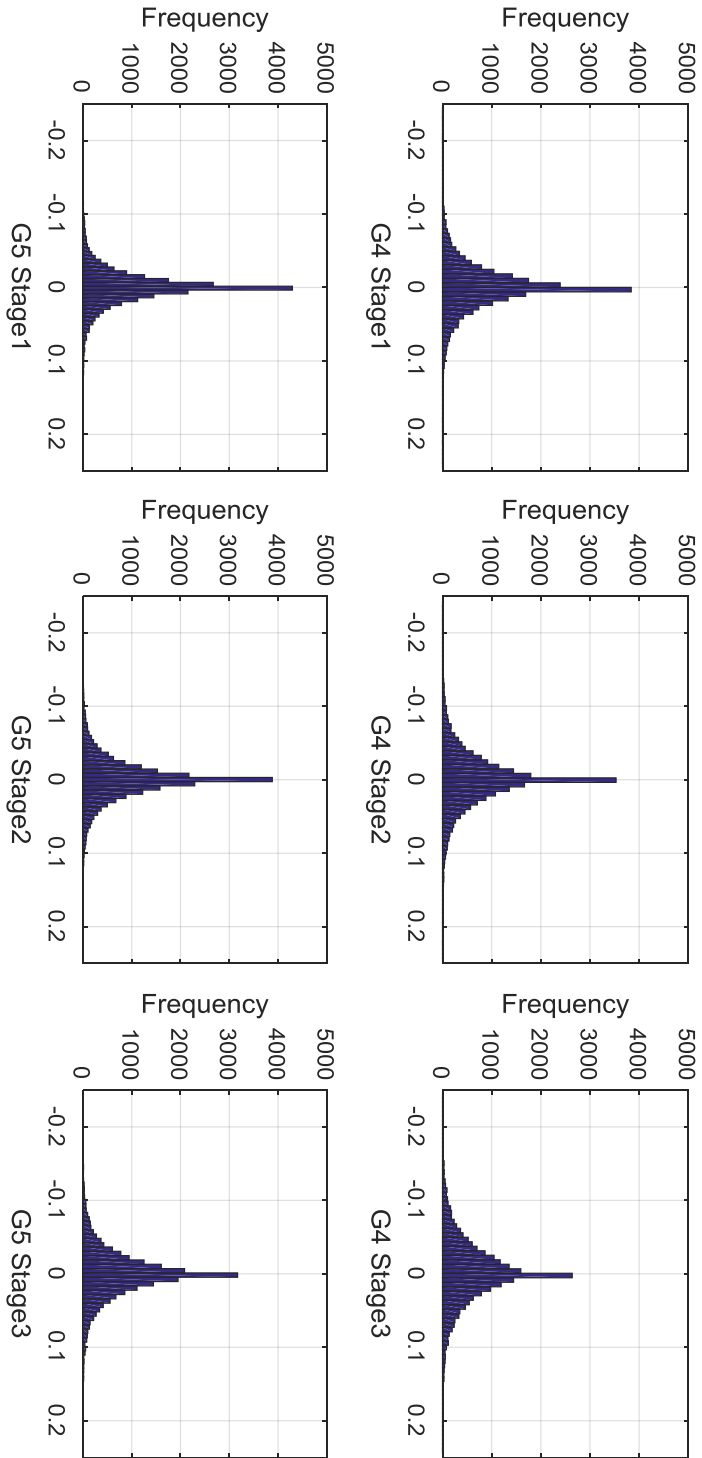
Figure 64. The forecasting errors distribution for G4 and G5 at Stage 1 to 3.

8. SUMMARY

In this chapter, the detailed implementation of the proposed AVC decision making algorithm is introduced. In order to assess the proposed AVC for the Danish transmission system, the offline simulation platform is built and presented in Figure 53. It imports the EMS measurement data and the forecasting data that are stored in the RAW format, and perform the proposed optimizations for the AVC system. In order to avoid the matrix singularity in the load flow and the ORPF calculations: (i). remove the isolated nodes using Brainy's tree sorting method; (ii). insert the defined minimum impedance values in the "zero-impedance" branches; (iii). deactivate the irrelevant models for the calculations; (iv). aggregate the parallel branches and thus the controllers to build the node-branch model. The load flow is then performed to obtain the system initial information, such as the grid loss and the maximum voltage magnitude etc. The load flow can be solved either by NR method or HELM that are described in Chapter 2.

The PDIPM is applied to solve the MORPF problem. All discrete variables are firstly treated as continuous variables, and then discretized via the penalty function. The analytical gradients and hessian matrices are needed to accurately and efficiently solve both the continuous optimization problem and the discretization problem. The finite differences method can be used to validate the analytical representations in the programming implementation phase.

The sinusoidal penalty function is applied for discretization, which gradually force the discrete variables close to the integers. The status of the variables shunts is determined during the discretization process, where the tap position is a function of the susceptance.

If improving the solution robustness, then the VSM is estimated with given covariance matrix of the forecasting errors after the optimization is converged. The optimal solutions are therefore updated by performing the optimization again including the VSM in the voltage magnitude constraints. In this way, the sensitivity based approach can well estimate the voltage variations caused by the WPFE, as WPFE is minor as required.

In the case of executing a number of optimizations, the platform is able to systematically read the data, processing the data and find out the solution automatically. If a series of simulations are performed, then these setpoints are fed into the upcoming stages as the initial values of the control variables. In some cases, the calculation may not be converged, and no setpoints are available. The recalculation may therefore be needed, e.g. freely set the setpoints in their feasibility ranges as the new initial guess to start the searching process.

During the simulations, the platform continually stores the calculation results in external files. The specific information in the documentation is presented in Appendix D – Report.

A modified 9-bus system is used to demonstrate the calculations, which verifies that the MORPF is able to provide better solution on the cost reduction. The voltage security is improved by reserving the VSM in the voltage magnitude constraints. The voltage magnitude after realizing the controller setpoints are without any violation in the Monte Carlo simulations in this study. The expected loss is increased as a consequence due to the reduced acceptable voltage band.

CHAPTER 6. CASE STUDY ON THE WESTERN DANISH POWER SYSTEM

The installed wind power capacity in Denmark is doubled since 2400 MW in 2000 to 5000 MW by 2015. The electricity market is considered to be an essential tool to integrate such a large amount of wind power. It provides a common platform for all market players to balance the system including the fluctuated wind power. In addition, it balances the production and consumption over large geographic zones, e.g. using the hydro power in Norway as storage to compensate the intermittence of the Danish wind power via the market. The power flow in the Danish system is therefore very flexible, where the transits in the main corridors can change significantly and even reverse the flow direction within few hours. The electricity price varies to reflect the balance of the production and consumption. The voltage control system under these conditions to minimize the operational cost, may not really reduce the total operational cost, as the price of the grid loss can be very small or even negative while the reactive power component regulation costs are constant from the estimations. It means that the optimum depends on the energy price in each hour that affects the reactive power delivered from the continuous and discrete reactive power components.

In the current Danish system, the reactive power regulation capability of large offshore wind farms is not applied to control the system voltage. These wind farms connect to the onshore transmission grid over long cables. The voltage control ability is therefore limited by these long cables [90]. If the wind turbines are Type I, i.e. the asynchronous generator directly connects to the grid, then continuous reactive power component such as SVC, may be needed onshore to regulate the reactive power according to the intermittent wind power production for smoothing the voltage. The modern wind farms, constructed with Type III or Type IV wind turbines, i.e. the power electronic device based wind turbines, are capable of fast regulating the reactive power output to control the system voltage. For such modern wind farms, reactor banks may be placed onshore to compensate the cables according to the loading, while the wind turbines can help to maintain the voltage offshore.

As the central power plants are gradually decommissioning, the utilization of the reactive power from the large offshore wind farms regained attention. They are expected to participate in the coordinated voltage control system to enhance the overall system control ability. The barrier lies on the price for this ancillary service provided by the wind farms if no grid code mandatorily requires the wind farms to contribute to the voltage control in the normal operation conditions.

Since the proposed AVC decision making algorithm does include the generator operation cost in the objective function, the assessment for employing the wind farms in the voltage control system to minimize the total operational cost can be carried out. As described in Chapter 4 Section 3.1, the objective is formulated to minimize the total system operational cost including the grid loss cost and the regulation cost. All costs are converted in terms of expense value, where the electricity market price is associated to the grid loss and the regulation cost for each component is estimated.

In this chapter, the developed simulation tool is applied to the western Danish transmission grid, DK1, for assessing the potential benefits from having AVC system with the proposed decision making process. The investigations are carried out step by step, from the conventional ORPF based algorithm to the proposed MORPF algorithm.

1. SIMULATION SETUP

The western Danish transmission system (DK1) is presented in Figure 65. It comprises of 400kV, 220kV and 150 kV grids. The distributed generation units, e.g. the wind turbines and the CHPs aggregated to the closest 60 kV stations that connect to the 150 kV station via aggregated

transformers. These aggregated transformers represent the estimated impedances between the unit terminals to the 150/60 kV transformers.

The conventional power plants are electrically close to each other. More information about these machines in the AVC system can be found in Table 30. The unit commitment of conventional power plants and large offshore wind farms highly depends on the market price.
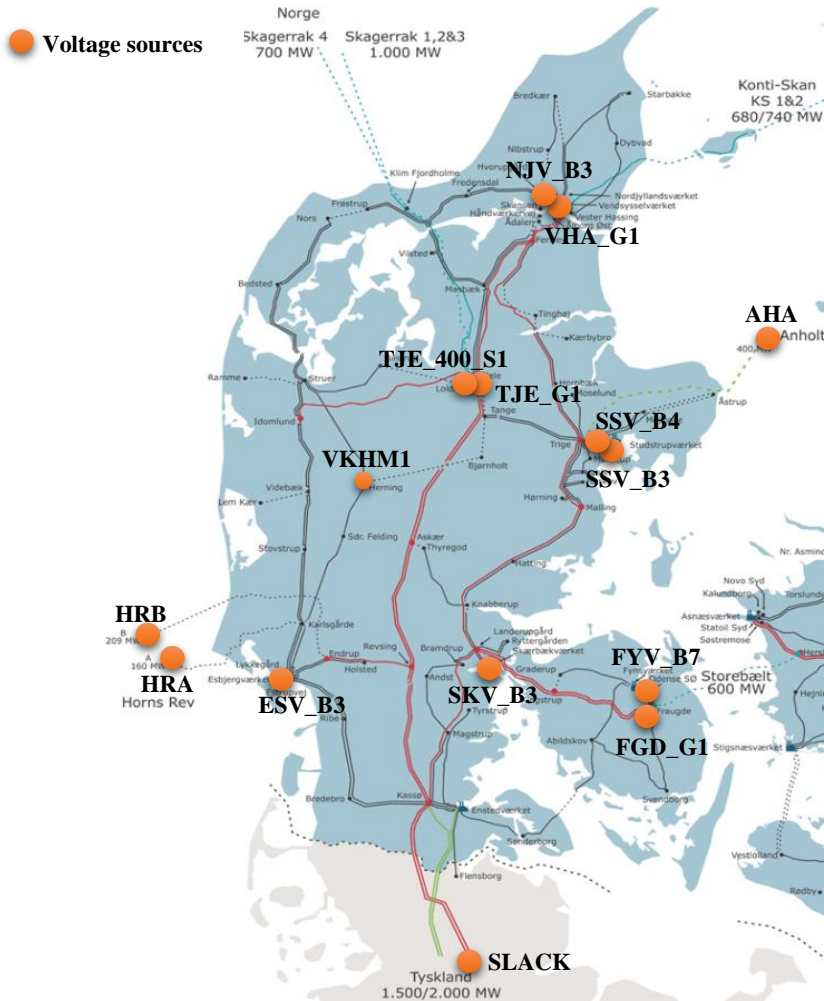
Figure 65. The DK1 system by the end of 2015.

The three large offshore wind farms, Horns Rev A (160 MW), Horns Rev B (209 MW) and Anholt (400 MW) are presented. There are 3 LCC-HVDC and 1 VSC-HVDC links connected to Norway with 1600 MW transfer capacity, 2 LCC-HVDC links connected to Sweden with 740 MW transfer capacity, 1 LCC-HVDC link connected to the eastern Danish power system with 600 MW transfer capacity. In the south, two 400 kV, two 220 kV and one 150 kV AC transmission lines connected to Germany, allowing 1500 MW import and 2000 MW export by the end of 2015.

The LCC-HVDC links are modelled as constant power and the VSC-HVDC link is modelled as a generator with limited reactive power regulation capability, connecting to the PV node. The large wind farms are modelled as generators connecting to the PV nodes. The reactive power regulation capability should refer to the active power production, which is defined as constants, i.e. +/- 30% of the maximum active power production in these studies.

Table 30. The modelled voltage sources of the western Danish transmission grid in the AVC system.

Name	Voltage (kV)	Min. Q (MVar)	Max. Q (MVar)	Type
AHA	400	-120	120	Wind farm
HRB	400	-63	63	
HRA	150	-48	48	
FYV_B7	400	-180	250	Power plant
NJV_B3		-185	290	
SKV_B3		-110	330	
SSV_B4		-110	230	
ESV_B3	150	-155	245	
SSV_B3		-110	230	
VKHM1		-20	28	
FGD_G1	400	-100	200	Synchronous condenser
TJE_G1	150	-30	160	
VHA_G1		-36	100	
TJE_400_S1	400	-85	85	VSC-HVDC
SLACK	400	None	None	Aggregated machine

The estimated cost of each regulatory is presented in Table 31. The cost for regulating the transformer tap is found by using the total cost including the capital cost and the maintenance cost over the maximum allowed regulation times over the lifetime[2]. In the optimization framework, it will be converted to the cost per off-nominal ratio. The cost of switching a shunt is found similar to the transformer tap cost, which is finally converted to the expense value per MVar.

As mentioned in Chapter 4, the generator cost can be counted as two parts, i.e. the loss in the circuit in (4.10) and the other cost counted in (4.16). Normally, the data of the generator internal cost is not valid for TSO. The observed loss measured from the HV side of the power plant is treated as other transmission branches, which is minimized by the AVC system. The cost for providing the reactive power to the grid is an estimated value and aggregated in (4.16) in terms of kr/MVar. In this study, assuming that the cost of the generator reactive power is varied from 0.0001 to 1 kr/MVar, where the actual price of the ancillary service should depend on the agreement between TSO and the power plant owners. The introduced physical cost on the step-up transformers is counted in (4.10) with the market price.

Table 31. The value ranges of the objectives in this study. 1€ = 7.5 kr DKK.

Objectives	Est. Price
Grid loss	Market price
Tap change	10 kr/tap
Shunt switching	1kr/MVar
Generator reactive power	0.0001 - 1 kr/MVar

---

[2] If considering the power transformer will anyhow be equipped with a tap changer, then the estimated regulation cost in the AVC system can be reduced by taking off the cost for the transformer itself. The capital cost may include the depreciate cost of the tap changer when the tap changer needs to be renewed due to wear.

The formulated optimization problem is subjected to a set of constraints, as described in Chapter 4 Section 3.2, where the voltage magnitude constrains in the transmission grids are presented in Table 32. In the real operations, the preferable voltage may be further limited to cover the measurement errors. However, it may introduce extra cost.

Table 32. The acceptable voltage band in the western Danish power system.

Voltage level (kV)	Maximum voltage (kV)	Minimum voltage (KV)
400	420	360
220	244	210
150	170	150

The measurement data from 2015 December 24th 00:00 – 2015 December 26th 23:45, are extracted from EMS system. The data represents the whole Danish transmission system snapshots in the addressed period with 15-minute intervals. As shown in Figure 66, the wind power is generally large in the studied period, and the production from other types is much lower than the wind power production. In some hours, the spot market price even becomes to the negative due to the excessive power production. In the study period, the flows in the main corridors change significantly, e.g. vary from exporting 1600 MW to Norway to importing 1000 MW from Norway, as shown in Figure 67.
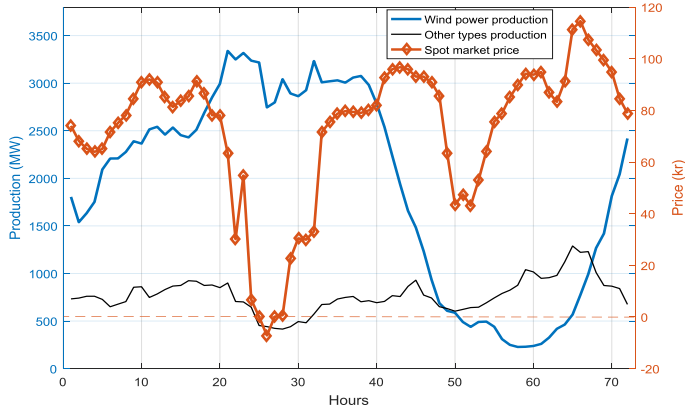

Figure 66. The wind power production and other type production in DK1 under the spot market price.
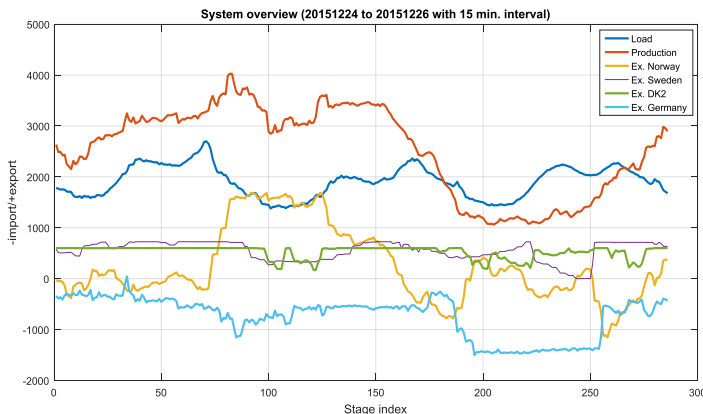

Figure 67. The load flow measurements extracted from EMS with 15-minute resolutions, i.e. 1 hour comprises of 4 stages.

Total 288 snapshots are extracted for the study cases. Each snapshot comprises of both DK1 and DK2 systems. As DK1 and DK2 are interconnected via a HVDC link, then the voltage control at each of them will not affect the other system. Therefore, the DK1 system is separated from each snapshot by using the load to represent the HVDC-link connected to DK2.

In many stages, the voltage magnitudes are slightly higher than the upper limits, which may due to the data transfer errors from the EMS to the offline platform. The stages with unrealistic large magnitudes in the load flow condition are therefore filtered out.

The simulation studies are performed on a computer with an Intel® Core i7-4600M dual 2.9 GHz processor and 16 GB RAM. The convergences tolerances are $1e-5$ for the nonlinear programming, PDIPM, and $1e-4$ for the discretization process, respectively. In the discretization process, the weight of the penalty function increases starting from $1e-4$, with the incremental rate 1.5. If the calculation is not able to be converged within 500 iterations for the PDIPM and 100 iterations for the discretization, respectively, then it is considered to be diverged.

2. LOSS MINIMIZATION

Loss minimization is widely applied in the conventional AVC system that focuses on minimizing the grid loss while maintaining the voltage. The conventional AVC is applied in the large scale systems, where the series branch loss dominates the total operational cost. The regulation cost comparing to the grid loss cost is minor. Therefore, the regulation cost is not considered in such AVC systems. Instead taking into account the detail regulation cost into the objective function, the switching times of shunts are always limited over a period to roughly limit the regulation cost of the shunts.

The study starts from assessing the potential saving from the loss minimization algorithm based on the prepared snapshots that are extracted from the EMS of the Danish control center and tailored to include only DK1. In the loss minimization algorithm, the generators, switchable shunts, variable shunts and the transformers are controlled without considering the introduced regulation cost. The objective of the loss minimization for each stage is presented in (4.13), where the price of the grid loss, λ, is set to unity.
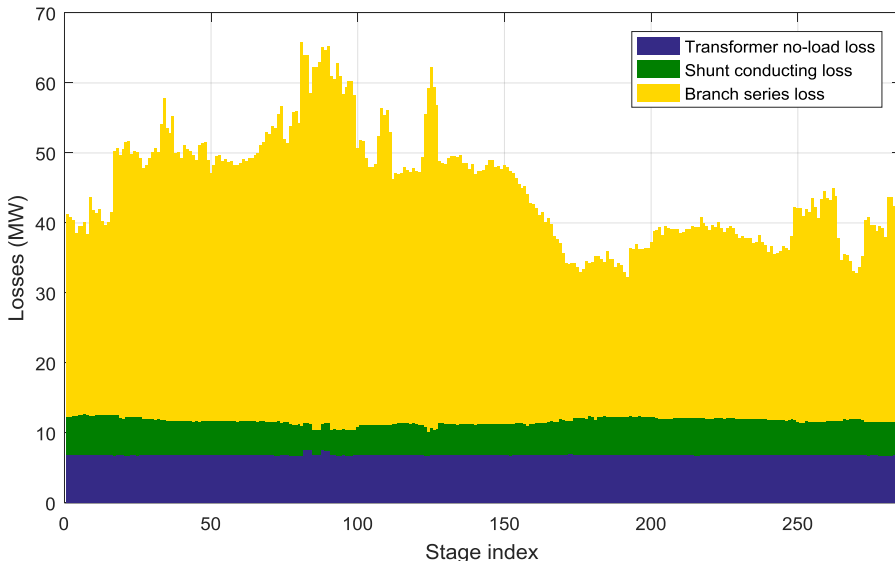
Figure 68. The grid loss composition without any optimization.

As described in Chapter 4 Section 3.1, the grid loss taking into account the objective function comprises of the series branch loss, the transformer no-load loss and the shunt conducting loss. As shown in Figure 68, the branch series loss is much larger than the other losses, which is strongly affected by the reactive power flow in the grid. The branch series loss includes the loss in both the transmission lines and the transformers. The transformer no-load loss is more or less constant, as it is only affected by the terminal voltage magnitude that typically varies insignificantly.
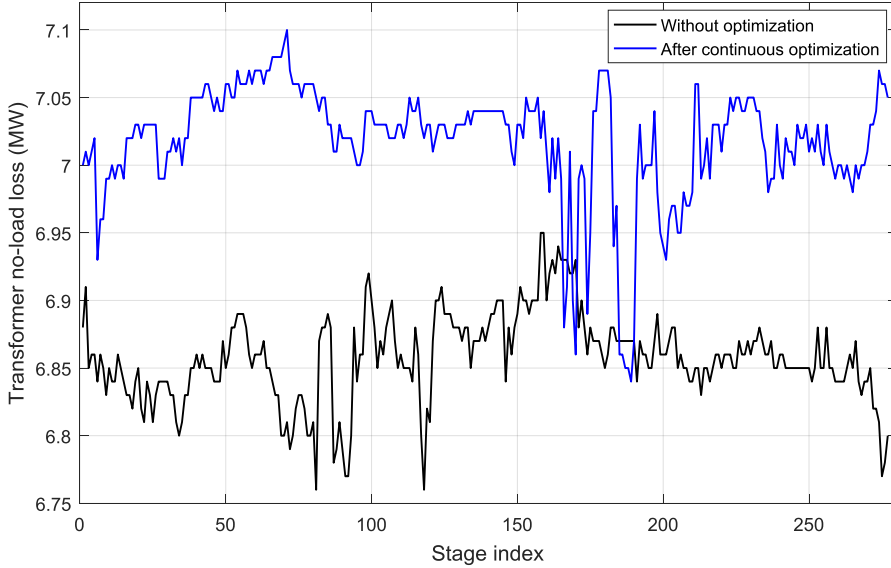
Figure 69. The transformer no-load loss before and after the continuous optimization.
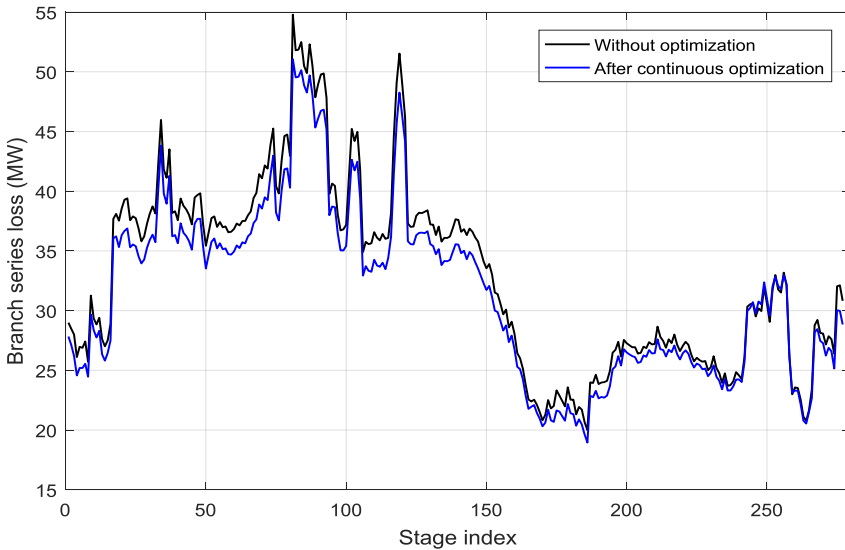
Figure 70. The branch series loss before and after the continuous optimization.
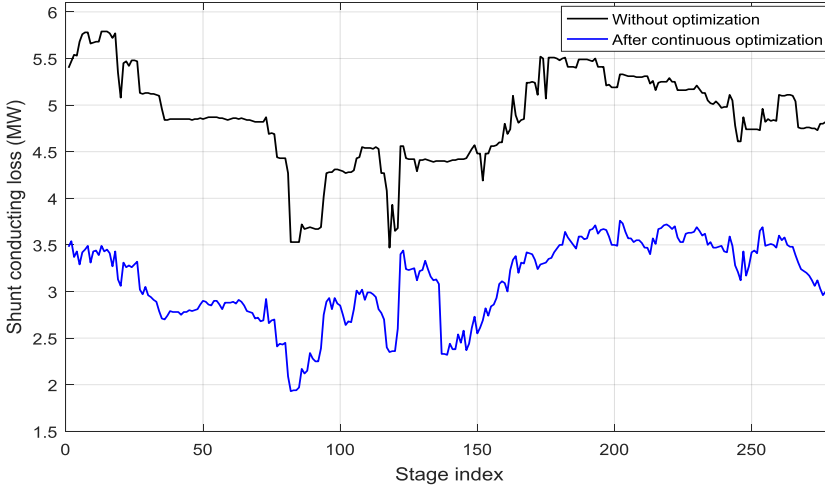
Figure 71. The shunt conducting loss before and after the continuous optimization.

Figure 69 to Figure 72 demonstrate the losses before and after the continuous optimizations on the involved snapshots. It can be seen from Figure 69 that the transformer no-load loss after the optimization is higher than the case without any optimization. It is due to the fact that the AVC regulates the reactive power components to raise the voltage profile in the system in order to reduce the branch series loss, as shown in Figure 70. The saved series branch loss is much larger than the increased transformer no-load loss due to the increased voltage profile. Moreover, the shunt conducting loss is reduced by switching off the shunts after the optimization, as shown in Figure 71. As described in Chapter 4 Section 3.3, the discretization applying the sinusoidal penalty function is performed to force the discrete variables to be close to the integer values. Therefore, the total grid loss is a little bit higher after discretization than the case only with the continuous optimization, as shown in Figure 72. However, the grid loss after the discretization process is still generally lower than the case without any optimization.
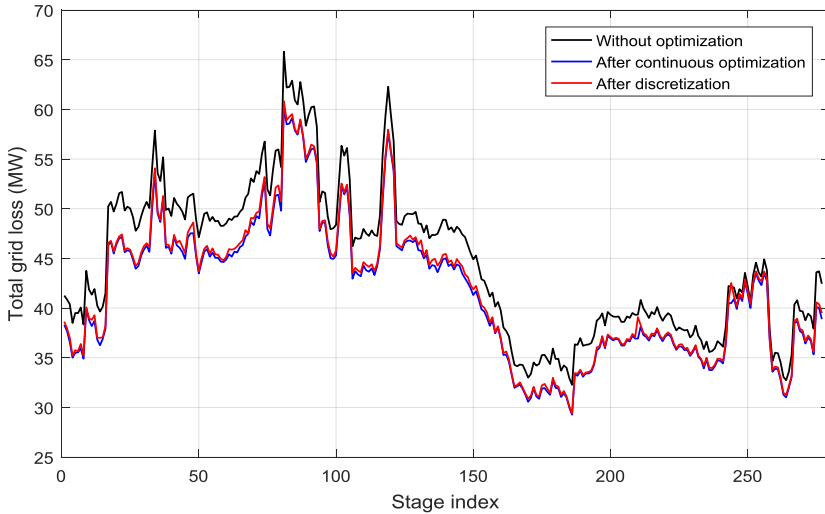
Figure 72. The total grid loss without optimization, after the continuous optimization and after the discretization.

In case 1, the AVC focuses on the grid loss saving, and uses all regulation capability to save the loss while maintaining the voltage in the acceptable band. As mentioned, the grid loss is typically purchased by the system operator. In Denmark, the price of the grid loss is referred to the zone price in the spot market. Therefore, the saved cost in the Danish krone after the optimization can be found with the spot market price that is shown in Figure 66. The converted results are presented in Figure 73. The saved loss introduces more cost than the case without the optimization, on the snapshots under the negative price period.
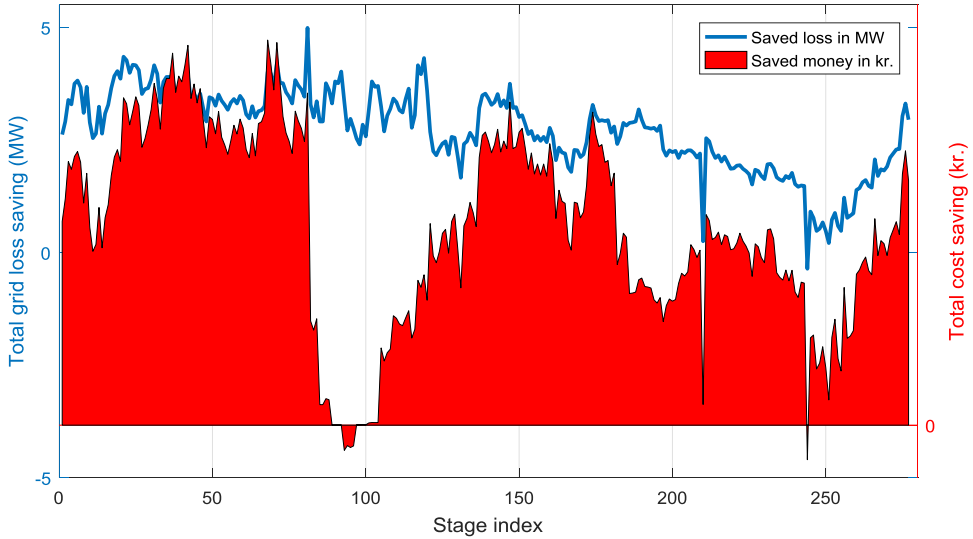
Figure 73. The saved loss in MW and the converted cost saving in Danish krone in Case 1.
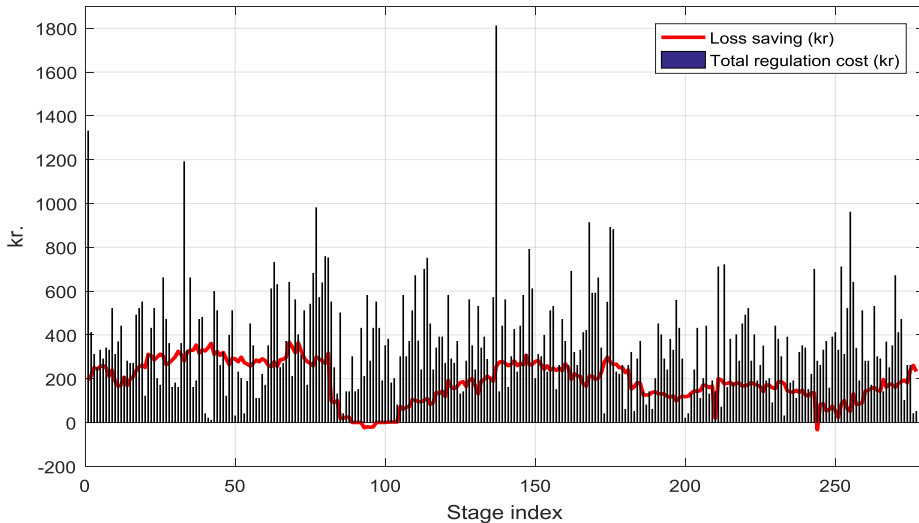
Figure 74. The saving against regulation cost after the loss minimization in Case 1.

In Figure 74, the regulation cost in the involved stages is summarized. The total regulation cost comprises of the transformer tap changing cost, the shunt switching cost and the generator reactive power cost. The price of regulating each type of component is presented in Table 31, where the generator reactive power output cost in this case is set to 0.0001 kr/MVar. It is assumed the generator cost is negligible. Therefore the regulation cost in Figure 74 is dominated by the cost on the discrete components. The generator reactive power output is nearly free to be regulated for grid loss saving. The total reactive power output after the optimization is shown in Figure 75. The average total reactive power outputs are about 450 MVar in this period.

From this case, it can be concluded that without considering the regulation cost the total operational cost is increased in the end. This is not expected to happen in the real system. Moreover, after the loss minimization, only the voltage profile is increased to close to the upper limits. The actual cost saving is much lower than the expected value without considering the price of the grid loss.
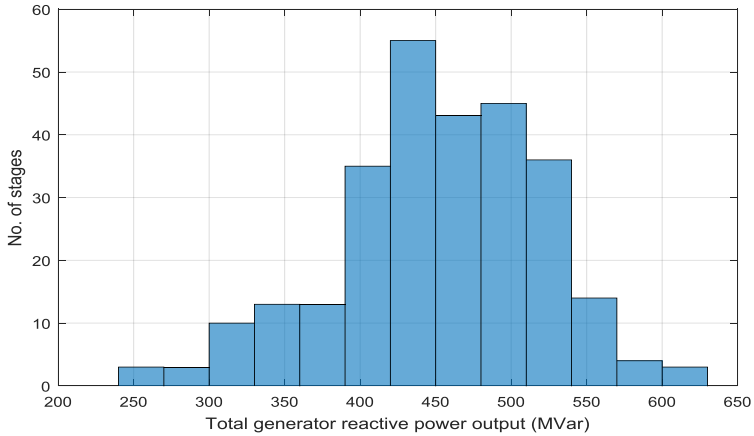
Figure 75. The total generator reactive power output after the optimization in Case 1.
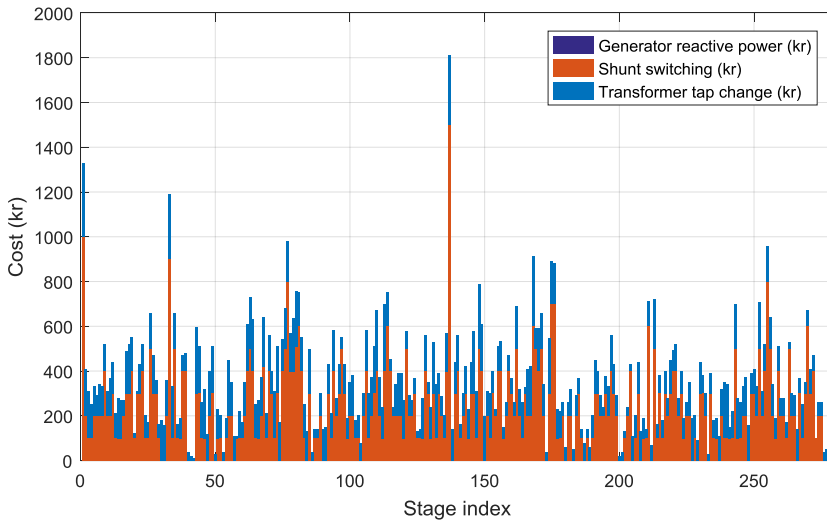
Figure 76. The regulation cost composition in Case 1.

If applying regulation price as shown in Table 31, where the generator reactive power is 0.0001 kr/MVar, then the regulation cost composition for the Case 1, loss minimization, is presented in Figure 76. It can be seen that, the generator reactive power cost is negligible. The shunt switching introduces the most regulation cost.

Case 1, loss minimization is considered to be the reference case. The results of the following cases will compare to the reference case for the demonstrations.

3.   COST MINIMIZATION

The spot market is cleared day-ahead for 24 hours in the next day. The hourly price can be found before the physical dispatch period when the AVC is operating. The found market price can be assigned as the weight to the grid loss in the objective function in the AVC decision making process, as presented in Chapter 4. If the price of regulating the reactive power components can be well estimated, like shown in Table 31, then the AVC can find precise operational cost for each snapshot. It provides clear information of the operational cost in the term of money to the system operators.

Figure 77 presents the updated calculation results with the sport market price and the estimated regulation cost as shown in Table 31, where the generator reactive power output is still set to 0.0001 kr/MVar, as the same in Case 1. The objective of the cost minimization is (4.13)-(4.16).
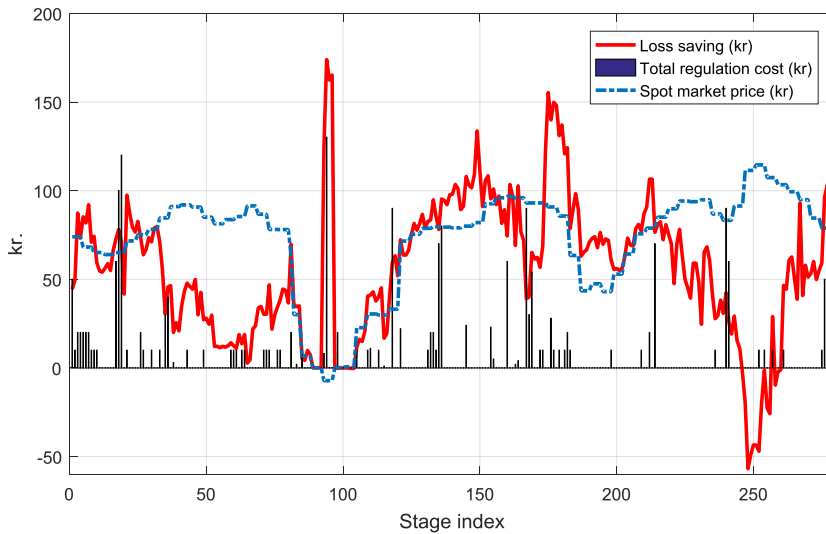
Figure 77. The saving against regulation cost after the cost minimization in Case 2.

The loss saving in Figure 77 after the cost minimization in this case can cover the regulation cost in most of the stages, even in the negative price period. The negative loss saving is due to the increased grid loss after the cost minimization. On the snapshots where the market price is negative, the AVC generates the grid loss in order to obtain the positive profit, as shown in in Figure 78. The regulation cost is dominated by the transformer tap changing cost, as shown in Figure 79, where the total regulation times on the shunts and the transformer taps higher than 10 times are only on 2 snapshots. The shunt switching occurs at Stage 148 in Figure 79. The number of the regulation times is lower than 5 in most of the stages. In all the involved stages, there is only one shunt switching in Case 2.
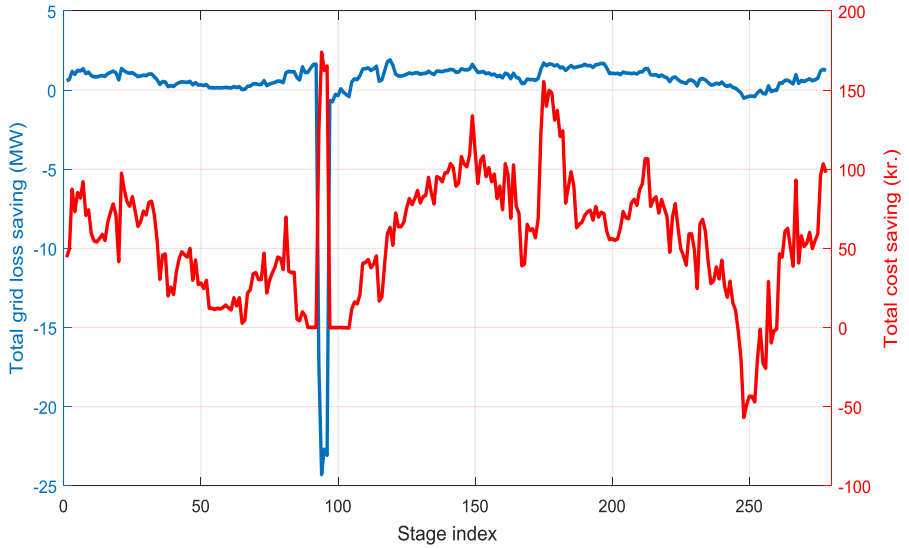
Figure 78. The actual grid loss saving and converted to the cost through the market price in Case 2.
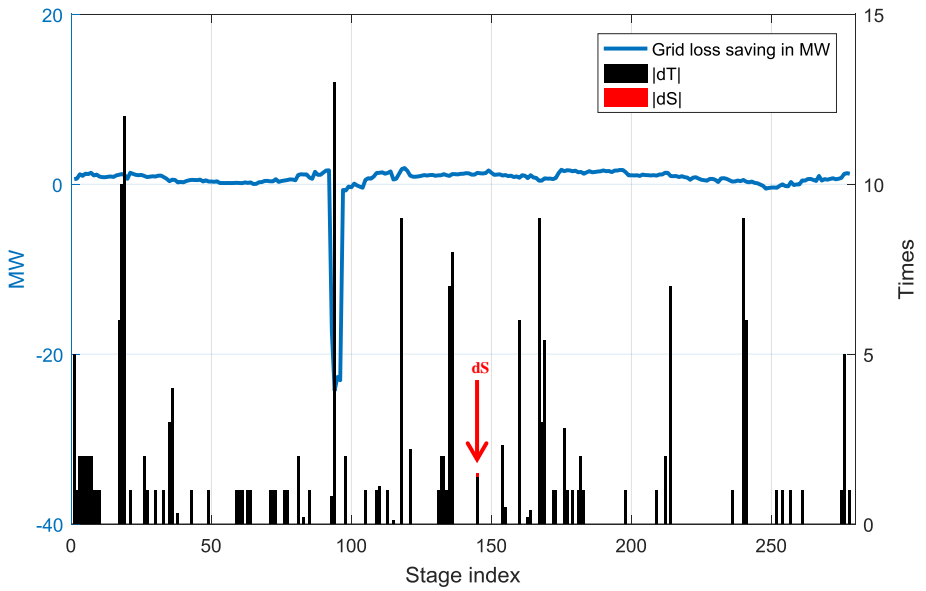
Figure 79. The regulation times of the discrete controllers in Case 2.
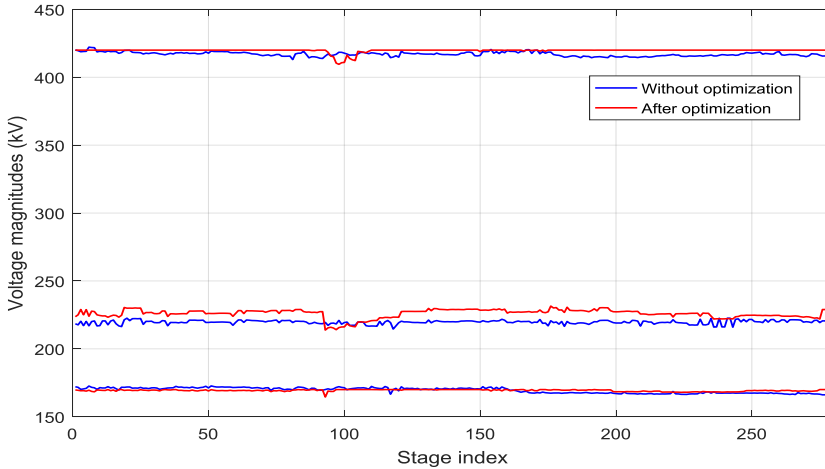
Figure 80. The maximum voltage of each stage in Case 2.
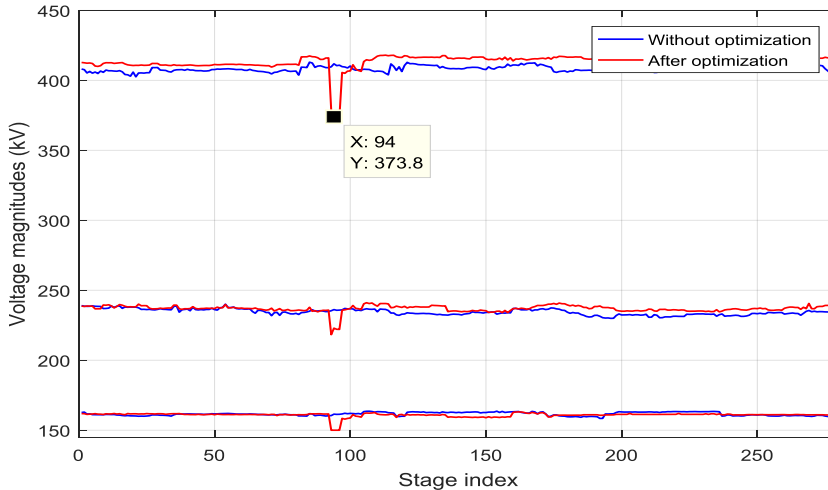
Figure 81. The minimum voltage of each stage in Case 2.

The voltage profile in Case 2 is presented in Figure 80 and Figure 81. During the negative price period, the AVC lowers down the system voltage in order to generate the grid loss. If this approach is implemented in the real system, it should be operated with carefulness. For the same amount of the voltage drop after a fault, it can increase the chance to trigger the under-voltage relay if the pre-fault voltage is low, e.g. the under-voltage relays of Danish Type I wind turbines trigger if the terminal voltage lowers than 0.7 p.u. for 500 ms, and many small scale CHPs in the Danish power system are equipped with the under voltage relays that disconnect the plants if the terminal voltage is lower than 0.7 pu for 50 ms. Therefore, the lower voltage magnitude limit at the busbar that located in the area where many such Type I wind turbines and CHP are connected, may be set to a higher value to avoid that the pre-fault voltage is too low when the market price is negative.

4. MORPF FOR THE COST MINIMIZATION

The wind power production fluctuates over the time. It brings the large variability into the system. In order to capture the wind power variability, the forecasting system is applied, as described in Chapter 4 Section 5. It is mainly to predict the power production in the upcoming days, which is able to foreseen the possible power balance. The AVC is used to optimally regulate the reactive power for controlling the voltage when the active power flow is determined. Therefore, if the predicted active power conditions in the upcoming stages are determined, the optimal reactive power flow calculations can be carried out. The objective for MORPF is presented in (4.33)-(4.44).

As mentioned in Chapter 4 Section 5, the Danish forecasting system can generate the predictions with 5-minute resolutions up to 10 hours. It means that the active power flow conditions for the upcoming stages can be obtained as well with 5-minute resolutions. If taking the system variability into account, the AVC should optimize the system for a period rather than a single instant. The predicted snapshots are therefore involved, which formulate the MORPF problem. The problem can be seen as the energy flow over a period that is discretized into several stages. Be aware that, MORPF based on the forecasting system is used to optimize the system considering the system variability. The case study of handling the forecasting errors composed uncertainty is described following.

Total 4 cases are carried out in this section, as shown in Table 33. MORPF are applied in Case 3 to Case 6, where the impact of different numbers of stages in each execution is studied. The data is originally extracted from EMS with 15-minute resolutions, which represents the system load flow conditions gathered from the SCADA system and SE. In order to perform MORPF at a time point, the future stages are assumed to be predicted stages out of the forecasting system. As described in Chapter 5 Section 5, MORPF will initialize the calculation by setting the same initial values to the control variables in all involved stages, though the load flow may be not converged in the upcoming stages after the initialization. MORPF will then search for the optimal solution and regain the convergence for all involved stages through the optimization routine.

All these cases employ the market price as the weight of the grid loss in the objective function. The regulation cost is taken into account. The cost function of each type of component is presented in Table 31. The cost of the generator reactive power is assumed to be negligible, 0.0001 kr/MVar. It is increased to 1 kr/MVar in Case 6 to force the generator reserving the reactive power.

Table 33. The study cases for MORPF.

Case ID	Market price	Regulation cost	No. of stages in MORPF	Gen. reactive power cost (DKK/MVar)
3	X	X	2	0.0001
4	X	X	3	0.0001
5	X	X	4	0.0001
6	X	X	4	1
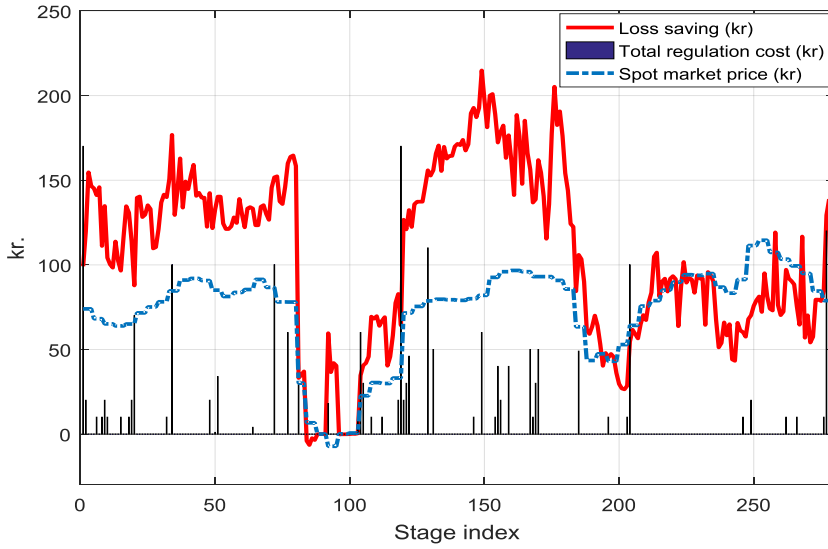
Figure 82. The saving against regulation cost after the cost minimization in Case 3.
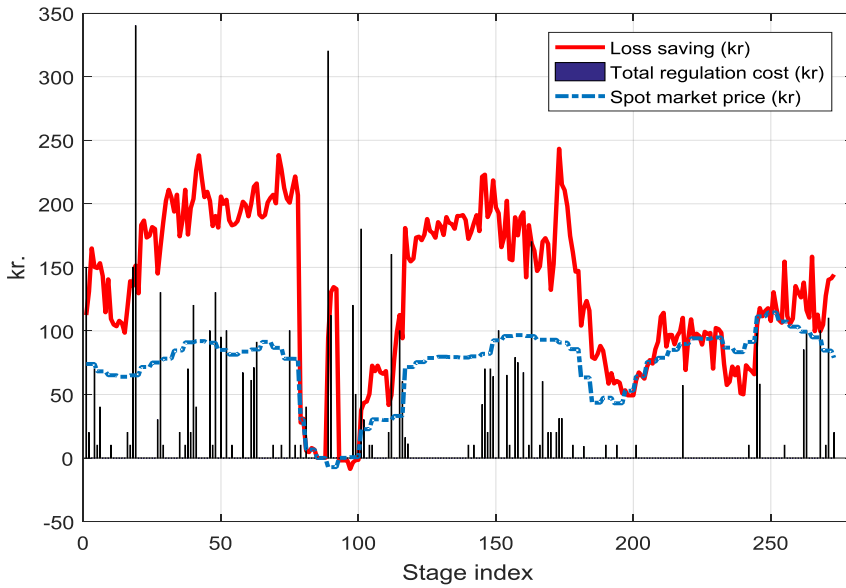
Figure 83. The saving against regulation cost after the cost minimization in Case 5.
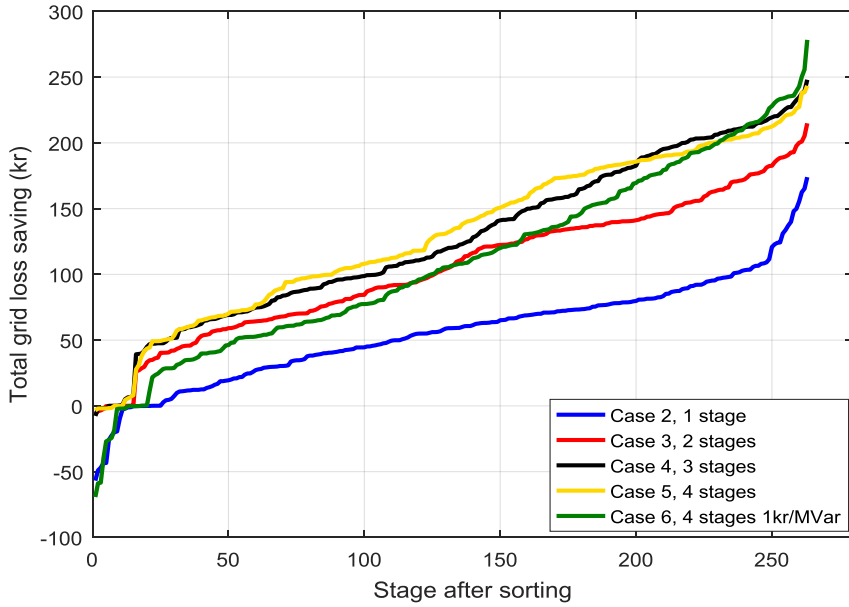
Figure 84. The grid loss saving comparisons of Case 2 to Case 6.
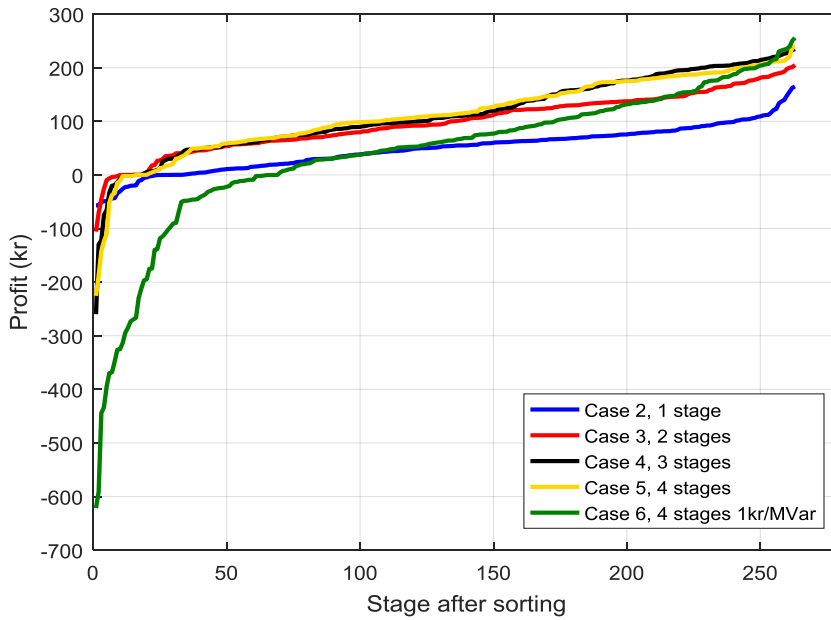
Figure 85. The profit comparisons of Case 2 to Case 6.
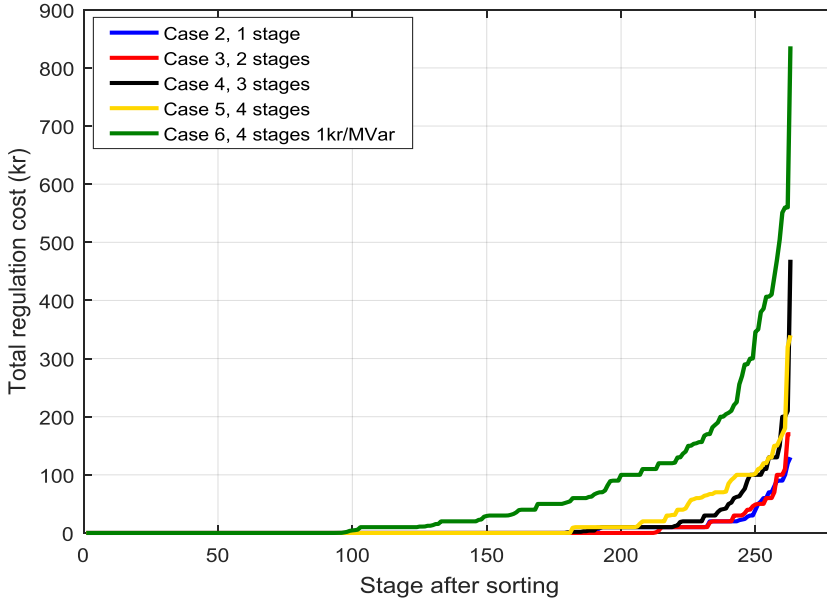
Figure 86. The total regulation cost comparisons of Case 2 to Case 6.
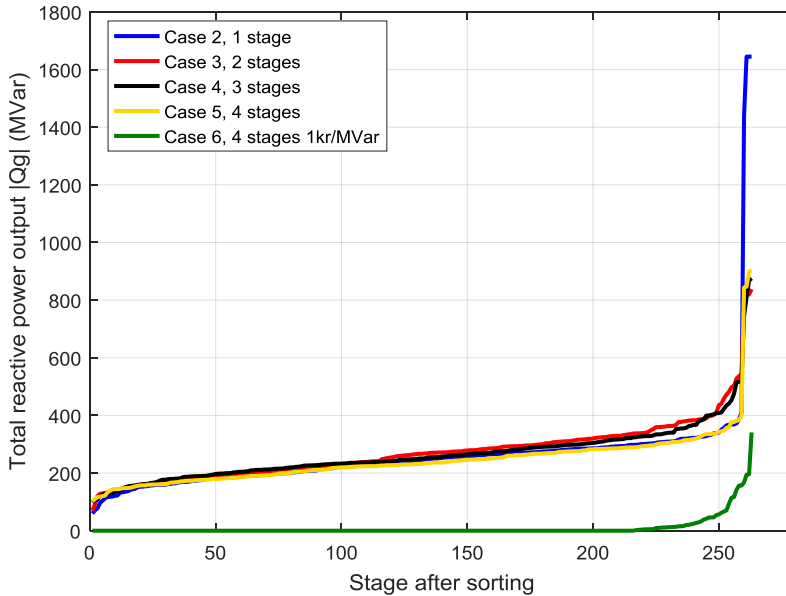
Figure 87. The generator reactive power output comparisons of Case 2 to Case 6.

The converged simulation results of Case 2 to 6 are shown in Figure 82 to Figure 87, where the result from Case 2 is also shown for comparisons. Similar to the result of Case 2 shown in Figure 77, The grid loss saving in Case 3 to Case 6 coupling to the market price and considering the regulation cost is able to cover the regulation cost in most of the stages, as presented in Figure 82 and Figure 83 as examples.

Comparing to the single stage optimization in Case 2, MORPF in Case 3 involves 2 stages, in Case 4 involves 3 stages and in Case 5 and Case 6 involves 4 stages, respectively, have more cost saving from the grid loss in the studied period, as shown in Figure 84. The saved total cost from the grid loss is largest in Case 5, where 4 stages are involved in each MORPF execution. Case 2 with ORPF focusing on the single snapshot optimization has the smallest cost saving from the grid loss.

Case 5 has the highest profit that is found through the difference between the cost saving from the grid loss and the regulation cost, as shown in Figure 85.

The price of the generator reactive power output is the same in Case 2 to Case 5, 0.0001 kr/MVar. The regulation cost of the generator reactive power in these cases is negligible. As shown in Figure 86, the total regulation cost in Case 5 is largest out of Case 2 to Case 5. It is due to the fact that MORPF in Case 5 is more aggressive than other cases to reduce the grid loss, which results in the highest profit in Case 5 than other cases. The regulation cost in Case 6 is highest in Figure 86, due to the high cost of the generator reactive power output. However, the total generator reactive power output, no matter the reactive power injection or absorption, $|Q_g|$, is smallest in Case 6, which indicates the reactive power reserve in the continuous reactive power components is largest in Case 6.

In summary, taking into account the system variability in the AVC system by including the predicted load flow in the upcoming stages formulates the MORPF, which is capable of providing better solutions than the conventional ORPF in term of the operational cost minimization. Moreover, more stages involved in MORPF, better solution is obtained. In the case that the ancillary service should be purchased, e.g. 1 kr/MVar in Case 6, then the overall profit will be reduced significantly, while more reactive power reserve can be expected.

5.   MORPF EMPLOYING LARGE WIND FARMS

The large wind farms are normally located far away from the consumption center and connected to the transmission grid. Especially for the offshore wind farm, they are connected to the onshore grid via long submarine cables. The modern wind farms are typically constructed with Type III and Type IV wind turbines. The equipped power converters are capable of fast regulating the reactive power to control the power factor or the voltage. In addition, these wind farms need to comply with the Low Voltage Fault Ride Through (LVRT) requirement. They should stay in connection during the normative faults to provide the voltage control service under certain conditions. For the future large wind farms, they are expected to be operated as the power plants, not only produce the power to the consumers but also provide the ancillary service like voltage control in the normal situations.

As shown in Figure 88 and Figure 89, according to the Danish grid code, the modern wind farms should be able to regulate the reactive power by +/- 33% of the maximum active power when the active power output is within 20% to 80% of the rated power and the voltage is within +/- 5% nominal. However, if activating the wind farm for controlling the voltage at Point of Common Coupling (PCC), then TSO should purchase this service, which calls for an assessment of the wind farms contribution to the AVC system.
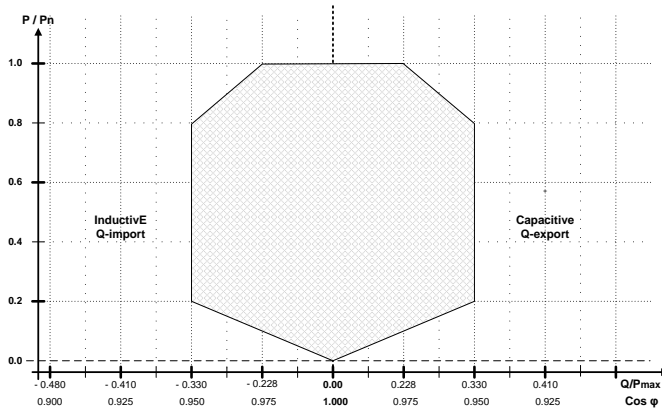
Figure 88. Reactive power requirements for wind farms with power output greater than 25 MW [7].
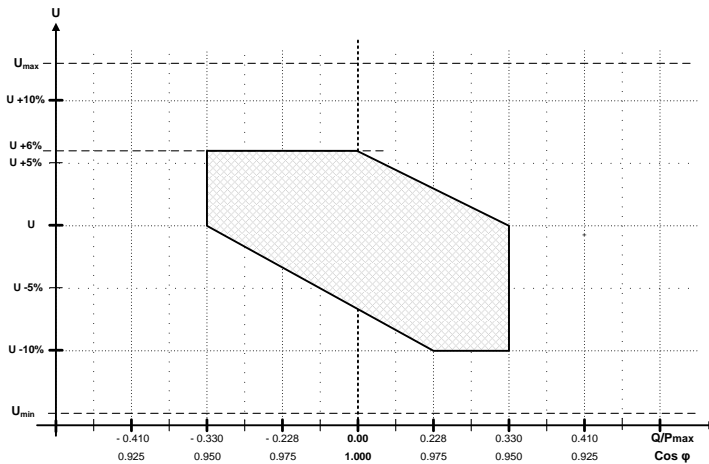
Figure 89. Voltage control requirements for wind farms with power output greater than 25 MW [7].
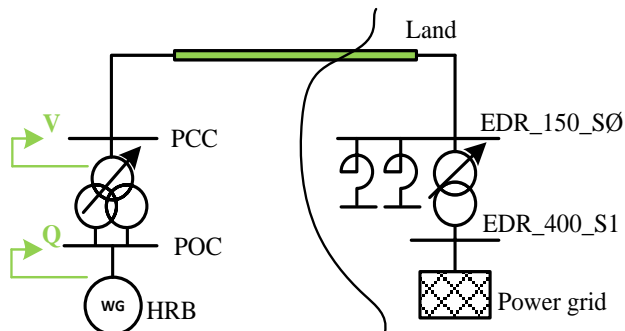
Figure 90. Horns Rev B wind farm (HRB) is connected to the grid over the submarine cable.

In the normal operational conditions, the long transmission distance of large wind farms is typically a barrier for the wind farms to support the voltage in a large area. Therefore, the large wind farms in

Denmark are not forced to provide the voltage control in the normal operational condition, only keep a constant power factor or ensure nearly neutralized reactive power flowing into the Point of Connection (POC) that is typically the transformer between the collector and the transmission grid, as shown in Figure 90. In addition, the voltage at the high-voltage side of the transformer, PCC, is maintained by the tap changer at the step-up transformer, which is controlled by TSO. The cost of regulating the tap changer on the transformer is covered by TSO without coordinating control with the wind farms.

The simulation platform can be applied for assessing the potential benefit from employing the large offshore wind farms to participate in the AVC system. The studies in this section are carried out on the same involved stages, where the price of the generator reactive power output varies from 0.0001 to 1 kr/MVar. Both the conventional ORPF and the proposed MORPF with 4 stages in each execution are used for the assessments. The settings of different study cases are presented in Table 34.

Table 34. The study cases for employing the large offshore wind farms in the AVC system.

Case ID	Market price	Wind farms in AVC	Max. no. of reg. times	Regulation cost	No. of stages in MORPF	Gen. reactive power cost (kr/MVar)
7	X	X		X	1	0.0001
8	X	X		X	1	0.25
9	X	X		X	1	0.5
10	X	X		X	1	1
11	X	X		X	4	0.1
12	X	X		X	4	1
13	X	X	X	X	4	0.01
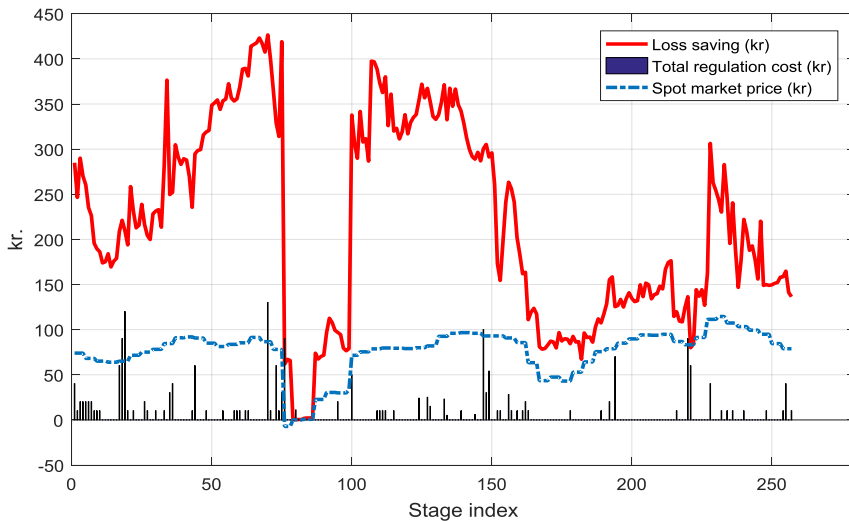
Figure 91. The saving against regulation cost after the cost minimization in Case 7.
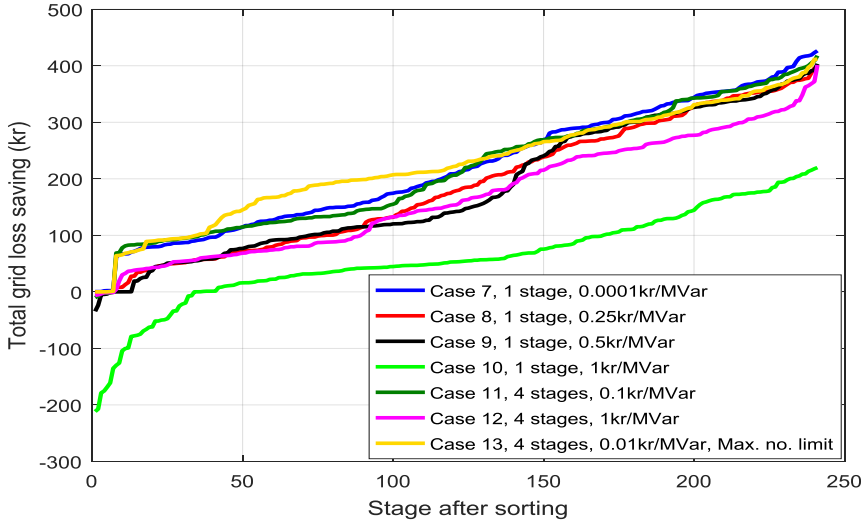
Figure 92. The grid loss saving comparisons of Case 7 to Case 13.
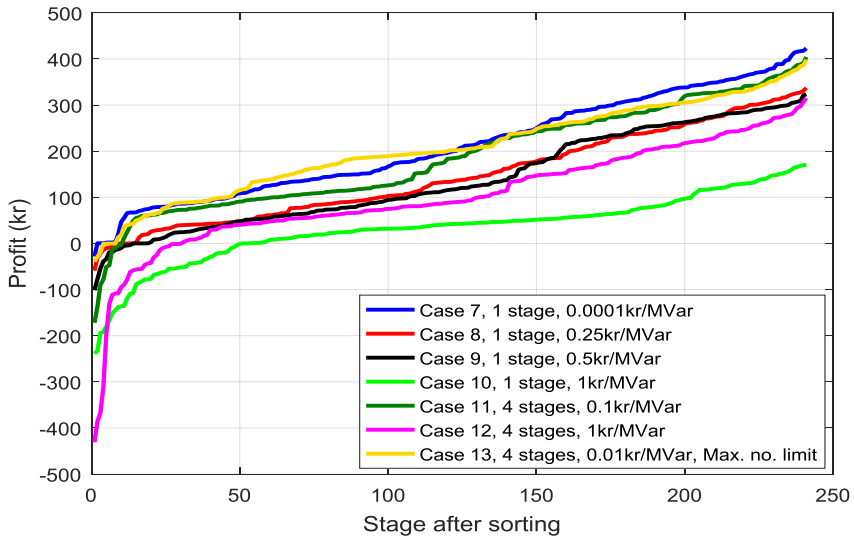
Figure 93. The profit comparisons of Case 7 to Case 13.

Thee large offshore wind farms are activated to participate in the AVC system. The locations of them presented in Figure 65, and the reactive power regulation capabilities are presented in Table 30. The conventional ORPF coupling to the market price with these wind farms are carried out in Case 7, where the generator reactive power output cost is negligible, as shown in Table 34. The result is presented in Figure 91, where the cost saving from the grid loss can cover the regulation cost for the entire study period.

If increase the cost of the generator reactive power output up to 1kr/MVar, as carried out in Case 8 to Case 10, the cost saving from the grid loss will drop, as shown in Figure 92. It is due to that generator regulation capability is limited as the price increases and then not able to be fully applied for the grid loss reduction. However, if applying MORPF in Case 12, though the generator reactive power price is 1 kr/MVar, the resulted cost saving from the grid loss is compete-able to the one in Case 9 where the

price is 0.5 kr/MVar. It is more clearly to see from the profit in Figure 93 that MORPF in Case 13 with higher price for the generator reactive power than ORPF can still provide the compete-able solution to Case 7. Moreover, Case 12 employing MORPF provides more profit than Case 10, where the generator reactive power prices in these cases are the same.
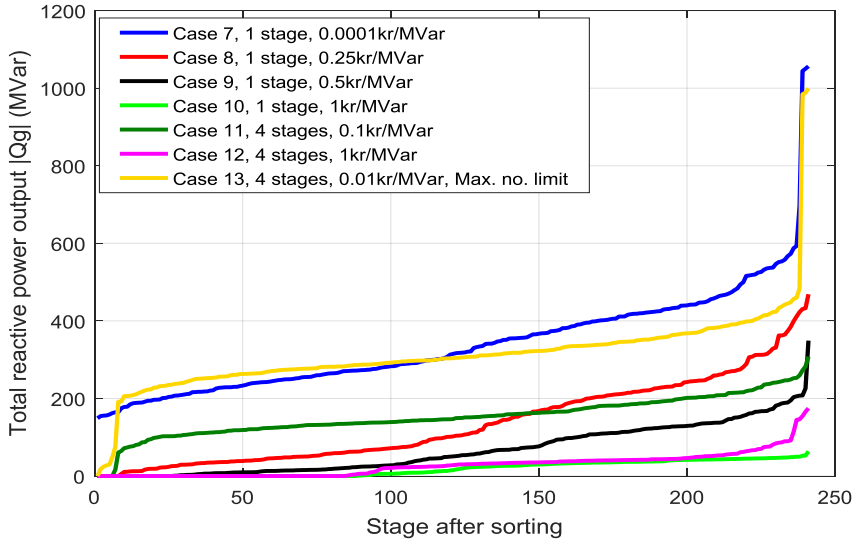
Figure 94. The generator reactive power output comparisons of Case 7 to Case 13.
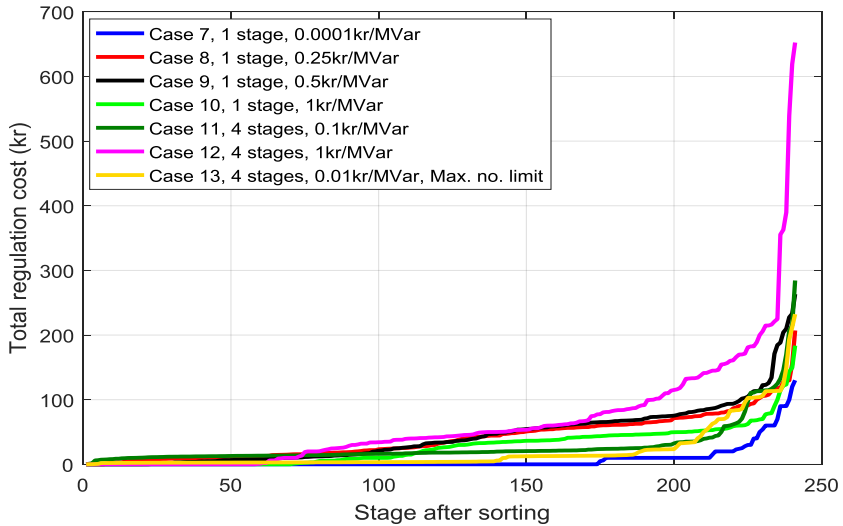
Figure 95. The total regulation cost comparisons of Case 7 to Case 13.

As the generator reactive power price increases, less generator reactive power outputs are observed. As shown in Figure 94, though Case 7 and Case 13 are the cases providing the most profits, the generator reactive power outputs in most snapshots are higher than 200 MVar. In the Danish power system, a conventional power plant can normally inject about 200 MVar reactive power. It means, by roughly speaking, Case 10 and Case 12 with high price, 1 kr/MVar, can reserve more reactive power

that is equivalent to a power plant comparing to Case 7 and Case 13. The total regulation cost in Case 12 is highest, as shown in Figure 95 due to the high reactive power output cost and aggressive actions for the loss saving.
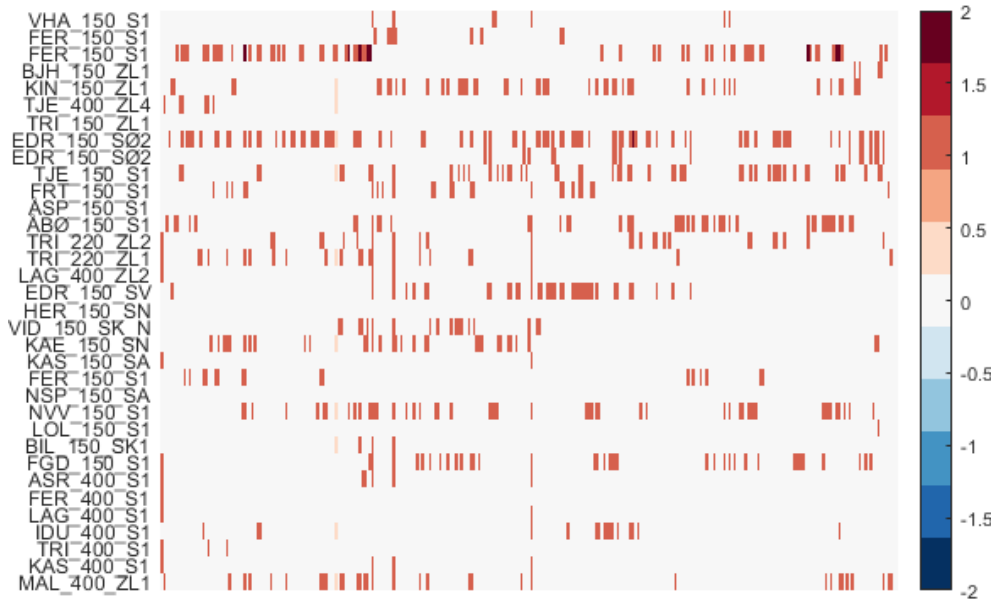
Figure 96. The shunt steps for the involved stages in Case 1 (loss minimization).
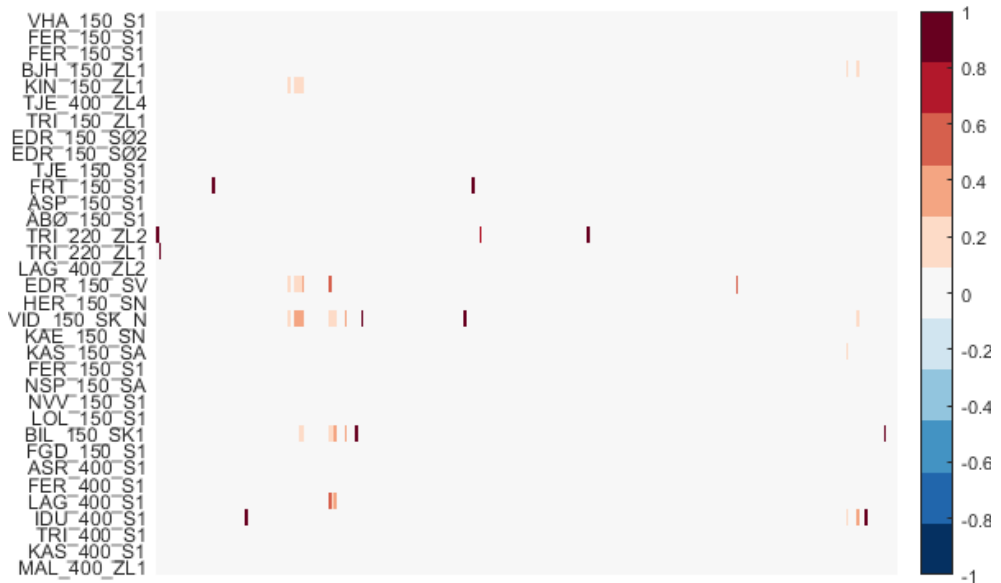
Figure 97. The shunt steps for the involved stages in Case 13 (Cost minimization via 4-stage MORPF with wind farms contribution and the max. regulation numbers on the discrete components).
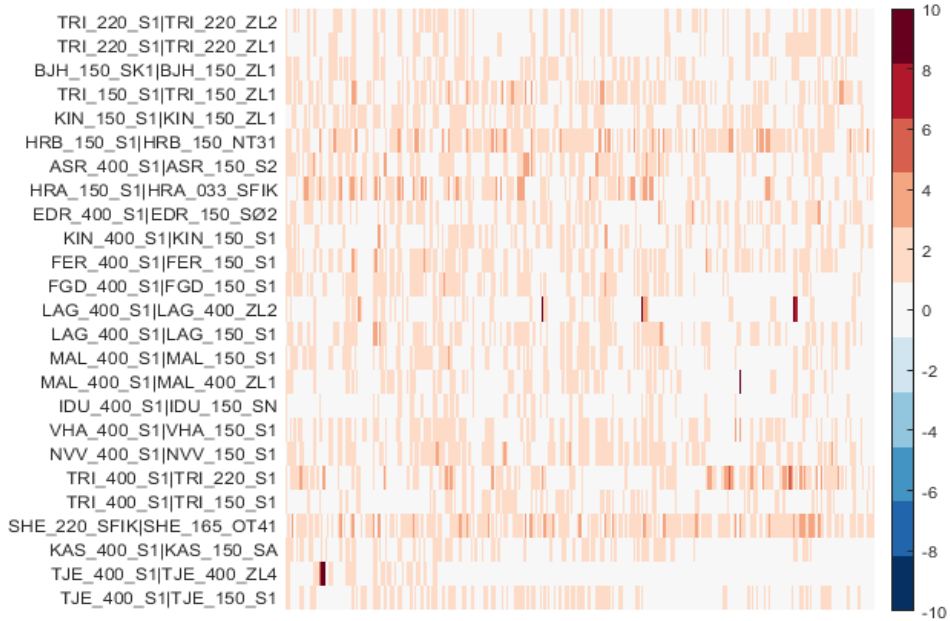
Figure 98. The tap changes including the tap changer at power transformers and the variable shunts in Case 1 (loss minimization).
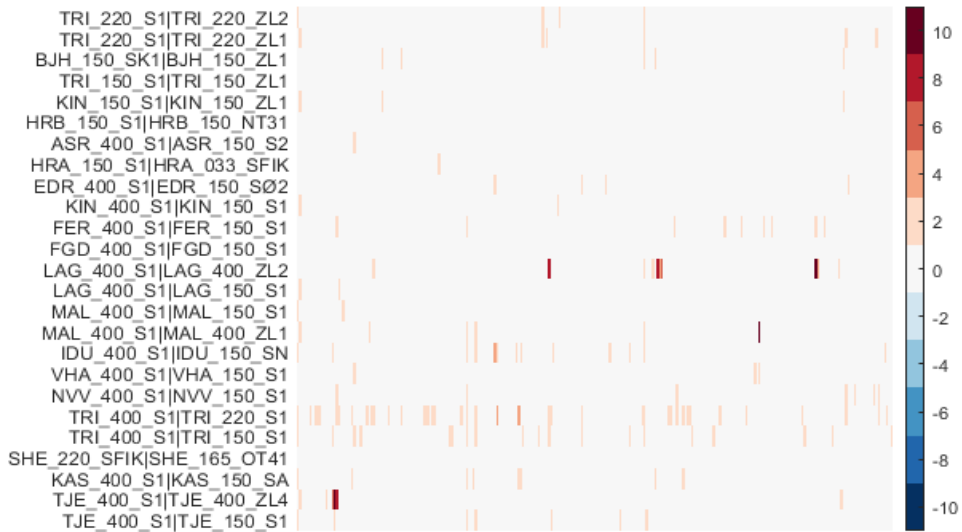
Figure 99. The tap changes including the tap changer at power transformers and the variable shunts in Case 13 (Cost minimization via 4-stage MORPF with wind farms contribution and the max. regulation numbers on the discrete components).
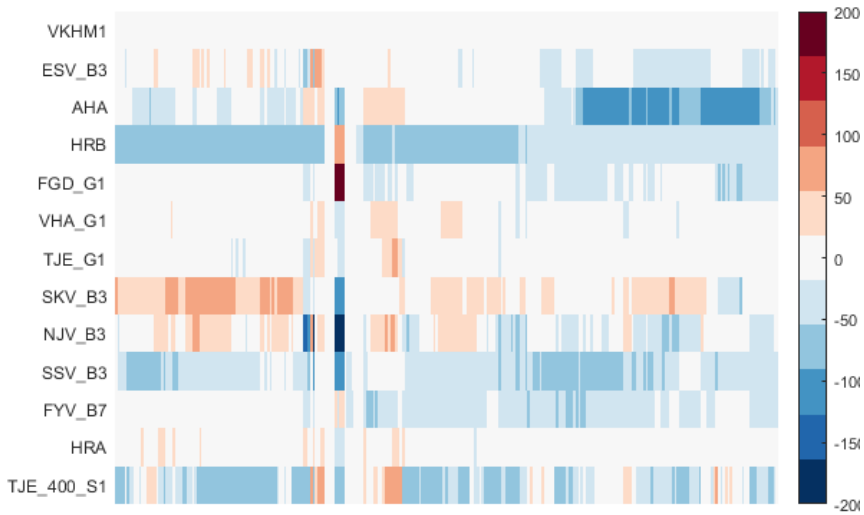
Figure 100. The reactive power output of the continuous reactive power components in Case 13 (Cost minimization via 4-stage MORPF with wind farms contribution and the max. regulation numbers on the discrete components).

Figure 96 to Figure 100 present the heat maps for the controllers along the stages for the selected cases. In these plots, each row represents a controller's state changes along the converged stages in a certain case. The values of the changes are presented by the colors. Recall the reference case, Case 1, the shunts and the transformer taps are operated frequently to save the grid loss. As shown in Figure 96, the shunts at FER_150_S1 and EDR_150_SØ2 are mostly regulated. In contrast, the shunts are rare regulated in Case 13 due to the maximum regulation times constraint at discrete components (2 times/stage), as shown in Figure 97. The regulations of the transformer tap changers including the power transformers and the variable shunts in Case 1 is presented in Figure 98. It can be seen that, the tap changers on the offshore platforms at HRB_150_S1 to HRB_150_NT31 and HRA_150_S1 to HRA_033_SFIK are frequently changed. This is due to the fact that (i). the voltage on the offshore platform is maintained only by this transformer tap that should adapt the tap positon according to the wind power production; (ii). the loss reduction over the long cables between the offshore platform and the onshore stations can trigger the tap regulation. If considering the components on the offshore platform are typically operational expensive in the real systems, then the price of such taps should be increased in the optimization formulations. By employing the 3 offshore wind farms in the AVC system, the tap changers on the offshore platform have nearly no change in Case 13, as shown in Figure 99. The voltage regulation on the offshore platforms is therefore carried out by the wind farms. As show in Figure 100, e.g. HRB absorbs the reactive power to compensate the capacitive cables in most stages.

6. MORPF WITH VOLTAGE SECURITY MARGIN

The MORPF based AVC system can provide better solution than the conventional ORPF in term of the cost minimization. It requires the forecasting system that captures the system variability, and then optimizes the system over a period. The uncertainty always exists in the forecasting system, which is the invisible deviation from the expected values, or say, the forecasting errors in the formulated MORPF framework. The forecasting errors can be observed when and only when the system is realized, which is found through the differences between the forecasting and the measurement values.

As described in Chapter 4 Section 6, there is risk of the voltage violation after realization if the forecasting errors are not taken into account. In Chapter 4 Section 4.1.4, it shows that the WPFE are the main uncertainty sources that can be represented by the multivariate normal distribution, where the covariance is used to capture the spatio-temporal correlation of the WPFE. The VSM at each node in the grid can be found by converting the covariance of the WPFE to the covariance of the voltage magnitude variations via the sensitivity matrices [78]. The MORPF is therefore search for the solution after reserving the found VSM in the voltage magnitude constraints. As this approach requires the sensitivity matrices that is a linear approximation of the original nonlinear equation, the MORPF is thus firstly solved without VSM and then using the sensitivity matrices to obtain the VSM, and updates the results by reserving VSM in the constraints, as shown in Figure 101.
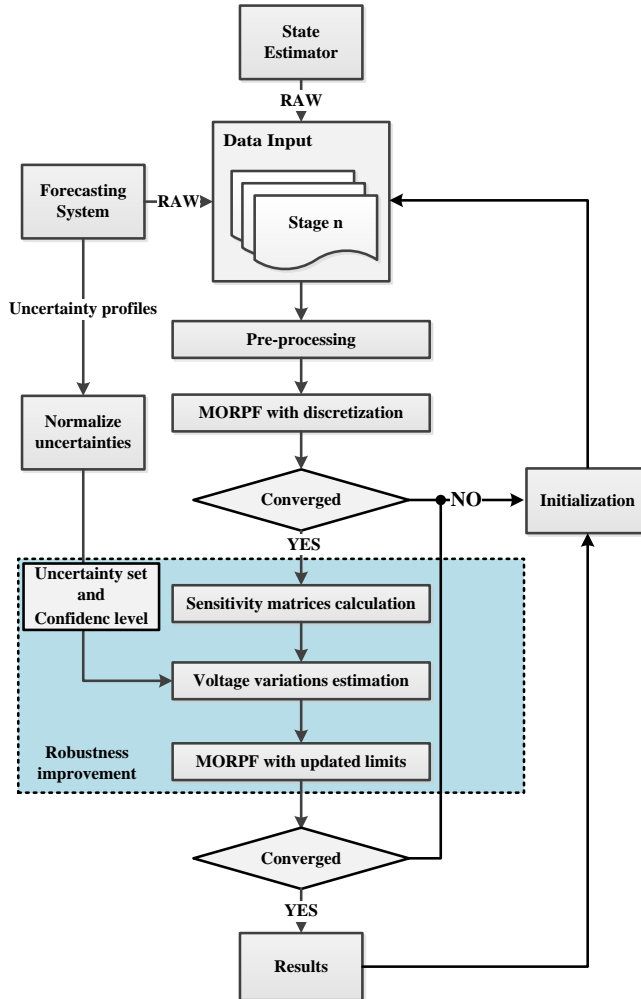
Figure 101. MORPF with VSM calculation procedure [78].

The historical WPFE is extracted from the forecasting system in the control center, as shown in Figure 43. The correlation matrix is found, as shown in Figure 44 in the Chapter 4 Section 5. The assumptions are made: (i). Different wind turbines in the same zone have the same zonal WPFE

profile and fully correlated, which is considered to be the worst case; (ii). Reactive power at each aggregated 60 kV stations is without any forecasting errors, as the reactive power variations in the short-term are minor. It highly depends on the load conditions; (iii). Four snapshots in a MORPF are involved. They are the current snapshot from the measurement and 3 predicted snapshots with 15 minutes, 30 minute and 45 minutes lead time, respectively; (iv). The WPFE for 15-minute, 30-minute, 45-minute and 60-minute lead times are assigned to the 4 snapshots. In the real time application, Stage 1 of each MORPF loop is considered to be without any forecasting error. Therefore, more conservative solutions are expected.

In the calculations, the zonal WPFE should be mapped to the corresponding nodes via the assumptions (i)-(iv). The covariance matrix representing the zonal WPFE is therefore converted to an expanded covariance matrix for the nodes with wind turbines [78].
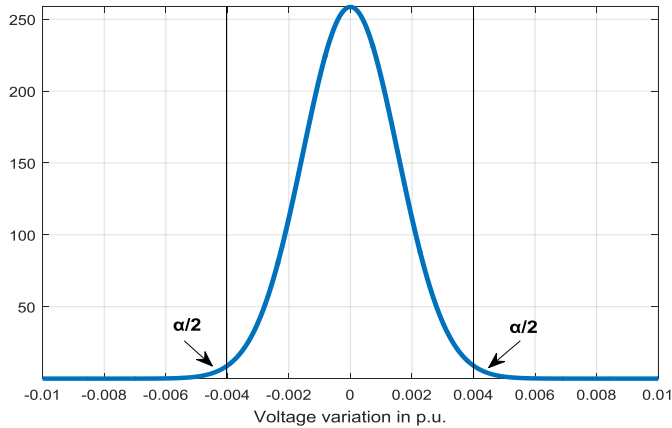
Figure 102. An example of a marginal distribution of the voltage variations.

The voltage variation profile at each node can be found through affine transformation (4.59)-(4.62). An example is shown in Figure 102. The confidence level, α, can be applied to adjust the size of the VSM, to compromise the introduced cost and the risk taking.

Table 35. The study cases for reserving the VSM.

Case ID	Market price	Wind farms in AVC	Voltage security margin	Max. no. of reg. times	Regulation cost	No. of stages in MORPF	Gen. reactive power cost (DKK/MVar)
14	X		X		X	1	0.1
15	X		X	X	X	4	0.1
16	X	X	X	X	X	4	0.1
17	X	X	X	X	X	4	1

In this section, total 4 cases are carried out, i.e. Case 14 to 17. The settings of each case are presented in Table 35. Comparing to the previous studies, the difference is to reserve the VSM and search for the optimal solution as proposed in Figure 101, where the confidence level is set to 0.01. Similar to the observation in the previous sections, MORPF is superior to the ORPF in the term of the cost minimization, even with VSM in the voltage magnitude constraints.

As shown in Figure 103 for the generator reactive power output in Case 17, HRB always absorbs reactive power though the cost of the generator reactive power is high. It indicates the importance to have HRB to participate in AVC system.
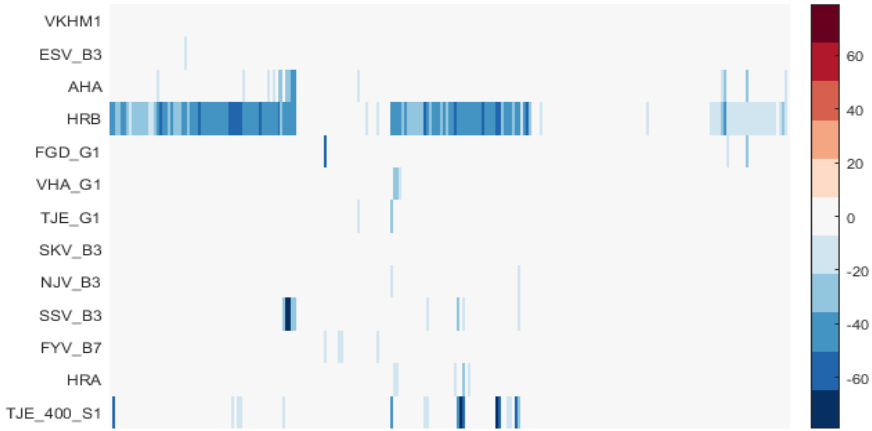
Figure 103. The generator reactive power output in Case 17.
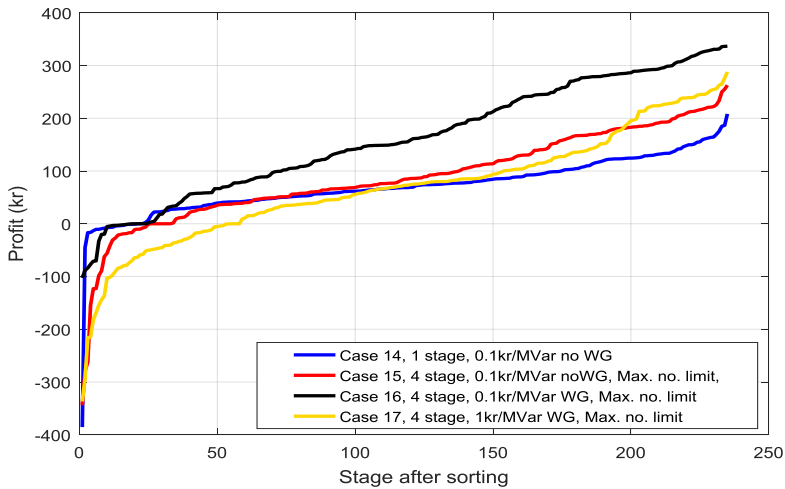
Figure 104. The profit comparisons of Case 14 to Case 17.

Comparing to Case 11, the profits in Case 14 to Case 17 shown in Figure 104 are less, due to the reserved VSM that reduces the cost saving from the grid loss. The comprehensive comparisons between difference study cases are presented in Table 36.

In the calculations, the voltage magnitudes are converted to the per unit values. The VSM is found for all nodes at involved stages in a MORPF execution. As shown in Figure 105, the VSM for a certain MORPF that involves 4 stages is presented, where the confidence level, α, varies. The VSM in an example of a MORPF execution in Case 17 is presented in Figure 105, where the largest VSM at a node in each stage under different confidence levels are shown. VSM increases as the lead time of the forecasting increases, i.e. the maximum VSM of a node is larger in Stage 4 than Stage 3 etc. As observed from the historical data in Figure 43, the forecasting errors can be up to 30% of the installed

capacity at a node, which can introduce the voltage variation at a node in the transmission level up to 0.0044 pu (under 2 kV) when $\alpha = 1e - 6$ in this particular case.

The operational cost will generally decrease as the confidence level increases [78][91]. The increased cost for reserving the VSM is a combination of the extra loss and the redundant regulation costs.
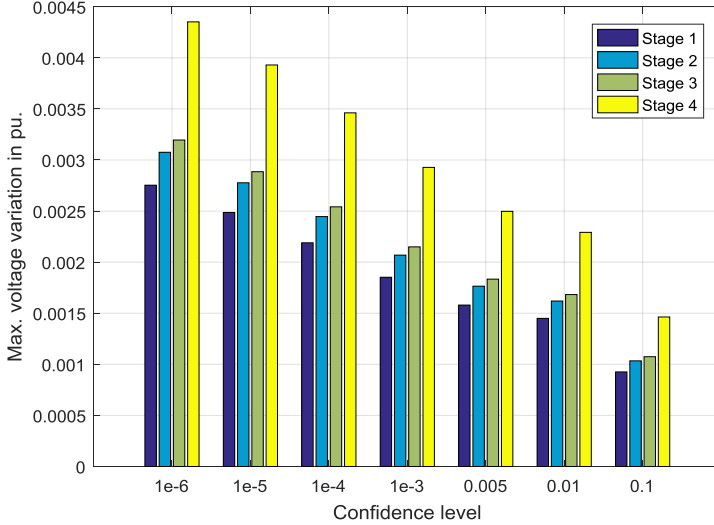
Figure 105. The maximum VSM at a node in a MORPF with 4 stages.

After the MORPF employing VSM is solved, the optimal control variables can be obtained. They are therefore used to update the setpoints of the reactive power components in the modes to emulate the dispatch. The Monte Carlo simulations are carried out afterwards. Total 1,000 samplings are generated based on the NORTA techniques (see Chapter 3, Section 7), to cover the possible node power variations caused by WPFE. The load flow for each sampling is thus performed after implementation the suggested optimal setpoints for the controllers. The maximum and the minimum voltage magnitudes are respectively recorded. Different confidence levels are considered, which results in different voltage profiles, as shown in Figure 106. In this case, as the confidence level lower than 0.1, there in to voltage violation observed. Moreover, no under-voltage violation found, as the entire voltage profile is close to the upper limit to reduce the grid loss.
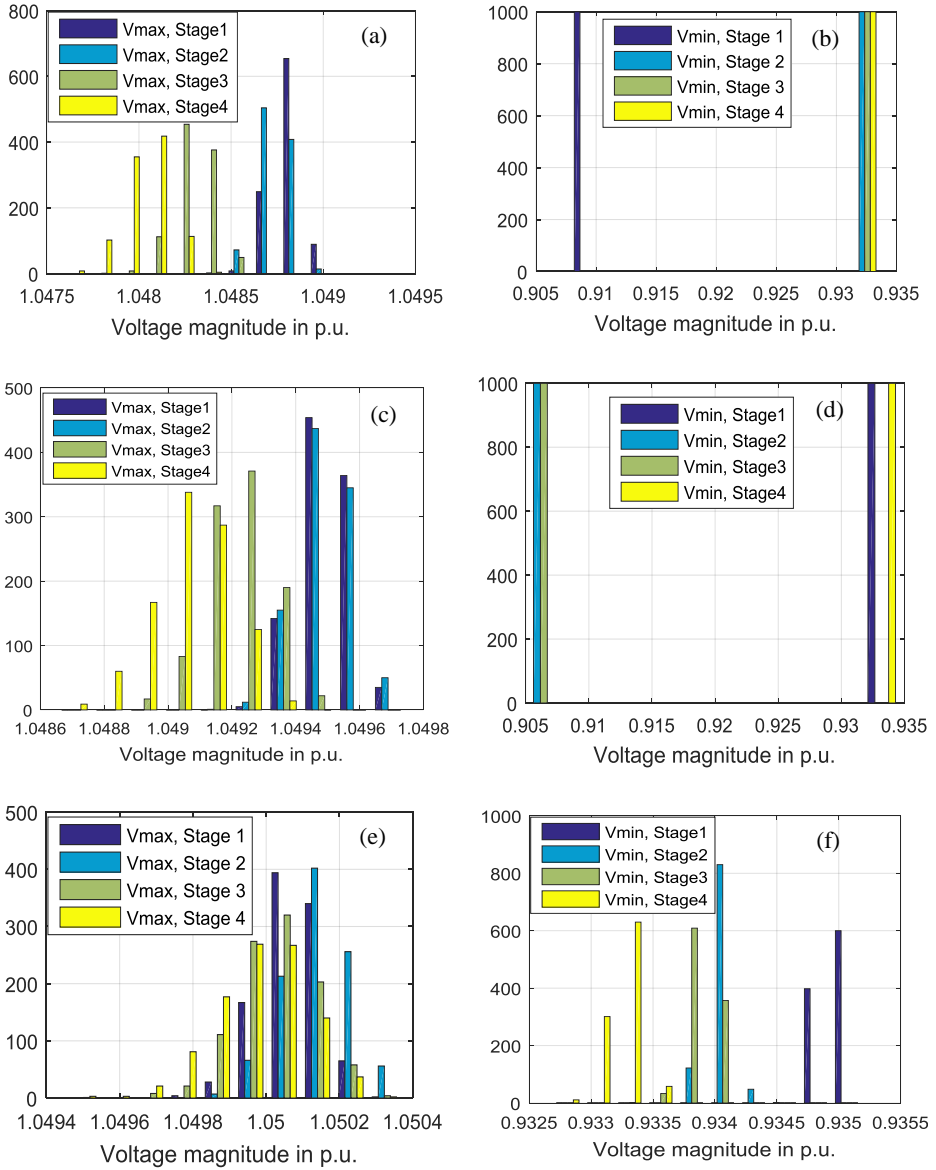
Figure 106. Voltage magnitudes under the 1000 samplings Monte Carlo simulations based on a single MORPF decision results, with different confidence levels. In (a) and (b) $\alpha = 0.001$. In (c) and (d) $\alpha = 0.1$. In (e) and (f) $\alpha = 1$.

7. RESULTS SUMMARY

Total 17 study cases are carried out, as shown in Table 36. The values in each case are normalized by the numbers of converged snapshots. Therefore, the numbers for the profit, loss saving and the total regulation cost in Table 36 are the average cost in each snapshot.

Case 1 applied the conventional ORPF algorithm focus on the loss saving without considering the regulation cost. The loss saving is the most in Case 1. However, the total operational cost in Case 1 is much more than the loss saving, which results in a negative profit. Comparing to Case 1, Case 2 minimizes the total operational cost including the regulation cost with the coupled market price, which reduces the regulation cost significantly. As the market price coupled to the AVC system, many regulations triggered when the price is high that leads to large loss saving. As the market price becomes negative, there are also many regulations to lower down the voltage in order to generate grid loss to obtain the negative cost.

In Case 3 to 6, the MORPF based decision making process are studied. As the number of involved stages increases, more profit is obtained. If the generator reactive power output is low, then Case 5 is preferred that involves 4 stages in each MORPF execution. It concludes that MORPF captures the system variability is able to provide better solution than ORPF in term of the cost minimization. Moreover, as the number of the involved stages in the MORPF increases, more profit can be expected, which are presented in Case 3 to Case 5.

In Case 7 to Case 13, three large offshore wind farms are activated for the AVC system. The single stage ORPF in Case 7 to 10 are studied, where different generator reactive power prices are assigned. In Case 7, the cost of the wind farm reactive power output is assumed to be negligible. However, the wind farms internal loss is generally larger than the conventional generators due to the relative large loss on the power converters and the internal networks. It is not considered in these studies due to absence of the detailed wind farm models. The other generators as competitors are assumed to always have the same price with the wind farms on the reactive power output.

Case 8 to Case 13 employing ORPF method are studied for different generator reactive power costs. Using the regulation capability of offshore wind farms is capable of providing more profit than Case 2 when the price of the generator reactive power is lower than 0.5 DKK/MVar in Case 7 to 9. However, the profit in Case 12 is still higher than it in Case 2 though the price of the generator reactive power is 1 kr/MVar, as 4-stage MORPF method is applied.

Table 36. Summary of the simulation results. "MP": market price in the objective; "WG": employing 3 offshore wind farms; "VSM": reserving VSM; "Lim.": limitation of switching times; "Reg. cost": considering the regulation cost; "Stage": number of stages in an execution. "p_Q": the weight of the generator reactive power output (1€ = 7.5 kr).

Case ID	MP	WG	VSM	Lim	Reg. cost	Stages in MORPF	p_Q (kr./MVar)	Conv. (%)	No. of stages	Time (sec.)	Profit (kr.)	Loss saving (kr.)	Total regulation cost (kr.)
1						1	0.0001	98.26	288	39.93	-184.6	185.5	370.2
2	X				X	1	0.0001	98.61	288	12.81	45.2	52.8	7.6
3	X				X	2	0.0001	98.61	287	70.80	85.7	97.0	11.3
4	X				X	3	0.0001	97.55	286	103.49	99.7	119.1	19.4
5	X				X	4	0.0001	97.19	285	218.15	100.7	123.7	23.0
6	X				X	4	1	94.74	285	121.19	24.7	101.4	76.7
7	X	X			X	1	0.0001	95.83	288	9.64	189.5	197.3	7.8
8	X	X			X	1	0.25	95.49	288	13.19	120.9	167.6	46.8
9	X	X			X	1	0.5	94.79	288	12.18	108.5	163.0	54.5
10	X	X			X	1	1	96.18	288	15.54	25.4	54.5	29.1
11	X	X			X	4	0.1	97.19	285	112.95	171.8	202.9	31.1
12	X	X			X	4	1	96.49	285	114.90	80.7	154.3	73.6
13	X	X		X	X	4	0.01	96.49	285	122.67	190.2	210.8	20.7
14	X		X		X	1	0.1	98.96	288	19.67	54.1	76.0	21.8
15	X		X	X	X	4	0.1	94.39	285	220.16	77.1	126.5	22.4
16	X	X	X	X	X	4	0.1	94.74	285	213.37	154.5	193.6	39.1
17	X	X	X	X	X	4	1	88.07	285	250.06	54.1	146.1	92.0

The VSM is found for each node at each stage to protect the solution against the impact from the WPFE. In the example, about maximum 0.0044 pu. at a node can be introduced by the WPFE that varies between +/- 30% of the installed capacity. After reserving the VSM, the solution is robust that is feasible in the entire variation range of WPFE for the studied case.

The simulation time increases as more stages are involved in the optimization framework. It takes about 250 seconds to solve a MORPF with 4 stages in Case 17, whereas it takes only about 13 seconds for solving a ORPF problem in Case 2. However, if MORPF is executed every 15 minutes, then 250 seconds are still sufficient to obtain the results for the AVC system.

8. EXTREME CASE

In the real operations, it is observed that the wind farms immediately ramp down the production to zero as long as the market price becomes negative. As shown in Figure 107, Anholt wind farm reduced the power from full to null within 2 minutes.
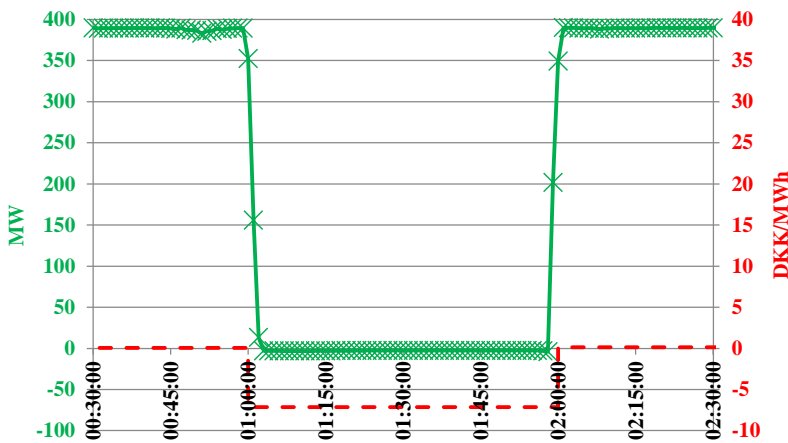
Figure 107. Anholt offshore wind farm (rated 400 MW) power production responses to the market price at 01:00 December 25th, 2015.

The measurement data representing the snapshot at 01:00, December 25th, 2015 is extracted from EMS. The snapshot is modified to become more severe situation. The assumptions are made as below: (i). the market price is negative that results in disconnection of the wind power. In the same time, CHP and other type of production units reduce the production close to the minimum output; (ii). the number of in-service central power plants are depending on the market price. Assuming only 3 synchronous condensers and the VSC-HVDC link are in operation, and no central power plants in service due to the negative price. This is considered to be the worst case for this study; (iii). the 3 offshore wind farms ramp down the power production to zero within 1 minute. The small scaled wind turbines spread in the distribution grid is scaled down in order to obtain 2 snapshots with 1000 MW and 2000 MW power drops, respectively; (iv). the maximum change of the reactive power flow at the German border is limited to 200 MVar; (v). the maximum number of the tap change for each transformer is limited to 2 by assuming 30 sec. response time for each tap (it is about 10 sec. in reality); (vi). the unbalance due to the power drop is fully compensated by the slack machine at the German border without considering the thermal limits.

After the large amount of power drop, the system voltage rises and violates the acceptable limits. This study case is to assess if the voltage is capable of being controlled within the acceptable band with limited regulations. If the regulation is not sufficient, a ramping limit should be defined as a requirement. Total 5 snapshots are prepared. At the first snapshot, the total power production is 3200

MW and no central power plants are in service. The power production drops at second snapshot by 1000 MW that is achieved by disconnecting 3 offshore wind farms and scale down the distributed production. In the third snapshot, another 1000 MW power drops by further scale down the distributed power production. The fourth and the fifth snapshots are the same as the second and the first snapshot, respectively, which represent the power production restoration when the market price becomes positive.
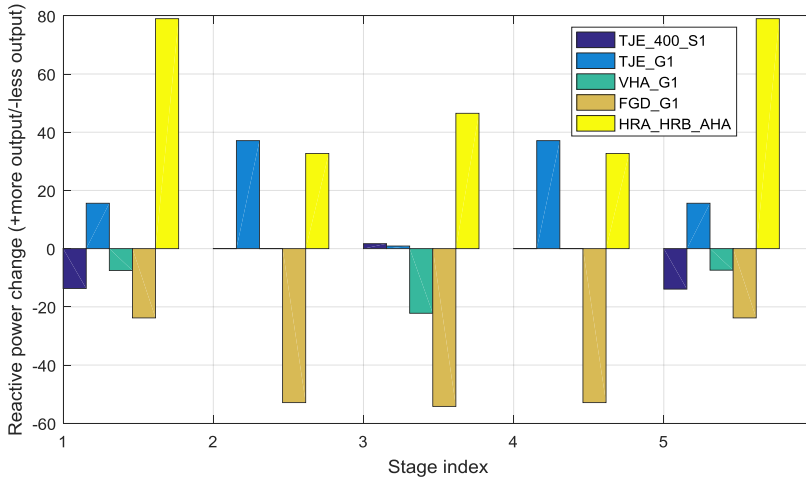
Figure 108. The change of the reactive power output for the continuous reactive power components in the critical scenarios, where wind farms participate in AVC. "AHA": Anholt wind farm; "HRA" and "HRB": Horns Rev A and B wind farm, respectively; "FGD_G1", "VHA_G1" and "TJE_G1" are synchronous condensers; TJE_400_S1 is VSC-HVDC link. Positive means more reactive power output from the components after employing the wind farms and vice versa.

In these critical scenarios, the voltage is capable of being maintained by 3 synchronous condensers and the VSC-HVDC link. In this case, as the wind power drop by 1000 MW in 1 minute, the import from Germany reaches up to 2000 MW that violates the maximum transfer capacity at the German border. After 2000 MW wind power shunt down, nearly 3000 MW total amount of power is imported from Germany. The entire system voltage will drop as a significant amount of power flowing from German border to the northern DK1 system. Along the main corridor, the synchronous condenser TJE_G1 and the VSC-HVDC link SK4 at TJE_40_S1, shown in Figure 65, produce their maximum reactive power to support the voltage. In addition, HRB wind farm produce 46 MVar that close to its maximum reactive power output.

There are 2 more tap changes without the wind farms being in AVC system. If 3 wind farms participate in the AVC system, neither tap change nor shunt switching is observed. In addition, the reactive power output at "FGD_G1" and "TJE_400_S1" are less than the case without the wind farms in AVC, as shown in Figure 108.

9. SUMMARY

A decision making algorithm for the Danish AVC system is proposed, which focuses on minimizing the total operational cost including the grid loss cost, the shunt switching cost, the tap changing cost and the generator reactive power output cost. The proposed approach formulates the problem in term of the expense value, which can be used directly assess the operational cost and the profit. As the market price is applied in the AVC system, the regulation follows the market price to save the loss when the market price is high, and even generate the loss in the case of negative price. Moreover,

with the contribution of the wind farms to the AVC system, more profit is obtained, as the loss saving is increased, the cost on the discrete components is less and more reactive power reserve can be expected. This is considered to be a good argument to employ the wind farms to participate in the AVC system.

The WPFE may cause the voltage variations. In the proposed AVC system, the VSM is applied to cover the voltage uncertainty caused by WPFE that is modelled as the multivariate normal distribution. The optimization employing VSM provides solutions that are robust against the uncertainty.

Total 17 study cases are carried out based on the historical data for the specified period. The results are summarized in Table 36, where the benefit and the cost for different approaches are presented. The results in Table 36 are finally converted to average values for comparisons. By considering the power variability, MORPF is proposed that provides better solution in term of the cost minimization. If the speed of the power changes is increased in the future, the time interval in a MORPF execution should be reduced in order to capture the variability. The voltage uncertainty caused by WPFE is included in MORPF approach. MORPF employing VSM is able to improve the solution robustness. However less cost saving and more regulation cost are the price to pay.

In the conventional ORPF based AVC system, the uncertainty is also existing though it is minor and can be neglected. In MORPF, the uncertainty in the involved stages increases as the lead time increases. The cost to protect the solution against the uncertainty in MORPF is not able to be neglected. However, the cost saving due to capturing the variability is generally able to cover the cost of protection against the uncertainty, if the forecasting system is well functioning. This is a vital consideration to decide if the MORPF is applied in an AVC system.

Based on the studied cases in this report, the annual profit is about 5.3 million Danish kroner referring to the results in Case 16 in Table 36, where the potential loss saving is 6.6 million Danish kroner and the total regulation cost is 1.3 million.

CHAPTER 7. FALLBACK SCHEME

The AVC system is expected to be operated in the closed loop. In case the AVC is malfunctioning, the system will suffer the risk of the voltage violation and even the voltage collapse. The fallback scheme is expected to be implemented in the important stations, in order to automatically maintain the local voltage. It is supposed to be activated in abnormal conditions, e.g. lost the communications between the stations. It can also designed for some special applications, e.g. fast release the reactive power in the reactor shunts to support the voltage where lots of Type I wind turbines are connected, in order to compensate the reactive power consumption by these wind turbines during the voltage re-establishment periods.

As shown in Figure 109. The fallback scheme is designed to be slower but more aggressive than the relay functions to control the passive shunts for maintaining the voltage [52]. It can be specified to two operational modes.

- Mode 1: slow response when the telecommunication between the stations and the control center is lost. The fallback scheme will maintain the station voltage to a predefined value by controlling the assigned shunts locally. In the case of the continuous reactive power components are connected beside the shunts, the station voltage is controlled by the continuous reactive power components. In this case, the shunts can be used to compensate the continuous reactive power components for being close to the neutral in order maintain the reactive power reserve.
- Mode 2: fast response when the voltage violation occurs. The fallback scheme will automatically control the assigned shunts to support the voltage towards the acceptable band. If several shunts are placed in the same busbar, a predefined order is needed to trigger the shunt for correcting the voltage locally. Mode 2 will have highest priority in order to maintain the voltage.
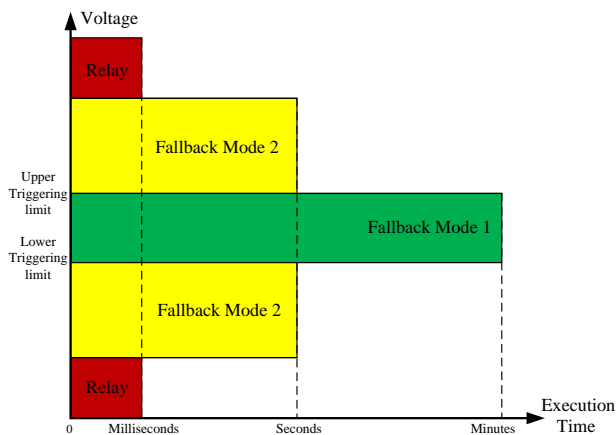
Figure 109. Fallback scheme concept [52].

1. FALLBACK CONTROLLER

The fallback scheme is designed to be operated locally. In stations, the fallback controllers require the fast measurements from the Remote Terminal Unit (RTU) devices. RTU can measure the local voltage in hundreds of milliseconds. Considering the AVC loop that requires at least 1 minute for SCADA to

refresh the measurement, the fallback scheme is possible to assist the centralized AVC system for maintaining the voltage between two AVC dispatches.

As shown in Figure 110, the fallback controller in each station will monitor (i). The signal of telecommunication (ii). the station voltage (iii). the status of the assigned shunts and (iv). the reactive power output of the continuous reactive power components if there is any. If the telecommunication is lost but the voltage is still within the acceptable operational band, then Mode 1 will be activated, to control the shunts for either maintaining the voltage to the predefined value or compensating the continuous reactive power components. If the voltage violation occurs, then the Mode 2 will take over the controllability to correct the voltage. In order to avoid the large voltage jump and the frequently wear on/off the shunts, only one shunt can be switched in/out at a time. The time intervals between two switching comply with the inverse time characteristic (ITC) [52], e.g. triggering the control action fast if the voltage violation is severe and slow if the violation is minor.
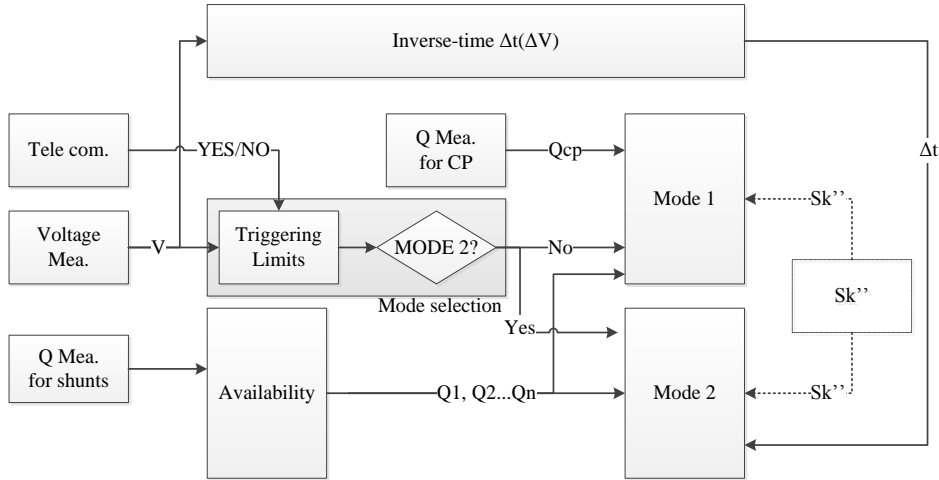
Figure 110. The fallback controller [52].

The ITC of triggering shunt switches for correcting the voltage violation can be expressed in (7.1) to (7.3) [52].

$$\Delta t = \frac{A}{\Delta V^P} + B$$	(7.1)
$\Delta T_{min} \leq \Delta t \leq \Delta T_{max}$	(7.2)
$\Delta V > 0 \ and \ \Delta t > 0$	(7.3)

where Δt is time interval between two switching that is limited between the minimum and the maximum response time, ΔT_{min} and ΔT_{max}, respectively. A, B and P are parameters for tuning to obtain an desired Δt according to the voltage violation ΔV. Equation (7.1) can also be replaced by a look-up table. Different ITC for the violations on the upper or the lower limits can be specified.

Figure 111. An example of the ITC for Mode 2 [52].

As shown in Figure 111, if the voltage U_{mea} violates either upper or lower limit over the deadband, i.e. $\Delta U > 0$, then the immediate response time Δt can be found based on (7.1) to (7.3). A internal clock, $\frac{1}{s}$, is needed for counting and triggering. The clock will be reset to zero either a triggering occurs or the voltage violation is removed. The slow reset can be specified, e.g. -1 instead of -99 in Figure 111. In this way to reduce the response time for triggering if the voltage oscillates around the deadband. For each triggering, the introduced voltage variation, ΔV_{sh}, due to switching shunt can be estimated in (7.4).

$$\Delta V_{sh} = \frac{\Delta Q_{sh}}{\Delta Q_{sh} + S_k''} \approx \frac{\Delta Q_{sh}}{S_k''} \tag{7.4}$$

where ΔQ_{sh} is the reactive power change of a shunt after a triggering. S_k'' is the short-circuit capacity at the station where the switching is triggered, which is not always available. The online short-circuit capacity estimation can be implemented, e.g. the PMU based estimator [92]. However, the quality of the estimation is still not sufficient for applications.

The expected voltage corrections for all shunts connected at the same busbar can be sorted in a merit order. If the short-circuit capacity can be known, then the merit order respected to the effectiveness on the voltage variation can be built. The voltage correction is therefore carried out by picking up the shunt that can mostly correct the violations. An alternative approach is to build the merit order according to the size of the shunts without requiring the accurate short-circuit capacity. As the short-circuit capacity is normally much larger than the shunt power, i.e. the voltage change due to the shunt switching should be smaller than 3% in the intact grid and up to 6% in the N-1 situations, the voltage correction starting from the largest shunt is also valid.

The short-circuit capacities at the controlling buses are dominated by the synchronous generators in the transmission level, where the generators commitments are strongly depending on the market price. In order to assess the possible voltage variation offline, the 2015 network and the hourly economic dispatches scenarios for the whole year are using to calculate the minimum short-circuit capacities through IEC 60909 method at the controlling buses, as the example shown in Figure 112. Assuming all shunts connected at the same bus are switched in/out simultaneously, the voltage variations at each controlling station can thus be estimated from the total shunt nominal reactive power and short-circuit capacities. The results are summarized in Table 37, where the maximum, minimum and the mean short-circuit capacities of the statistic results are presented. The total rated power of shunts can be found from the summarized shunt information in the Appendix E – Shunt controllers in DK1. The N-1 calculation of each balance is not carried out.

Table 37 The voltage variations at each controlling station if all connected shunts are triggered.

Station	Min. Δ%	Mean Δ%	Max. Δ%	Station	Min. Δ%	Mean Δ%	Max. Δ%
ASR400	0.71	0.73	0.84	LOL150	0.79	0.83	1.00
BED150	0.92	0.94	1.20	NSP150	1.03	1.08	1.32
BIL150	0.89	0.92	1.15	NVV150	1.06	1.12	1.48
BJH150	3.19	3.15	4.06	REV400	1.13	1.16	1.34
EDR150	3.51	3.61	4.55	STR150	0.72	0.74	0.92
FER150	1.69	1.75	2.23	TJE150S(Line)	2.24	1.11	2.95
FER400	1.26	1.33	1.82	TJE150(HVDC)	1.92	2.07	4.14
FGD150	1.27	1.32	1.51	TJE400	1.22	3.35	4.31
FGD400	4.02	4.22	5.06	TRI220	5.79	5.91	6.55
IDU400	1.14	1.33	1.36	TRI400	1.53	1.6	1.99
KAE150	0.69	0.72	0.94	VHA150	0.57	0.59	0.75
KAS150SA	1.81	1.84	2.07	VHA400	4.31	4.54	6.26
KAS400	0.64	0.66	0.75	VID150	1.00	1.01	1.22
KIN150	1.36	1.38	1.50	ÅBØ150	0.55	0.58	0.75
LAG400	1.96	2.09	2.55	ÅSP150	1.88	1.92	2.27
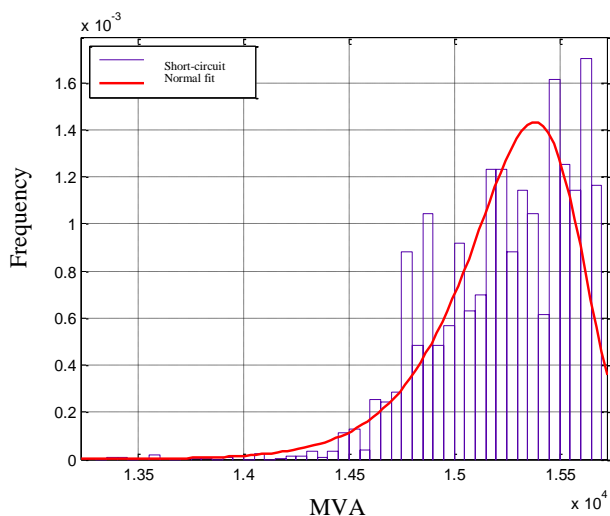
Figure 112. The short-circuit capacity at KAS400 found through the intact network with hourly dispatch scenarios from the market model.

2. GRID DECOMPOSITION FOR THE FALLBACK CONTROLLERS

Triggering a shunt in a station can introduces the voltage changes in the neighboring stations. The purpose of the grid decomposition is to separate the controllers to the different zones according to the controllability on the system. The sensitivity analyses based clustering technique can be applied for grid decomposition [42].

Step 1: Define the controlling bus set, C, and the observation bus set, L, for grid decomposition calculations. The controlling buses are the bus where at least one shunt is connected for the fallback control. The observation buses are the buses where the voltage changes after a shunt is switched in/out at the controlling bus.

Step 2: Compute the sensitivity matrix, $S_{ij} = \frac{\Delta V_{L,i}}{\Delta Q_{C,j}}$. It indicates the voltage changes at the observation bus i respected to the reactive power adjustment on the controlling bus j. As described in Chapter 4 Section 6.1, the sensitivity matrix S_{ij} can be found through (7.5).

$$S_{ij} = (-J_{Q\delta}J_{P\delta}^{-1}J_{PV} + J_{QV})^{-1} \qquad (7.5)$$

Step 3: Calculate the coordinates in the sensitivity space. In the constructed sensitivity matrix, each controlling bus i, is projected to a multidimensional space, represented by a vector $\{S_{i1}, S_{i2} \ldots, S_{ij}\}$, where j denotes the number of the observation bus. In order to enlarge the differences between entries of this matrix, the calculation of their logarithm values is carried out in (7.6).

$$x_{ij} = -log_{10}(|S_{ij}|) \qquad (7.6)$$

Step 4: The data clustering technique is applied to group the controlling buses according to the distance in the sensitivity space. The distances are found through (7.7).

$$D_{mn} = \sqrt{\sum_{k=1}^{N} |x_{mk} - x_{nk}|^2}, \qquad \forall m, n \in C \ \ \forall k \in L \qquad (7.7)$$

Step 5: After cluttering the controlling buses in a particular power balance, the same procedure are carried out for different load flow conditions, e.g. sweep 8760 hourly scenarios to generates a matrix Z_{it}, where i denotes the controlling bus index and t is the hour. The entries of this matrix represent the zone indices of a particular controlling bus i in an hour t over 8760 scenarios.

Step 6: Cluster the busses again based on Z_{it} matrix. In this step, the data clustering techniques is applied again. Step 5 and 6 are considered because the Danish system is a market-driven system, where the unit commitment is depending on the market price. It results in a flexible system with significantly different power flow conditions over a year.

The grid decomposition based on whole year balances for the intact grid is carried out, where total 8760 snapshots are involved, and 8758 snapshots are available for calculations. The result is shown in Table 38 and Figure 113. It can be seen that, Zone 5 and 6 are geographically overlapped based on the proposed method, which indicates (i). the DK1 system is small that nodes are closely sensitive to each other; (ii). the system is very flexible that no fixed zone division can be found. If considering the impact of the shunt switching for a zone, then the zone division should be updated periodically.

Table 38 The zone divisions and corresponding reactive power capacities for fallback controllers.

Zone	Stations	No. of Shunts	Max. valid Q for the fallback (MVar)
1	ASR400,EDR150,KAS150,KAS400,REV400	5	537
2	FGD150,FGD400,KIN150,LAG400	5	415
3	TRI220,TRI400,ÄSP150	2	185
4	BED150,BIL150,BJH150,IDU400,LOL150, STR150,TJE150,TJE400,VID150	13	686
5	FER150,NSP150,NVV150,VHA150,ÅBØ150	7	306
6	FER400,VHA400,TJE150S11	7	441
7	KAE150	1	38
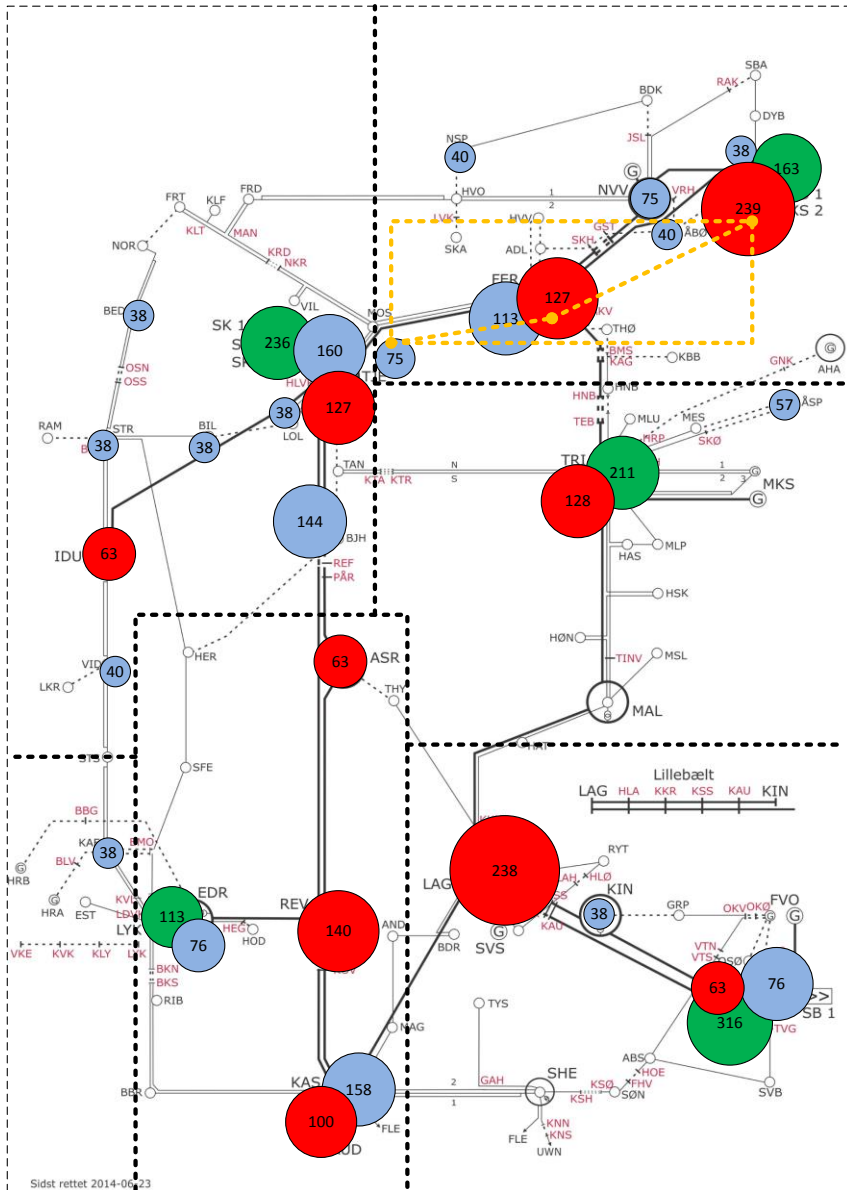
Figure 113. Grid decomposition for DK1. Red and blue colors stand for 400 kV and 150 kV, respectively. The green color stand for the RPC controlled shunts. The value in each colorful circle represents the summation of the nominal reactive power at stations. Black and yellow dash lines split the system into zones. Notice that the yellow zone includes FER400, VHA400 and TJE150S11, that is geographically located inside a black zone. The stations without shunts are not considered.

If cluttering the fallback controllers into zones, the shunts will be grouped into different zones as well. For example, all shunts under fallback scheme in a predefined zone are shown in Table 39. If considering the largest interaction between VHA400 and TJE150S11, i.e. the voltage change at VHA400 of triggering a shunt in TJE150S11 is the same as triggering this shunt at VHA400. If triggering the shunt switching according to the merit order considering the short-circuit capacity, then

the shunts in each zone can be placed at a curve of the time inverse characteristic, as the example shown in Figure 114. Therefore, if the voltage violation occurs at any of the bus in this zone, the largest shunt in this zone will be triggered firstly. The other stations will wait and see how the voltage changes at their terminals and determine if to trigger the next shunt in this zone. This approach treats several buses as one node, and all connected shunts on these buses are considered to be connected to the common node. It requires communications between these stations in the same zone to update the status of the shunt switching in the neighboring stations.

Table 39. Fallback regulation capability in a predefined zone.

Station	Shunts	Shunt size (MVar)	Short-circuit Cap. (MVA)	ΔV(%)
VHA400	VHA_400-ZC1	55.3	8000	0.69
	VHA_400-ZF1	55.3		0.69
	VHA_400-ZF2	20.1		0.25
	VHA_400-ZF3	55.3		0.69
	VHA_400-ZL1	53.5		0.67
FER400	FER_400-ZL1	63.5	9500	0.67
	FER_400-ZL2	63.5		0.67
TJE150S11	THE_150-ZL1-	75.4	3800	1.98
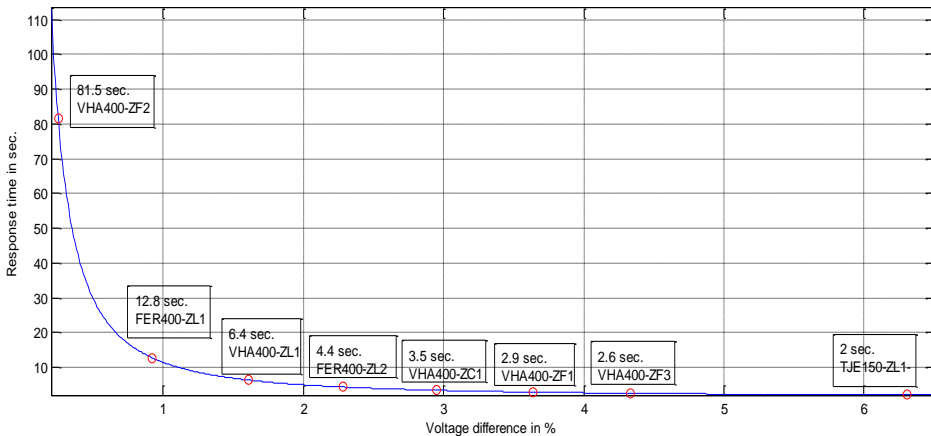
Figure 114. The inverse-time characteristic of a predefined zone.

3. CASE STUDY

The proposed fallback scheme is implemented in the Powerfactory model of the western Danish transmission system (DK1) to demonstrate the effect. The upper and the lower triggering limits in DK1 are defined based on the acceptable operational voltage range, as shown in Table 40. The fallback controlles are implemented in 26 stations.

Table 40 The upper and the lower triggering limits for Mode 2 in DK1.

Nominal Voltage (kV)	Lower triggering limit (kV)	Upper triggering limit (kV)
400	385	420
232	200	245
165	148	170

The purpose of this study is to investigate the impacts of the fallback scheme in the system level. Two scenarios are set up, as shown in Figure 115, where only one central power station and two synchronous condensers are in operation. The fallback controllers employing either the fixed response time or the ITC, are without any coordination in thses studies, and no zone devision is applied.

In Scenario 1, all old type wind turbines are producing the rated power and nearly full import/export capacities on the inter ties. The purpose is to obtain a critical case that the voltage recoveries slowly. In this study, the voltage drops due to the three-phase short-circuit fault at Kassø 400 kV station, marked in Figure 115, (1). The fault is cleared after 150 ms, and one of two 400 kV circuit to Germany is tripped after the fault.
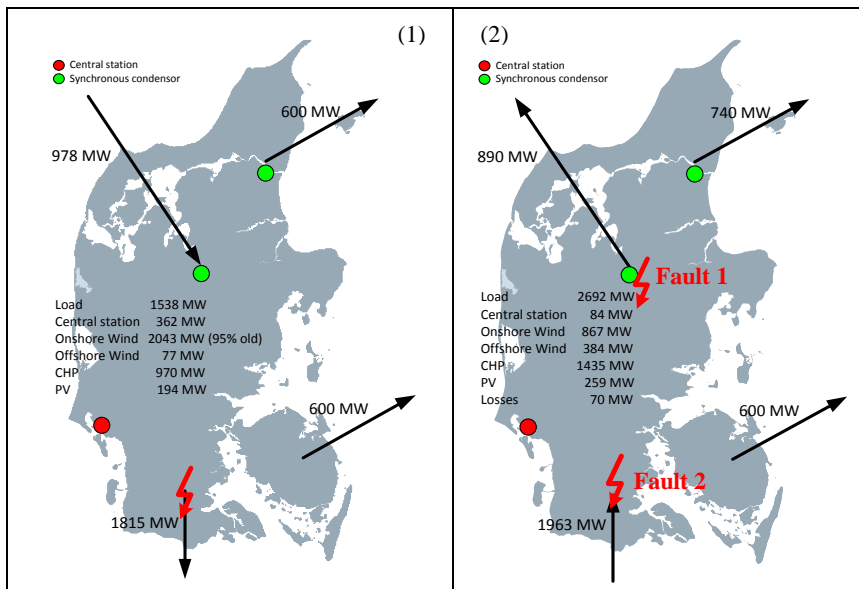
Figure 115. Scenarios of DK1 for the case studies. The short-circuit faults are marked in the figures.

Many CHP units are tripped by the under voltage relays (0.7 pu. for 50 ms.) during the fault. Short after the fault, many old type wind turbines are also tripped by the under voltage relays (0.7 pu. for 500 ms.). Three simulation cases are carried out in Scenario 1, (i). no fallback control; (ii). fallback Mode 2 control triggers the switching with a fixed response time for 1 sec. (iii). Fallback Mode 2 control triggers the switching with a fixed response time for 2 sec. In these cases, Mode 1 is also activated that is under a fixed 15 seconds response time and no inverse time characteristic is applied.
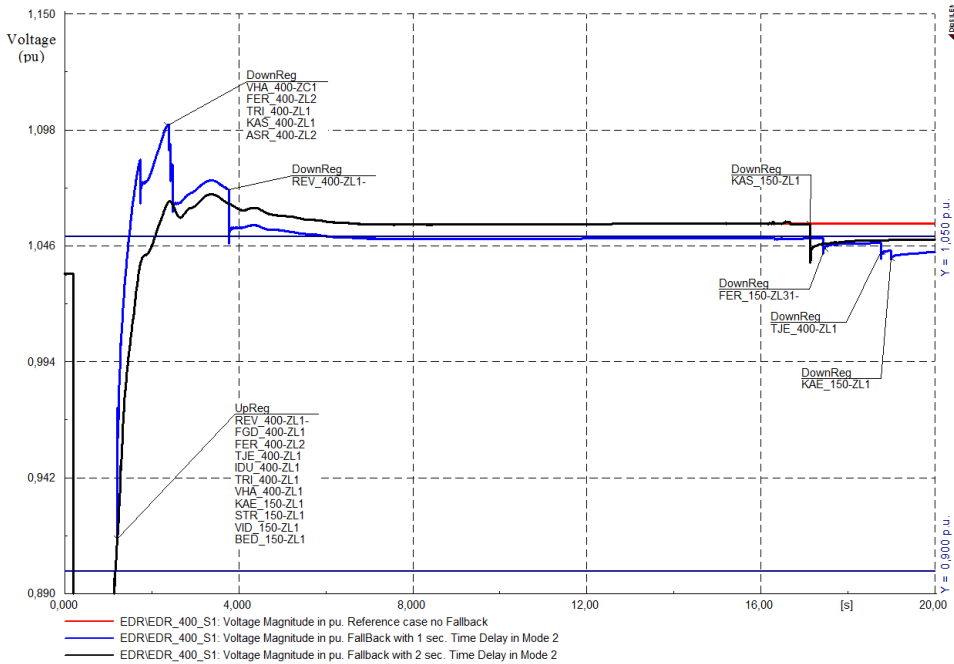
Figure 116. The simulation results without Fallback, with "fast Fallback" (1 sec. time delay in Mode 2) and "slow fallback" (2 sec. time delay in Mode 2).

For all 3 cases in Figure 116, the same amount of CHP and old type wind turbines are disconnected. All the units trip before 1.3 seconds. The voltage suddenly recoveries after many old type wind turbines are disconnected. The voltage magnitude at the end of the simulation is higher than 420 kV in EDR400 kV station and the neighboring stations. If the fallback control is activated, the final voltage can be controlled down into the acceptable range by Mode 1 after 15 sec. The time delay in Mode 2 is set to 1 second and 2 seconds in two simulations, respectively. It seems that 2 sec. is better in this case to avoid the redundant switching. It is due to the fact that it takes more than 1 sec. for the voltage to be higher than 0.9 pu., where many shunts are controlled by the fallback controllers for up regulations. However, the old type wind turbines trip out after the up regulations, which results in the over voltage that requires the down regulation of the fallback control. After about 4 sec. the maximum 400 kV voltage at EDR400 kV station is very close to 1.05 pu. but still higher than it, since there is no available shunt for down regulations. After 15 sec. some shunts in the neighboring stations are cut off for down regulation by Mode 1 of fallback control, which results in the voltage drop down to the acceptable band at EDR 400 kV station.

In this case, it can be seen that many shunts are switched. Moreover, many stations release the reactive power in the beginning of the fault clearance but consume the reactive power later on, e.g. VHA and FER stations. This is due to the missing of the ITC in the fallback controllers.

In Scenario 2, two faults are simulated, where the ITC is applied to all stations. Mode 1 in these studies is blocked. The purpose of these studies is to investigate the voltage correction effeteness of fallback Mode 2 with ITC. In the Fault 1, the HVDC load rejection is simulated following the three phase to ground fault at the HVDC terminal, TJE400. Moreover, the overvoltage relay at TJE400 is malfunctioning that is not able to decouple the filter banks. In the Fault 2, a N-2 situation occur after a busbar fault at KAS400. Two branches from KAS00 to FLE400 and LAG400 are tripped. The results are respectively shown in Figure 117 and Figure 118 [52].

163
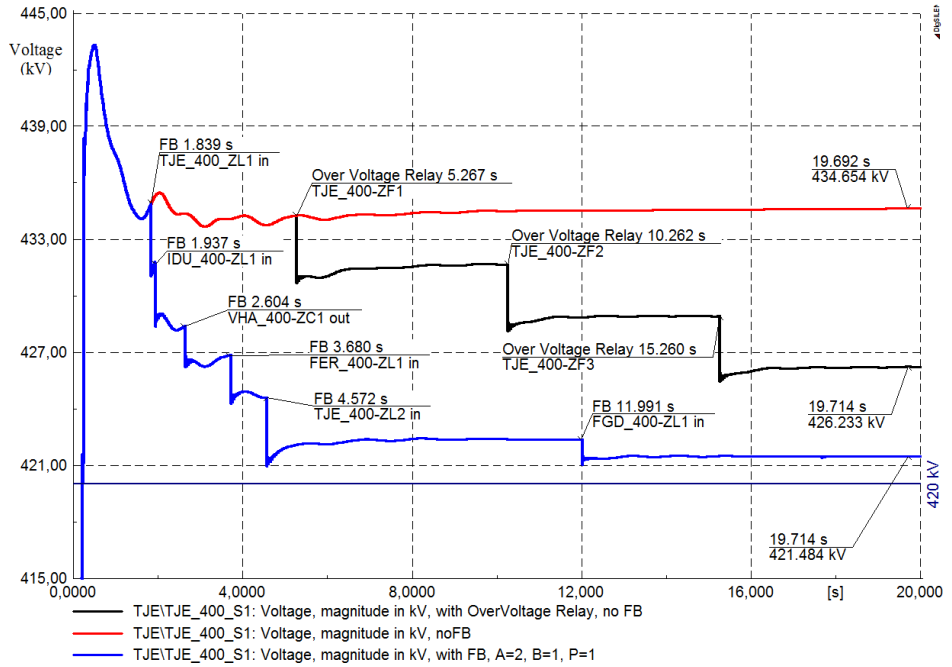
Figure 117. The voltage magnitudes after Fault 1. Red: Over-voltage relays are malfunctioning; Black: over-voltage relays are activated; Blue: Over-voltage relays are malfunctioning but fallback scheme is activated [52].
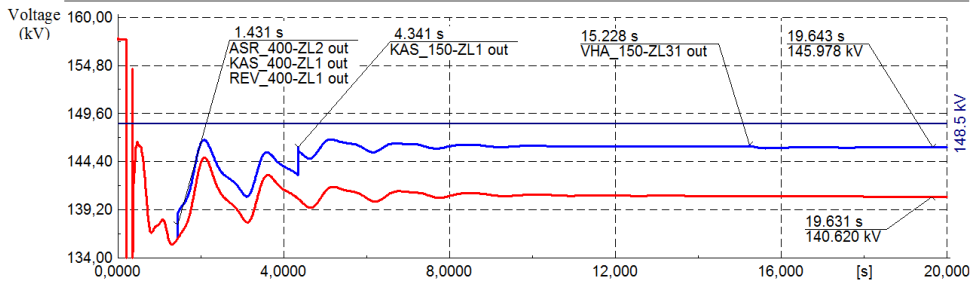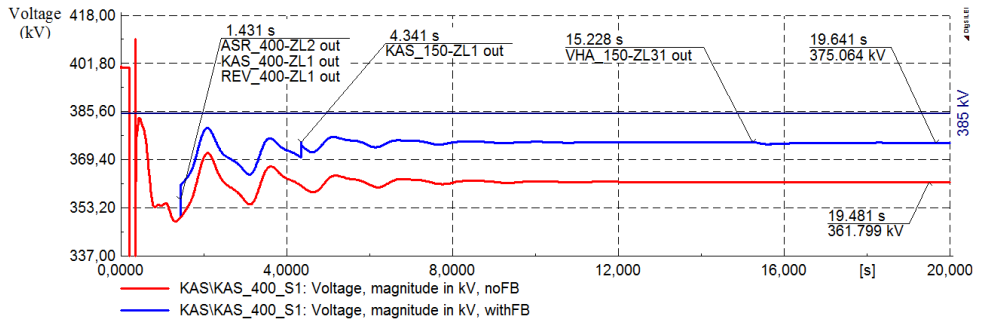
Figure 118. The voltage magnitudes after Fault 2. Red and blue are the results without and with fallback scheme, respectively [52].

As shown in Figure 117, after Fault 1, the over-voltage problem occurs after HVDC load rejection. If the capacitor banks are disconnected by the over-voltage relays, then the voltage can finally settle down to about 426 kV. Otherwise, the voltage will rise to about 435 kV. In case, the over-voltage relays are malfunctioning, the fallback controllers in other stations will connect the available shunt reactors into the grid, by which the voltage can lower down to about 421 kV.

As shown in Figure 118, after Fault 2, the under-voltage problem occurs. It is due to the fault occurs in an important station, which leads to disconnection of the generation units. The import from Germany is therefore increased and heavily loaded the remained grid. It is observed that the fallback controllers in the neighboring stations decouple the reactors to release the reactive power for voltage support. The voltage with the fallback controllers is closer to the acceptable limits than the case without it.

4. SUMMARY

The fallback scheme is expected to be operated if the centralized AVC is malfunctioning. It is designed to have two modes by controlling the assigned shunts, i.e. (i). locally maintain the voltage or compensate the reactive power output of the central units if the telecommunication is lost; (ii). fast correct the voltage violations. Only one mode can be activated at a moment. As the fallback is activated, only one controller can be triggered.

The simulations show that the fallback scheme can locally control the voltage by autonomously switches in/out the station shunts. The inverse time characteristic is a promising approach to avoid the over-regulation for distributed fallback controllers in the different stations to control the voltage without any communication. In the case that several shunts connected to the same busbar, the triggering sequence can be specified via a merit order, e.g. starting from the one with the largest size to the one with the smallest size.

CHAPTER 8. CONCLUSIONS

This ph.d project has mainly been focusing on the three issues, i.e. the Danish AVC concept, the potential benefit assessment of the Danish AVC system and the robustness improvement on such AVC system. In this Chapter, the objectives introduced in Chapter 1 Section 4 are answered, the contribution of this project is described and the future work is proposed.

1. ANSWER TO THE OBJECTIVES

The objective is broken into 5 sub-objectives in short, i.e. (i). Benefit from the loss saving; (ii). Switching cost in the AVC; (iii). Reactive power reserve; (iv). Robustness; and (v). Scalability.
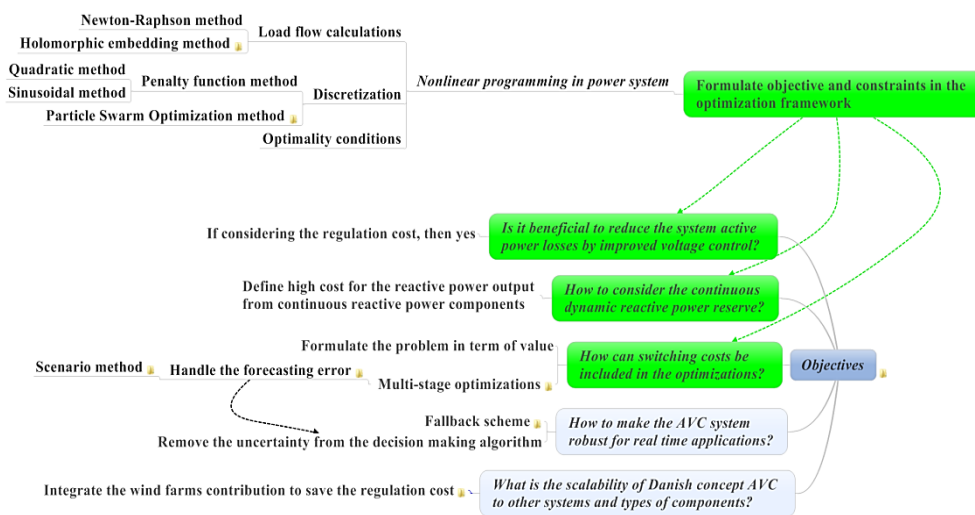
Figure 119. The project objectives and the relevant studies. There are papers for the marked topics, which are presented in Table 41 and Table 42.

The relevant studies are carried out to answer the objective, as shown in Figure 119. This project has been focusing on the problem formulation, implementation and assessments. In order to answer the 5 sub-objectives, a simulation platform is built for assessing the proposed approaches to the AVC decision making process, where the measurement data from EMS of the Danish national control center can be imported for simulations.

The objectives and the relevant constraints including the load flow calculations and discretization are formulated in the optimization framework, which is finally converted to the zero-finding problem through the optimality conditions and solved by Newton iterations. The proposed improvements for the AVC system are therefore proposed based on this framework, which remain the strong tractability and are able to be solved by the sophisticated numerical optimization methods.

The potential saving from the operational cost is investigated through the platform based on the measurement data from EMS. The spot price is coupled to the objective. The cost of each controller to participate in the optimizations is estimated. The different terms in the objective are therefore converted to the common unit, value of the expense. The result is the expected operational cost in term of the expense value at a certain time point.

- Loss minimization

The grid loss can be reduced by optimally control the reactive power components. Two main factors should be considered. The grid loss mainly includes the series loss and shunt loss in the branches, where the series loss dominates the grid loss. In order to minimize the grid loss, the current flowing in the branches should be as small as possible. For the series branches that connecting between two nodes in the grid, the current can be reduced by increasing the voltage magnitude and reduce the voltage magnitude difference between two nodes as much as possible, when the same amount of power is transferred. The shunt branch losses include the transformer no-load loss and the reactor conducting loss, which can be reduced by reducing the terminal voltage magnitude. It is therefore a trade-off between increasing and reducing the voltage magnitude at a node in the system in order to reduce the total grid loss the most. The optimization routines are needed to search for the solutions.

- Considering the regulation cost

The grid loss saving will be finally reflected by the electricity bills to the end consumers. The regulation cost on the components for obtaining the cost saving from the grid loss should also be included. It is meaningless to spend more money on the regulations than the cost saving from the grid loss. In fact the regulation cost should be minimized as well. It is another trade-off between the grid loss saving and the introduced regulation cost. The problem is therefore formulated in term of the expense, where the market price for purchasing the grid loss and the estimated price of regulating each component are takin into account.

The price of the spot market is indeed the Lagrangian multiplier of the power balance in the market clearing algorithm. The value of the spot market price indicates how much money to pay in order to maintain the power balance while maximizing the social welfare. The grid loss may improve or harm the system balance in the physical dispatch period, by increasing or reducing the amount of the unbalance power. The total amount of unbalance power should be purchased from the balancing market. However, the grid loss is settled according to the price from the spot market. In the proposed reactive power flow optimization, the regulation is carried out more reasonable after coupling to the spot price. The voltage under the negative price period can even be reduced for generating the loss for obtaining the negative cost of the grid loss. It can be considered as a consequence of integrating the large amount of the wind energy, i.e. excessing power leads to the negative price that force the voltage profile reduces in order to save the money by increasing the grid loss. By considering the real cost of each term in the optimization framework, the solutions provide precise values of the operational cost to the operators and operate the system in a more economical way.

The high penetration of the wind power in the Danish system introduces large variability into the system. The MORPF is proposed to optimize the voltage addressing the system variability. By capturing the system variability, the solution is better in term of the cost minimization than the conventional ORPF method. The optimality condition of the MORPF and its relation to the dynamic programming is derived. The case studies validate the superiority.

In the optimization framework, the discrete components are linearized. The continuous optimization is firstly carried out to find a local optimal solution. The discretization process is then performed applying the sinusoidal penalty functions to force the discrete variables approaching to the integers. In this ways, the entire formulation is pure nonlinear programming problem that can be solved efficiently by the existing sophisticated nonlinear programming techniques, such as combined PDIPM and TR method. Strong tractability can be expected.

- Reactive power reserve

The reactive power inside the continuous reactive power components should be maintained as much as possible, in order to provide the emergent voltage support by quickly injecting the reactive power within several milliseconds. In the AVC system, the reactive power output of the generator is expected to be limited close to the neutral. It can be considered by either setting the hard limits on the

regulation capabilities or by setting the regulation cost function on the reactive power outputs. The former approach is rigid that may bring the difficulty to the tractability. The latter approach is therefore preferred. There is normally no clear cost function for the generator to regulate the reactive power, as the power plants owners are reluctant to share the information. Physically, injecting the reactive power will introduce the loss inside the machines and the step-up transformers. However, considering the business case that the plant owner needs to take the responsibility for providing the ancillary service when it is needed by the transmission operators, the price of the reactive power output may be increased significantly. After estimating the cost in term of kr/MVar, the optimization procedure can take the cost function into account and find the solution to minimize the total operational cost.

In some period when there are few central power plants in the operation, the price of generator reactive power output can be increased to force the reactive power being reserved inside the generators. It represents the latent attitude of the system operators to maintain the system security, though the actual cost may be small.

- Robustness

On top of the operational cost minimization, the voltage security has the highest priority. It means that the voltage magnitude should be always controlled within the acceptable band though it may lead to large operational cost in some periods.

In the proposed AVC system, MORPF addressing the system variability to provides the better solution that has lower operational cost than it found from the conventional ORPF. It involves several stages that are obtained from the forecasting system. However, the variability is not the uncertainty.

The uncertainty is the invisible deviations from the expected values that only observed from the realizations. Though the power forecasting system can well predict the short-term system condition and capture the system variability, however, the uncertainty always exists that is the forecasting errors. The robustness improvement is proposed to take into account the uncertainty by reserving the VSM in the decision making process of the AVC system. In the case that the forecasting system can successfully estimate the system condition, it will result that forecasting errors concentrate to zero mean and spread around zero mean in an acceptable range. The multivariate normal distribution can be applied to approximate the forecasting errors. The VSM can therefore be derived analytically. Depending on the accuracy of the forecasting system, the size of the VSM to cover the wind power forecasting errors can vary. From the simulations based on the measurement data in the DK1 system, it can conclude that reserving the VSM for addressing the uncertainty will result in more operational cost but acceptable when the forecasting errors are minor.

The fallback scheme is a backup solution that can be operated locally without telecommunications. It takes place when the central AVC is malfunctioning. The inverse-time characteristic is employed for each local station. The fallback controller monitors the station voltage and triggers the shunt switching to correct the voltage violations in the predefined order. The simple logic to trigger the switching is from the shunt that has the largest size to the one that has the smallest size. The performance can be improved if estimating the possible voltage change after each switching. However, it requires the online short-circuit capacity estimations. The robustness of the entire AVC system is considered to be promoted by embedding the fallback scheme.

- Scalability

Different components can be modelled and placed in the formulation of the decision making process of the AVC system. The large wind farms are considered as power plants in the system that can regulate the reactive power to participate in the voltage control. The response time of the wind farm should be considered, as the wind farm needs to find out the required reactive power injection for each wind turbine and dispatch the setpoints for implementations. However, in the proposed MORPF

framework that dispatches the setpoint every 15 minutes, it is sufficient for the wind farm controller to further dispatch the setpoints for each wind turbine. The reactive power regulation capability of the wind farm depends on the number of operating wind turbines in a time point. Therefore, the wind farms should periodically inform the central AVC about the current regulation capability.

With the contribution of the wind farms in the AVC system, the loss on the long submarine cables connecting between the offshore wind farms to the onshore stations are reduced. In the case study, the estimated annual profit from the proposed MORPF will be about 5.3 million DKK, if the reactive power cost is 0.1 DKK/MVar for all continuous reactive power components including the large offshore wind farms. Furthermore, the transformer regulation cost on the offshore platform is reduced by applying the reactive power regulation capability of the wind farm to maintain the voltage. In addition to the cost reduction, more reactive power can be reserved in the continuous reactive power components, which increases the system security.

2.   THE CONTRIBUTIONS

This project focuses on the AVC system design, formulation and decision making algorithm implementation. The AVC decision making process is well formulated in the MORPF framework. It is derived in the recursive manner, where the problem is solved using combined PDIPM and TR methods. The optimality condition is achieved by approximating the problem into the nonlinear programming framework and finally converting to the zero-finding problem, and solved by Newton iterations. The discrete variables including the shunt susceptance and the transformer tap positions are treated as continuous variables in the framework and discretized applying the sinusoidal penalty function to force them to close to the integer values while complying with the optimality conditions. During the discretization process, the variables shunts, i.e. ideal transformers connected to switchable shunts in series, requires the logic to determine the tap position, i.e. identifying the shunt states and then determine if fixing the tap position to the bottom when shunt is switched off. The MORPF formulation solved by the nonlinear programming techniques and the penalty function based method is strongly tractable and robust, which is considered a promising approach for the real time applications comparing to the heuristic methods.

In order to demonstrate the proposed approach, the offline simulation platform is built, where the real measurement data can be imported for the calculations. This platform can be used for future case studies and analyses in the industrial applications. In addition, all functions in the simulation platform are coded in the Matlab® environment, which are easy to be used and modified for other applications. The simulation platform is based on the MatPower [89] with great extensions. MatPower is originally used for educations, which can solve the load flow equations and the economical dispatch problem. In order to solve the ORPF problem, new functions are developed, e.g. defining the control variables for the ORPF optimization, the relevant gradients and hessian matrices of the objective and the constraints w.r.t. to the decision variables etc. The discretization algorithm including handling the variable shunt, the SBA and VSM based robustness improvement methods and NORTA for generating the random vectors to capture the spatio-temporal correlation of the forecasting errors for the Monte Carlo simulations. In addition, in order to symmetrically assess a large number of cases, the automatic simulation procedure is implemented, which consequently executes the optimization, updating the setpoints from the previous result, executing the optimization algorithm and exporting the results to external files. The result files include the system conditions, the control variable values before/after the optimizations, the numerical settings and the general assessments such as the maximum/minimum voltage magnitude before/after the optimizations. It provides a systematical way to assess the results.

The proposed AVC system is centralized control system that dispatches the setpoints to the reactive power components periodically. In case the voltage violation occurs after the dispatch, it needs to wait at least a cycle to update the setpoints. In addition, if the AVC is malfunctioning, the system voltage should be able to be maintained without any severe problems. Therefore, the fallback scheme

is proposed that is embedded in the substation to control the local shunts for maintaining the local voltage. The triggering signals are created if the voltage magnitude at the local station is violated and the shunts will triggered from the large to the small size following the inverse time characteristic. In this way, these localized controllers can maintain the voltage profile without any communication. The overall robustness, in this way, is enhanced.

During this project, some papers are published to share the experience during the research, as shown in Table 41. Paper E. is a state-of-art study of the existing AVC systems, which inspires the Danish AVC concept. Paper D. presents the fallback scheme that controls the local shunts to maintain the voltage without communication in case the centralized AVC is malfunctioning. Paper C. is a preliminary study of the MORPF approach for the AVC decision making process, where the IEEE-39 node system is used to demonstrate the idea. Paper B. presents the SBA to handle the voltage uncertainty caused by the wind power forecasting errors. Paper A. studies the MORPF in detail, i.e. the MORPF framework is derived in the recursive manner, and the VSM is proposed to improve the robustness under the uncertainty. The measurement data is applied for the case studies in a symmetrical way, verify the superiorities of the proposed method for the Danish AVC system.

Table 41. Publication list.

A. **N. Qin**, C. L. Bak, H. Abildgaard and Z. Chen, "Multi-stage optimization based automatic voltage control systems considering wind power forecasting errors," *IEEE Transaction on Power Systems*, May 2016.

B. **N. Qin**, H. Abildgaard, D. Flynn *et al.*, "Voltage control system under uncertainty from wind power," *Power Systems Computation Conferences*, Genoa, June 2016.

C. **N. Qin**, S. Chen, C. Liu *et al.*, "Multi-period optimization for voltage control system in transmission grid," *IEEE PES General Meeting*, Denver, July 2015.

D. **N. Qin**, E. Dmitrova, T. Lund, P. Lund, H. Abildgaard, C. L. Bak and Z. Chen, "Robust fallback scheme for Danish voltage control system," *PES PowerTech*, Eindhoven, June 2015.

E. **N. Qin**, H. Abildgaard, P. Lund *et al.*, "Automatic voltage control (AVC) of Danish transmission system – concept design," *Cigré USNC*, Houston, October 2014.

F. C. Liu, **N. Qin** and C. L. Bak, "A hybrid optimization method for reactive power and voltage control considering power loss minimization," *PES PowerTech*, Eindhoven, June 2015.

In addition, Paper F. proposes a discretization method that combines the PDIPM and the Particle Swarm Optimization method, intent to search for the global optimal solution in the discretization process. It is time-consuming and unreliable that is not finally applied in the later studies.

Table 42. The planned publications.

G. **N. Qin**, C. L. Bak, H. Abildgaard and Z. Chen, "Automatic voltage control system employing large wind farms considering market price," *Electric Power Systems Research*.

H. **N. Qin,** C. Liu, H. Abildgaard *et al.*, "Implementation of holomorphic embedding load flow method with phase-shifting transformers and generators remote voltage control," *Electric Power Systems Research*.

Two articles are planned to be published, that are shown in Table 42. Paper G. is a case study to employ the wind farm in the AVC system and systematically assess the contributions of the wind farms to the voltage control system considering the prices of the reactive power outputs. Paper H. presents the implementation work of the HELM method for the load flow calculations. It will compare the existing method to handle the ill conditioning cases.

3. THE FUTURE WORK

There is an ongoing project in the Danish TSO, Energinet.dk, to implement the centralized AVC system in the transmission grid. This project is expected to shed light on the industrial applications. In return, new ideas and improvements will be obtained to further develop the proposed approach.

The offline simulation platform can be further improved for the business cases in the planning stage or to assist the operations. The method to include the variable shunts in the AVC decision making process as well as reserving the VSM for handling the uncertainty are ready to be implemented. Coupling to the forecasting system to capture the system variability and the market price to operate the system in an economic way needs much work to establish the interfaces. Energinet.dk has already started to predict the wind power in the substation levels in addition to the zone levels, which is considered to be the first step towards the final Danish AVC system.

The fallback scheme is already on the process of implementation, and applied as a countermeasure to prevent the voltage instability caused by the Type I wind turbines after fault clearance. The field test data is expected to be obtained to improve the performance, e.g. tune the inverse-time characteristic to properly release the reactive power to support the voltage after the normative faults in the areas where many Type I wind turbines are connected.

In this project, the HVDC links are modelled by either load connected to the PQ nodes or the generator connected to the PV nodes. The large wind farms are modelled as the generators connected to the PV nodes. The internal losses of them are neglected. The representations of these components can be improved, e.g. modeling these components separately and coupled to the network model via interfaces through PQ/PV variables. In this way, more precise results can be expected for assessing the operational cost and the component status.

The numerical optimization methods are still a core of the AVC decision making process. In this project, the existing sophisticated nonlinear programming techniques are applied to solve the formulated problem. It is a local optimal solution. The method to obtain the global optimal solution for the real time applications is still a challenging task.

In the AVC system, HELM is able to identify if a solution to an ill conditioning load flow condition physically exists. It can be an additional function of the AVC system to secure the validity of the calculations. It would also be interesting to develop the optimization method coupling to HELM. The results from the HELM are polynomial series. The new optimization routine is needed, to efficiently solve the optimization problem involving the high degree polynomial series. If so, the newton based method to solve the optimization problem in the AVC system can be replaced.

The uncertainty in the AVC system can conduct many studies. Implementation of the SBA in the large scale system may be carried out by applying the parallel calculation methods to increase the calculation speed. The tractability should be assessed. Furthermore, the scenario generation/reduction methods for better approximate the uncertainty distributions can be conducted. The VSM for handling the uncertainty can be implemented both offline and online. In the offline studies, the VSM at each substation can be derived based on the historical observations. In the online applications, the VSM will be updated according to the results of the forecasting system, i.e. a probabilistic forecasting

system provides the possible deviation from the expected values that can be used to derive the VSM in the AVC decision making process. More analyses and assessments will be conducted.

The measurement system and the state estimator can be updated in the future AVC system, as more and more PMU devices are placed in the grid. The transition from the conventional SCADA/SE system to the mixture PMU and SCADA system and finally to the PMU/SE system can be studied. In the state estimator, the different measurements cycles from SCADA and PMU should be well handled. The method to treat the uncertainty including the measurement failures in the state estimator in such system can be conducted. It is considered to be an important issue related to the performance of the future AVC system.

REFERENCES

[1] Energinet.dk, "Annual report 2015," 2015. Available online.

[2] Danish Ministry of Climate and Energy, "Release of Danish Energy Strategy 2050," Feb. 2011.

[3] NordPool, Available online: http://www.nordpoolspot.com/About-us/History/

[4] Energinet.dk, "Analysis of assumptions," 2015. Available online.

[5] Energinet.dk, "System plan," 2015. Available online.

[6] Energinet.dk, "Cable action plan 132-150 kV," May 2011. Available online.

[7] Energinet.dk, "Technical regulation 3.2.5 for wind power plants with a power output greater than 11 kW," Sep. 2010.

[8] C. Bengtsson, T. Olsson, K. Olsson *et al*. "*Design and testing of 300 Mvar shunt reactors,*" 42nd *CIGRÉ session*, Paris, 2008,

[9] Energinet.dk, Fingrid, Statnett and Svenska Kraftnät, "Agreement regarding operation of the interconnected Nordic power system". 2006. Available online.

[10] D. S. Popovic and V. A. Levi, "Extension of the load flow model with remote voltage control by generator," *Electric Power Systems Research*, vol. 25, no. 3, pp. 207-212, Dec. 1992.

[11] W. Tinney and C. E. Hart, "Power flow solution by newton's method," *IEEE Trans. on Power Apparatus and Systems.*, vol. PAS-86, no.11, pp. 1449-1460, Nov. 1967.

[12] S. Iwamoto and Y. Tamura, "A Fast Load Flow Method Retaining Nonlinearity," in *IEEE Transactions on Power Apparatus and Systems*, vol. PAS-97, no. 5, pp. 1586-1599, Sept. 1978.

[13] S. Iwamoto and Y. Tamura, "A Load Flow Calculation Method for Ill-Conditioned Power Systems," in *IEEE Transactions on Power Apparatus and Systems*, vol. PAS-100, no. 4, pp. 1736-1743, April 1981.

[14] M. D. Schaffer and D. J. Tylavsky, "A nondiverging polar-form Newton-based power flow," in *IEEE Transactions on Industry Applications*, vol. 24, no. 5, pp. 870-877, Sep/Oct 1988.

[15] V. Ajjarapu and C. Christy, "The continuation power flow: a tool for steady state voltage stability analysis," in *IEEE Transactions on Power Systems*, vol. 7, no. 1, pp. 416-423, Feb 1992.

[16] A. Trias, "The Holomorphic Embedding Load Flow Method," *IEEE PES GM,* San Diego, CA, Jul. 2012.

[17] S. S. Baghsorkhi and S. P. Suetin, "Embedding AC Power Flow with Voltage Control in the Complex Plane: The Case of Analytic Continuation via Padé Approximants," *arXiv.org*, available online: http://arxiv.org/pdf/1504.03249v1.pdf, Mar. 2015.

[18] A. Trias, "Fundamentals of the Holomorphic Embedding Load-Flow Method," *arXiv.org*: http://arxiv.org/pdf/1509.02421.pdf, Sep. 2015.

[19] M. K. Subramanian, "Application of Holomorphic Embedding to the Power-Flow Problem," *Master Thesis*, Arizona State Univ., Aug. 2014.

[20] M. K. Subramanian, Y. Feng and D. Tylavsky, "PV bus modeling in a holomorphically embedded power-flow formulation," *North American Power Symposium*, Manhattan, KS, USA, Sep. 2013.

[21] G. Baker and P. Graves-Morris, "Padé approximants," *Series: Encyclopaedia of Mathematics and its applications*, Cambridge University Press, New York, 1996.

[22] H. Stahl, "On the Convergence of Generalized Padé Approximants," *Constructive Approximation*, vol. 5, no. 1, pp. 221–240, 1989.

[23] H. Stahl, "The Convergence of Padé Approximants to Functions with Branch Points," *Journal of Approximation Theory*, vol. 91, no. 2, pp. 139–204, 1997.

[24] A. Cuyt and L. Wuytack. "Nonlinear methods in numerical analysis," *North Holland*, 1987.

[25] A. Trias, "Fundamentals of the Holomorphic Embedding Load-Flow Method," *arXiv.org*: http://arxiv.org/pdf/1509.02421.pdf, Sep. 2015.

[26] A.Cuyt, V.B.Petersen, B.Verdonk, H.Waadeland and W.B.Jones, "Handbook of Continued fractions for special functions," *Springer*, 2008.

[27] M. K. Subramanian, Y. Feng and D. Tylavsky, "PV bus modeling in a holomorphically embedded power-flow formulation," *North American Power Symposium*, Manhattan, KS, USA, Sep. 2013.

[28] S. S. Baghsorkhi and S. P. Suetin, "Embedding AC Power Flow with Voltage Control in the Complex Plane: The Case of Analytic Continuation via Padé Approximants," *arXiv.org*, available online: http://arxiv.org/pdf/1504.03249v1.pdf, Mar. 2015.

[29] S. Granville, "Optimal reactive dispatch through interior point methods," *IEEE Trans. Power Sys.,* vol. 9, no. 1, pp. 136-146, Feb. 1994.

[30] S. Granville, J. C. O. Mello and A. C. G. Melo, "Application of interior point methods to power flow unsolvability," *IEEE Trans. on Power Systems*, vol. 11, no. 2, pp. 1096-1103, May 1996.

[31] J. Nocedal and S. J. Wright, "Numerical Optimization Second Edition," *Springer*, 2006.

[32] Byrd, R. H., J. C. Gilbert, and J. Nocedal, "A Trust Region Method Based on Interior Point Techniques for Nonlinear Programming," *Mathematical Programming*, vol. 89, no. 1, pp. 149–185, 2000.

[33] A. A. Sousa, G. L. Torres and C. A. Canizares, "Robust Optimal Power Flow Solution Using Trust Region and Interior-Point Methods," in *IEEE Transactions on Power Systems*, vol. 26, no. 2, pp. 487-499, May 2011.

[34] Mohamed A.H. El-Sayed, "Artificial neural network for reactive power optimization," *Neuromputing*, vol 23, issues 1-3, pp. 255-263, Dec. 1998.

[35] V.Ya. Lyubchenko, D.A. Pavlyuchenko, "Reacive Power and Voltage Control By Genetic Algorithm and Artificial Neural Network," *International Journal on Technical and Physical Problems of Engineering*, vol. 1, no. 1, pp 23-26, Dec. 2009.

[36] Aftaf Q.H. Badar, B.S. Umre, A.S. Junghare, "Reactive Power control using dynamic particle swarm optimization for real power loss minimization*," International Koruna of Electrical Power & Energy Systems*, vol 41, issue 1, pp 133 – 136, Oc. 2012.

[37] G. Blanchon, "A new aspect of studies of reactive energy and voltage of the networks," *proceedings of the Power Systems Computation Conference*, Grenoble, 1972.

[38] H. Vu, P. Pruvot, C. Launay and Y. Harmand, "An improved voltage control on large-scale power system," in *IEEE Trans. on Power Systems*, vol. 11, no. 3, pp. 1295-1303, Aug. 1996.

[39] H. Lefebvre, D. Fragnier, J. Y. Boussion, P. Mallet and M. Bulot, "Secondary coordinated voltage control system: feedback of EDF," *Power Engineering Society Summer Meeting, 2000. IEEE*, pp. 290-295 vol. 1, Seattle, WA, 2000.

[40] S. Corsi, "Closure of "The coordinated automatic voltage control of the Italian transmission grid - part I: reasons of the choice and overview of the consolidated hierarchical system"," in *IEEE Transactions on Power Systems*, vol. 21, no. 1, pp. 445-446, Feb. 2006.

[41] P. Lagonotte, J. C. Sabonnadiere, J. Y. Leost and J. P. Paul, "Structural analysis of the electrical system: application to secondary voltage control in France," in *IEEE Transactions on Power Systems*, vol. 4, no. 2, pp. 479-486, May 1989.

[42] H. Sun, Q. Guo, B. Zhang, W. Wu and B. Wang, "An Adaptive Zone-Division-Based Automatic Voltage Control System With Applications in China," in *IEEE Transactions on Power Systems*, vol. 28, no. 2, pp. 1816-1828, May 2013.

[43] J. P. Paul, J. Y. Leost and J. M. Tesseron, "Survey of the Secondary Voltage Control in France : Present Realization and Investigations," in *IEEE Transactions on Power Systems*, vol. 2, no. 2, pp. 505-511, May 1987.

[44] M. D. Ilic, Xiaojun Liu, G. Leung, M. Athans, C. Vialas and P. Pruvot, "Improved secondary and new tertiary voltage control," in *IEEE Transactions on Power Systems*, vol. 10, no. 4, pp. 1851-1862, Nov. 1995.

[45] M. Geidl, "Implementation of coordinated voltage control for the Swiss transmission system," *Melecon 2010 - 2010 15th IEEE Mediterranean Electrotechnical Conference*, pp. 230-236, Valletta, 2010.

[46] N. Qin, H. Abildgaard, P. Lund *et al.*, "Automatic voltage control (AVC) of Danish transmission system – concept design," *Cigré USNC*, Houston, Oct. 2014.

[47] J. H. Walker, "Operating characteristics of salient-pole machines," in *Proceedings of the IEE - Part II: Power Engineering*, vol. 100, no. 73, pp. 13-24, February 1953.

[48] N. Janssens, "Tertiary and secondary voltage control for the Belgian HV system," *International Practices in Reactive Power Control, IEE Colloquium on*, pp. 8/1-8/4, London, 1993.

[49] P. Frias, T. Gomez and D. Soler, "Voltage control and reactive power support in the Spanish transmission network," *MELECON 2006 IEEE Mediterranean Electrotechnical Conference*, pp. 916-919, Malaga, 2006.

[50] V. R. Vinnakota, B. Brewer, D. Atanackovic, A. Steed, G. Dwernychuk and D. Cave, "Implementation of OPF as a supportive system voltage control tool in real-time for British Columbia transmission network," *IEEE PES General Meeting*, pp. 1-8, Minneapolis, MN, 2010.

[51] N. Qin, S. Chen, C. Liu, H. Abildgaard, C. L. Bak and Z. Chen, "Multi-period optimization for Voltage Control system in transmission grids," *2015 IEEE Power & Energy Society General Meeting*, pp. 1-5, Denver, CO, 2015.

[52] N. Qin *et al*., "Robust fallback scheme for the Danish automatic voltage control system," *PowerTech, 2015 IEEE Eindhoven*, pp. 1-6, Eindhoven, 2015.

[53] Energinet.dk, "Cell Controller Pilot Project Public Report," 2011. Available online.

[54] Å. Carlson, "Shunt Reactor Manual, "*ABB Power Technology Products/Transformers*, Ludvika-Sweden, Aug. 2002.

[55] Mohammad Khorami, "Application Fields and Control Principles of Variable Shunt Reactors with Tap-Changer," *Master of Science Thesis*, Dep. Of Energy and Environment, Division of Electric Power Engineering, Chalmers University of Technology, Göteborg, Sweden, 2011.

[56] J. C. Villumsen, G. Brønmo and A. B. Philpott, "Line capacity expansion and transmission switching in power systems with large-scale wind power," in *IEEE Transactions on Power Systems*, vol. 28, no. 2, pp. 731-739, May 2013.

[57] NordPool, Available online: http://www.nordpoolspot.com/How-does-it-work/Day-ahead-market-Elspot-/

[58] Yong-jun Zhang and Zhen Ren, "Optimal Reactive Power Dispatch Considering Costs of Adjusting the Control Devices," in *IEEE Transactions on Power Systems*, vol. 20, no. 3, pp. 1349-1356, Aug. 2005.

[59] Entso-e, "UCTE operation handbook, Policy 3," Jun, 2004.

[60] R. Caponetto, L. Fortuna, S. Fazzion and M.G. Xibilia, "Chaotic sequences to improve the performance of evolutionary algorithms," *IEEE Trans. Evol. Comput.*, vol. 7, no. 3, pp. 289-304, Jun. 2003.

[61] P. Bajpai and S. N. Singh, "Fuzzy adaptive particle swarm optimization for bidding strategy in uniform price spot market," *IEEE Trans. Power Syst.*, vol. 22, no. 4, pp. 2152-2160, Nov. 2007.

[62] E.M. Soler, E.N. Asada and G.R.M. de Costa, "Penalty-Based Nonlinear Solver for Optimal Reactive Power Dispatch with Discrete Controls," *IEEE Trans. Power Sys.*, vol. 28, no. 3, pp. 2174-2182, Apr. 2013.

[63] M. Liu, S. K. Tso and Y. Cheng, "An extended nonlinear primal-dual interior-point algorithm for reactive-power optimization of large-scale power systems with discrete control variables," *IEEE Trans. Power Sys*, vol.17, no.4, pp.982-991, Nov. 2002.

[64] Matlab R2014a, available online: http://www.mathworks.com

[65] R. Bellman, "The Theory of Dynamic Programming," The Rand Corporation, Jul. 1954.

[66] Energinet.dk, "Technical regulation for thermal power station units of 1.5 MW and higher," *Regulation for gird connection*, Oct. 2008.

[67] X. Zhu and M. G. Genton, "Short-Term Wind Speed Forecasting for Power System Operations," *International Statistical Review*, vol. 80, no. 1, pp 2–23, Apr. 2012.

[68] P. Ramirez and J. A. Carta, "Influence of the Data Sampling Interval in the Estimation of the Parameters of the Weibull Wind Speed Probability Density Distribution: A Case Study, " *Energy Conversion and Management*, vol. 46, no. 15-16, pp. 2419-2438, 2005.

[69] J. Tastu, P. Pinson, P. J. Trombe and H. Madsen, "Probabilistic Forecasts of Wind Power Generation Accounting for Geographically Dispersed Information," in *IEEE Transactions on Smart Grid*, vol. 5, no. 1, pp. 480-489, Jan. 2014.

[70] B. Fox, L. Bryans, D. Flynn *et al.*, "Wind Power Integration: Connection and System Operational Aspects (2nd Edition)," Chapter 6, *IET Power and Energy Series 50*, 2014.

[71] G. Giebel, "The State-of-art in short-term prediction of wind power – a literature overview," Project report, *Project ANEMOS*, Aug. 2003.

[72] J. Tastu, P. Pinson and H. Madsen, "Multivariate conditional parametric models for a spatio-temporal analysis of short-term wind power forecast errors," *Proceedings of the European Wind Energy Conference*, Warsaw, Poland, 2010.

[73] P. Pinson, G. Papaefthymiou, B. Klockl *et al*., "From probabilistic forecasts to statistical scenarios of short-term wind power production," *Wind Energy*, vol. 12, No. 1, pp.51-62. 2009.

[74] J. Tastu, P. Pierre, E. Kotwa *et al*., "Spatio-temporal analysis and modeling of short-term wind power forecast errors," *Wind energy*, vol.14, no. 1, pp.43-60, 2011.

[75] J. Tastu, P. Pinson and H. Madsen, "Space-time trajectories of wind power generation: Parameterized precision matrices under a Gaussian copula approach," *Lecture Notes in Statistics: Modeling and Stochastic Learning for Forecasting in High Dimension*, Springer, pp. 267-296.

[76] L. Xie, Y. Gu, X. Zhu and M. G. Genton, "Short-term Spatio-temporal Wind Power Forecast in Robust Look-ahead Power System Dispatch," *IEEE Transactions on Smart Grid*, Vol.5, No.1, pp. 511 - 520, Jan 2014.

[77] M. He, L. Yang, J. Zhang and V. Vittal, "A spatio-temporal analysis approach for short-term wind-farm generation forecast," *IEEE Transactions on Power Systems*, vol. 28, no. 4, pp. 1611-1622, 2014.

[78] N. Qin, C. L. Bak, H. Abildgaard and Z. Chen, "Multi-stage optimization based automatic voltage control systems considering wind power forecasting errors," *IEEE Transaction on Power Systems* (Accepted).

[79] B. Hodge, D. Lew, M. Milligan *et al.*, *"*Wind power forecasting error distributions: An international comparison,*" 11th International Workshop on Large-Scale Integration of Wind Power into Power System,* Lisbon, Portugal, 2012.

[80] H. Heitsch and W. Romisch, "Generation of multivariate scenario trees to model stochasticity in power management," in *Power Tech, IEEE Russia*, vol., no., pp.1-7, 27-30 June 2005.

[81] L. Wu, M. Shahidehpour and T. Li, "Stochastic Security-Constrained Unit Commitment," *Power Systems, IEEE Transactions on* , vol.22, no.2, pp.800-811, May 2007.

[82] N. Qin, H. Abildgaard, D. Flynn *et al*., "Voltage control system under uncertainty from wind power," *Power Systems Computation Conferences*, Genoa, Jun. 2016.

[83] M. Vrakopoulou, S. Chatzivasileiadis, E. Iggland *et al.*, "A Unified Analysis of Security-Constrained OPF Formulations Considering Uncertainty, Risk, and Controllability in Single and Multi-area Systems," *IREP Symposium-Bulk Power System Dynamics and Control*, Greece, Aug. 2013.

[84] M. C. Cario and B. L. Nelson, "Modeling and generating random vectors with arbitrary marginal distributions and correlation matrix," *Technical Report*, Dep. Of Industrial Engineering and Management Sciences, Northwestern University, Evanston, Illinois, 1997.

[85] J.D. Gibbons, "Nonparametric Statistical Inference," 2nd ed., *M. Dekker*, 1985.

[86] F. C. Schweppe and J. Wildes, "Power System Static-State Estimation, Part I: Exact Model," in *IEEE Trans. on Power Apparatus and Systems*, vol. PAS-89, no. 1, pp. 120-125, Jan. 1970.

[87] PowerWorld, available online: http://www.powerworld.com

[88] PSS®E Raw File Format Documentation, version 32, 2009.

[89] R. D. Zimmerman, C. E. Murillo-Sanchez and R. J. Thomas, "MATPOWER: Steady-State Operations, Planning, and Analysis Tools for Power Systems Research and Education," in *IEEE Transactions on Power Systems*, vol. 26, no. 1, pp. 12-19, Feb. 2011.

[90] V. Akhmatov, "Experience with voltage control from large offshore windfarms: The Danish case," *Wind Energy*, vol.12, no.7, pp.692-711, Oct. 2009.

[91] D. Bertsimax and M. Sim, "The price of robustness," *Oper. Res.*, vol. 52, no. 1, pp. 35-53, 2004.

[92] K. O. H. Pedersen, A. H. Nislsen and N. K. Poulsen, "Short-circuit impedance measurement, " *IEE Proceeeding-Generation Transmission and Distribution,* vol.150, Issue 2, PP. 169-174, Mar. 2003.

APPENDIX A – VOLTAGE CONTROL BY TAP RATIO IN HELM

Normally, if a PQ node voltage magnitude is under control by the transformer tap, then this node becomes to PVQ node. The PV or PVQ nodes already controlled by other control devices, cannot be controlled by transformers, which will introduce the conflict between the control components. In addition, without sharing the contributions, there will be infinite numbers of solutions, which leads to intractable problem.

For the PVQ bus that is under the transformers control, the node current equation is:

$$\sum_k Y_k^{tr} v_k(s) = s(P_i - jQ_i)w_i^*(s) - sY_i^{sh} v_i(s) \tag{A.1}$$

The transformer tap is also defined as complex variable, which is spited from the admittance matrix. If define:

$$t = \frac{1}{\tau e^{j\theta_{shift}}} \tag{A.2}$$

Then the admittance (2.58)-(2.59) matrix becomes to:

$$Y^{tr} = \begin{bmatrix} y_s t^* & -y_s t^* \\ -y_s t & y_s t \end{bmatrix} = \begin{bmatrix} t^* \\ t \end{bmatrix} \cdot \begin{bmatrix} y_s & -y_s \\ -y_s & y_s \end{bmatrix} \tag{A.3}$$

$$Y^{sh} = \begin{bmatrix} \left(y_s + j\frac{b_c}{2}\right)tt^* - y_s t^* & 0 \\ 0 & \left(y_s + j\frac{b_c}{2}\right) - y_s t \end{bmatrix}$$

$$= \begin{bmatrix} t^* \\ t \end{bmatrix} \cdot \begin{bmatrix} \left(y_s + j\frac{b_c}{2}\right)t - y_s & 0 \\ 0 & \frac{\left(y_s + j\frac{b_c}{2}\right)}{t} - y_s \end{bmatrix} \tag{A.4}$$

The transformer branches are related to two nodes (A.5), move $\begin{bmatrix} t^* \\ t \end{bmatrix}$ of Y^{tr} to the right hand, yields (A.6).

$$\begin{bmatrix} t^* \\ t \end{bmatrix} \cdot \begin{bmatrix} y_s & -y_s \\ -y_s & y_s \end{bmatrix} \begin{bmatrix} v_k(s) \\ v_i(s) \end{bmatrix} = \begin{bmatrix} (P_i - jQ_i)w_i^*(s^*) - Y_i^{sh} v_i(s) \\ (P_k - jQ_k)w_k^*(s^*) - Y_k^{sh} v_k(s) \end{bmatrix} \tag{A.5}$$

$$\begin{bmatrix} y_s & -y_s \\ -y_s & y_s \end{bmatrix} \begin{bmatrix} v_k(s) \\ v_i(s) \end{bmatrix}$$

$$= s \begin{bmatrix} \dfrac{(P_i - jQ_i)w_i^*(s^*)}{t^*} \\ \dfrac{(P_k - jQ_k)w_k^*(s^*)}{t} \end{bmatrix}$$

$$- s \begin{bmatrix} \left(y_s + j\dfrac{b_c}{2}\right)t - y_s & 0 \\ 0 & \dfrac{\left(y_s + j\dfrac{b_c}{2}\right)}{t} - y_s \end{bmatrix} \begin{bmatrix} v_i(s) \\ v_k(s) \end{bmatrix} \tag{A.6}$$

Since the voltage magnitude is controlled by the tap ratio, the transformer phase angle is known and the tap ratio is unknown. If embedding the tap ratio with the complex variable s, then the tap ratio can be expressed as (A.7), and the reciprocal is (A.8), where (A.9) is valid.

$$t(s) = \sum_{n=0}^{\infty} t[n]s^n \tag{A.7}$$

$$\frac{1}{t(s)} = m(s) = \sum_{n=0}^{\infty} m[n]s^n \tag{A.8}$$

$$\sum_{n=0}^{\infty} t[n]s^n \sum_{n=0}^{\infty} m[n]s^n = s^n \sum_{k=0}^{n} t[n-k] \cdot m[k] = 1 \tag{A.9}$$

Substituting (A.7)-(A.8) to (A.6), yields (A.10).

$$\begin{bmatrix} y_s & -y_s \\ -y_s & y_s \end{bmatrix} \begin{bmatrix} \sum_{n=0}^{\infty} v_k[n]s^n \\ \sum_{n=0}^{\infty} v_i[n]s^n \end{bmatrix}$$

$$= s \begin{bmatrix} (P_i - jQ_i)\sum_{n=0}^{\infty} w_i^*[n]s^n \sum_{n=0}^{\infty} m^*[n]s^n \\ (P_k - jQ_k)\sum_{n=0}^{\infty} w_k^*[n]s^n \sum_{n=0}^{\infty} m[n]s^n \end{bmatrix}$$

$$- s \begin{bmatrix} \left(y_s + j\dfrac{b_c}{2}\right)\sum_{n=0}^{\infty} t[n]s^n - y_s & 0 \\ 0 & \left(y_s + j\dfrac{b_c}{2}\right)\sum_{n=0}^{\infty} m[n]s^n - y_s \end{bmatrix} \begin{bmatrix} \sum_{n=0}^{\infty} v_i[n]s^n \\ \sum_{n=0}^{\infty} v_k[n]s^n \end{bmatrix} \tag{A.10}$$

Equating the coefficients of each order at two sides of (A.10), yields (A.11). Taking $k = 0$ terms in the right-hand-side of (A.11), yields (A.12). Substituting (A.9) to (A.12), yields (A.13). In the no-load condition, $t[0] = 1, m[0] = 1$ and $m^*[0] = 1$ that represents no tap ratio control at $s = 0$. Therefore, (A.14) is obtained.

$$\begin{bmatrix} y_s & -y_s \\ -y_s & y_s \end{bmatrix}\begin{bmatrix} v_k[n] \\ v_i[n] \end{bmatrix} = $$

$$-\begin{bmatrix} (P_i - jQ_i)\left(\displaystyle\sum_{k=0}^{n-1} m^*[n-k]w_i^*[k]\right) & 0 \\[2ex] (P_k - jQ_k)\left(\displaystyle\sum_{k=0}^{n-1} m[n-k]w_k^*[k]\right) & 0 \\[2ex] \left(y_s + j\dfrac{b_c}{2}\right)\left(\displaystyle\sum_{k=0}^{n-1} t[n-k]v_i[k]\right) - y_s v_i[n-1] & \left(y_s + j\dfrac{b_c}{2}\right)\left(\displaystyle\sum_{k=0}^{n-1} m[n-k]v_k[k]\right) - y_s v_k[n-1] \end{bmatrix} \tag{A.11}$$

$$\begin{bmatrix} y_s & -y_s \\ -y_s & y_s \end{bmatrix}\begin{bmatrix} v_k[n] \\ v_i[n] \end{bmatrix} = $$

$$-\begin{bmatrix} (P_i - jQ_i)\left(\displaystyle\sum_{k=1}^{n-1} m^*[n-k]w_i^*[k] + \boldsymbol{m}^*[\boldsymbol{n}]\right) & 0 \\[2ex] (P_k - jQ_k)\left(\displaystyle\sum_{k=1}^{n-1} m[n-k]w_k^*[k] + \boldsymbol{m}[\boldsymbol{n}]\right) & 0 \\[2ex] \left(y_s + j\dfrac{b_c}{2}\right)\left(\displaystyle\sum_{k=1}^{n-1} t[n-k]v_i[k] - \boldsymbol{t}[\boldsymbol{n}]\right) - y_s v_i[n-1] & \left(y_s + j\dfrac{b_c}{2}\right)\left(\displaystyle\sum_{k=1}^{n-1} m[n-k]v_k[k] + \boldsymbol{m}[\boldsymbol{n}]\right) - y_s v_k[n-1] \end{bmatrix} \tag{A.12}$$

$$\begin{bmatrix} y_s & -y_s \\ -y_s & y_s \end{bmatrix}\begin{bmatrix} v_k[n] \\ v_i[n] \end{bmatrix}$$

$$=\begin{bmatrix} (P_i - jQ_i)\left(\sum_{k=1}^{n-1} m^*[n-k]w_i^*[k] + \boldsymbol{m}^*[\boldsymbol{n}]\right) \\ (P_k - jQ_k)\left(\sum_{k=1}^{n-1} m[n-k]w_k^*[k] + \boldsymbol{m}[\boldsymbol{n}]\right) \end{bmatrix}$$

$$-\begin{bmatrix} \left(y_s + j\frac{b_c}{2}\right)\left(\sum_{k=1}^{n-1} t[n-k]v_i[k] - \sum_{k=1}^{n-1} t[k]m[n-k] - \boldsymbol{m}[\boldsymbol{n}]\right) - y_s v_i[n-1] & 0 \\ 0 & \left(y_s + j\frac{b_c}{2}\right)\left(\sum_{k=1}^{n-1} m[n-k]v_k[k] + \boldsymbol{m}[\boldsymbol{n}]\right) - y_s v_k[n-1] \end{bmatrix} \tag{A.13}$$

$$\begin{bmatrix} y_s & -y_s \\ -y_s & y_s \end{bmatrix}\begin{bmatrix} v_k[n] \\ v_i[n] \end{bmatrix}$$

$$=\begin{bmatrix} (P_i - jQ_i)\left(\sum_{k=1}^{n-1} m^*[n-k]w_i^*[k] + \boldsymbol{m}^*[\boldsymbol{n}]\right) \\ (P_k - jQ_k)\left(\sum_{k=1}^{n-1} m[n-k]w_k^*[k] + \boldsymbol{m}[\boldsymbol{n}]\right) \end{bmatrix}$$

$$-\begin{bmatrix} \left(y_s + j\frac{b_c}{2}\right)\left(\sum_{k=1}^{n-1} t[n-k]v_i[k] - \sum_{k=0}^{n-1} \frac{\boldsymbol{t}[\boldsymbol{k}]\boldsymbol{m}[\boldsymbol{n}-\boldsymbol{k}]}{\boldsymbol{t}[\boldsymbol{0}]}\right) - y_s v_i[n-1] & 0 \\ 0 & \left(y_s + j\frac{b_c}{2}\right)\left(\sum_{k=1}^{n-1} m[n-k]v_k[k] + \boldsymbol{m}[\boldsymbol{n}]\right) - y_s v_k[n-1] \end{bmatrix} \tag{A.14}$$

182

Assuming if there is no phase angle control, then $m(s) = m^*(s^*)$, i.e. the phase angle equals to zero. It can be seen that, there is one more unknown variable, $m[n]$ in (A.14). In addition, as mentioned, if a PQ node voltage magnitude is controlled by the transformer tap ratio, then the node becomes PVQ node, and the voltage magnitude constraint (2.55) and then (2.78) are valid. Therefore, the total number of unknown variables matches the total number of equations, and the load flow equations can be solved. The detailed implementation including the tap ratio control is not carried out during the Ph.d study, though the analytical expressions are well derived. The validation is the future work.

APPENDIX B – DERIVATIVE

In the programming, the analytical gradient and the hessian matrices of the objective and the constraints w.r.t. the decision variables are required, which are summarized in the following [89]. Notice that, in the programming, not only the analytical expression should be correctly presented, but also the entries positions in the relevant matrices should be correct in (B.1)-(B.2). For the large power system that presented in the node-branch model, the correction matrices are needed to link the node and the corresponding branches in the matrices. Here define C_f and C_t are the connection matrices from sending and the receiving ends, respectively. The size of C_f and C_t are $N_{br} \times N_b$. The entries are either 1 or 0, i.e. $C_f(i,j) = 1$ means the i branch sending end is connect to the j node.

$$
\begin{bmatrix}
\nabla J_{\delta\delta} & \nabla J_{\delta V} & \nabla J_{\delta\tau} & 0 & 0 & 0 & 0 & 0 \\
\nabla J_{V\delta} & \nabla J_{VV} & \nabla J_{V\tau} & \nabla J_{Vb} & 0 & 0 & 0 & 0 \\
\nabla J_{\tau\delta} & \nabla J_{\tau V} & \nabla J_{\tau\tau} & & & & & \vdots \\
0 & \nabla J_{bV} & & \ddots & & & & \vdots \\
0 & 0 & & & \ddots & & & \vdots \\
0 & 0 & & & & \ddots & & \vdots \\
0 & 0 & & & & & 0 & 0 \\
0 & 0 & \cdots & \cdots & \cdots & \cdots & 0 & 0
\end{bmatrix}
\tag{B.1}
$$

$$
\begin{bmatrix}
\nabla G_{\delta\delta} & \nabla G_{\delta V} & \nabla G_{\delta\tau} & 0 & 0 & 0 & 0 & 0 \\
\nabla G_{V\delta} & \nabla G_{VV} & \nabla G_{V\tau} & \nabla G_{Vb} & 0 & 0 & 0 & 0 \\
\nabla G_{\tau\delta} & \nabla G_{\tau V} & \nabla G_{\tau\tau} & & & & & \vdots \\
0 & \nabla G_{bV} & & \ddots & & & & \vdots \\
0 & 0 & & & \ddots & & & \vdots \\
0 & 0 & & & & \ddots & & \vdots \\
0 & 0 & & & & & 0 & 0 \\
0 & 0 & \cdots & \cdots & \cdots & \cdots & 0 & 0
\end{bmatrix}
\tag{B.2}
$$

In the normal operation, the loss minimization is to minimize the real power losses under a certain balance, where the active power outputs of the generators are fixed as dispatched. In the AVC system, the grid loss is minimized by adjusting the status of the reactive power outputs of generators, Q_g, shunt compensation susceptance, b, and tap-ratio of transformers, τ. The branch loss can be allocated in the sending and the receiving ends, respectively.

$$
P_{br} = \sum Real(S_f + S_t) = \sum Real(v_f i_f^* + v_t i_t^*) = \sum Real\left(\boldsymbol{v_f}(\boldsymbol{Y_f v})^* + \boldsymbol{v_t}(\boldsymbol{Y_t v})^*\right)
\tag{B.3}
$$

where S_f and S_t are the power flowing in the two ends of a branch, respectively. The branch loss in (B.3) is a function of the **state variable**, V and δ of the complex voltage, and the **control variable** τ of the admittance. The transformer is modelled as a branch connecting to an ideal transformer. The impedance change due to the tap changer is neglected in this platform. The regulation on tap position is converted to tap ratio change of the ideal transformer, and finally reflected to the change on the equivalent admittance between two nodes. By definition, the tap ratio and the phase angle are represented in the primary side. The branch model including the equivalent transformer admittance model is presented in (B.4), where the tap ratio, τ and the phase shift angle, θ_{shift}, are included.

$$
Y_{br} = \begin{bmatrix} Y_{ff} & Y_{ft} \\ Y_{tf} & Y_{tt} \end{bmatrix} = \begin{bmatrix} \left(y_s + j\dfrac{b_c}{2}\right)\dfrac{1}{\tau^2} & -y_s\dfrac{1}{\tau e^{-j\theta_{shift}}} \\ -y_s\dfrac{1}{\tau e^{j\theta_{shift}}} & y_s + j\dfrac{b_c}{2} \end{bmatrix}
\tag{B.4}
$$

Therefore, the gradient of the branch loss respected to the decision variables can be obtained, which composes the derivatives of the loss respected to voltage angle, voltage magnitude and the tap ratio, respectively. The resulted derivatives in (B.5)-(B.6) are $N_{br} \times N_{br}$ matrices, in which the row and the column indices represent the sending and the receiving end nodes indices and each row corresponds to a branch. The derivative of receiving end power flow w.r.t. the voltage, $\frac{\partial S_t}{\partial \delta}$ and $\frac{\partial S_t}{\partial V}$ are similar to (B.5)-(B.6). If the branch is transformer with tap changer, then (B.7)-(B.9) are needed. The total branch loss derivatives w.r.t. the voltage and the tap ratio are then obtained via (B.10)-(B.13).

$$\begin{aligned}\frac{\partial S_f}{\partial \delta} &= [\![i_f^*]\!]\frac{\partial v_f}{\partial \delta} + [\![v_f]\!]\frac{\partial i_f^*}{\partial \delta} = [\![Y_f^* v^*]\!]jC_f[\![v]\!] + [\![C_f v]\!]\frac{\partial (Y_f v)^*}{\partial \delta} \\ &= [\![Y_f^* v^*]\!]jC_f[\![v]\!] - [\![C_f v]\!]jY_f^*[\![v^*]\!]\end{aligned} \tag{B.5}$$

$$\frac{\partial S_f}{\partial V} = [\![i_f^*]\!]\frac{\partial v_f}{\partial V} + [\![v_f]\!]\frac{\partial i_f^*}{\partial V} = [\![Y_f^* v^*]\!]C_f[\![e^{j\delta}]\!] + [\![C_f v]\!]Y_f^*[\![e^{-j\delta}]\!] \tag{B.6}$$

$$\frac{\partial Y_{br}}{\partial \tau} = \begin{bmatrix} \frac{\partial Y_f}{\partial \tau} \\ \frac{\partial Y_t}{\partial \tau} \end{bmatrix} = \begin{bmatrix} \frac{\partial Y_{ff}}{\partial \tau} & \frac{\partial Y_{ft}}{\partial \tau} \\ \frac{\partial Y_{tf}}{\partial \tau} & \frac{\partial Y_{tt}}{\partial \tau} \end{bmatrix} = \begin{bmatrix} -\frac{2}{\tau}Y_{ff} & -\frac{1}{\tau}Y_{ft} \\ -\frac{1}{\tau}Y_{tf} & 0 \end{bmatrix} \tag{B.7}$$

$$\frac{\partial Y_{br}}{\partial \tau} = C_f^{\mathsf{T}}\frac{\partial Y_f}{\partial \tau} + C_t^{\mathsf{T}}\frac{\partial Y_t}{\partial \tau} \tag{B.8}$$

$$\frac{\partial S_f}{\partial \tau} = [\![C_f v]\!]\left[\!\!\left[\frac{\partial Y_f}{\partial \tau}v\right]\!\!\right]^* = [\![C_f v]\!]\left[\!\!\left[\left[-\frac{2}{\tau}Y_{ff} \quad -\frac{1}{\tau}Y_{ft}\right]^* v^*\right]\!\!\right] \tag{B.9}$$

$$\frac{\partial S_t}{\partial Y_t} = [\![C_t v]\!]\left[\!\!\left[\frac{\partial Y_t}{\partial \tau}v\right]\!\!\right]^* = [\![C_t v]\!]\left[\!\!\left[\left[-\frac{1}{\tau}Y_{tf} \quad 0\right]^* v^*\right]\!\!\right] \tag{B.10}$$

$$\frac{\partial P_{br}}{\partial \delta} = \sum Real\left(\frac{\partial S_f}{\partial \delta} + \frac{\partial S_t}{\partial \delta}\right) \tag{B.11}$$

$$\frac{\partial P_{br}}{\partial V} = \sum Real\left(\frac{\partial S_f}{\partial V} + \frac{\partial S_t}{\partial V}\right) \tag{B.12}$$

$$\frac{\partial P_{br}}{\partial \tau} = \sum Real\left(\frac{\partial S_f}{\partial \tau} + \frac{\partial S_t}{\partial \tau}\right) \tag{B.13}$$

The transformer no-load loss is placed in the primary side as a constant impedance load, (B.14). The no-load loss derivative respected to the voltage magnitude is expressed in (B.14).

$$\frac{\partial P_{tr}}{\partial V} = \sum Real(2V_{tr} \cdot G_{tr}) \tag{B.14}$$

The shunt compensation and the reactive power outputs of the generators are not directly change the power loss in the branches. However, they have significant impact on the bus voltage that change the reactive power flow and finally influence on the branch loss.

The shunts modelled as the conductance and the susceptance, which are embedded to the bus data. The bus number of the shunts should be converted to the internal index according to the bus dataset. The shunt loss is formulated in (B.15). The derivative of the shunt loss respected to the terminal voltage magnitude is shown in (B.15). If the connecting conductance of the shunt reactor is a linear function of the connecting susceptance, then (B.15) will be extended to (B.16), where Q_r is a scalar, e.g. the quality factor.

$$\frac{\partial P_{sh}}{\partial V} = \sum Real(2V_{sh} \cdot G_{sh}) \tag{B.15}$$

$$\frac{\partial P_{sh}}{\partial V} = \sum Real(2V_{sh} \cdot Q_r b_{sh}) \qquad (B.16)$$

The second order derivatives of the branch flow respected to the voltage and the tap ratio are summarized in (B.17)-(B.26).

$$
\begin{aligned}
\frac{\partial}{\partial \delta}\left(\frac{\partial S_f}{\partial \delta}\right) &= \frac{\partial}{\partial \delta}\left(\llbracket Y_f^* v^* \rrbracket j C_f \llbracket v \rrbracket - \llbracket C_f v \rrbracket j Y_f^* \llbracket v^* \rrbracket\right)^{\mathsf{T}} \\
&= j \llbracket v \rrbracket C_f^{\mathsf{T}} Y_f^* \left\llbracket \frac{\partial}{\partial \delta} v^* \right\rrbracket + j \llbracket C_f^{\mathsf{T}} Y_f^* v^* \rrbracket \left\llbracket \frac{\partial}{\partial \delta} v \right\rrbracket - j \llbracket Y_f^{*\mathsf{T}} C_f v \rrbracket \left\llbracket \frac{\partial}{\partial \delta} v^* \right\rrbracket \\
&\quad - j Y_f^{*\mathsf{T}} C_f \left\llbracket \frac{\partial}{\partial \delta} v \right\rrbracket \llbracket v^* \rrbracket \\
&= \llbracket v \rrbracket C_f^{\mathsf{T}} Y_f^* \llbracket v^* \rrbracket - \llbracket C_f^{\mathsf{T}} Y_f^* v^* \rrbracket \llbracket v \rrbracket - \llbracket Y_f^{*\mathsf{T}} C_f v \rrbracket \llbracket v^* \rrbracket + Y_f^{*\mathsf{T}} C_f \llbracket v \rrbracket \llbracket v^* \rrbracket
\end{aligned} \qquad (B.17)
$$

$$
\begin{aligned}
\frac{\partial}{\partial \delta}\left(\frac{\partial S_f}{\partial V}\right) &= \frac{\partial}{\partial \delta}\left(\llbracket Y_f^* v^* \rrbracket C_f \llbracket e^{j\delta} \rrbracket + \llbracket C_f v \rrbracket Y_f^* \llbracket e^{-j\delta} \rrbracket\right)^{\mathsf{T}} \\
&= C_f^{\mathsf{T}} Y_f^* \left\llbracket \frac{\partial}{\partial \delta} v^* \right\rrbracket \llbracket e^{j\delta} \rrbracket + \llbracket C_f^{\mathsf{T}} Y_f^* v^* \rrbracket \left\llbracket \frac{\partial}{\partial \delta} e^{j\delta} \right\rrbracket + \left\llbracket \frac{\partial}{\partial \delta} v \right\rrbracket Y_f^{*\mathsf{T}} C_f \llbracket e^{-j\delta} \rrbracket \\
&\quad + \llbracket Y_f^{*\mathsf{T}} C_f v \rrbracket \left\llbracket \frac{\partial}{\partial \delta} e^{-j\delta} \right\rrbracket \\
&= -j C_f^{\mathsf{T}} Y_f^* \llbracket v^* \rrbracket \llbracket e^{j\delta} \rrbracket + j \llbracket C_f^{\mathsf{T}} Y_f^* v^* \rrbracket \llbracket e^{j\delta} \rrbracket + j \llbracket v \rrbracket Y_f^{*\mathsf{T}} C_f \llbracket e^{-j\delta} \rrbracket \\
&\quad - j \llbracket Y_f^{*\mathsf{T}} C_f v \rrbracket \llbracket e^{-j\delta} \rrbracket
\end{aligned} \qquad (B.18)
$$

$$
\begin{aligned}
\frac{\partial}{\partial V}\left(\frac{\partial S_f}{\partial \delta}\right) &= \frac{\partial}{\partial V}\left(\llbracket Y_f^* v^* \rrbracket j C_f \llbracket v \rrbracket - \llbracket C_f v \rrbracket j Y_f^* \llbracket v^* \rrbracket\right)^{\mathsf{T}} \\
&= C_f^{\mathsf{T}} Y_f^* \left\llbracket \frac{\partial}{\partial V} v^* \right\rrbracket j \llbracket v \rrbracket + \llbracket C_f^{\mathsf{T}} Y_f^* v^* \rrbracket j \left\llbracket \frac{\partial}{\partial V} v \right\rrbracket - \llbracket Y_f^{*\mathsf{T}} C_f v \rrbracket j \left\llbracket \frac{\partial}{\partial V} v^* \right\rrbracket \\
&\quad - Y_f^{*\mathsf{T}} C_f \left\llbracket \frac{\partial}{\partial V} v \right\rrbracket j \llbracket v^* \rrbracket \\
&= C_f^{\mathsf{T}} Y_f^* \llbracket e^{-j\delta} \rrbracket j \llbracket v \rrbracket + \llbracket C_f^{\mathsf{T}} Y_f^* v^* \rrbracket j \llbracket e^{j\delta} \rrbracket - \llbracket Y_f^{*\mathsf{T}} C_f v \rrbracket j \llbracket e^{-j\delta} \rrbracket \\
&\quad - Y_f^{*\mathsf{T}} C_f \llbracket e^{j\delta} \rrbracket j \llbracket v^* \rrbracket
\end{aligned} \qquad (B.19)
$$

$$
\begin{aligned}
\frac{\partial}{\partial V}\left(\frac{\partial S_f}{\partial V}\right) &= \frac{\partial}{\partial V}\left(\llbracket Y_f^* v^* \rrbracket C_f \llbracket e^{j\delta} \rrbracket + \llbracket C_f v \rrbracket Y_f^* \llbracket e^{-j\delta} \rrbracket\right)^{\mathsf{T}} \\
&= C_f^{\mathsf{T}} Y_f^* \left\llbracket \frac{\partial}{\partial V} v^* \right\rrbracket \llbracket e^{j\delta} \rrbracket + Y_f^{*\mathsf{T}} C_f \left\llbracket \frac{\partial}{\partial V} v \right\rrbracket \llbracket e^{-j\delta} \rrbracket \\
&= C_f^{\mathsf{T}} Y_f^* \llbracket e^{-j\delta} \rrbracket \llbracket e^{j\delta} \rrbracket + Y_f^{*\mathsf{T}} C_f \llbracket e^{j\delta} \rrbracket \llbracket e^{-j\delta} \rrbracket = C_f^{\mathsf{T}} Y_f^* + Y_f^{*\mathsf{T}} C_f
\end{aligned} \qquad (B.20)
$$

$$
\begin{aligned}
\frac{\partial}{\partial \tau}\left(\frac{\partial S_f}{\partial \delta}\right) &= \frac{\partial}{\partial \tau}\left(\llbracket Y_f^* v^* \rrbracket j C_f \llbracket v \rrbracket - \llbracket C_f v \rrbracket j Y_f^* \llbracket v^* \rrbracket\right) = \left\llbracket \frac{\partial Y_f^*}{\partial \tau} v^* \right\rrbracket j C_f \llbracket v \rrbracket - \llbracket C_f v \rrbracket j \frac{\partial Y_f^*}{\partial \tau} \llbracket v^* \rrbracket \\
&= j\left(\left\llbracket \left[-\frac{2}{\tau} Y_{ff} \quad -\frac{1}{\tau} Y_{ft}\right]^* v^* \right\rrbracket C_f \llbracket v \rrbracket \right. \\
&\quad \left. - \llbracket C_f v \rrbracket \left[-\frac{2}{\tau} Y_{ff} \quad -\frac{1}{\tau} Y_{ft}\right]^* \llbracket v^* \rrbracket\right)
\end{aligned} \qquad (B.21)
$$

$$
\begin{aligned}
\frac{\partial}{\partial \tau}\left(\frac{\partial S_f}{\partial V}\right) &= \frac{\partial}{\partial \tau}\left(\llbracket Y_f^* v^* \rrbracket C_f \llbracket e^{j\delta} \rrbracket + \llbracket C_f v \rrbracket Y_f^* \llbracket e^{-j\delta} \rrbracket\right) \\
&= \left\llbracket \frac{\partial Y_f^*}{\partial \tau} v^* \right\rrbracket C_f \llbracket e^{j\delta} \rrbracket + \llbracket C_f v \rrbracket \frac{\partial Y_f^*}{\partial \tau} \llbracket e^{-j\delta} \rrbracket \\
&= \llbracket C_f v \rrbracket \left[-\frac{2}{\tau} Y_{ff} \quad -\frac{1}{\tau} Y_{ft}\right]^* \llbracket e^{-j\delta} \rrbracket + \left\llbracket \left[-\frac{2}{\tau} Y_{ff} \quad -\frac{1}{\tau} Y_{ft}\right]^* v^* \right\rrbracket \\
&\quad * C_f \llbracket e^{j\delta} \rrbracket
\end{aligned} \qquad (B.22)
$$

$$\frac{\partial}{\partial \tau}\left(\frac{\partial Y_{br}}{\partial \tau}\right) = \begin{bmatrix} \frac{\partial}{\partial \tau}\left(\frac{\partial Y_f}{\partial \tau}\right) \\ \frac{\partial}{\partial \tau}\left(\frac{\partial Y_t}{\partial \tau}\right) \end{bmatrix} = \begin{bmatrix} \frac{\partial}{\partial \tau}\left(\frac{\partial Y_{ff}}{\partial \tau}\right) & \frac{\partial}{\partial \tau}\left(\frac{\partial Y_{ft}}{\partial \tau}\right) \\ \frac{\partial}{\partial \tau}\left(\frac{\partial Y_{tf}}{\partial \tau}\right) & \frac{\partial}{\partial \tau}\left(\frac{\partial Y_{tt}}{\partial \tau}\right) \end{bmatrix} = \begin{bmatrix} \frac{6}{\tau^2}Y_{ff} & \frac{2}{\tau^2}Y_{ft} \\ \frac{2}{\tau^2}Y_{tf} & 0 \end{bmatrix}$$	(B.23)
$$\frac{\partial}{\partial \tau}\left(\frac{\partial Y_{br}}{\partial \tau}\right) = C_f^\mathsf{T}\frac{\partial}{\partial \tau}\left(\frac{\partial Y_f}{\partial \tau}\right) + C_t^\mathsf{T}\frac{\partial}{\partial \tau}\left(\frac{\partial Y_t}{\partial \tau}\right)$$	(B.24)
$$\frac{\partial}{\partial \tau}\left(\frac{\partial S_f}{\partial \tau}\right) = [\![C_f v]\!]\left[\frac{\partial}{\partial \tau}\left(\frac{\partial Y_f}{\partial \tau}\right)v\right]^* = [\![C_f v]\!]\left[\begin{bmatrix} \frac{6}{\tau^2}Y_{ff} & \frac{2}{\tau^2}Y_{ft} \end{bmatrix}v\right]^*$$	(B.25)
$$\frac{\partial}{\partial \tau}\left(\frac{\partial S_t}{\partial \tau}\right) = [\![C_t v]\!]\left[\frac{\partial}{\partial \tau}\left(\frac{\partial Y_t}{\partial \tau}\right)v\right]^* = [\![C_t v]\!]\left[\begin{bmatrix} \frac{2}{\tau^2}Y_{tf} & 0 \end{bmatrix}v\right]^*$$	(B.26)

The matric size for (B.17)-(B.20) are $N_b \times N_b$, for (B.21) and (B.22) are $N_\tau \times N_b$, and $N_\tau \times N_\tau$ for (B.23)-(B.26).

The equality constraints, i.e. the load flow equations, respected to the voltage are presented in (B.27)-(B.28). The complex power is expressed in (B.3), where the voltage is a complex variable. The voltage angle and the voltage magnitude defined as unknown variables are to be determined via Newton-Raphson method. The first-order derivatives of the unknown variables w.r.t. the power mismatches compose the Jacobian matrix. Equation (B.27)-(B.28) are used to construct the Jacobian matrix in the load flow calculations, $J_1 = Real\left(\frac{\partial \Delta s}{\partial \delta}\right)$, $J_2 = Real\left(\frac{\partial \Delta s}{\partial V}\right)$, $J_3 = Imag\left(\frac{\partial \Delta s}{\partial V}\right)$ and $J_4 = Imag\left(\frac{\partial \Delta s}{\partial V}\right)$.

The secondary derivatives of the constraints w.r.t the voltage are (B.29)-(B.31). The load flow constraints first derivative w.r.t. the node reactive power injection is -1 if defining the production is negative, w.r.t the shunt is square of the node voltage magnitude, and w.r.t. the tap ratio that can be expressed in (B.32). (B.32) can be solved through (B.9). The secondary derivatives w.r.t. the voltage are also trivial to be found. (B.33) for the load flow equations w.r.t. the tap ratio can be solved through (B.23)-(B.26).

$$\frac{\partial S}{\partial \delta} = [\![i^*]\!]\frac{\partial v}{\partial \delta} + [\![v]\!]\frac{\partial i^*}{\partial \delta} = [\![Y^* v^*]\!]j[\![v]\!] + [\![v]\!]Y^*\left[\frac{\partial v^*}{\partial \delta}\right]^* = [\![Y^* v^*]\!]j[\![V]\!] - [\![v]\!]jY^*[\![v^*]\!]$$	(B.27)
$$\frac{\partial S}{\partial V} = [\![i^*]\!]\frac{\partial v}{\partial V} + [\![v]\!]\frac{\partial i^*}{\partial V} = [\![Y^* v^*]\!][\![e^{j\delta}]\!] + [\![v]\!]Y^*\left[\frac{\partial v^*}{\partial V}\right]^* = [\![Y^* v^*]\!][\![e^{j\delta}]\!] + [\![v]\!]Y^*[\![e^{-j\delta}]\!]$$	(B.28)
$$\begin{aligned} \frac{\partial}{\partial \delta}\left(\frac{\partial S}{\partial \delta}\right)_{\lambda_g} &= \frac{\partial}{\partial \delta}\left(\frac{\partial S^\mathsf{T}}{\partial \delta}\lambda_g\right) = \frac{\partial}{\partial \delta}\left([\![Y^* v^*]\!]j[\![v]\!]\lambda_g - [\![v]\!]jY^{*\mathsf{T}}[\![v^*]\!]\lambda_g\right) \\ &= Y^*\left[\frac{\partial}{\partial \delta}v^*\right]j[\![v]\!][\![\lambda_g]\!] + [\![Y^* v^*]\!]j\left[\frac{\partial}{\partial \delta}v\right][\![\lambda_g]\!] \\ &\quad - \left[\frac{\partial}{\partial \delta}v\right]jY^{*\mathsf{T}}[\![v^*]\!][\![\lambda_g]\!] - [\![Y^{*\mathsf{T}}[\![v]\!]\lambda_g]\!]j\left[\frac{\partial}{\partial \delta}v^*\right] \\ &= Y^*[\![v^*]\!][\![v]\!][\![\lambda_g]\!] - [\![Y^* v^*]\!][\![v]\!][\![\lambda_g]\!] + [\![v]\!]Y^{*\mathsf{T}}[\![v^*]\!][\![\lambda_g]\!] \\ &\quad - [\![Y^{*\mathsf{T}}[\![v]\!]\lambda_g]\!][\![v^*]\!] \end{aligned}$$	(B.29)

$$\frac{\partial}{\partial\delta}\left(\frac{\partial S}{\partial V}\right)_{\lambda_g} = \frac{\partial}{\partial\delta}\left(\frac{\partial S^\top}{\partial V}\lambda_g\right) = \frac{\partial}{\partial\delta}\left(\llbracket Y^*v^*\rrbracket\llbracket e^{j\delta}\rrbracket\lambda_g + \llbracket v\rrbracket Y^{*\top}\llbracket e^{-j\delta}\rrbracket\lambda_g\right)$$

$$= Y^*\left[\frac{\partial}{\partial\delta}v^*\right]\llbracket e^{j\delta}\rrbracket\llbracket\lambda_g\rrbracket + \llbracket Y^*v^*\rrbracket\left[\frac{\partial}{\partial\delta}e^{j\delta}\right]\llbracket\lambda_g\rrbracket$$

$$+ \left[\frac{\partial}{\partial\delta}v\right]Y^{*\top}\llbracket e^{-j\delta}\rrbracket\llbracket\lambda_g\rrbracket + \llbracket Y^{*\top}\llbracket v\rrbracket\lambda_g\rrbracket\left[\frac{\partial}{\partial\delta}e^{-j\delta}\right]$$

$$= -jY^*\llbracket v^*\rrbracket\llbracket e^{j\delta}\rrbracket\llbracket\lambda_g\rrbracket + j\llbracket Y^*v^*\rrbracket\llbracket e^{j\delta}\rrbracket\llbracket\lambda_g\rrbracket + j\llbracket v\rrbracket Y^{*\top}\llbracket e^{-j\delta}\rrbracket\llbracket\lambda_g\rrbracket$$

$$- j\llbracket Y^{*\top}\llbracket v\rrbracket\lambda_g\rrbracket\llbracket e^{-j\delta}\rrbracket$$

(B.30)

$$\frac{\partial}{\partial V}\left(\frac{\partial S}{\partial V}\right)_{\lambda_g} = \frac{\partial}{\partial V}\left(\frac{\partial S^\top}{\partial V}\lambda_g\right) = \frac{\partial}{\partial V}\left(\llbracket Y^*v^*\rrbracket\llbracket e^{j\delta}\rrbracket\lambda_g + \llbracket v\rrbracket Y^{*\top}\llbracket e^{-j\delta}\rrbracket\lambda_g\right)$$

$$= Y^*\left[\frac{\partial}{\partial V}v^*\right]\llbracket e^{j\delta}\rrbracket\llbracket\lambda_g\rrbracket + \llbracket Y^*v^*\rrbracket\left[\frac{\partial}{\partial V}e^{j\delta}\right]\llbracket\lambda_g\rrbracket$$

$$+ \left[\frac{\partial}{\partial V}v\right]Y^{*\top}\llbracket e^{-j\delta}\rrbracket\llbracket\lambda_g\rrbracket + \llbracket Y^{*\top}\llbracket v\rrbracket\lambda_g\rrbracket\left[\frac{\partial}{\partial V}e^{-j\delta}\right]$$

$$= Y^*\llbracket e^{-j\delta}\rrbracket\llbracket e^{j\delta}\rrbracket\llbracket\lambda_g\rrbracket + \llbracket e^{j\delta}\rrbracket Y^{*\top}\llbracket e^{-j\delta}\rrbracket\llbracket\lambda_g\rrbracket = \llbracket\lambda_g\rrbracket\left(Y^* + Y^{*\top}\right)$$

(B.31)

$$\frac{\partial S}{\partial\tau} = \frac{\partial S_f}{\partial\tau} + \frac{\partial S_t}{\partial\tau}$$

(B.32)

$$\frac{\partial}{\partial\tau}\left(\frac{\partial S}{\partial\tau}\right) = \frac{\partial}{\partial\tau}\left(\frac{\partial S_f}{\partial\tau}\right) + \frac{\partial}{\partial\tau}\left(\frac{\partial S_t}{\partial\tau}\right)$$

(B.33)

Recall the penalty function that presented in (B.34), where x_z is the variable under discretization. x_{zmax} and x_{zmin} are the upper and the lower limits of the variable, that are integers. For example, the transformer tap ratio τ is under discretization, then x_z is firstly found by converting the tap ratio to the tap position, (B.35), and then be forcing to the integers in the discretization process.

For the shunt controllers that may be an aggregated shunt including several shunts, they are firstly split to individual shunts through the predefined logic, i.e. list all the possible combinations to approach the total reactive power injection of the aggregated shunt, and then pick up the combination that the total step is minimum. In this way to avoid capacitive and inductive shunts connecting at the same time in order to approach to the total required amount of reactive power.

Assigning the step for each individual shunt, the total reactive power injection, $b_z(step)$ in (B.36), can be found that may be different from the total aggregated reactive power output. The mismatch should be minimized in the discretization process. To avoid redundant shunt switching, the total mismatch is allocated by the smallest shunt, which leads to x_{zmax} and x_{zmin} in (B.37)-(B.38), should be adapted according to the addressed smallest shunt in the iterations.

The first and the secondary derivatives of the penalty function w.r.t. to the control variables are presented in (B.39)-(B.43), where the basic formula (B.43) is applied.

$$f(x_z) = \left[sin\left(\frac{x_z}{x_{zmax} - x_{zmin}}\pi\right)\right]^2$$

(B.34)

$$x_{\tau z} = \frac{\tau - \tau_0}{\Delta u} + x_{\tau z,0}$$

(B.35)

$$x_{bz} = \frac{b - b_z(step)}{\Delta b_{min}}$$

(B.36)

$$x_{zmax} = ceil(x_{bz})$$

(B.37)

$$x_{zmin} = floor(x_{bz})$$

(B.38)

$$\frac{\partial}{\partial \tau} f(x_z) = \frac{\partial}{\partial \tau}\left(\left[sin\left(\frac{\frac{\tau - \tau_0}{\Delta u} + x_{\tau z,0}}{x_{zmax} - x_{zmin}}\pi\right)\right]^2\right)$$

$$= 2\, sin\left(\frac{\frac{\tau - \tau_0}{\Delta u} + x_{\tau z,0}}{x_{zmax} - x_{zmin}}\pi\right) cos\left(\frac{\frac{\tau - \tau_0}{\Delta u} + x_{\tau z,0}}{x_{zmax} - x_{zmin}}\pi\right)\left(\frac{\pi}{x_{zmax} - x_{zmin}}\right)\frac{1}{\Delta u}$$

(B.39)

$$\frac{\partial}{\partial b} f(x_z) = \frac{\partial}{\partial b}\left(\left[sin\left(\frac{\frac{b - b_z(step)}{\Delta b_{min}}}{x_{zmax} - x_{zmin}}\pi\right)\right]^2\right)$$

$$= 2\, sin\left(\frac{\frac{b - b_z(step)}{\Delta b_{min}}}{x_{zmax} - x_{zmin}}\pi\right) cos\left(\frac{\frac{b - b_z(step)}{\Delta b_{min}}}{x_{zmax} - x_{zmin}}\pi\right)\left(\frac{\pi}{x_{zmax} - x_{zmin}}\right)\frac{1}{\Delta b_{min}}$$

(B.40)

$$\frac{\partial^2}{\partial^2 \tau} f(x_z) = 2\left(\frac{\pi}{x_{zmax} - x_{zmin}}\right)\frac{1}{\Delta u}\left(\left(\frac{\pi}{x_{zmax} - x_{zmin}}\right)\frac{1}{\Delta u}\left[cos\left(\frac{\frac{\tau - \tau_0}{\Delta u} + x_{\tau z,0}}{x_{zmax} - x_{zmin}}\pi\right)\right]^2\right.$$

$$\left. - \left(\frac{\pi}{x_{zmax} - x_{zmin}}\right)\frac{1}{\Delta u}\left[sin\left(\frac{\frac{\tau - \tau_0}{\Delta u} + x_{\tau z,0}}{x_{zmax} - x_{zmin}}\pi\right)\right]^2\right)$$

(B.41)

$$\frac{\partial^2}{\partial^2 b} f(x_z)$$

$$= 2\left(\frac{\pi}{x_{zmax} - x_{zmin}}\right)\frac{1}{\Delta b_{min}}\left(\left(\frac{\pi}{x_{zmax} - x_{zmin}}\right)\frac{1}{\Delta b_{min}}\left[cos\left(\frac{\frac{b - b_z(step)}{\Delta b_{min}}}{x_{zmax} - x_{zmin}}\pi\right)\right]^2\right.$$

$$\left. - \left(\frac{\pi}{x_{zmax} - x_{zmin}}\right)\frac{1}{\Delta b_{min}}\left[sin\left(\frac{\frac{b - b_z(step)}{\Delta b_{min}}}{x_{zmax} - x_{zmin}}\pi\right)\right]^2\right)$$

(B.42)

$$\frac{d}{dx}(sin(x) \cdot cos(x)) = cos^2(x) - sin^2(x)$$

(B.43)

The first order and the second order derivatives of the rest functions, like the quadratic functions, are straightforward to be found, which are not presented in this section.

APPENDIX C – DATASET

The simulation platform is built based on the data structure in MatPower version 5.1 with extensions. The missing data for AVC studies are the switchable shunt and the tap-able transformers models. The relevant data are therefore extracted from the RAW files.

In MatPower, the data is well organized in a so called "mpc" structure. The three extra "fields" for tap controllers, the switchable shunts and the voltage setpoints are built. The variable shunts are not separated from the shunt or the transformer tap controller fields.

Table 43 The data structure of switchable shunts in MatPower format.

Column	Content
1	Bus number
2	Number of step
3	Rated reactive power per step (negative is inductive)
4	Total initial MVar for each bus
5	Current step
6	Status

Switchable shunt data conversion from Raw ver.32 to the MatPower format.

Table 44 The shunt data structure in Raw version 32.

Column	Content
I - bus number	Bus number.
MODSW - Control mode	'0' or '1' in Danish grid. '1' indicates switchable mark in powerfactory. '0' indicates this shunt is controlled by shunt controllers. In OPF, both of them are treated as individual switchable shunts.
ADJM - Adjustment method	'0' in Danish case, which indicates stepwise regulation. For the tap-able shunts, they are modelled as two components i.e. a shunt with a tap-able transformer.
STAT - Initial status	'0' indicates out of service.
VSWHI - Controlled voltage upper limit	Do not need for OPF, since OPF uses bus voltage constraints.
VSWLO - Controlled voltage lower limit	
SWREM - The controlled bus number	Not relevant for OPF, since it is used for local shunt controller.
RMPCT - Percentage of MVar of shunt for control	100% for Danish case.
RMIDNT – for FACTs	Not relevant for Danish case.
BINIT – Initial switched shunt admittance in MVar based on unity voltage	Used to calculate the current step in MatPower.
Ni – Number of steps for each shunt	Total number of steps for a shunt i.
Bi – Admittance for each step in each shunt	Rated MVar for each step of a shunt i.

It can be seen that only the total initial MVar of each node is provided in the raw file. In case several shunts connected to the same bus, the current status of each bus should be specified based on values of BINIT, Ni and Bi. In case of several multi-steps shunts at the same bus, it may result in different combinations of shunts steps to meet the same total initial MVar at the bus. In this case, a simple rule

is made to find out the minimum total steps of shunts, i.e. bridging Table 43 and Table 45. An extra function is made to update the steps of the switchable shunts after the adjustments are mode on the source data in MatPower format, as described in Chapter 5.

Table 45 The data structure of switchable shunts in MatPower format.

Column	Content
1	Bus number
2	Min. Q
3	Max. Q
4	Total initial MVar for each bus
5	Optimal Q

- Extra transformer data in MatPower

The transformer in MatPower is converted to the branch model with fixed the tap-positions. In order to including the adjustable taps, more data are recorded from RAW files. The branch model in MatPower is therefore extended to include the data of the tap controllers.

Table 46. The data read from RAW files for the transformer tap control.

Column	Content
14	Phase Shifting
15	Upper voltage limits
16	Lower voltage limits
17	Total steps
18	Voltage change per tap in pu.
19	The minimum tap position
20	The maximum tap position
21	The current tap position

APPENDIX D – REPORT

In the simulation platform for assessing the AVC decision making algorithm, the optimization results with the grid information and the numerical settings are exported to external files.

The report includes:
- The basic information, i.e. the date and time for executions. The version of RAW files, the version of Matlab and the version of the interface of MPMO.
- The setting of the MPMOs, i.e. the numerical settings of the optimizations, the weights of MPMOs, the prices of each objective terms, the number of involved stages for each MPMO, the involved RAW files names for each MPMO.
- The information of the execution process, i.e. the index of the MPMO execution, the execution time, the convergence of the optimization process, the convergence of the discretization process, the penalty value in the discretization process and the rollback times in case non-convergence occurs for a certain MPMO.
- The results of MPMOs, i.e. the power loss, the total reactive power output, the total number of switching for the shunts, the total number of tap changing of the transformers and the values of the control variables.

The results are exported to the external files for the post processing, e.g. plot the figures for comparisons. The following reports are obtained via the post-processing.

Decision variables:
- The setpoints of the decision variables over the time horizon, i.e. the tap position, the shunt step and the reactive power outputs. It can be used to compare the results against the existing tool, VVD of the EMS.
- The changes of the setpoints over the time and the total changes for the evaluated period, i.e. $\sum|d\tau|$, $\sum|dB_{sh}|$ and $\sum d|Q_{pv}|$. It is can be used to fine-tuning the weights of the MPMO.
- The total numbers of controllers for each category of stages over the time, i.e. taps, shunt stations, shunts and generators.

Convergence:
- The convergence time of continuous MPMO and the discretization process over the time.
- The iterations of the discretization. It can be used to tune the increasing factor.
- The rollback times of stages over the time.

Objectives:
- The series losses over the time, i.e. results from SE, continuous MPMO and discretization of MPMO.
- The cost of each objective with/without the discretization, i.e. the loss cost, the tap changing cost, the shunt switching cost, the reactive power output cost and the total cost, over the time.

Voltage profile:

- The node voltage.
- The max/min voltage magnitudes in different voltage levels before/after the optimizations.

APPENDIX E – SHUNT CONTROLLERS IN DK1

Table 47. Categorize the stations into types.

Station	Shunt	Cap/ Ind	Voltage (KV)	Size (MVar)	Local Controls	Variable
ASR400	ASR_400-ZL2	ZL	420	70	NO	No
BED150	BED_150-ZL1	ZL	170	40	NO	No
BIL150	BIL_150-ZL1	ZL	170	40,37	NO	Yes
BJH150	BJH_150-ZL1	ZL	170	100	NO	Yes
	BJH_150-ZL2--$	ZL	165	50	NO	No
EDR150	EDR_150-ZL1	ZL	170	80,97	NO	No
	EDR_150-ZL2	ZL	170	80	RPC2	No
	EDR_150-ZL3	ZL	170	40	RPC2	No
FER150	FER_150-ZL31	ZL	170	80	NO	No
	FER_150-ZL32	ZL	170	40	NO	No
FER400	FER_400-ZL1	ZL	420	70	NO	No
	FER_400-ZL2	ZL	420	70	NO	No
FGD150	FGD_150-ZL1	ZL	170	80,68	NO	No
FGD400	FGD_400-ZF1	ZC	420	87	RPC1	No
	FGD_400-ZF2	ZC	420	87	RPC1	No
	FGD_400-ZF3	ZC	420	87	RPC1	No
	FGD_400-ZF4	ZC	420	87	RPC1	No
	FGD_400-ZL1	ZL	420	70	NO	No
IDU400	IDU_400-ZL1	ZL	420	70	NO	No
KAE150	KAE_150-ZL1	ZL	170	40	NO	No
KAS150	KAS_150-ZL1	ZL	170	168	NO	No
KAS400	KAS_400-ZL1	ZL	400	100,3	NO	No
KIN150	KIN_150-ZL11--$	ZL	170	40	NO	Yes
LAG400	LAG_400-ZL1	ZL	420	141,12	NO	No
	LAG_400-ZL2	ZL	400	110	NO	Yes
LOL150	LOL_150-ZL1	ZL	170	40	NO	No
NSP150	NSP_150-ZL31	ZL	165	40	NO	No
NVV150	NVV_150-ZL1	ZL	170	80	NO	No
REV400	REV_400-ZL1-	ZL	400	140	NO	Yes
STR150	STR_150-ZL1	ZL	170	40	NO	No
TJE150	TJE_150-ZA1	ZC	165	40	(YES)	No
	TJE_150-ZA2	ZC	165	80	(YES)	No
	TJE_150-ZA3	ZC	165	40	(YES)	No
	TJE_150-ZL1-	ZL	170	80	NO	No
TJE400	TJE_400-ZF1	ZC	420	65	RPC1	No
	TJE_400-ZF2	ZC	420	65	RPC1	No
	TJE_400-ZF3	ZC	420	65	RPC1	No
	TJE_400-ZF4	ZC	420	65	RPC1	No
	TJE_400-ZL1	ZL	420	70	NO	No
	TJE_400-ZL2	ZL	420	70	NO	No

Station	Shunt	Cap/ Ind	Voltage (KV)	Size (MVar)	Local Controls	Variable
TRI220	TRI_220-ZL1	ZL	235	120,3	RPC2	Yes
	TRI_220-ZL2	ZL	235	120,3	RPC2	Yes
TRI400	TRI_400-ZL1	ZL	420	141,12	NO	No
VHA150	VHA_150-ZL31	ZL	170	40	NO	No
VHA400	VHA_400-ZC1	ZC	400	55,3	NO	No
	VHA_400-ZF1	ZC	400	55,3	NO	No
	VHA_400-ZF2	ZC	400	20,1	NO	No
	VHA_400-ZF3	ZC	400	55,3	NO	No
	VHA_400-ZF4	ZC	420	60	RPC1	No
	VHA_400-ZF5	ZC	420	60	RPC1	No
	VHA_400-ZF6	ZC	420	60	RPC1	No
	VHA_400-ZL1	ZL	420	58,93	NO	No
VID150	VID_150-ZL1	ZL	165	40	NO	No
ÅBØ150	ÅBØ_150-ZL31	ZL	165	40	NO	No
ÅSP150	ÅSP_150-ZL1	ZL	170	60	NO	No

The summary is end up June 1st in 2016.

The nominal reactive power of each shunt should be converted based on the same voltage base in the model.

The data source is Elvis database:
(1). Version 20140520 1131-PUB-REF
(2). Info from Automation section – 'Reactive Components after HSC comments'

ZL – Shunt reactors
ZC – Shunt capacitors

Local Control:
RPC – There is local control via Reactive Power Controllers.
NO – There is no local control devices.
(YES) – There is physical device of RPC but not activated.

TJE150, VHA150 and FGD400 are installed synchronous condensers.

Location	Min. Q (MVar)	Max. Q (MVar)
VHA_150	-50	105
TJE_150	-30	160
FGD_400	-100	200

Each variable shunt is counted as two controllers i.e. the tap controller on the ideal transformer and the switch of the whole variable shunt.

Table 48 The existing switchable shunts and the synchronous condenser in DK1.

TYPE	Nr. of stations	Name of stations	Comments	Nr. of Controllers
I	15	The rest	Single switchable shunt	1
Iv	3	BJL150, KIN150 and REV400	Single variable shunt	1
Ic	2	VHA150 + FGD400(RPC)	Single switchable shunt with synchronous condenser	1
II	3	FER150 and FER400 + TJE400(RPC)	Two switchable shunts	2
IIv	2	BJH150 and LAG400	One switchable shunt and one variable shunt	3
IIv2	1	TRI220(RPC) – Not included	Two variable shunts	4
III	1	EDR150(RPC) (II + I) – Not included	Three switchable shunts	3
IVc	1	TJE150 (IIIc + I)	Four switchable shunts with synchronous condenser	4
V	1	VHA400(RPC)	Four switchable shunts	5

Notice the variable shunts may have different tap directions for regulations. The shunts in EDR150 and TJE150 may be separated into two buses if the couplers of buses are closed. Many capacitor shunts are in VHA400 that require the charging time before cut in to the grid. These capacitor shunts are therefore not taken into account for the up regulations. They participate only in the down regulations, in which they are cut off if the terminal voltage is higher than the reference in Mode 1 or the upper triggering limit in Mode 2. All the shunts addressed by RPCs are not assigned by the fallback controllers.